UNIVERSITÉ DE STRASBOURG

ÉCOLE DOCTORALE DES SCIENCES CHIMIQUES

UMR 7006 – Institut de Science et d'Ingénierie Supramoléculaires (I.S.I.S.)

THÈSE

présentée par :

Mirella EL GEMAYEL

soutenue le : **19 Juin 2014**

pour obtenir le grade de : **Docteur de l'université de Strasbourg**

Discipline/ Spécialité : Chimie-Physique

Dispositifs et architectures supramoléculaires électroactives à base de graphène

THÈSE dirigée par :

M. SAMORÌ Paolo	Professeur, Université de Strasbourg, France

RAPPORTEURS :

M. BISCARINI Fabio	Professeur, Université de Modena et Reggio Emilia, Modena, Italie
M. CAMPIDELLI Stéphane	Docteur, Laboratoire d'Electronique Moléculaire, CEA, Gif-sur-yvette, France

---

AUTRES MEMBRES DU JURY :

M. BERCIAUD Stéphane	MCF, Université de Strasbourg– Examinateur interne

Résumé

Les technologies émergentes exigent de plus en plus un développement de nouveaux matériaux semi-conducteurs.[1] Ces derniers nécessitent à la fois une bonne solubilité, une stabilité à conditions ambiantes et une haute mobilité des porteurs de charge pour des applications en électronique organique et plus particulièrement en transistors organiques à effet de champ nommés OFETs. Ces derniers sont non seulement des éléments essentiels pour la prochaine génération de circuits organiques flexibles à prix réduit, mais aussi un outil pour étudier la relation entre la structure et les propriétés des systèmes π-conjugués. La morphologie des couches à base de semi-conducteur organiques est l'un des principaux facteurs qui affecte les caractéristiques électroniques des dispositifs et en particulier le transport des porteurs de charge. Dans le cas des polymères semi-conducteurs, malgré le fait qu'ils soient capables de former des réseaux étendus facilitant le transport des charges, ils sont polycristallins; de ce fait le film obtenu est caractérisé par la présence de défauts morphologiques, des joints de grains et des domaines amorphes restreignant ainsi un transport efficace de charges.[2] Récemment, une nouvelle stratégie a été utilisée [3-8] afin de résoudre ce problème, dans le but d'obtenir les propriétés requises pour un dispositif particulier. Cette méthode consiste à mélanger des composants différents pour permettre de dépasser les performances des composants individuels tout en bénéficiant des propriétés avantageuses apportées par chacun. Idéalement, pour faciliter la fabrication, il est préférable de déposer en même temps les deux composants dissous dans un même solvant en une seule étape.

Dans cette thèse, on a adopté cette approche pour:

1. Stimuler le comportement ambipolaire d'un polymère semi-conducteur de type *n* en le déposant simultanément avec du graphène produit par exfoliation en phase liquide.

2. Améliorer la percolation des charges dans un polymère semi-conducteur de type *p* à l'aide d'un nanoruban de graphène (nommé GNR) de type armchair *N*=18 nouvellement conçu.
3. Conférer de nouvelles propriétés au dispositif en variant ses propriétés électriques via un stimulus lumineux.

Mélange avec le graphène

La fabrication de transistors à effet de champ ambipolaire capables de transporter à la fois des électrons et des trous dans des conditions de sollicitation appropriées dans un seul appareil est très importante en raison de leur application dans des circuits logiques complémentaires.[9] Le comportement ambipolaire peut être obtenu soit par conception sophistiquée d'un composant unique constitué de molécules semi- conductrices à bande étroite, c'est à dire inférieur à 2 Ev ;[10] soit en utilisant des bicouches de semi-conducteurs[11-14] avec des niveaux d'énergie choisis avec soin de manière à minimiser la barrière d'injection pour un type de charges lorsque des électrodes de même type de matériau sont employées. Au contraire, cette ambipolarité peut être obtenue par évaporation simultanée [15-16] ou déposition simultanée[17-20] de la solution d'un mélange de semi-conducteurs de type *n* et *p*. Basés sur le concept de mélange de matériaux, on montre que le comportement ambipolaire, et en particulier le courant de trou d'un polymère semi-conducteur de type *n* (disponible sur le marché), le poly [N, N 9-bis(2-octyldodecyl)-naphthalene-1,4,5,8-bis(dicarboximide)-2,6-diyl]-alt-5,59-(2,29-bithiophene)], P(NDI2OD-T2), peut être stimulé par co-dépôt avec du graphène produit par exfoliation en phase liquide. Le graphène est un matériau ambipolaire 2D ayant une mobilité des porteurs de charge supérieure à 15 000 $cm^2 V^{-1} s^{-1}$, même à conditions ambiantes, [21] ce qui est une performance qui dépasse celle de tout semi-conducteur organique ou même silicium. Malgré ses propriétés optiques, électroniques et mécaniques exceptionnelles, le plus grand défi reste sa production en grande quantité et en très haute qualité à l'aide de méthodes évolutive à l'échelle industrielle. Parmi les différentes méthodes valables, on a choisi l'exfoliation en phase liquide tout en commençant par la poudre de graphite. Cette technique est extrêmement polyvalente et très facile pour la production de graphène et bénéficie d'un rendement élevé.[23] Le graphène produit, a été étudié par spectroscopie ultraviolet-visible et par microscopie électronique à balayage

(MEB) en collaboration avec le groupe du Dr. Ovidiu Ersen (de l'IPCMS à l'université de Strasbourg en France).

En outre, le graphène est un semi-conducteur dont la bande interdite vaut zéro.[21] Par conséquence, il est impossible d'éteindre les dispositifs basés sur le graphène comme matériau actif dans leurs chaînes, ce qui les rends inconvenables pour des applications dans des circuits logiques. Pour résoudre ce problème, il est possible de l'incorporer dans une matrice d'un polymère semi-conducteur.[24-26] Donc, on a préparé et caractérisé des transistors à effet de champ FETs (dont la géométrie est telle que la grille est déposée en premier et le semi-conducteur est déposé sur les électrodes) de différentes longueurs de chaînes. Ils sont basés sur P(NDI2OD-T2) mélangé avec du graphène à concertations massiques différentes (déposés par spin-coating). L'effet de l'incorporation du graphène sur la performance du transistor a été étudié. La morphologie a été examinée par microscopie à force atomique (AFM). D'une part, la mobilité à effet de champ pour les électrons augmente légèrement avec la hausse de la concentration du graphène pour les dispositifs à chaîne courte. D'autre part, la mobilité à effet de champ pour les trous a été remarquablement améliorée avec l'augmentation de la quantité du graphène jusqu'à un mélange de fraction massique de 150:1. Pour cette fraction et par comparaison avec les dispositifs basés sur P(NDI2OD-T2) tout seul, le facteur d'augmentation de la mobilité était de 45 pour les dispositifs ayant 2.5 µm comme longueur de chaîne ; leur I_{on}/I_{off} ainsi que leur tension de seuil étaient 10^3 et proche de zéro respectivement. Cette amélioration peut être dûe à un alignement de niveau d'énergie du graphène avec la fonction de travail des électrodes, ainsi qu'à la formation des voies de percolation qui facilitent le transport de charges suite à l'introduction des feuillets de graphène dans la matrice du polymère de type *n*. Nos résultats montrent que plus la longueur de la chaîne diminue, plus la probabilité des feuillets de graphène connectés entre les deux électrodes s'élève et donc meilleur est le transport de charge. Néanmoins, cette performance améliorée a été accompagnée par un compromis de l'état "off" du courant de drain qui tend à diminuer de plus d'un ordre de grandeur à concentrations élevées de graphène réduisant ainsi le rapport I_{on}/I_{off}.

Mélange avec des nanorubans de graphène

Pour résoudre le problème indiqué ci-dessus, et pour offrir au graphène la capacité de changer entre l'état off et l'état on, il est possible de le confiner dans l'espace tout en réduisant sa largeur

et former par conséquence des nanorubans (nommés GNR).[27]La majorité des méthodes utilisées pour la production des GNRs souffrent du contrôle de la largeur des nanorubans ainsi que des défauts sur leurs bords,[28-30]ce qui aboutit à des structures avec des propriétés électroniques non-uniformes. En collaboration avec le groupe du Prof. Klaus Müllen (de l'Institut Max-Planck de recherche sur les polymères en Allemagne) nous avons bénéficié d'un nouveau nanoruban N = 18 de type armchair synthétisé par Akimitsu Narita en suivant l'approche bottom-up. Ce GNR possède une largeur latérale d'environ 2,1 nm et de plus celui-ci est soluble dans des solvants organiques courants. On l'a intégré dans un réseau de polymère de type *p* (disponible sur le marché), le (3- hexylthiophène) - P3HT. Des transistors ont été fabriqués par spin-coating et ensuite caractérisés. On a étudié l'effet de l'ajout des GNRs à différentes concentrations (au P3HT) sur les propriétés électriques des dispositifs tels que la mobilité, la tension de seuil et le I_{on}/I_{off}. Comparés aux transistors basés sur du P3HT pure, ceux avec du GNR montrent un accroissement de la mobilité de charge d'un facteur de trois. Ceci est probablement dû aux GNRs qui facilitent le transport de charges au sein de la chaîne de conduction tout en connectant les domaines du film semi-conducteur. Le rapport I_{on}/I_{off} n'as pas été affecté par l'addition des GNRs à des concentrations différentes. De plus, la morphologie a été étudiée par AFM. Pour clarifier si la cristallinité du film P3HT a été modifiée par la présence des GNRs, des mesures de diffraction des rayons X en incidence rasante (GIXD) ont été effectuées en collaboration avec Dr Adam Kiersnowski et Dr. Wojciech Pisula (de l'Institut Max- Planck de recherche sur les polymères en Allemagne). En plus, nous avons étudié l'influence de l'illumination en utilisant une lumière monochromatique sur les caractéristiques électriques des dispositifs visant à explorer l'utilisation potentielle de ce mélange comme couche active dans des phototransistors organiques hybrides (OPT). En particulier, l'influence des GNRs sur les porteurs photo–générés a été étudiée. Pour gagner plus d'informations sur l'origine locale de la photo-réponse générée et du rôle des GNRs sous l'éclairage, nous avons étudié ces transistors en utilisant la microscopie à balayage photoélectrique en collaboration avec Dr. Ravi S. Sundaram et Prof. Andrea C. Ferrari (de l'Université de Cambridge, Royaume-Uni).

Nanographènes comme chaîne

Nous avons également étudié le potentiel d'ionisation d'une série de nanographenes chlorés et non-chlorés[31] ayant un nombre de carbone allant de 42 à 222 qui ont été fournis par le groupe du Prof. Klaus Müllen. Une des structures avec des bords chlorés a été choisie et étudiée comme un matériau de chaîne du FET. Ces transistors ayant des électrodes soit en or ou en aluminium ont montré un transport de type *n* avec une faible mobilité à effet de champ. De plus, les électrodes en Au ont également été fonctionnalisées avec des monocouches auto-assemblées pour améliorer l'injection de charges.

Mélange avec des molécules photochromiques

Basé sur la réussite de notre approche consistant à utiliser des mélanges soit avec graphène ou GNRs comme matières actives dans la chaîne du FET, nous avons pensé à étendre notre étude à des molécules photochromiques où la lumière peut servir comme paramètre de contrôle supplémentaire pour la modulation des propriétés électriques et plus précisément la conductivité électrique.[32] Ce type de dispositifs est important pour les mémoires optiques. Dans ce projet, nous avons choisi comme molécules photochromiques deux dérivés de diaryléthènes (DAE) qui ont différents substituants alkyles et qui ont été synthétisés par Dr. Martin Herder dans le groupe du Prof. Stefan Hecht (de l'Université Humboldt de Berlin en Allemagne).

Pourtant, avant de poursuivre avec l'utilisation du graphène comme électrodes, nous avons préféré comprendre s'il y a une différence dans la séparation de phase lors du mélange de DAE soit avec un semi-conducteur à base de polymère ou avec une molécule de petite taille. En particulier, il est nécessaire de comprendre si cela affecte les propriétés électroniques des dispositifs; notamment, si l'environnement dans lequel les molécules photochromiques sont ajoutées influence leurs photocommutation. Comme molécule de petite taille, on a sélectionné 2,7-dialkyl-benzothieno[3,2-b]benzothiophene (BTBT) avec $C_{12}H_{25}$ comme chaine alkyle (C_{12} BTBT) à cause de sa mobilité de champ supérieure à 0.1 $cm^2 \cdot V^{-1} \cdot s^{-1}$[33] pour une couche mince déposée par spin-coating et 16.4 $cm^2 \cdot V^{-1} \cdot s^{-1}$[34] pour le monocristal; ce qui le classe parmi les meilleurs matériaux de type *p*. Cette molécule a été synthétisée par le groupe du Prof. Yves Geerts (de l'Université libre de Bruxelles en Belgique). Comme polymère, le P3HT a été choisi. Des dispositifs de différentes géométries ont été fabriqués par spin-coating et dont le film est

composé du mélange de DAE soit avec P3HT soit avec BTBT. Les résultats montrent que la performance des transistors est affectée par le type des substituants sur les DAEs lorsqu'ils sont mélangés avec le BTBT, ce qui n'était pas le cas du mélange avec P3HT. Pour clarifier cette constatation, on a effectué des mesures GIXD en collaboration avec le groupe du Prof. Alberto Salleo (de l'Université de Stanford aux Etats-Unis). En plus, la morphologie a été étudiée par AFM. Nous avons étudié l'effet de la lumière sur le courant de drain des dispositifs qui a été varié par la photoisomérisation de DAE sous irradiations de lumière visible ou ultraviolette. On a constaté que la modulation du courant de drain peut être variée différemment en fonction des niveaux d'énergie de la molécule accueillante pour le DAE (i.e. s'il s'agit d'un polymère ou d'une petite molécule). La spectroscopie a été utilisée pour étudier la photoisomérisation de films composés des dérivés de DAE dans BTBT révélant des constantes de vitesse différentes pour l'isomérisation lors de la transition de la forme ouverte à la forme fermée du DAE. Cela prouve que les DEA étudiées interagissent différemment avec les molécules accueillantes et en fonction de leur type de substituants.

En conclusion, le graphène préparé par exfoliation en phase liquide peut être utilisé dans des dispositifs à couches minces préparées par dépôt simultané d'un semi-conducteur polymère afin d'augmenter l'ambipolarité de ce dernier. Notre stratégie qui consiste à combiner les performances élevées du graphène et la capacité idéale des polymères conjugués à former un film par un procédé de dépôt en une étape simple, fournit un potentiel pour l'application des matériaux hybrides à base de graphène dans les circuits logiques.

Puis, on a également démontré qu'il est possible d'augmenter d'un facteur de trois la mobilité à effet de champ dans un dispositif de P3HT en ajoutant 24 % de GNRs, sans altérer les autres caractéristiques électroniques pertinentes du transistor tels que le I_{on}/I_{off}. On a constaté que la photoréponse de transistors basés sur GNR-P3HT dépend de la quantité de chaque composant dans le mélange ainsi que de la longueur de la chaîne. Ceci est avantageux pour l'utilisation de ces dispositifs en optoélectronique.

Et enfin, l'effet de mélange de semi-conducteurs organiques / polymériques avec des molécules photochromiques (exposant différents substituants alkyle) sur les performances électriques des transistors à couches minces a été étudié. Lors d'une irradiation, la photoisomérisation de DAE module le courant qui peut être varié différemment selon les niveaux d'énergie de la molécule

avec laquelle le DAE est mélangé; si c'est un polymère ou une petite molécule. Ce résultat offre une possibilité pour des applications dans des mémoires optiques.

Abstract

Emerging technological demands are attracting more and more attention into the development of new semiconducting materials[1] combining solution processability, stability under ambient conditions and high charge carrier mobility for application in organic electronics and particularly in organic field-effect transistors (OFETs). The latters are not only essential building blocks for the next generation of cheap and flexible organic circuits, but they also act as a tool for exploring the structure-property relationship of π-conjugated systems. Among the influencing factors affecting the device physics and particularly the charge carrier mobility, is the morphology of the organic semiconducting layer. In the case of polymer semiconductors, despite the fact that they can form extended networks for efficient percolation of charges, due to their polycrystalline nature, the obtained material is characterized by the presence of morphological defects, grain boundaries and amorphous domains hampering efficient charge transport.[2] To circumvent this problem and in order to obtain the required properties for a particular device, new strategy has been used recently.[3-8] It consists of blending different components with the aim of exceeding the performance of the individual components and benefiting of the advantageous properties brought by each one. Ideally, for ease of fabrication, a simple co-deposition step using common solvent for both components is preferred.

In this thesis, we have adopted this approach for:

1. Boosting the ambipolar behavior of *n*-type polymer semiconductor by co-deposition with liquid phase exfoliated graphene.

2. Improving the percolation of charges in a *p*-type polymer semiconductor using newly designed *N*=18 armchair graphene nanoribbon (GNR).
3. Conferring new properties to the device by tuning its electrical properties via light stimulus.

Blend with graphene

Fabrication of ambipolar field-effect transistors capable of transporting both electrons and holes under suitable biasing conditions in one device is very important due to their application in complementary logic circuits.[9] Ambipolar behavior can be achieved by designing sophisticated single component semiconducting molecules with narrow band gaps, i.e. lower than 2 eV[10] or by using bilayers of semiconductors[11-14] with energy levels selected carefully in a way to minimize the injection barrier for one type of charges when a single electrode material is employed. Conversely, ambipolarity can be obtained by co-evaporation[15-16] or co-deposition[17-20] from solution of a blend of n and *p*-type material. Based on the concept of blending materials, we show that the ambipolar behavior, and particularly the hole current of a commercially available *n*-type polymer semiconductor poly [N, N 9-bis(2-octyldodecyl)-naphthalene-1,4,5,8-bis(dicarboximide)-2,6-diyl]-alt-5,59-(2,29-bithiophene)], P(NDI2OD-T2) can be boosted by co-deposition with liquid phase exfoliated graphene. Graphene is a well-defined functional 2-dimensional ambipolar material with a mobility for charge carriers exceeding 15,000 $cm^2 V^{-1} s^{-1}$ even under ambient conditions,[21] thus outperforming any organic semiconductor or even silicon. Despite its exceptional optical, mechanical and electronic properties,[22] the greatest challenge remains the ability to process it in large quantities and high quality making use of up-scalable methods. Among the various proposed methods, we used liquid-phase exfoliation starting from graphite powder. This procedure is extremely versatile and easily accessible for producing graphene with high yield.[23] We investigated the exfoliated graphene by UV-vis spectroscopy, Scanning Electron Microscopy (SEM). The number of layers in a flake were determined by High Resolution Transmission Electron Microscopy (HR-TEM) in collaboration with Dr. Ovidiu Ersen from IPCMS, France.

Furthermore, graphene is a zero bandgap semiconductor,[21] thus devices with channels made with graphene cannot be switched off and therefore are not suitable for applications in logic circuits; however, for solving this issue, it can be incorporated in a matrix of polymer semiconductor.[24-26]

Therefore, we prepared and characterized bottom-gate bottom-contact FETs (with different channel lengths) based on P(NDI2OD-T2) blends with graphene at different weight ratios (deposited by spin coating). The effect of adding graphene on the device performance was investigated. The morphology was examined by Atomic Force Microscopy (AFM). On the one hand the field-effect mobility of electrons slightly increases with increasing the concentration of graphene for the short channel lengths devices. On the other hand, the field-effect mobility of holes was substantially improved with increasing the amount of graphene up to a blend ratio of 150:1 in weight. At this ratio and for the 2.5 μm channel length devices, the increasing factor was by 45 folds while the I_{on}/I_{off} ratio was as high as 10^3 and the threshold voltage closer to zero as compared to the devices based on pure P(NDI2OD-T2). The improvement is due to a better energy level alignment of the graphene with the work function of the electrodes, and to the creation of percolating pathways for the transport of charges as a result of the embedment of the graphene sheets in the *n*-type polymer matrix. Our results show that the smaller the channel length, the better charge transport, due to the higher probability of the connected graphene sheets to bridge the electrodes. Nevertheless, this enhanced performance was accompanied by a trade off with the drain current in the "off state" which tends to decrease by more than one order of magnitude at high concentrations of graphene thus lowering the I_{on}/I_{off} ratio.

Blend with GNR

To overcome the above mentioned problem and to impart to graphene a capacity to switch *on* and *off,* one can confine it in space by generating graphene nanoribbon (GNR).[27] Most of the methods used for obtaining GNRs result in structures with non-uniform electronic properties since neither the GNRs' width distribution nor the defects on the edges can be controlled.[28-30] In collaboration with Prof. Klaus Müllen from Max-Planck Institute for Polymer Research in Germany, we have used an unprecedented $N = 18$ armchair GNR synthesized by Akimitsu Narita using bottom-up approach. This GNR possesses a lateral width of ~2.1 nm and is soluble

in common organic solvents. We have added it to a matrix of commercially available regioregular poly(3-hexylthiophene) - P3HT. Bottom-gate bottom-contact FETs were fabricated (by spin coating) and characterized. The effect of the GNRs at different concentrations (in the blend with P3HT) on the device performance in dark such as the field-effect mobility, threshold voltage and the I_{on}/I_{off} has been investigated. The resulting FETs have a three-fold increase in the charge carrier mobilities in blend films, when compared to pure P3HT devices. This behavior can be ascribed to GNRs facilitating the transport of the charges within the conduction channel by connecting the domains of the semiconductor film.[24] The I_{on}/I_{off} ratio was not affected by the addition of GNRs at different loads. The morphology was studied by AFM. In order to investigate if the order within P3HT film is altered upon addition of GNRs, Grazing Incidence X-ray Diffraction (GIXD) measurements were carried out in collaboration with Dr. Adam Kiersnowski and Dr. Wojciech Pisula from Max-Planck Institute for Polymer Research in Germany. Furthermore, we have studied the influence of illumination with monochromatic light on the electrical characteristics of the devices aiming at exploring the potential use of this blend as active layer in hybrid organic phototransistors (OPTs). In particular the influence of the GNRs on the photo-generated carriers was investigated. To gain more information about the local origin of the generated photoresponse and the role of the GNRs under illumination, we studied these devices using scanning photocurrent microscopy in collaboration with Dr. Ravi S. Sundaram and Prof. Andrea C. Ferrari from Cambridge University, UK.

Nanaographenes as channel

We have also investigated the ionization potential of a series of chlorinated and pristine nanographenes[31] with carbon numbers ranging from 42 to 222 which were provided by the group of Prof. Klaus Müllen. One structure with chlorinated edges was selected and studied as a channel of FET. It displays *n*-type transport with low field-effect mobility. Devices were prepared either using Al or Au electrodes. In the latter case, Au was also functionalized with self-assembled monolayers in order to improve the charge injection.

Blends with photochromic molecules

Based on our successful approach using blends with either graphene or GNRs as active materials in the channel of FETs, we thought of extending our study to photochromic molecules where light is used as additional control parameter for the modulation of the electrical properties and more precisely the electrical conductivity.[32] This kind of devices is important for optical memories. We selected as photochromic molecules two diarylethenes (DAE) derivatives with different alkyl substituents which were synthesized by Dr. Martin Herder from the group of Prof. Stefan Hecht from Humboldt-University Berlin, Germany.

Yet, before carrying on with the use of graphene as electrodes, we preferred to understand if there is a difference in phase separation when blending DAE with either small molecule or a polymer semiconductor and how does that affect the electronic properties of the devices; particularly, the influence of the hosting environment on the photoswitching of DAE. As small molecule, 2,7-dialkyl-benzothieno[3,2-b]benzothiophene (BTBT) with $C_{12}H_{25}$ alkyl chains (C_{12} BTBT) was chosen because of its high field-effect mobility i.e. higher than 0.1 $cm^2.V^{-1}.s^{-1}$[33] for spin-coated films and 16.4 $cm^2.V^{-1}.s^{-1}$[34] for the single crystal, which is among the highest for *p*-type material. It was provided by the group of Prof. Yves Geerts, from the Université libre de Bruxelles in Belgium. P3HT was chosen as polymer for our case study. Bottom-gate bottom-contact and bottom-gate top-contact devices were fabricated by spin-coating the blends with either P3HT or BTBT with DAE. It was found that the device performance is affected by the type of the substituents on the photochromic molecules when mixed with BTBT, which wasn't the case of the blend with P3HT. To gain further insight, we performed XRD in collaboration with Prof. Alberto Salleo from Stanford University, USA. Also we investigated the morphology by AFM. We explored the effect of light on the drain current of the devices which was found to vary by triggering the photoisomerisation of DAE under UV or visible light irradiations. We found that the drain current modulation can be tuned differently depending on the energy levels of the hosting molecule whether it is a polymer or a small molecule. Spectroscopy study was used to investigate the photoisomerisation of films of DAE derivatives in BTBT revealing

different rate constants for the isomerization of the open to closed transition of DAEs. This proves that the investigated DAEs interact differently with the host depending on the substituents and on their hosting environment.

Summary

In summary, graphene prepared by liquid-phase exfoliation can be used in thin-film devices prepared by co-deposition with a polymeric semiconductor in order to boost the ambipolar character of the latter. Our strategy of combining the high performance of graphene and the ideal film forming ability of conjugated polymers in a simple one-step deposition process, provides a prospective pathway for the application of graphene based hybrid materials for logic circuits.

We also demonstrated that it is possible to obtain a three-fold increase in the field-effect mobility in a P3HT device by adding 24% of GNRs to the thin film, without altering the other relevant electronic characteristics of the transistor such as the I_{on}/I_{off}. We found that the transistor's photoresponse in GNR – P3HT binary mixtures depends on the quantity of each component in the blend as well as on the channel length. This finding represents a step forward toward the potential use of these devices in (opto)electronics.

Moreover, the effect of the blending of organic/polymeric semiconductors with photochromic molecules exposing different alkyl substituents on the electrical performance of TFTs was studied. Upon irradiation, the photoisomerisation of DAE results in drain current modulation which can be tuned differently depending on the energy levels of the hosting molecule whether it is a polymer or a small molecule paving the way for potential applications in optical memories.

References

[1] C. Wang, H. Dong, W. Hu, Y. Liu, D. Zhu, *Chem. Rev.* **2011**, *112*, 2208.
[2] J. Smith, R. Hamilton, Y. B. Qi, A. Kahn, D. D. C. Bradley, M. Heeney, I. McCulloch, T. D. Anthopoulos, *Adv. Funct. Mater.* **2010**, *20*, 2330.
[3] R. Hamilton, J. Smith, S. Ogier, M. Heeney, J. E. Anthony, I. McCulloch, J. Veres, D. D. C. Bradley, T. D. Anthopoulos, *Adv. Mater.* **2009**, *21*, 1166.

[4] E. Lim, B. J. Jung, M. Chikamatsu, R. Azumi, K. Yase, L. M. Do, H. K. Shim, *Org Electron* **2008**, *9*, 952.
[5] E. Orgiu, A. M. Masillamani, J.-O. Vogel, E. Treossi, A. Kiersnowski, M. Kastler, W. Pisula, F. Dotz, V. Palermo, P. Samorì, *Chem. Commun.* **2012**, *48*, 1562.
[6] D. M. Russell, C. J. Newsome, S. P. Li, T. Kugler, M. Ishida, T. Shimoda, *Appl. Phys. Lett.* **2005**, *87*, 222109.
[7] J. Smith, R. Hamilton, M. Heeney, D. M. de Leeuw, E. Cantatore, J. E. Anthony, I. McCulloch, D. D. C. Bradley, T. D. Anthopoulos, *Appl. Phys. Lett.* **2008**, *93*, 253301
[8] J. Smith, W. Zhang, R. Sougrat, K. Zhao, R. Li, D. Cha, A. Amassian, M. Heeney, I. McCulloch, T. D. Anthopoulos, *Adv. Mater.* **2012**, *24*, 2441.
[9] K.-J. Baeg, M. Caironi, Y.-Y. Noh, *Adv. Mater.* **2013**, *25*, 4210.
[10] E. J. Meijer, D. M. de Leeuw, S. Setayesh, E. van Veenendaal, B. H. Huisman, P. W. M. Blom, J. C. Hummelen, U. Scherf, T. M. Klapwijk, *Nat. Mater.* **2003**, *2*, 678.
[11] F. Dinelli, R. Capelli, M. A. Loi, M. Murgia, M. Muccini, A. Facchetti, T. J. Marks, *Adv. Mater.* **2006**, *18*, 1416.
[12] C. Rost, D. J. Gundlach, S. Karg, W. Rieß, *J. Appl. Phys.* **2004**, *95*, 5782.
[13] J. Wang, H. Wang, X. Yan, H. Huang, D. Yan, *Appl. Phys. Lett.* **2005**, *87*.
[14] S. D. Wang, K. Kanai, Y. Ouchi, K. Seki, *Org Electron* **2006**, *7*, 457.
[15] C. Rost, S. Karg, W. Riess, M. A. Loi, M. Murgia, M. Muccini, *Appl. Phys. Lett.* **2004**, *85*, 1613.
[16] K. N. N. Unni, A. K. Pandey, S. Alem, J.-M. Nunzi, *Chem. Phys. Lett.* **2006**, *421*, 554.
[17] S. Cho, J. Yuen, J. Y. Kim, K. Lee, A. J. Heeger, *Appl. Phys. Lett.* **2006**, *89*.
[18] M. Shkunov, R. Simms, M. Heeney, S. Tierney, I. McCulloch, *Adv. Mater.* **2005**, *17*, 2608.
[19] K. Szendrei, D. Jarzab, Z. Chen, A. Facchetti, M. A. Loi, *J. Mater. Chem.* **2010**, *20*, 1317.
[20] M. Treier, J.-B. Arlin, C. Ruzie, Y. H. Geerts, V. Lemaur, J. Cornil, P. Samorì, *J. Mater. Chem.* **2012**, *22*, 9509.
[21] K. S. Novoselov, A. K. Geim, S. V. Morozov, D. Jiang, Y. Zhang, S. V. Dubonos, I. V. Grigorieva, A. A. Firsov, *Science* **2004**, *306*, 666.
[22] A. K. Geim, K. S. Novoselov, *Nat. Mater.* **2007**, *6*, 183.
[23] A. Ciesielski, P. Samorì, *Chem. Soc. Rev.* **2014**, *43*, 381.
[24] J. Huang, D. R. Hines, B. J. Jung, M. S. Bronsgeest, A. Tunnell, V. Ballarotto, H. E. Katz, M. S. Fuhrer, E. D. Williams, J. Cumings, *Org Electron* **2011**, *12*, 1471.
[25] A. Liscio, G. P. Veronese, E. Treossi, F. Suriano, F. Rossella, V. Bellani, R. Rizzoli, P. Samorì, V. Palermo, *J. Mater. Chem.* **2011**, *21*, 2924.
[26] F. Torrisi, T. Hasan, W. Wu, Z. Sun, A. Lombardo, T. S. Kulmala, G.-W. Hsieh, S. Jung, F. Bonaccorso, P. J. Paul, D. Chu, A. C. Ferrari, *ACS Nano* **2012**, *6*, 2992.
[27] L. Chen, Y. Hernandez, X. Feng, K. Müllen, *Angew. Chem. Int. Ed.* **2012**, *51*, 7640.
[28] L. Jiao, L. Zhang, X. Wang, G. Diankov, H. Dai, *Nature* **2009**, *458*, 877.
[29] D. V. Kosynkin, A. L. Higginbotham, A. Sinitskii, J. R. Lomeda, A. Dimiev, B. K. Price, J. M. Tour, *Nature* **2009**, *458*, 872.
[30] ShimizuT, HaruyamaJ, D. C. Marcano, D. V. Kosinkin, J. M. Tour, HiroseK, SuenagaK, *Nat. Nanotech.* **2011**, *6*, 45.
[31] Y.-Z. Tan, B. Yang, K. Parvez, A. Narita, S. Osella, D. Beljonne, X. Feng, K. Müllen, *Nat Commun* **2013**, *4*.

[32] E. Orgiu, N. Crivillers, M. Herder, L. Grubert, M. Pätzel, J. Frisch, E. Pavlica, D. T. Duong, G. Bratina, A. Salleo, N. Koch, S. Hecht, P. Samorì, *Nat Chem* **2012**, *4*, 675.
[33] H. Ebata, T. Izawa, E. Miyazaki, K. Takimiya, M. Ikeda, H. Kuwabara, T. Yui, *J. Am. Chem. Soc.* **2007**, *129*, 15732.
[34] Z. Qi, X. Liao, J. Zheng, C.-a. Di, X. Gao, J. Wang, *Appl. Phys. Lett.* **2013**, *103*.

Contents

Symbols and Abbreviations

AFM	atomic force microscopy
a-GNR	armchair graphene nanoribbon
BC	bottom-contact
BE	back scattered electrons
BG	bottom-gate
BTBT	2,7-dialkyl-benzothieno[3,2-b]benzothiophene
CFL	capillary force lithography
C_i	capacitance of the dielectric per unit area [$F \cdot cm^{-2}$]
CMOS	complementary metal-oxide semiconductor
CNT	carbon nanotube
CV	cyclic voltammetry
CVD	chemical vapor deposition
DAE	diarylethene
DFT	density functional theory
D_{it}	interface-trap density
DOS	density of states
E_a	activation energy [$Kj \cdot mol^{-1}$]
e-beam	electron beam
E_D	Dirac energy
EDX	energy dispersive X-ray
E_F	Fermi Energy [eV]
E_g	band gap energy [eV]
eq.	equation
FET	field-effect transistor
GIXD	grazing incidence X-ray diffraction
GNR	graphene nanoribbon
HBC	hexabenzocoronene
HMDS	hexamethyldisilazane
HOMO	highest occupied molecular orbitals

HR-TEM	high resolution transmission electron microscopy
I_D	source-drain current for a grounded source [A]
I_{dark}	current in dark [A]
IE	ionization energy
I_{light}	current under illumination [A]
I_{off}	drain current in the off state [A]
I_{on}	drain current in the on state [A]
I_{ph}	photocurrent [A]
ITO	indium tin oxide
k_B	Boltzmann constant
L	channel length [μm]
LCAO	linear combination of atomic orbitals
LUMO	lowest unoccupied molecular orbitals
MO	molecular orbital
MS	Mott-Schottky
MTR	multiple trapping and thermal release
N_a	number of dimer chains
NMP	N-methyl-2-pyrrolidone
N_z	number of zigzag chains
o-DCB	orthodichlorobenzene
OFET	organic field-effect transistor
OPT	organic phototransistor
OTDS	octadecyl-trichlorosilane
OTS	octatrichlorosilane
P	pressure [mbar]
P	photosensitivity
P(NDI2OD-T2)	poly [N, N 9-bis(2-octyldodecyl)-naphthalene-1,4,5,8-bis(dicarboximide)-2,6-diyl]-alt-5,59-(2,29-bithiophene)]
P3HT	poly(3-hexylthiophene)
PAH	polycyclic aromatic hydrocarbon
PDIs	perylenebis(dicarboximide)s
PEDOT: PSS	poly (3,4-ethylenedioxythiophene):poly(4-styrenesulfonate))
PET	polyethylene terephthalate
ϕ_M	work function [eV]
PMMA	poly(methylmethacrylate)
PS	photoelectron spectroscopy
PS	polystyrene
PTFE	polytetrafluoroethylene
R	responsivity [$A.W^{-1}$]
RF	radio frequency
R_{bulk}	resistance of the bulk

R_c	contact resistance [Ω cm]
R_{ch}	channel resistance
rr-P3HT	regioregular poly(3-hexylthiophene)
R_T	total resistance
S	subthreshold swing [$V \cdot dec^{-1}$]
SAM	self-assembled monolayer
S-D	source-drain electrodes
SE	secondary electrons
SEM	scanning electron microscope
T	temperature [K or ˚C]
TC	top contact
TEM	transmission electron microscopy
TFT	thin-film transistor
THF	tetrahydrofuran
TLM	transfer line method
TM-AFM	tapping mode atomic force microscopy
UV	ultraviolet
V_D	source-drain bias for a grounded source [V]
V_G	source-gate bias for a grounded source [V]
VRH	variable range hopping
V_{SD}	source-drain bias [V]
V_{SG}	source-gate bias [V]
V_{Th}	threshold voltage [V]
$V_{Th,e}$	threshold voltage for electrons [V]
$V_{Th,h}$	threshold voltage for holes [V]
W	channel width [mm]
W_a	width of arm-chair ribbon
WF	workfunction [eV]
wt %	total weight %
W_z	width of zigzag ribbon
XRD	X-ray diffraction
z-GNR	zigzag graphene nanoribbon
γ	surface tension [$mJ.m^{-2}$]
ΔΦ	energy difference
λ	wavelength [nm]
σ	electrical conductivity [$S \cdot m^{-1}$]
Φ_B	energy barrier

β	degree disorder
τ	relaxation lifetime [s]
μ	field-effect mobility [$cm^2 \cdot V^{-1} \cdot s^{-1}$]
μ_e	field-effect mobility of electrons [$cm^2 \cdot V^{-1} \cdot s^{-1}$]
μ_{eff}	effective mobility [$cm^2 \cdot V^{-1} \cdot s^{-1}$]
μ_h	field-effect mobility of holes [$cm^2 \cdot V^{-1} \cdot s^{-1}$]

2D	two dimensional
2D-GIXD	two dimensional Grazing Incidence X-Ray Diffraction

Chapter 1 Introduction

1.1 Background

Electronic devices invaded our daily life which involves the continuous use of cell phones, personal computers, flat panel displays, etc…. The fundamental and key building block in these devices is the field-effect transistor. The first patent on field-effect transistor (FET) appeared in 1926[1] by Julius E. Lilienfeld suggesting a method and an apparatus with a three-electrode structure using copper-sulfide semiconductor material for controlling the electric current. The control of the current flow in a semiconductor via capacitive coupling at an electrode was proposed by Oskar Heil in 1934.[2] It took until 1947, when John Bardeen, William Shockley and Walter Brattain proved a working device[3-4] with two terminals which was announced as revolutionary state device. Later on, integrated circuits were built involving FETs and in 1965, Moore predicted the future of the development of integrated electronics.[5] He projected that the number of components per chip doubles every year which is an exponential increase over time. This prediction emerged as one of the driving principles of the semiconductor technology. Therefore, the challenge that technologists are facing is to deliver annual breakthrough by reducing the dimensions of the transistor and obtaining a better performance to cost ratio of products. Conventional FETs are based on inorganic materials, in particular Silicon. They require expensive, complicated fabrication techniques and clean rooms. Moreover, Silicon is very brittle both in the amorphous or single crystal phase and there are limits to what it can do. However, to extend the lifetime of Moore's law, it is necessary to develop new device concepts and architectures. Consequently, researchers focused their attention on finding alternative materials whose properties can be controlled by the electric field for use in electronic devices that create novel properties impossible to replicate with silicon. An appealing class of chemical

compounds called organic materials appeared in 1980s. It was always thought that these carbon based small molecules and polymers materials are insulators, until they were proved to be able to conduct electricity and the first polymer reported to do so was polyacetylene.[6] This discovery has attracted considerable research interest in this kind of materials that has semiconducting properties (called organic semiconductors) for electronic applications; and the first FET fabricated utilizing polythiophene (an organic material) as active semiconductor material in the channel instead of Silicon was reported in 1986 with a charge carrier mobility of 10^{-5} $cm^2 \cdot V^{-1} \cdot s^{-1}$.[7] The charge-carrier mobility is one of the crucial parameters in a transistor and refers to the average charge carrier drift velocity per unit electric field. For practical applications this parameter should be at least 10^{-3} $cm^2 \cdot V^{-1} \cdot s^{-1}$. Therefore, since the introduction of polythiophene in organic field-effect transistors (OFET) (i.e. field-effect transistors based organic molecules), lots of efforts have been devoted to design new π-conjugated systems, stable under ambient conditions, solution processable with a performance comparable or higher than amorphous silicon based devices. Over the past decades, remarkable progress has been made in this field with a significant improvement in OFET performance[8] driven by not only the design and the synthesis of novel organic semiconductors,[9-10] but also by the optimization of the device physics, the deep investigation of the structure/property relationship and the interface engineering. The state-of-the-art of the value for mobility is around 43 $cm^2 \cdot V^{-1} \cdot s^{-1}$[11] for a solution processable small molecule (deposited at room temperature by unconventional spin-coating technique) which is the highest value to date for all organic molecules. This fascinating result indicates that organic molecules can compete and even replace their inorganic counterparts in applications requiring large-area coverage, low temperature processing and simple manufacturing technologies. Many organic semiconducting materials can be deposited with solution based techniques such as spin-coating, ink-jet or roll-to-roll printing without the need of high end clean rooms laboratories which would result in a dramatic reduction of manufacturing cost. Despite their advantages such as solution processability and their unique physical (optical and electrical) properties and their ability to mechanically flex, the commercialization of OFETs, however, faces several technical obstacles regardless of the progress in this field. For instance, not all organic molecules are commercially available; some require expensive synthesis with low yields and some others require expensive deposition techniques such as vacuum evaporation which limits their use at the industrial level where

commercially available organic semiconductors are required. So far, the devices based on these materials still suffer from low charge carrier mobility and high operation voltage restricting their use in many applications; easy degradation in air and instability under stress which usually make their lifetime too short to be useful; and high contact resistance that limits the charge injection to the semiconductor. Therefore, the challenge remains to achieve high performance devices to sustain the continued advancement in electronics and fuel the expected demands of our society in the future.

1.2 Objectives and approach

Several attempts have been carried out to impart the above mentioned problems and in the 1990s, an alternative approach to tailoring new materials with improved performance was introduced for use in semiconducting devices. It consists of blending organic molecules in the aim of benefiting of the properties brought by each one. It was first used in light-emitting diodes for the enhancement of the electroluminescence.[12-13] Later on, it was extended to other devices including OFETs for: *i)* either the enhancement of the field-effect mobility,[14] or *ii)* for designing multi-functional device by adding for example new properties to the device such as current modulation under the effect of irradiation,[15] or *iii)* for the achievement of ambipolar OFETs (i.e OFET with organic material capable of transporting both electrons and holes under suitable biasing conditions). Another approach consists of replacing the key component of the device (i.e. the semiconductor utilized in the channel of the device) by carbon allotropes which gained enormous attention recently. They hold tremendous promise for organic electronics because of the wealth of their chemical and physical properties associated with their different forms. Fullerenes[16] and carbon nanotubes[17] were first produced, then in 2004, graphene, a two dimensional sheet of carbon atoms, was successfully isolated and reported to exhibit an electric field dependence[18] which ignited an explosion of interest in this field. Now graphene is considered among the candidate materials for post-silicon electronics and the exploration of this material in different fields has literally exploded in all academic and industrial research laboratories around the world. The measured record charge carrier mobility in graphene is as high as 100 000 $cm^2 \cdot V^{-1} \cdot s^{-1}$ at room temperature.[19] Graphene is an excellent conductor instead of a semiconductor. This is because it features a zero band gap which has a consequence on the

operation of the transistor. The major drawback is that a transistor with a gapless channel do not switch off and therefore is not suited for complex logic circuits. Nevertheless, organic electronics benefited from the advantageous properties brought by graphene and took the risk of having it in the channel of an OFET. This was done by combining both approaches and incorporating it to only organic semiconducting polymer matrices which were selected for a specific reason. Most polymer films are characterized by the coexistence of crystalline and amorphous domains lowering the performance of the device which can be improved by adding graphene to the semiconductor film instead of controlling the morphology of the film. It was demonstrated that the addition of graphene can increase the charge carrier mobility by providing good interconnection between the crystalline semiconducting domains.[20-22] Though the enhanced performance was accompanied by a trade off with another very important parameter in OFET which is the I_{on}/I_{off} ratio that determines the ability of the device to switch between the "On" and the "Off" states under the influence of an applied bias. Nevertheless, all these studies were performed on polymers where the majority of charge carriers are holes (called *p*-type semiconductor) and graphene has never been investigated in matrices where the majority of the charge carriers are electrons (called *n*-type semiconductor). That is because *n*-type semiconductors still suffer from several issues such as high injection barrier when using Au electrodes and the *n*-type behavior is very sensitive to the traps at the dielectric interface which can quench it.[23] Moreover, on the other hand, in order to be useful in conventional field-effect transistors, the band gap of graphene has to be modified. There are several ways and one of them is to confine the size of graphene in one dimension to form graphene nanoribbons GNRs. However, still their fabrication remains a challenge and not yet up-scalable. It is worth noting that they have never been added to the semiconducting film of an OFET.

In this thesis, a study of graphene incorporation to an *n*-type polymer is presented. The effect of the addition of graphene at different concentrations on the electrical performance of the devices is investigated. Also the effect of an unprecedented graphene nanoribbons on the devices based on *p*-type polymer is examined for the first time. Preliminary study on multifunctional devices prepared by blends is demonstrated. In the latter case graphene can be potentially used as electrodes instead of active materials inside the channel.

1.3 Structure of the thesis

This thesis consists of 9 chapters and is organized as follows:

Chapter 1 provides a brief introduction about organic electronics.

Chapter 2 introduces in details the types of organic semiconducting molecules and the charge transport in them. It also describes the working principles of organic field effect-transistor, ambipolar transistor and phototransistor highlighting the important criteria affecting the performance of the device.

Chapter 3 a background on graphene and graphene nanoribbons is presented.

Chapter 4 describes the experimental techniques and methods used for the projects.

Chapter 5 presents the first experimental results done on blend of liquid phase exfoliated graphene with *n*-type semiconductor polymer, including devices fabrication, performance and discussion. It shows the effect of the addition of graphene at different concentrations on the electrical performance, particularly how the ambipolarity of an organic semiconductor can be boosted.

Chapter 6 explores and demonstrates novel bottom-up synthesized arm-chair graphene nanoribbon blended with *p*-type polymer. It shows how the performance can be improved when adding GNRs. It also highlights the problems faced with the single component material and evaluates the possibility of use of the devices as phototransistors

Chapter 7 presents polyaromatic hydrocarbons (PAHs) starting from a background on this material, then exploring the variation of the energy levels on a series of PAHs based on their size and their edge functionalization. It also shows the fabrication of FETs from one selected candidate of this series demonstrating the device performance and the possibilities of improving it either by thermal annealing, surface treatments or functionalization of the electrodes.

Chapter 8 introduces photochromic molecules and describes their use for obtaining multi-functional devices. It presents a comparative study exploring the effect of supramolecular organization mediated by the specific substitution pattern of photochromic molecules on its photoswitching behavior when incorporated in both polymeric and small molecules matrices.

Chapter 9 provides a summary of the thesis and a perspective into the future of graphene and organic electronics.

1.4 State of the art of organic electronics

Organic electronic devices have been widely commercialized. For example organic light-emitting diodes (OLEDs) are already used in displays of smartphones, digital media players, TVs and even watches; because they generate their own light via luminescence without the need of a backlight unlike other display technologies requiring backlight for the display to show. They have been also used for the production of electronic papers. Prototypes on flexible smartphones and curved OLEDs has been exhibited by several companies. Another application of organic electronics is in organic photovoltaics (OPVs) or organic solar cells mainly for the fabrication of light weight and flexible solar panels for harvesting the solar energy. They exist already in the market and their main advantage is that they can be integrated into places which were restricted for traditional glass panels due to their weight. As for organic field-effect transistors (OFETs), their application for large area displays has been demonstrated by number of companies. Moreover, OFETs are also highly sensitive to specific chemical and biological agents making them excellent candidates for biomedical sensors and other devices which interface with biological systems. Besides, Radio Frequency Identification (RFID) tag which is a wireless form of transferring data, is also an application for organic electronics. Several companies are involved in the production of flexible tags based on organic semiconductors. In general, organic electronics are targeted for cost effective, light weight mass productions thus complementing conventional silicon technology.

1.5 References

[1] J. E. Lilienfeld, *US Patent 1 745 175* **1930**.
[2] O. Heil, *UK Patent 439 457* **1934**.
[3] J. Bardeen, W. H. Brattain, *Phys. Rev.* **1948**, *74*, 230.
[4] W. Shockley, G. L. Pearson, *Phys. Rev.* **1948**, *74*, 232.
[5] G. E. Moore, *Proc. Of IEEE International Electron Devices Meeting (IEDM)* **1975**, *21*, 11.
[6] T. Ito, H. Shirakawa, S. Ikeda, *Journal of Polymer Science: Polymer Chemistry Edition* **1974**, *12*, 11.
[7] A. Tsumura, H. Koezuka, T. Ando, *Appl. Phys. Lett.* **1986**, *49*, 1210.
[8] Y. Zhao, Y. Guo, Y. Liu, *Adv. Mater.* **2013**, *25*, 5372.
[9] X. Guo, M. Baumgarten, K. Müllen, *Prog. Polym. Sci.* **2013**, *38*, 1832.
[10] C. Wang, H. Dong, W. Hu, Y. Liu, D. Zhu, *Chem. Rev.* **2011**, *112*, 2208.
[11] Y. Yuan, G. Giri, A. L. Ayzner, A. P. Zoombelt, S. C. B. Mannsfeld, J. Chen, D. Nordlund, M. F. Toney, J. Huang, Z. Bao, *Nat Commun* **2014**, *5*.
[12] J. Y. Park, H. M. Le, G. T. Kim, H. Park, Y. W. Park, I. N. Kang, D. H. Hwang, H. K. Shim, *Synt. Met.* **1996**, *79*, 177.
[13] G. Yu, H. Nishino, A. J. Heeger, T. A. Chen, R. D. Rieke, *Synt. Met.* **1995**, *72*, 249.
[14] J. Smith, R. Hamilton, I. McCulloch, N. Stingelin-Stutzmann, M. Heeney, D. D. C. Bradley, T. D. Anthopoulos, *J. Mater. Chem.* **2010**, *20*, 2562.
[15] E. Orgiu, P. Samorì, *Adv. Mater.* **2014**, DOI: 10.1002/adma.201304695.
[16] F. Wudl, *J. Mat. Chem.* **2002**, *12*, 1959.
[17] R. H. Baughman, A. A. Zakhidov, W. A. De Heer, *Science* **2002**, *297*, 787.
[18] K. S. Novoselov, A. K. Geim, S. V. Morozov, D. Jiang, Y. Zhang, S. V. Dubonos, I. V. Grigorieva, A. A. Firsov, *Science* **2004**, *306*, 666.
[19] A. S. Mayorov, R. V. Gorbachev, S. V. Morozov, L. Britnell, R. Jalil, L. A. Ponomarenko, P. Blake, K. S. Novoselov, K. Watanabe, T. Taniguchi, A. K. Geim, *Nano Lett.* **2011**, *11*, 2396.
[20] P. Yadav, C. Chanmal, A. Basu, L. Mandal, J. Jog, S. Ogale, *RSC Advances* **2013**, *3*, 18049.
[21] J. Huang, D. R. Hines, B. J. Jung, M. S. Bronsgeest, A. Tunnell, V. Ballarotto, H. E. Katz, M. S. Fuhrer, E. D. Williams, J. Cumings, *Org. Electron.* **2011**, *12*, 1471.
[22] A. Liscio, G. P. Veronese, E. Treossi, F. Suriano, F. Rossella, V. Bellani, R. Rizzoli, P. Samorì, V. Palermo, *J. Mater. Chem.* **2011**, *21*, 2924.
[23] L.-L. Chua, J. Zaumseil, J.-F. Chang, E. C. W. Ou, P. K. H. Ho, H. Sirringhaus, R. H. Friend, *Nature* **2005**, *434*, 194.

Chapter 2 Organic Semiconductors and Devices: Theory and Background

2.1 Organic semiconductors

2.1.1 Background

Organic molecules are defined as compounds whose skeletons contain the element carbon often associated with hydrogen, oxygen or nitrogen[1] which distinguish them from the inorganic materials. Their rich variety of properties and structures is offered by the unique chemistry of carbon which can form different type of bonds in a molecule depending on the hybridization of the atomic orbitals. An interesting feature of the organic semiconductors is the conjugated π-electron system formed by p_z orbitals of sp^2 hybridized carbon atoms in a molecule as shown in **Figure 2.1**.

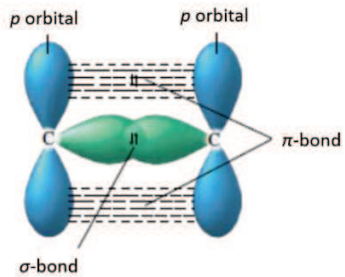

Figure 2.1 Carbon-carbon double bond consisting of a σ-bond and a π-bond. The π-bond is formed from the unhybridized p_z orbitals on the two carbon atoms. The shared electron pair occupies the space above and below a line joining the atoms (adopted from Ref. [2])

The double bond structure is formed of a strong σ-bond (formed by the electrons attached to the two nuclei and are localized) and of a weaker π-bond (formed by sharing electrons in between the p_z orbitals of the atoms). If a structure contains an appreciable number of carbon-carbon bonds and is capable of supporting electronic conduction, it is classified as organic semiconductor[3] and it is also said to be conjugated if the neighboring carbon atoms are sp^2 hybridized. Depending on their molecular size, organic semiconductors are categorized into two major classes: small molecules (i.e. low molecular weight materials) and polymers. The formers are monodisperse while the latters are polydisperse. They have in common the conjugated π-electron system. The structure of some among the most relevant small molecules and polymers is illustrates in **Figure 2.2** and **Figure 2.3**, respectively.

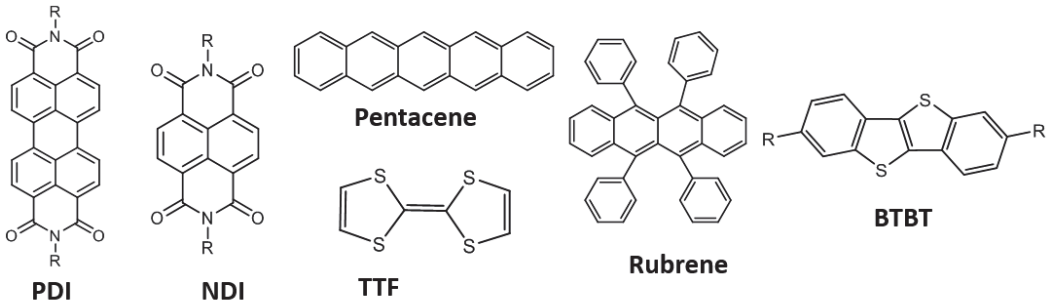

Figure 2.2 Examples of small molecule semiconductors

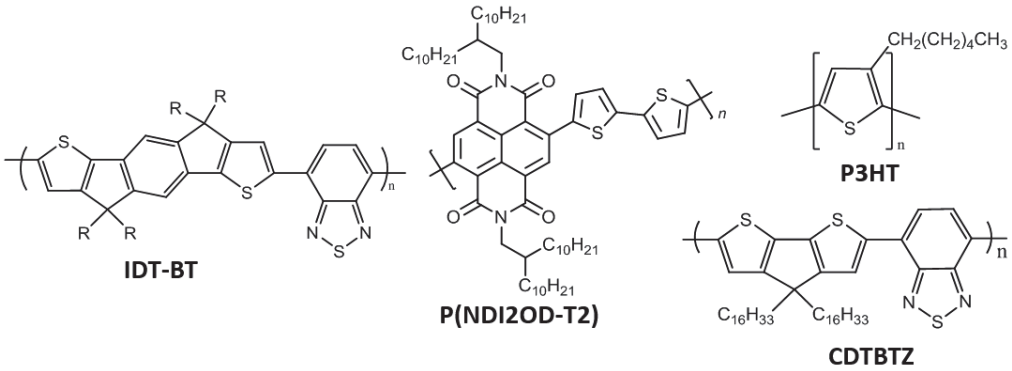

Figure 2.3 Examples of polymer semiconductors

Normally the electrons forming a π-bond are localized. However, in polymeric semiconductors for example, also called conjugated polymers, there is an alternation of single and double bonds

along their backbone. Thus, the π-orbitals of the neighboring double bond overlap due to the conjugated structure. Therefore, π-electrons are delocalized and can move from one bond to another one or along the entire backbone. An example of small molecule having such electronic structure with alternating single and double bonds forming an extended delocalized π-electron system is benzene molecule. It can have resonant structures and can be represented differently as shown in **Figure 2.4a** to indicate the possibility to interchange the position of single and double bonds. Since each carbon atom is sp^2 hybridized, the p_z-orbitals remaining on each carbon atom, can be used to form π-molecular orbitals as illustrated in **Figure 2.4b**. The electrons in the resulting π molecular orbitals are delocalized above and below the ring as shown in **Figure 2.4c**.

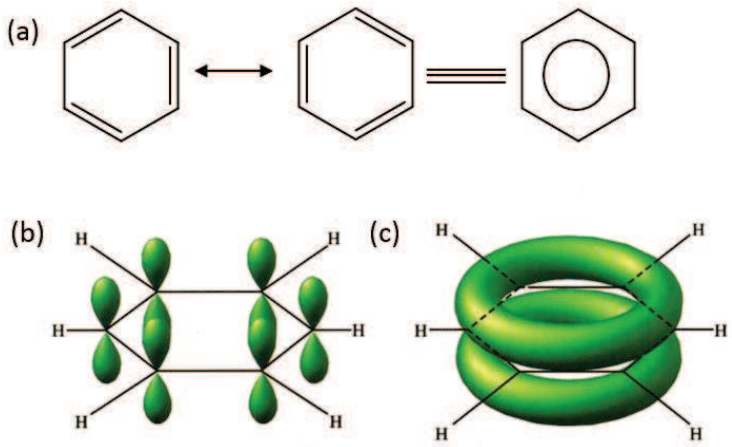

Figure 2.4 (a) Resonance structures of benzene molecule. (b) Six *p* orbitals of six sp^2 hybridized carbon atoms combine to form the π molecular orbital system in benzene. (c) Delocalization of the electrons in the resulting π molecular orbital over the entire ring of carbon atoms adopted from Ref. [2].

For a single molecule, when atoms close in energy interact, their energies split due to the overlap between the atomic orbitals giving rise to different molecular energy levels. Bonding (of low energy) and anti-bonding (of high energy) states are obtained. In the ground state, all bonding orbitals up to the highest occupied molecular orbital (defined as HOMO) are filled with two electrons of anti-parallel spins whereas all anti-bonding orbitals from the lowest unoccupied molecular orbital (defined as LUMO) onwards, are empty. In the case of a polymer or a solid composed of molecules, the π orbitals will overlap in one or more dimensions. Since there is n number of atomic orbitals, based on the concept of MO (Molecular Orbital theory) and the

LCAO (linear combination of atomic orbitals) approach, the superposition of all of the molecular orbitals interacting between them, results in a farther splitting with the appearance of valence band with higher energy and conduction band with lower energy analogous to the HOMO and LUMO respectively[4] as seen in **Figure 2.5a and b**. The energy difference between the valence band maximum and the conduction band minimum defines the band gap energy (E_g). Hence, E_g represents the threshold energy barrier from occupied to unoccupied states. The width of the band-gap determines the type of material; in conductors, conduction and valence bands overlap (**Figure 2.5c**) whereas if the space between them (i.e. the band gap) is too large the material is categorized as insulator, and called a semiconductor for narrow E_g.

The ionization energy I_E is defined as the energy required to excite an electron from the valence band maximum (i.e. the HOMO) to the vacuum level. For a metal, $I_E = \phi_M$ where ϕ_M is the work function and corresponds to the minimum energy required to promote an electron from the Fermi level E_F to the vacuum level (see **Figure 2.5c**).

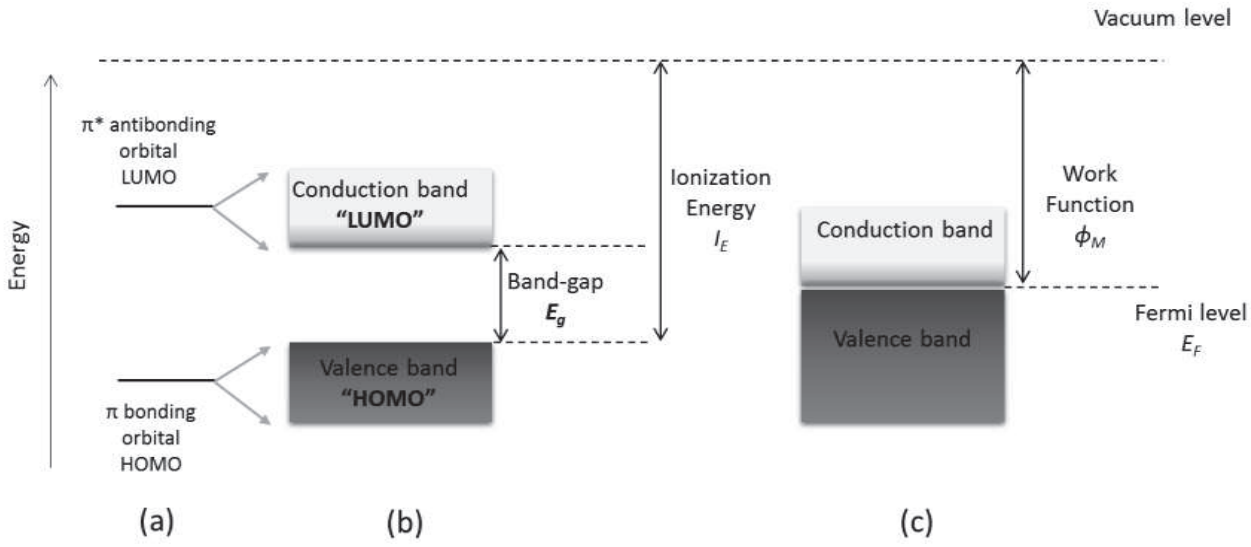

Figure 2.5 Band structure of: (a) a single molecule, (b) a semiconductor showing an energy gap separating the conduction and the valence bands; and (c) a conductor where the valence and the conduction bands overlap.

2.1.2 Charge transport models

In this section some fundamental concepts of the most interesting charge transport models in organic semiconductors will be presented briefly. A deep discussion about this topic is not the aim of this thesis and are extensively presented in [5-9].

2.1.2.1 Hopping

Charge transport in organic semiconductors cannot be described in the same manner as in inorganic semiconductors such as Silicon. The reason is that organic molecules have weak intermolecular interaction forces typically van der Waals interactions. In contrast, in their inorganic counterparts, the atoms are held together with very strong covalent bonds which leads to the formation of a crystalline lattice with long-range order; thus the charge carrier is delocalized in the conduction band and can move with a long mean free path which is limited by the lattice vibration (phonons) and scattering at crystal defects. In materials with less crystalline order, such as organic semiconductors and polymers this model is no longer valid. Because of the low crystallinity due to the small interaction between the molecules, there are no extended bands and hence no delocalized charge transport.[10] In contrast, the charge carriers are located on localized states, and charge transport is only possible by "hopping" (i.e. tunneling) between those localized states, as depicted in Figure 2.6, resulting in charge carrier mobilities which are orders of magnitude lower than those of crystalline semiconductors.[11]

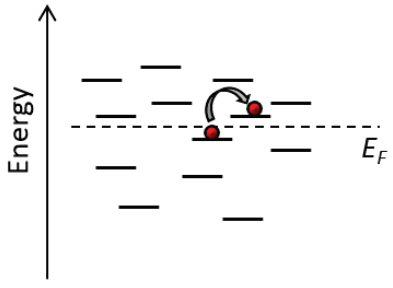

Figure 2.6 Sketch of hopping transport between the localized states of a disordered semiconductor system showing a "hopping" of the charge between two different sites of different energies over a certain distance reproduced form [12].

This transport mechanism is phonon assisted, therefore the charge mobility is temperature dependent. A well-known model describing such transport is the variable range hopping (VRH)

suggested by Davis[13] and Mott.[14] It assumes especially at low temperatures, that in the presence of enough hopping states, it is more favorable for a carrier to hop over a long distance to a site at similar energy rather than hopping over a short distance with high energy. Consequently the hop is not anymore limited to the nearest neighbor. In this model, the mobility and hence the conductivity σ varies with temperature T as per the following:[14]

$$\sigma = \sigma_0 \, exp\left[-(T_0/T)^{1/4}\right] \tag{2.1}$$

where σ_0 and T_0 are constants. However, in disordered semiconductors, the density of states DOS is not uniform and is assumed either Gaussian[15] or exponential.[16] In this case, the charge carrier mobility is not only temperature dependent but also depends on the applied electric field.[6]This phenomenon occurs through a Poole-Frenkel mechanism[17] in which the applied field modifies the Coulomb potential around the charged localized states in a way to increase the tunnel rate between the states. The general field dependence of the mobility is described by:

$$\mu\,(E) = \mu\,(0)\exp\left[\frac{q}{k\,T}\,\beta\,\sqrt{E}\right] \tag{2.2}$$

where $\mu(0)$ is the mobility at zero field (E=0), E is the magnitude of the electric field, q is the elementary charge and β is the Poole-Frenkel factor ($\beta = (\varepsilon/\pi\varepsilon\varepsilon_0)^{1/2}$. It was also found that the charge carrier mobility depends also on the gate bias[18-19] (i.e. the bias applied by one of the terminals of a field-effect transistor which will be discussed in the following paragraph) due to the density of the localized states. This means that more energy states are available at higher energies than at lower energies. Therefore by applying a gate bias, charges are injected in the system and will occupy the lower states of the DOS. At higher gate bias, additional charges to the ones present are injected and consequently will occupy the states with higher energy as depicted in **Figure 2.7**. Hence, these additional charges require less energy to hop away to other sites resulting in an enhanced mobility that increases with increasing the gate bias. Based on this assumption, a model was developed by Vissenberg and Matters[15] suggesting that at low carrier density, the transport is governed by the tail states of the Gaussian DOS and that the conductivity has an Arrhenius-like temperature dependence with an activation energy E_a that is weakly (logarithmically) temperature dependent:

$$\sigma \sim \exp[-(E_a/k_BT)] \tag{2.3}$$

where $k_B$is Boltzmann's constant. In addition to carrier concentration dependence, this model also predicts a gate-voltage dependent mobility that follows a power law.

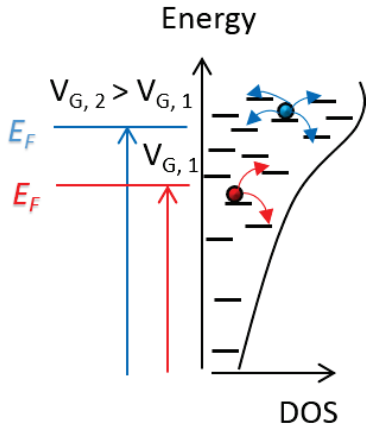

Figure 2.7 Sketch of gate voltage dependent mobility. With increasing the gate bias, more charges are accumulated and occupy states at higher energies, so that the Femi energy is increased. More empty states are available close to a carrier at Fermi energy (due to the Gaussian DOS) which facilitates the hopping of the charge. Reproduced from [12].

2.1.2.2 Multiple Trap and release

While hopping transport is appropriate to describe the charge transport in disordered materials, the multiple trapping and thermal release (MTR) model applies to well-ordered organic semiconductors such as polycrystalline oligothiophenes[20] which exhibit much better ordering than polymers. It has been first developed for describing the transport mechanism in amorphous Silicon.[21] It assumes that localized states are distributed in the vicinity of delocalized transport band edge. The basic assumption of this model is that when a charge carrier travels in the delocalized band, it interacts with the localized levels below the band that act as traps through trapping and thermal release as presented in **Figure 2.8**. In other words, if a charge carrier arrives to a state localized in the forbidden gap, it gets trapped. Then it can be released from the trap back to the transport band through a thermally activated process. For example, with decreasing temperature, the probability of thermal release from the localized state becomes smaller and hopping to a neighboring site will become the predominant transport mechanism.[21] When the traps are homogeneously dispersed, the effective mobility μ_{eff} is related to temperature by an equation of the form[22]:

$$\mu_{eff} = \mu_0 \, \alpha \exp[-(E_t/k_B T)] \qquad (2.4)$$

where μ_0 is the undisturbed mobility in the transport band, E_t is the energy difference between the transport band edge and a single trap level and α is the ratio between the density of delocalized levels available for transport and the density of traps. The other terms were previously defined.

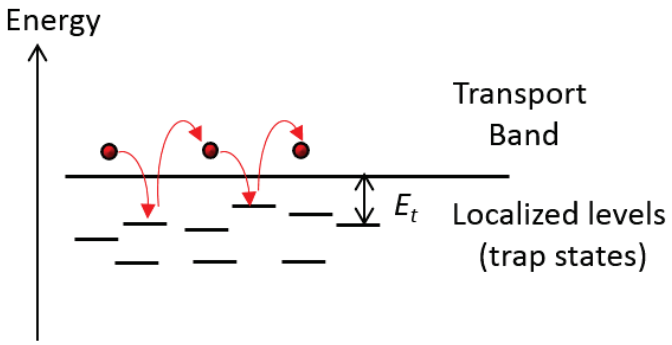

Figure 2.8 Sketch of the principle of the charge transport limited by multiple trapping and release. The transit of the charge carriers in the delocalized state (transport band) is accompanied by trapping of the charge in localized states with depth E_t from which they go back into the band by thermal excitation.

2.1.2.3 Polaron transport

A crucial phenomenon occurring in organic semiconductors due to the weak van der Waals intermolecular interactions is the polarization effect.[23] It is due to the localization of the charge carrier on a molecular site. During its residence time, the charge carrier tends to polarize the neighboring region. Consequently, the charge does not move as a free carrier but it is rather accompanied by a polarization cloud. Such quasiparticle (in which the electronic charge is dressed by a polarization cloud) is called *polaron*. The stability of a polaron is determined by the time it stays on a molecule and the time it takes to polarize the surrounding molecules.[22] The small polaron model that is one-dimensional one electron model developed by Holstein[24] was also used to describe the charge transport in organic materials. VRH and MTR models neglected the effect of polarons. However, Bässler et al[6] included the polarons in their model by giving an estimation about the importance of their effect on the transport mechanism. They found that polarons with binding energy in the range of meV do not have an effect on the

transport analysis and therefore the hopping transport is sufficient to describe the charge transport in disordered system.

Despite all the models proposed and the efforts devoted for understanding the charge transport in organic semiconductors, this topic remains a controversy.

2.2 Organic field-effect transistor

2.2.1 Device structure

An organic field-effect transistor OFET is made up of three main components as illustrated in **Figure 2.9**: *i)* three electrodes, *ii)* a dielectric and *iii)* an organic semiconductor layer which can be a solution-cast film or evaporated crystal. Two of the electrodes of width W (defined as channel width) and separated by a distance L (channel length) are in direct contact with the semiconductor. These electrodes are called source and drain electrodes and their role is to inject in and retrieve charge carriers from the semiconductor which is isolated from the third electrode called gate by an insulating dielectric. The gate modulates the current that flows between the source and the drain.

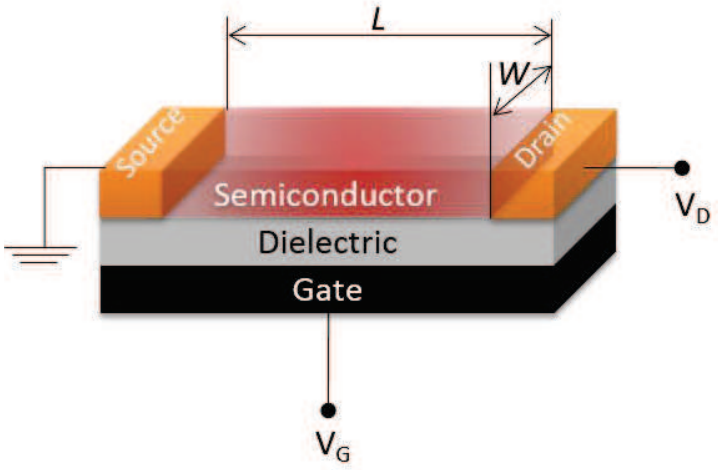

Figure 2.9 Structure of a field-effect transistor. V_G and V_D correspond to the applied gate and drain biases respectively. W is the channel width and L is its length.

Very often, highly doped silicon serves as substrate and gate electrode at once; but for a fully flexible device for example, plastic substrates such as Polyethylene terephthalate (PET)[25] can be used and the gate electrode can be made of a metal such as Au. As for the dielectric, the most commonly used are either inorganic insulators, some of which are SiO_2, Al_2O_3[26] or polymeric insulators[25, 27] such as poly(methylmethacrylate) (PMMA) or polystyrene (PS). Source drain S-D electrodes are carefully selected depending on the energy levels of the semiconductor and they can be metals with high work function e.g. Au (also Al,[28] Pt,[29] or Ag[30]) or conducting polymers (e.g. PEDOT: PSS[31-33] (poly (3,4-ethylenedioxythiophene):poly(4-styrenesulfonate))). Depending on the order of the deposition of the various elements on the substrate, different device geometries are obtained. Two of them were used in this thesis: bottom-gate bottom-contact and bottom-gate top-contact. In both cases, the gate is deposited first and thus referred as bottom-gate. While the S-D electrodes are either deposited prior to the semiconductor for a bottom-contact configuration, or on the top of the semiconductor for a top-contact configuration.

2.2.2 Operating mode

An OFET can be viewed as a parallel plate capacitor. By applying a bias between the source and the gate (V_{SG}) (Figure 2.9), charges but of opposite sign are induced at both sides of the dielectric. At the semiconductor side, this forms a conducting channel. The number of the accumulated charge carriers in the channel is proportional to the capacitance of the dielectric C_i and can be modulated by modifying the gate bias. This in turns modulates the current flowing between the source and the drain (I_{SD}) which can be measured by applying a source-drain bias (V_{SD}). Normally the source electrode is grounded and consequently the following notations are used: V_G and V_D for gate and drain biases respectively and I_D for the source-drain current.

There are two main regimes for the operation of an OFET: *i)* the linear and *ii)* the saturation regime. First, not all of the injected carriers contribute to the drain current. That is because of the presence of shallow traps in the organic semiconductor that need to be filled before mobile charges can be induced in the channel.[34] Therefore the device's "on" state occurs when the applied V_G goes beyond a threshold V_{Th} for the formation of the conducting channel between the source and the drain. Consequently the effective gate bias is V_G - V_{Th}. When no drain bias is

applied, the density of the charge carriers is uniform all along the channel. When a small source-drain bias is applied ($V_D < V_G - V_{Th}$) the charges carriers are present all along the channel and their concentration varies linearly with the gate bias (Figure 2.10a). This results in a drain current that follows Ohm's law. It is consequently proportional to V_G and V_D and is given by[35]:

$$I_D = \frac{W}{L} C_i \mu \left(V_G - V_{Th} - \frac{V_D}{2}\right) V_D \qquad (2.5)$$

where C_i is the capacitance per unit area of the dielectric and μ is the field-effect mobility. The other terms has been defined previously. This equation corresponds to the so-called linear regime, where $V_D < V_G - V_{Th}$;

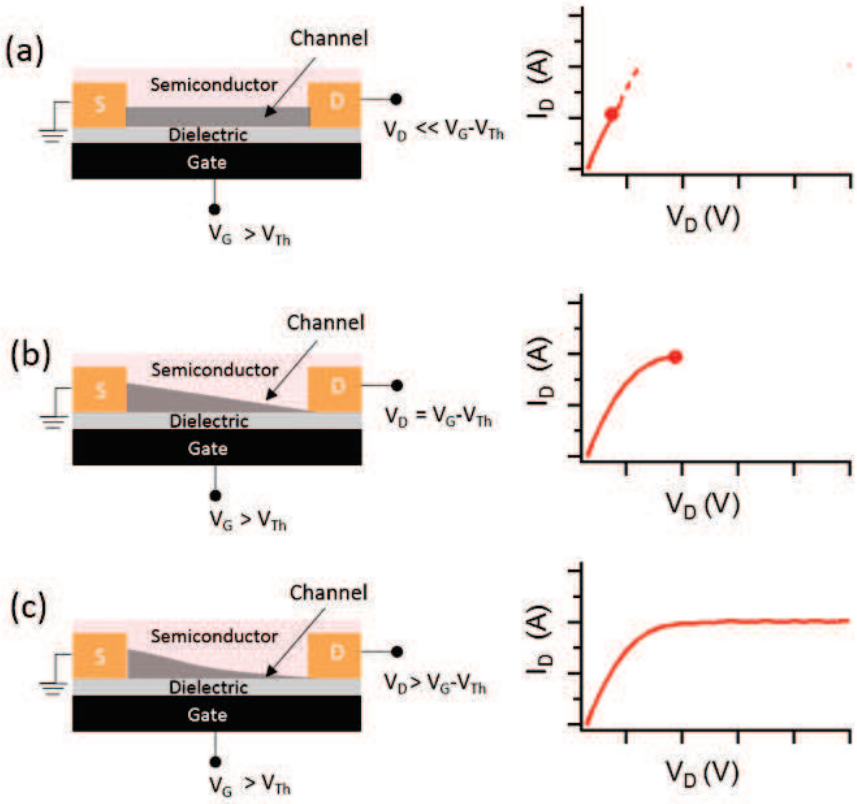

Figure 2.10 Operating principle of a field-effect transistor in different regimes and their corresponding drain current vs drain bias characteristic: (a) in the linear regime, (b) at the pinch off when the drain current starts to saturates and (c) in the saturation regime. S and D are the source-drain electrodes (reproduced from [35])

When the source-drain bias increases further up to $V_G - V_{Th}$ (i.e at $V_D = V_G - V_{Th}$), the potential at a point of the channel close to the drain electrode falls to zero and so does the charge in this

area of the channel thus forming a depletion region. At this point, there's a "pinch off" of the channel and I_D saturates because a space-charge limited current can flow across this narrow depletion zone (Figure 2.10b). A further increase of the source drain bias (at $V_D > V_G - V_{Th}$) will not increase the drain current which saturates and becomes independent of V_D; but will expand the depletion region (Figure 2.10c). This is the saturation regime where eq. 2.5 becomes:

$$I_D = \frac{W}{2L} C_i \mu (V_G - V_{Th})^2 \qquad (2.6)$$

In an OFET the application of V_G shifts the energy levels of the semiconductor electrostatically and therefore modulates the conductivity of the channel. Thus, an OFET can be classified as *n*-channel, *p*-channel or ambipolar based on the V_G sign on which it is active; hence if a negative gate voltage is applied, the HOMO and the LUMO levels of the organic material will shift up with respect to the Fermi level (E_F) of the metal electrode. If the HOMO becomes resonant with E_F, it will be possible to have flow of hole mobile charges between the HOMO and the metal. In this case, since the majority of the charger carriers are holes, the semiconductor is classified as a *p*-channel and the device is called organic *p*-channel FET. Otherwise, if a positive V_G is applied, the HOMO and LUMO orbitals will shift down, and if the LUMO becomes resonant with E_F, electrons will flow from the metal to the LUMO. This material is classified as an *n*-channel semiconductor and the device is said to be organic *n*-channel FET. Materials able to conduct electrons and holes are classified as ambipolar semiconductors thus an ambipolar FET will operate on both negative and positive gate biases. It is important to note that the type of the channel is not an intrinsic property of the material and depends on many factors of which the dielectric/semiconductor interface.[36]

2.2.3 Characterization

There are two sorts of current-voltage plots in a transistor: output (I_D-V_D) and transfer characteristics (I_D-V_G). For the former, a set of curves of drain current I_D vs drain bias V_D is measured at various gate biases V_G. For each curve, I_D is determined for a finely divided range of V_D at a fixed V_G as depicted in **Figure 2.11a**. While for the transfer characteristics, I_D is plot vs V_G (which is swept) for a given V_D (kept constant) **Figure 2.11b**.

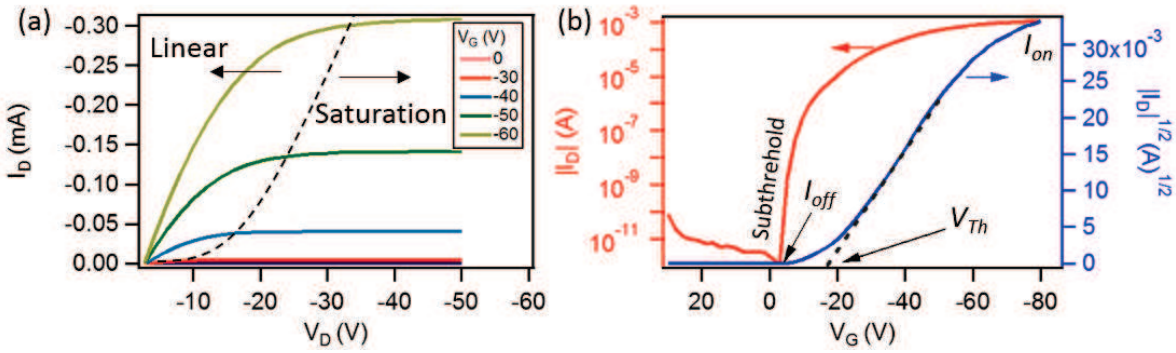

Figure 2.11 Representative example of: (a) output and (b) transfer characteristics of an OFET. Dashed line in (a) separates the linear from the saturation regime. In (b) left axis is plot in the logarithmic scale while the right axis is the square root of the drain current.

The key parameters that are used for judging the performance of an OFET are extracted from the transfer characteristics and include: the field-effect mobility, the ratio of the drain current in the on state to the drain current in the off state (I_{on}/I_{off}) (see Figure 2.11b) and the threshold voltage V_{Th}. Other parameters are also considered including the contact resistance R_c and the subthreshold behavior S.

2.2.4 Important parameters and their extraction

2.2.4.1 Mobility

The average drift velocity of an electron $\bar{v}_d$ per unit applied electric field E is defined as the charge carrier mobility μ and is given by[37]:

$$\mu = \frac{\bar{v}_d}{E} \tag{2.7}$$

as a consequence, the unit of μ is $cm^2 \cdot V^{-1} \cdot s^{-1}$.

This is related to I_D which corresponds to the passage of the charge along the channel during a time by:

$$I_D = QW\mu E_x \tag{2.8}$$

where W being the channel width, E_x is the electric field at a position x along the channel ($E_x = dV/dx$). Q is the induced mobile charges per unit area at a potential higher than the threshold

voltage $Q = C_i(V_G - V_{Th} - V(x))$ where *V(x)* is the potential at the position *x* of the channel induced by the application of the drain bias. The substitution of each of the terms in equation 2.8 gives:

$$I_D dx = C_i W \mu (V_G - V_{Th} - V(x))\, dV \qquad (2.10)$$

An integration of the current increase in eq. 2.10 from the source (at *x*=0 where the potential *V(x)* =0) to the drain (at *x*=*L* and the potential *V(x)* =*L*) leads to eq. 2.5 if $V_D < V_G - V_{Th}$ and to eq. 2.6 when $V_D = V_G - V_{Th}$. Consequently μ is either extracted from the linear regime from eq. 2.5 or from the saturation regime from eq. 2.6. The latter being the most commonly used method. A rearrangement of eq. 2.6 gives:

$$\sqrt{I_D} = \sqrt{\frac{W}{2L} C_i \mu}(V_G - V_{Th}) \qquad (2.11)$$

Hence μ is obtained from the linear fitting of the plot of the square root of I_D vs. V_G as shown in **Figure 2.11b**. It is worth mentioning that the disadvantage of utilizing such method is that it assumes that in the saturation regime, the mobility is constant all along the channel which is not the case in most organic semiconductors.[22, 34]

2.2.4.2 Threshold voltage

The threshold voltage is another important figure of merit of an OFET beside the field-effect mobility. It corresponds to the starting point of the formation of the conducting channel. In other words, it corresponds to the transition between a point where no current flows in the channel and the accumulation which turns the device "on". It can be extracted using different methods[38-41] and the most popular and convenient one is that obtained from the slope of the square root of the saturation current at V_G=0 V i.e. by extrapolating the line to zero current as shown in **Figure 2.11b**. Ideally V_{Th} should be around zero. More often in organic semiconductors it is shifted from this value. This is because it is influenced by several factors and mainly the density of the traps at the interface between the dielectric and the semiconductor.[42-43] Furthermore, it was demonstrated that the threshold voltage can depend on the thickness of the semiconductor film.[44-45] For example for bottom-gate top-contact pentacene based FET, V_{Th} was found to vary linearly with the thickness.[44] Moreover, experimental[45-46] and theoretical[47] studies showed that the presence of the dipoles at the dielectric interface strongly affects the energy of the

localized states of the semiconductor[47] which in turn alters V_{Th}. A deeper discussion about the role of this particular interface will be detailed later in this chapter.

2.2.4.3 I_{on}/I_{off}

The I_{on}/I_{off} ratio is the ratio of the drain current in the on state at a certain V_G to the drain current in the off state. It can be extracted also form the transfer characteristics as shown in **Figure 2.11b**. A high I_{on}/I_{off} ratio (i.e. a high switching behavior) is a desirable quality of an OFET. This parameter is not only dependent on the mobility of the semiconductor but also on the capacitance of the dielectric and on the thickness of the semiconductor layer.[11]

2.2.4.4 Contact Resistance

The efficiency of the charge injection into the semiconductor is evaluated by means of contact resistance R_c which is a measure indicating the ease of current flow across a metal-semiconductor interface. R_c can be understood as a series of resistances of two main components.[48] The first called R_{int} is the resistance originating from the energy mismatch between the Fermi level of the metal electrode and the HOMO (for a *p*-type) or the LUMO (for *n*-type) of the semiconductor; the second resistance called R_{bulk} is the resistance of the semiconductor itself from the injecting electrode to the channel (see Figure 2.12). Both resistances are important. R_{int} is crucially affected by the choice of the S-D electrodes.[49] That is because the metal/semiconductor interface is visualized according to the Mott-Schottky (MS) model where an ohmic contact is expected when the work function Φ_M of the S-D electrodes and thus E_F matches the energy levels of either the HOMO or the LUMO of the semiconductor if it is *p*-or *n*-type respectively.

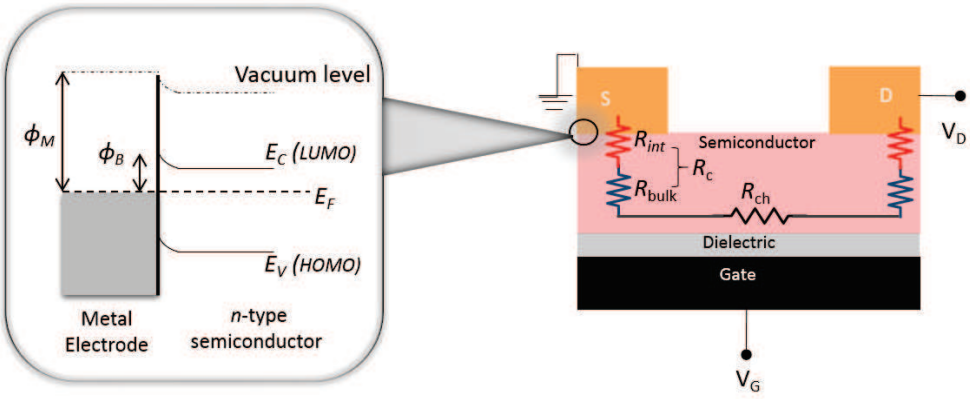

Figure 2.12 Sketch of the resistances in an OFET (right side) and a zoom in at the metal/semiconductor interface for an *n*-type semiconductor (left side). R_c is the contact resistance which includes the resistance at the electrode-semiconductor interface R_{int} added to the one in the bulk of the semiconductor R_{bulk}. R_{ch} is the channel; resistance. Φ_B is the injection barrier resulting from the energy mismatch between the work function Φ_M of the metal and the LUMO level of the semiconductor.

In a transistor an ohmic behavior results in a linear increase of the drain current at low drain biases. However, in the opposite case (i.e. in the case of a misalignment of these levels) an energy barrier forms Φ_B at the metal/semiconductor interface resulting in a poor charge injection and a non-ohmic contact (Figure 2.12). The larger is this barrier, the more difficult the injection of the charges into the semiconductor becomes and the higher is the contact resistance.[49] Moreover, R_c depends on the device geometry. For instance R_c in a bottom-contact configuration is higher than the one of a top-contact configuration.[50] This is due to the contact area between the semiconductor and the metal electrode (see Figure 2.13) which is small in bottom-contact OFET thus generating a large contact resistance.[51] Furthermore, in this type of geometry, the non-optimal growth morphology of the semiconductor on the contact surface of the metal electrode forms an injection barrier and contributes to R_c.[52] On the contrary, in a top-contact configuration, R_c is lower because the injection of the charge carriers takes place over a larger area (Figure 2.13a). However, in this type configuration, the thickness of the semiconductor layer should not be too large in order to minimize R_{bulk}. The latter is the main contributor to the contact resistance[53] and is not so important in a bottom-contact configuration because the contacts are in the same plane of the channel (Figure 2.13b).

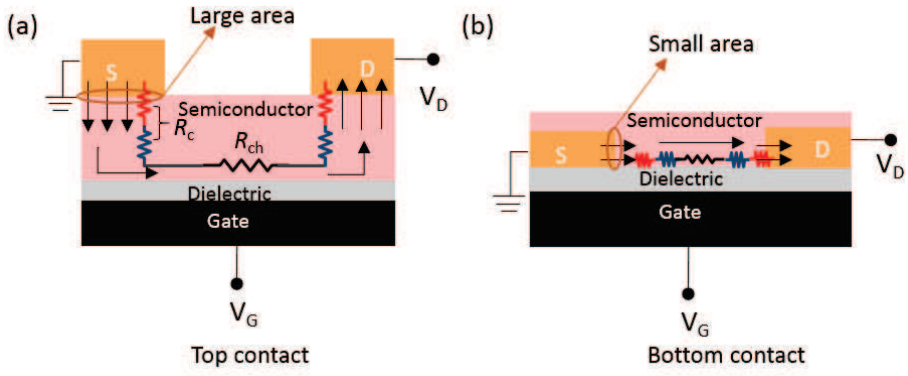

Figure 2.13 (a) top-contact vs. (b) bottom-contact OFET configuration showing the difference in the area at the electrode/semiconductor interface. The arrows indicate the flow of the charges from the injecting electrode to the channel and their collection by the other electrode.

More recently it was found that R_c depends also on the gate dielectric materials;[54] The primary factor behind the large R_c was attributed to the density of charge traps in the access region (from contact to channel) of devices rather than the energy mismatch between the energy levels of the metal electrode and the organic semiconductor.

There are several methods proposed for the extraction of this R_c.[55] The most widely used and adopted in this thesis is the transfer line method (TLM) which was first developed for amorphous silicon transistors.[56] In addition to R_c, the charge carrier faces another resistance R_{ch} when transported across the channel and the OFET can be viewed as a series of resistances. The TLM method is based on the assumption that the contact resistance is independent of the channel length unlike the channel resistance R_{ch} which is proportional to it. Thus, devices with different channel lengths are measured under the same gate and small drain biases. Accordingly, from the linear region of the output characteristics, one can extract the total resistance R_T (i.e. the sum of the channel resistance and the contact resistance) for each channel length as per the following:

$$R_T = \frac{\partial V_D}{\partial I_D}\Big|_{V_D \to 0}^{V_G} = R_{ch} + R_c \qquad (2.12)$$

Given that the channel resistance in the linear region is:

$$R_{ch} = \frac{L}{W\mu C_i(V_G - V_T)} \qquad (2.13)$$

The slope of the plot of the corresponding resistance R_T vs the channel length L is proportional to the channel resistance. Consequently, an extrapolation to zero channel length gives the contact resistance by substituting eq. 2.13 in eq. 2.12.

2.2.4.5 Subthreshold swing

The subthreshold swing S (expressed in V/dec) is a measure that indicates how much a gate potential is required to switch the device on. It is the inverse of slope of logI_D vs V_G (at a V_G of interest) measured in the region of the plot below the threshold (called subthreshold region):

$$S = \frac{dV_G}{d(logI_D)} \tag{2.14}$$

The slope (1/S) is taken at the steepest point of the subthreshold region when I_D starts to rise at a certain V_G. S depends on the gate dielectric and it is mainly used to estimate the density of the traps at the dielectric interface[57-60] from the following equation:

$$S = \left(\left(\frac{k_B T}{e}\right) \ln 10\right)\left(1 + \frac{D_{it}}{e\, C_i}\right) \tag{2.15}$$

Where D_{it} is the interface-trap density, C_i dielectric capacitance per unit area. k_B, e, and T are the Boltzmann constant, electric charge, and absolute temperature respectively.

It is worth mentioning that from all of the above mentioned parameters for OFETs mainly the field-effect mobility and the I_{on}/I_{off} ratio are often utilized for comparing the performance of devices based on various semiconductors. The other factors (i.e. V_{Th}, R_c and S) are more related into understanding the problems of the device and improving its performance through engineering the interfaces as will be discussed in the following part.

2.2.5 Factors influencing the device performance

The performance of an OFET is not restricted to the intrinsic properties of the organic semiconductor. It is an interplay between several interfaces and it is related (but not limited) to many parameters emphasized in the following section.

2.2.5.1 Charge injection control

As previously mentioned, the basic requirement for a good Ohmic contact is to have S-D electrodes with a work function matching one of the energy levels of the semiconductor in order to have optimal injection/collection of the charges at the electrode/semiconductor interface. In reality, such contact is not ideally Ohmic in most of organic devices and a contact resistance is obviously present. Several approaches have been utilized for optimizing the electrode/semiconductor interface and tuning its properties for a high performance OFET: *i)* inserting a buffer layer between the semiconductor and the metal electrode. This has an advantage of not only lowering the injection barrier but also preventing metal diffusion (while depositing metal electrodes by evaporation) or unfavorable water and oxygen molecules to penetrate the semiconducting layer which enhances the stability of the device.[61] *ii)* replacing the metal electrodes with polymer ones designed not only for improving the charge injection but also reducing the cost of the fabrication of the device.[62] *iii)* the last effective and widely used approach is the functionalization of the metal S-D electrodes with self-assembled monolayers SAM in order to minimize R_c and to smoothen the carrier injection. The formation of SAM on the surface of the metal changes the properties of the metal/semiconductor by forming an external dipole which improves the interfacial contact between the metal and the molecules of the semiconductor.[63-64] However, this approach is restricted to bottom-contact device geometry because SAMs are formed from solution or vapor phase. The most extensively studied and commonly used SAM are the thiol based SAMs which are composed of: *i)* –SH functional group called head group, *ii)* a terminal functional group and *iii)* a spacer in between. The head group binds to the metal surface by forming a strong covalent bond between the Sulfur and the metal atom on the surface by losing hydrogen atom. This process occurs because the surface of the metal tends to attract adsorbates which lower the free energy between the metal and the environment.[65] These thiol based adsorbates form a SAM with a stability, an ordering and a packing that depends on the linkage between the S-metal (i.e. the interaction with the surface) and on the interchain interaction (i.e. the lateral interactions between the organic components of the SAM; typically van der Waals interactions[66] with the neighboring molecules). It is worth mentioning that the structures of the SAMs are not defect free. The latter (i.e. the defect) can originate from external factors such as impurities present at the surface or in the solution, defects at grain boundaries and at the steps of the metal surface.[67]

Among the thiol based SAMS also used in this thesis, alkanethiol (where the thiol group is a substituent on an alkane) are the most investigated for tailoring the properties of the semiconductor/electrode interface because they have strong affinity to transition metal surfaces.[68] It was found that the performance of the device was influenced by the chain length of the alkanethiol.[69]

2.2.5.2 Dielectric-semiconductor interface

In the following paragraph, only the treatments used in this thesis will be detailed.

The semiconductor/dielectric interface is another crucial factor affecting the performance of the device since the charge transport mainly occurs at the first few monolayers of the semiconductor layer next close the dielectric.[70] The presence of traps at the dielectric interface, affects the threshold voltage and the transport of the carriers in the channel. For example, FETs with modified dielectric interface showed *n*-type transport which was quenched for unmodified dielectric surfaces.[71]

Ideally, the dielectric surface should provide an environment of highly ordered film without trapping of the charges. To tailor the properties of this interface, different surface treatments can be applied namely for SiO_2 dielectric: *i)* UV/ozone treatment that is primarily a well-established method for cleaning surfaces and removing organic contaminants.[72] Furthermore, it was shown that the reactivity of the SiO_2 surface is changed by this treatment which modified the semiconductor film growth and resulted in larger grain size thus improving the performance of the OFET.[73] *ii)* Alternatively, SAMs proved to be excellent candidates for the modification of surface properties. In fact a bare SiO_2 dielectric surface is characterized by the presence of a large number of SiOH (Silanol) groups which act as irreversible traps for the charges. Trapping of the electron, results in the formation of SiO^- ions as per the following mechanism:[74]

$$\equiv \mathrm{Si} - \mathrm{O} - \mathrm{Si} \equiv \ + \mathrm{H_2O} \ \rightleftarrows 2\ \mathrm{SiOH} \qquad (1)$$

$$\equiv \mathrm{Si} - \mathrm{OH} + \ \mathrm{H_2O} \ \rightleftarrows \mathrm{SiO^-} + \mathrm{H_3O^+} \qquad (2)$$

$$\mathrm{SiO^-} + \mathrm{H_3O^+} + e^- \rightarrow \mathrm{SiO^-} + \mathrm{H_2O} + \frac{1}{2}\mathrm{H_2} \qquad (3)$$

The silanol formed (in reaction 1) is deprotonized by water (reaction 2) and it is assumed that the electron can be captured by the fragments of the pair formed between the deprotonized silanol groups and the protonised water (reaction 3). The SiO^- groups in turn induce an electric field opposed to the gate bias thus quenching an efficient charge transport.[71] This is indicative of how important is to passivate these groups to avoid their effect on the charge transport. This can be possible by a treatment with SAMs of Hexamethyldisilazane (HMDS) or alkylsilane such as alkyltrichlorosilane family ($CH_3(CH_2)_{n-1}SiCl_3$) which are the most popular surface modifiers. Within the alkylsilane family, octatrichlorosilane (n=8) (OTS) and octadecyl-trichlorosilane (OTDS) are the frequently studied. These SAMs are often deposited from solution. They adsorb on the SiO_2 surface where they react with the silanol groups by forming covalent bonds[75] as illustrated in **Figure 2.14**

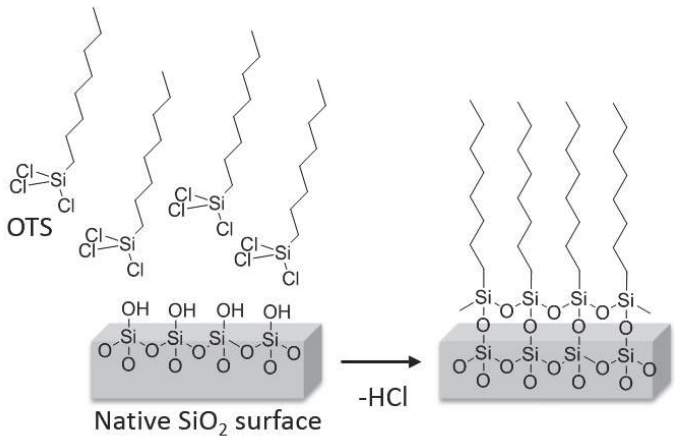

Figure 2.14 Schematic illustration of the assembly of the SAM of octatrichlorosilane (OTS) on a SiO_2 surface by reaction with the hydroxyl groups of the silanols**.**

Additional important influence of the SAMs is that by adjusting the terminal functional groups (i.e. in the ω-position), it is possible to tune the threshold voltage[46] and the surface energy of the SiO_2 dielectric which in turn affects the field-effect mobility.[76] For example, the molecular orientation can be changed from parallel form (face-on) to a perpendicular form (edge-on) by tuning the functional end groups of the SAMs which alters the interaction between the semiconductor and the dielectric surface.[77]Several studies have been conducted to understand the effect of the SAMs on the device performance particularly the charge trap density, V_{Th}[78] and μ.[79]

2.2.5.3 The molecular packing and film morphology

As mentioned above and particularly for polymer based OFETs, the molecular packing and the orientation of the organic semiconductor building blocks with respect to the substrate, in addition to their alignment relative to the electrodes have a strong influence on the charge transport in OFETs. For instance in a *p*-type polymer such as poly(3-hexylthiophene) (P3HT) an edge on orientation (i.e. perpendicular to the surface) is more favorable for the charge transport resulting in a high field-effect mobility.[77] This molecular orientation depends on the properties of the surface on which the semiconducting molecules are deposited. The molecule-surface interaction results in either an edge-on or face-on orientation which strongly influence the charge transport properties and therefore the performance of the device.

Moreover, the choice of the solvent from which the organic semiconductor is processed, the deposition techniques and thus the morphology of the semiconductor are also crucial for the performance of the OFETs. For the case of polymers, the semiconducting film is characterized by the co-existence of polycrystalline and amorphous domains. By using high boiling point solvents, the self-assembly of the crystalline domains occurs on a longer time frame, also the orientation of the polymer backbone with respect to the substrate are modified. As a consequence, the charge carrier mobility increases.[80] It is worth pointing that the molecular structure and the morphology of the organic semiconductor are largely determined by the underlying surface properties.

2.2.5.4 Other parameters

Additionally to all of the above mentioned parameters, the presence of impurities also influence the performance of an OFET. These impurities can originate from the synthesis of the organic semiconductor or from the ambient atmosphere. Most of the organic semiconductors are sensitive to oxygen and water which degrade the device and decreases its performance. For this reason most of the OFETs are prepared and tested in an inert atmosphere such as N_2. Nevertheless, several efforts have been devoted to develop materials that can form a barrier to atmospheric penetration. Alternatively, when exposed to air, the lifetime of the device can be extended by encapsulation.

In the next paragraphs, a very brief description of the operating principle of two types of OFETs will be presented in view of helping the reader understanding the discussion in the next chapters.

2.2.6 Ambipolar FET

An ambipolar OFET is a device able to operate for both positive and negative applied biases unlike unipolar device which can work only for either a positive or a negative bias where there is only one type of charge carriers in the channel. The advantage of an ambipolar OFET is that it can be used in complementary integrated circuits[81] where both *n*-channel and *p*-channel transports are required.

There are three various operating regimes of an ambipolar OFET depending on the drain bias, the gate bias and the threshold voltages for both electrons and holes ($V_{Th,e}$ and $V_{Th,h}$ respectively with $V_{Th,h} < V_{Th,e}$) : *i)* unipolar linear regime, *ii)* unipolar saturation regime, and *iii)* ambipolar regime.[35] A unipolar regime corresponds to the presence of only one type of carriers in the channel for a particular biasing condition similarly to a unipolar transistor discussed in section 2.2. Whereas in an ambipolar regime, both electrons and holes are present in the channel.

i) **unipolar linear regime**

For $V_D \leq (V_G - V_{Th,e})$ and $V_D \leq (V_G - V_{Th,h})$, when the gate bias is greater than the threshold voltage of electrons (at positive gate and drain biases), the transistor operates in the linear regime and the majority of the carriers in the channel are electrons. The standard drain current equation for the linear regime (i.e. eq. 2.5) can be utilized and it becomes:

$$I_D = \frac{W}{L} C_i \mu_e \left(V_G - V_{Th,e} - \frac{V_D}{2}\right) V_D \qquad (2.16)$$

where μ_e is the field-effect mobility of electrons

ii) **unipolar saturation regime**

The drain current saturates at a gate bias higher than the threshold voltage of electrons and for $V_D \geq (V_G - V_{Th,e})$ and $V_D \geq (V_G - V_{Th,h})$. Thus, eq. 2.6 can be used and it becomes:

$$I_D = \frac{W}{2L} C_i \mu \left(V_G - V_{Th,e}\right)^2 \quad (2.17)$$

The hole transport occurs when $V_G < V_{Th,e}$ and for $V_D \geq (V_G - V_{Th,h})$. In this case the drain current becomes dominated by holes and can be represented by:

$$I_D = \frac{W}{2L} C_i \mu_h \left(V_D - \left(V_G - V_{Th,h}\right)\right)^2 \quad (2.18)$$

Where μ_h is the field-effect mobility for holes.

iii) **ambipolar regime**

For $V_D \geq (V_G - V_{Th,h})$ and $V_G \geq V_{Th,e}$, the device exhibits an ambipolar behavior due to the presence of both electrons and holes in the channel (Figure 2.15). They both contribute to the drain current;

$$I_D = \frac{W}{2L} C_i \left[\mu_e \left(V_G - V_{Th,e}\right)^2 + \mu_h \left(V_D - \left(V_G - V_{Th,h}\right)\right)^2\right] \quad (2.19)$$

(A detailed description of the operating principle of an ambipolar OFET can be found in ref. [82])

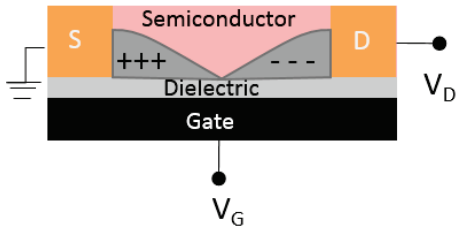

Figure 2.15 Schematic illustration of an OFET in the ambipolar regime where both holes and electrons are present in the channel.

The semiconductor layer of an ambipolar OFET consists of either a single component (with engineered HOMO and LUMO facilitating the injection of both holes and electrons) or a multiple components (double layered stack or a blend of *p*-type and *n*-type materials as will be detailed in chapter 4).

2.2.7 Phototransistor

Functional OFETs have attracted also attention in organic electronics for their potential application in light detection, medical diagnostics, signal storage etc…. In particular, organic phototransistors OPTs are of a great interest for use in photosensing devices.[83] An OPT is a four terminal device. Three of the terminals are the same as for an OFET and the fourth terminal is the light-irradiation which acts as additional control parameter for the drain current. The working principle is simple. Upon irradiation with light, the photons are absorbed by the organic semiconductor and an exciton (i.e. a bound electron/hole pair) is formed which subsequently separates into free electron and hole when encountering a dissociating site such as surface state or defect. Once dissociated, one type of these free charge carriers migrate towards the drain electrode under the influence of the electric field and the other charge carrier of opposite sign is trapped[84] as illustrated in **Figure 2.16**; thereby the carrier density in the channel increases and so does the drain current. The latter can be tuned using both gate bias and light intensity. Thus a single device works as light detector and signal amplifier.

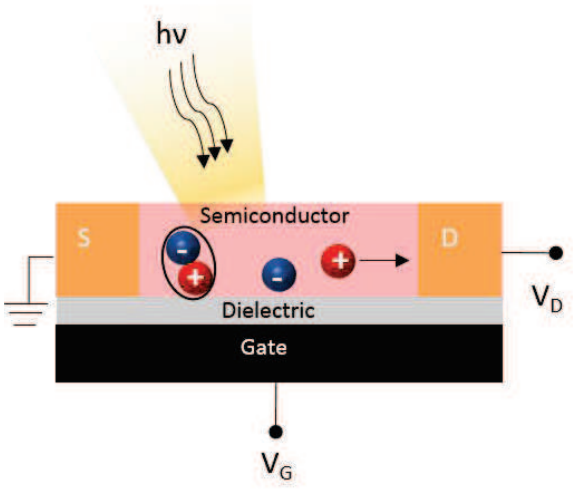

Figure 2.16 Schematic illustration of a *p*-type organic phototransistor under illumination showing the formation of exciton (bound electron (blue)/hole (red) pair) which dissociates. In this example the free hole move towards the drain electrode.

In addition to the fundamental parameters (i.e. μ, V_{Th} and I_{on}/I_{off}) of an OFET, there are two additional ones for evaluating the performance of an OPT. The first one is the responsivity R

(expressed in $A \cdot W^{-1}$) indicating the sensitivity of the OPT to the radiant energy and its effectiveness into converting it into an electric current. R is given by the following equation:[85]

$$R = \frac{I_{Ph}}{P_{ill}} = \frac{I_{light} - I_{dark}}{E \times A} \qquad (2.20)$$

where I_{ph} is the photogenerated current (i.e. the difference between the drain current measured under illumination I_{light} and the drain current obtained in dark I_{dark}). P_{ill} is the incident of the illumination power on the channel of the device, E is the irradiance of the incident light and A is the effective device area. The second equally important parameter is the photosensitivity P which provides a measure of the increase in signal upon illumination:[83]

$$P = \frac{I_{Ph}}{I_{dark}} = \frac{I_{light} - I_{dark}}{I_{dark}} \qquad (2.21)$$

Several criteria have to be considered in an OPT: *i)* broad absorption band and high absorption coefficient of an organic semiconductor for an efficient absorption of photons and generation of carriers;[86] *ii)* the morphology of the organic semiconductor layer. For instance the lifetime and the diffusion length of excitons is higher in crystalline structure;[87-88] and *iii)* the channel length of the device.[89]

2.3 Conclusion

In this chapter, a background on organic semiconductors was presented in addition to a brief explanation about some charge transport models in these systems. Furthermore, basic principle of organic field-effect transistor, ambipolar and organic phototransistor were explained. Finally, the important parameters for judging the performance of such devices were highlighted stressing the factors that can influence it.

2.4 References

[1] J. P. Farges, *Organic conductors: fundamentals and applications*, Vol. 4, CRC Press, **1994**.
[2] S. Zumdahl, Chemistry 7th Edition, **2007**, 395.
[3] N. J. Juster, *J. Chem. Educ.* **1963**, *40*, 547.
[4] J. S. Brooks, *Chem. Soc. Rev.* **2010**, *39*, 2667.
[5] Z. Bao, J. Locklin, *Organic Field-Effect Transistors*, **2007**.
[6] H. Bässler, *Phys Stat Sol B* **1993**, *175*, 15.
[7] J. Cornil, D. Beljonne, J. P. Calbert, J. L. Brédas, *Adv. Mater.* **2001**, *13*, 1053.
[8] V. Coropceanu, J. Cornil, D. A. da Silva Filho, Y. Olivier, R. Silbey, J.-L. Brédas, *Chem. Rev.* **2007**, *107*, 926.
[9] H. Sirringhaus, T. Sakanoue, J.-F. Chang, *Phys Stat Sol B* **2012**, *249*, 1655.
[10] V. I. Arkhipov, I. I. Fishchuk, A. Kadashchuk, H. Bässler., in *Semiconducting Polymers: Chemistry, Physics and Engineering, 2nd edition*, (Eds: G. Hadziioannou, G. G. Malliaras), **2006**, 275.
[11] G. Horowitz, *Adv. Mater.* **1998**, *10*, 365.
[12] B. Gburek, *Analysis and modelling of charge transport properties in organic field-effect transistors*, Ph.D. Thesis, Jacobs University, **2010**.
[13] E. A. Davis, N. F. Mott, *Philos. Mag.* **1970**, *22*, 0903.
[14] N. F. Mott, *Philos. Mag.* **1969**, *19*, 835.
[15] M. C. J. M. Vissenberg, M. Matters, *Phys. Rev. B* **1998**, *57*, 12964.
[16] A. Dieckmann, H. Bässler, P. M. Borsenberger, *J. Chem. Phys.* **1993**, *99*, 8136.
[17] J. Frenkel, *Phys. Rev.* **1938**, *54*, 647.
[18] A. R. Brown, C. P. Jarrett, D. M. De Leeuw, M. Matters, *Synt. Met.* **1997**, *88*, 37.
[19] C. D. Dimitrakopoulos, S. Purushothaman, J. Kymissis, A. Callegari, J. M. Shaw, *Science* **1999**, *283*, 822.
[20] G. Horowitz, M. E. Hajlaoui, R. Hajlaoui, *J Appl. Phys.* **2000**, *87*, 4456.
[21] P. G. Le Comber, W. E. Spear, *Phys. Rev. Lett.* **1970**, *25*, 509.
[22] G. Horowitz, in *Organic Field-Effect Transistors*, (Eds: Z. Bao, J. Locklin), **2007**, 73.
[23] E. A. Silinsh, V. Cápek, *Organic Molecular Crystals: Interacton Localization, and Transport Phenomena*, AIP Press, New York, **1994**.
[24] T. Holstein, *Annals of Physics* **1959**, *8*, 343.
[25] H. Yan, Z. Chen, Y. Zheng, C. Newman, J. R. Quinn, F. Dotz, M. Kastler, A. Facchetti, *Nature* **2009**, *457*, 679.
[26] J. Lee, J. H. Kim, I. Seongil, *Appl. Phys. Lett.* **2003**, *83*, 2689.
[27] J. Li, J. Du, J. Xu, H. L. W. Chan, F. Yan, *Appl. Phys. Lett.* **2012**, *100*, 033301.
[28] K. Shiju, T. Praveen, J. Aneesh, J. Manuvel, *AIP Conf. Proc.* **2013**, *1536*, 1139.
[29] L. A. Majewski, R. Schroeder, M. Grell, *Appl. Phys. Lett.* **2004**, *85*, 3620.
[30] J. Tate, J. A. Rogers, C. D. W. Jones, B. Vyas, D. W. Murphy, W. Li, Z. Bao, R. E. Slusher, A. Dodabalapur, H. E. Katz, *Langmuir* **2000**, *16*, 6054.
[31] T. Kawase, T. Shimoda, C. Newsome, H. Sirringhaus, R. H. Friend, *Thin Solid Films* **2003**, *438–439*, 279.
[32] H. Sirringhaus, T. Kawase, R. H. Friend, T. Shimoda, M. Inbasekaran, W. Wu, E. P. Woo, *Science* **2000**, *290*, 2123.

[33] C. W. Sele, T. von Werne, R. H. Friend, H. Sirringhaus, *Adv. Mater.* **2005**, *17*, 997.
[34] G. Horowitz, R. Hajlaoui, H. Bouchriha, R. Bourguiga, M. Hajlaoui, *Adv. Mater.* **1998**, *10*, 923.
[35] J. Zaumseil, H. Sirringhaus, *Chem. Rev.* **2007**, *107*, 1296.
[36] N. Benson, C. Melzer, R. Schmechel, H. v. Seggern, *Phys Stat Sol A* **2008**, *205*, 475.
[37] M. C. Petty, in *Molecular electronics from principle to practice*, **2007**, 69.
[38] A. Ortiz-Conde, F. J. García Sánchez, J. J. Liou, A. Cerdeira, M. Estrada, Y. Yue, *Microelectronics Reliability* **2002**, *42*, 583.
[39] A. Ortiz-Conde, A. Cerdeira, M. Estrada, F. J. García Sánchez, R. Quintero, *Solid-State Electron.* **2001**, *45*, 663.
[40] F. J. García Sánchez, A. Ortiz-Conde, G. De Mercato, J. A. Salcedo, J. J. Liou, Y. Yue, *Solid-State Electron.* **2000**, *44*, 673.
[41] H.-S. Wong, M. H. White, T. J. Krutsick, R. V. Booth, *Solid-State Electron.* **1987**, *30*, 953.
[42] A. Wang, I. Kymissis, V. Bulović, A. I. Akinwande, *Appl. Phys. Lett.* **2006**, *89*, 112109.
[43] A. Wang, I. Kymissis, V. Bulovic, A. I. Akinwande, *IEEE Trans. Electron Devices* **2006**, *53*, 9.
[44] R. Schroeder, L. A. Majewski, M. Grell, *Appl. Phys. Lett.* **2003**, *83*, 3201.
[45] W. Ou-Yang, M. Weis, D. Taguchi, X. Chen, T. Manaka, M. Iwamoto, *J. Appl. Phys.* **2010**, *107*.
[46] K. P. Pernstich, S. Haas, D. Oberhoff, C. Goldmann, D. J. Gundlach, B. Batlogg, A. N. Rashid, G. Schitter, *J. Appl. Phys.* **2004**, *96*, 6431.
[47] L. Li, N. Lu, M. Liu, *Appl. Phys. Lett.* **2013**, *103*, 253303.
[48] T. Minari, T. Miyadera, K. Tsukagoshi, Y. Aoyagi, H. Ito, *Appl. Phys. Lett.* **2007**, *91*, 053508
[49] L. Bürgi, T. J. Richards, R. H. Friend, H. Sirringhaus, *J. Appl. Phys.* **2003**, *94*, 6129.
[50] P. Cosseddu, A. Bonfiglio, *Thin Solid Films* **2007**, *515*, 7551.
[51] M. Halik, H. Klauk, U. Zschieschang, G. Schmid, W. Radlik, S. Ponomarenko, S. Kirchmeyer, W. Weber, *J. Appl. Phys.* **2003**, *93*, 2977.
[52] D. Braga, G. Horowitz, *Adv. Mater.* **2009**, *21*, 1473.
[53] P. V. Pesavento, K. P. Puntambekar, C. D. Frisbie, J. C. McKeen, P. P. Ruden, *J. Appl. Phys.* **2006**, *99*, 094504
[54] T. Minari, L. Chuan, "Origin of large contact resistance in organic field-effect transistors", presented at *Interconnect Technology Conference (IITC), 2013 IEEE International*, 13-15 June 2013, 2013.
[55] M. C. Panzer, J. D. Frisbie, in *Organic Field-Effect Transistors*, (Eds: Z. Bao, J. Locklin), CRC Press, **2007**, 148.
[56] S. Luan, G. W. Neudeck, *J. Appl. Phys.* **1992**, *72*, 766.
[57] A. Takshi, J. Madden, *J Comput Electron* **2011**, *10*, 154.
[58] R. Hayakawa, K. Higashiguchi, K. Matsuda, T. Chikyow, Y. Wakayama, *ACS Appl. Mater. Interfaces* **2013**, *5*, 3625.
[59] M. S. Pope, C, *Electronic Processes in Organic Crystals and Polymers* **1999**, 2nd ed Oxford University Press.
[60] S. Scheinert, G. Paasch, M. Schrödner, H.-K. Roth, S. Sensfuß, T. Doll, *J. Appl. Phys.* **2002**, *92*, 330.
[61] C.-W. Chu, S.-H. Li, C.-W. Chen, V. Shrotriya, Y. Yang, *Appl. Phys. Lett.* **2005**, *87*, 193508.

[62] L. Li, L. Jiang, W. Wang, C. Du, H. Fuchs, W. Hu, L. Chi, *Adv. Mater.* **2012**, *24*, 2159.
[63] J.-P. Hong, A.-Y. Park, S. Lee, J. Kang, N. Shin, D. Y. Yoon, *Appl. Phys. Lett.* **2008**, *92*, 143311.
[64] B. H. Hamadani, D. A. Corley, J. W. Ciszek, J. M. Tour, D. Natelson, *Nano Lett.* **2006**, *6*, 1303.
[65] Adamson, A. W., A. P. Gast, *Physical Chemistry of Surfaces, 6th ed.*, Wiley-Interscience, New York **1997**.
[66] J. P. Bareman, M. L. Klein, *J. Phys. Chem.* **1990**, *94*, 5202.
[67] J. C. Love, L. A. Estroff, J. K. Kriebel, R. G. Nuzzo, G. M. Whitesides, *Chem. Rev.* **2005**, *105*, 1103.
[68] T. Laiho, J. A. Leiro, *Appl. Surf. Sci.* **2006**, *252*, 6304.
[69] P. Stoliar, R. Kshirsagar, M. Massi, P. Annibale, C. Albonetti, D. M. De Leeuw, F. Biscarini, *J. Am. Chem. Soc.* **2007**, *129*, 6477.
[70] C. Tanase, E. J. Meijer, P. W. M. Blom, D. M. De Leeuw, *Org. Electron.* **2003**, *4*, 33.
[71] L.-L. Chua, J. Zaumseil, J.-F. Chang, E. C. W. Ou, P. K. H. Ho, H. Sirringhaus, R. H. Friend, *Nature* **2005**, *434*, 194.
[72] M. Claes, S. De Gendt, C. Kenens, T. Conard, H. Bender, W. Storm, T. Bauer, P. Mertens, M. M. Heyns, *J. Electrochem. Soc.* **2001**, *148*, G118.
[73] D. Guo, S. Entani, S. Ikeda, K. Saiki, *Chem. Phys. Lett.* **2006**, *429*, 124.
[74] W. Olthuis, P. Bergveld, *IEEE Trans. Electr. Insul.* **1992**, *27*, 691.
[75] Y. Wang, M. Lieberman, *Langmuir* **2003**, *19*, 1159.
[76] T. Umeda, D. Kumaki, S. Tokito, *J. Appl. Phys.* **2009**, *105*, 024516.
[77] D. H. Kim, Y. D. Park, Y. Jang, H. Yang, Y. H. Kim, J. I. Han, D. G. Moon, S. Park, T. Chang, C. Chang, M. Joo, C. Y. Ryu, K. Cho, *Adv. Funct. Mater.* **2005**, *15*, 77.
[78] J. Takeya, T. Nishikawa, T. Takenobu, S. Kobayashi, Y. Iwasa, T. Mitani, C. Goldmann, C. Krellner, B. Batlogg, *Appl. Phys. Lett.* **2004**, *85*, 5078.
[79] Y. Jang, J. H. Cho, D. H. Kim, Y. D. Park, M. Hwang, K. Cho, *Appl. Phys. Lett.* **2007**, *90*.
[80] J.-F. Chang, B. Sun, D. W. Breiby, M. M. Nielsen, T. I. Sölling, M. Giles, I. McCulloch, H. Sirringhaus, *Chem. Mater.* **2004**, *16*, 4772.
[81] T. D. Anthopoulos, D. M. de Leeuw, E. Cantatore, S. Setayesh, E. J. Meijer, C. Tanase, J. C. Hummelen, P. W. M. Blom, *Appl. Phys. Lett.* **2004**, *85*, 4205.
[82] A. Risteska, K.-Y. Chan, T. D. Anthopoulos, A. Gordijn, H. Stiebig, M. Nakamura, D. Knipp, *Org. Electron.* **2012**, *13*, 2816.
[83] Y. Guo, G. Yu, Y. Liu, *Adv. Mater.* **2010**, *22*, 4427.
[84] G. Konstantatos, E. H. Sargent, *Nat Nano* **2010**, *5*, 391.
[85] M. C. Hamilton, S. Martin, J. Kanicki, *IEEE Trans. Electron Devices* **2004**, *51*, 877.
[86] H. Dong, H. Zhu, Q. Meng, X. Gong, W. Hu, *Chem. Soc. Rev.* **2012**, *41*, 1754.
[87] N. M. Johnson, A. Chiang, *Appl. Phys. Lett.* **1984**, *45*, 1102.
[88] R. R. Lunt, J. B. Benziger, S. R. Forrest, *Adv. Mater.* **2010**, *22*, 1233.
[89] M. E. Gemayel, M. Treier, C. Musumeci, C. Li, K. Müllen, P. Samorì, *J. Am. Chem. Soc.* **2012**, *134*, 2429.

Chapter 3 Graphene and Graphene nanoribbons

3.1 Graphene

Introduced in Chapter 1, graphene is as a single-atom thick membrane of carbon atoms arranged into a two-dimensional (2D) honeycomb lattice[1] (Figure 3.1a). It can be viewed as well as an elegant 2D material consisting of fused benzene rings. The name graphene originates from the Greek word: "Graphein" which means to write and this was one of the earliest uses of this material. The stacking of graphene layers (that are weakly bonded by Van der Waals forces) on the top of each other's forms a three dimensional material called graphite[2] (Figure 3.1b) that was used in pencils in 1564.[3] Graphite had several applications throughout the history,[4] essentially in the molds to make cannon balls or as electrodes due to its high conductivity.

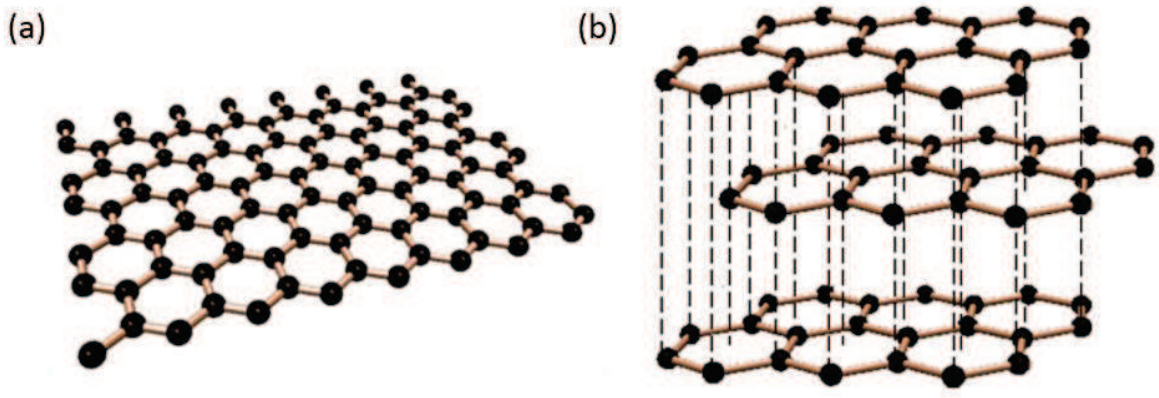

Figure 3.1 (a) A single-atom thick membrane of carbon atoms arranged in a honeycomb lattice forming graphene. (b) Stacked layers of graphene forming graphite. Dashed lines represent the weak van der Waals forces between the layers.

Previous to 2004, graphene was presumed that it is unstable and cannot exist in the free state due to the thermal fluctuations that prevent long-range crystalline order at finite temperatures[5] and was described as an "academic" material. Before being known as graphene, the band structure of a single graphene layer was calculated in 1947,[6] predicting a zero band gap (which will be discussed in the following paragraph). Then later, graphene was observed on Platinum[7] and has been produced from silicon carbide SiC by high temperature annealing.[8] However, the results didn't receive an important attention from the community. Later in 1994, the single atomic layer of graphite was named "graphene"[9] and started to gain increased interest more precisely after the successful isolation of a single graphene sheet in 2004 by splitting graphite via brute force by pealing using an adhesive tape.[10] The isolation of the sheets allowed the exploitation of the properties of this fascinating 2D material which showed exceptional physical properties. Since this experimental discovery, the "gold rush" started worldwide and lots of efforts are devoted for developing techniques that can produce large quantities of graphene in order to fabricate products (such as smart displays or ultra-fast transistors) benefiting of the properties offered by this "wonder" material.

3.1.1 Fundamental properties

3.1.1.1 Basic electronic properties

As above mentioned, electronic properties of graphene have been studied in 1947[6] well before its experimental discovery. The unit cell of the honeycomb lattice of graphene contains two non-equivalent types of carbon atoms designated A and B. These two sublattices are separated by a Carbon-Carbon bond with a length of 1.42 A°[2] (Figure 3.2a). What makes graphene so special is that it is a semimetal with a zero band gap where the conduction and valence bands touch at six points called the charge neutrality or Dirac point as illustrated in **Figure 3.2b**. Hence the band structure of graphene can be viewed as two cones touching at the Dirac point. This behavior is attributed to the bonding π-states and anti-bonding π^*-states that are orthogonal and thus the nearest neighbor tight-binding approximation is used to determine the band structure of graphene shown in **Figure 3.2b**. The energy dispersion relation of bonding and antibonding bands can be written as:[11]

$$E\left(k_x, k_y\right) = \pm\gamma\sqrt{1 + 4\cos\left(\frac{\sqrt{3}k_x a}{2}\right)\cos\left(\frac{k_y a}{2}\right) + 4\ \left[\cos\left(\frac{k_y a}{2}\right)\right]^2} \quad (3.1)$$

where k_x and ky are the coordinates of the vectors $\vec{K}$ that belong to the first hexagonal region called Brillouin zone BZ (i.e. the hexagon shown in Figure 3.2c). γ is equal to 2.75 eV and is the overlap integral between first (nearest) neighbors. The "±" sign designates the conduction and the valence bands respectively. This equation leads to symmetric conduction and valence bands (with respect to the Fermi energy) which degenerate at the points situated on the corners of the BZ also called *K* and *K*' valleys that are connected by time reversal symmetry[11] (Figure 3.2c). In graphene, the low-energy dispersion near the *K* points is linear unlike common materials which have parabolic distribution.[4] Therefore, graphene charge carriers are called Dirac Fermions because they behave like massless relativistic particles obtained from the Dirac equation:[2]

$$E_D(k) = \pm\sqrt{m^2c^4 + \hbar^2c^2|k|^2} \quad (3.2)$$

where E_D is the Dirac energy, m and c are the relativistic mass and the speed of light respectively. $\hbar$ is the Planck's constant divided by 2π. For a massless particle (m=0) eq. 3.2 becomes:

$$E_D(k) = \pm\hbar c|k| \quad (3.3)$$

The above mentioned electronic properties are actually characteristics of a single layer (called also monolayer) of graphene. However in case of many layers, these properties change with the stacking order (relative position of the atoms in adjacent layers) and the number of layers.[13] Therefore in a bilayer graphene (composed of 2 layers), the sheets can stack in a way where each atom sits on the top of the other atom and this is called *AA* stacking. In another possible stacking way, a set of atoms from the second layer sit in the voids at the center of the hexagon of the first layer and this is called *AB* stacking. The stacking order becomes more and more complicated with increasing the number of layers. Among other factors influencing the electronic properties of graphene is the folding as depicted in **Figure 3.3a** which results in a slight indirect overlap of 8 meV around the *K* point[14] (see Figure 3.3b).

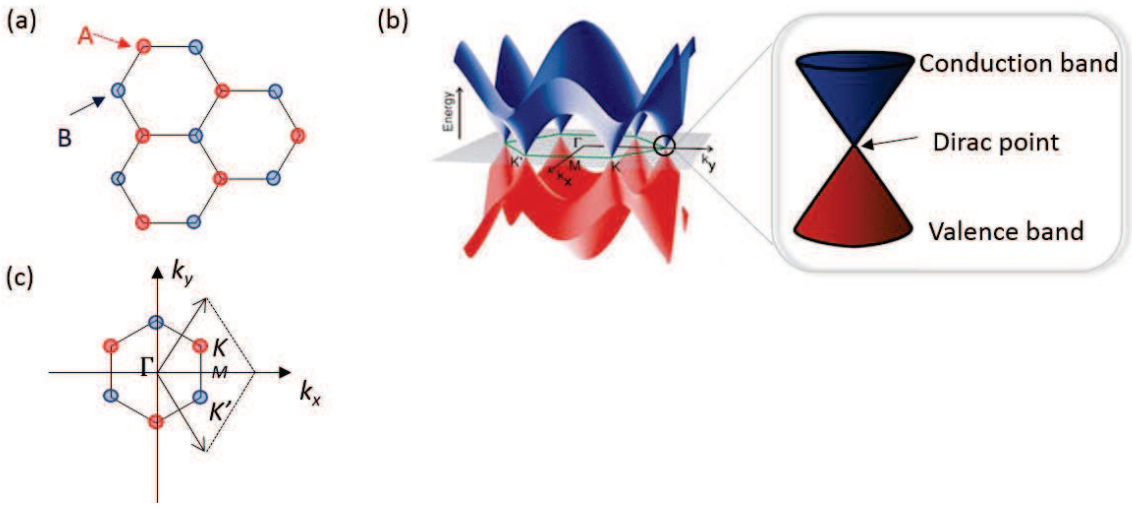

Figure 3.2 (a) Honeycomb lattice of graphene. Red (A) and blue (B) show two subsets of carbon atoms in graphene. (b) Electric band structure of graphene obtained via tight binding approximation. The "zoom in" highlights the conical shape of the dispersion around the Dirac point. (c) First Brillouin zone BZ marked by black full lines. K and K' are the two inequivalent points of the BZ and Γ is the center of the BZ. (a) and (c) redrawn from [2] and (b) taken and redesigned from [12].

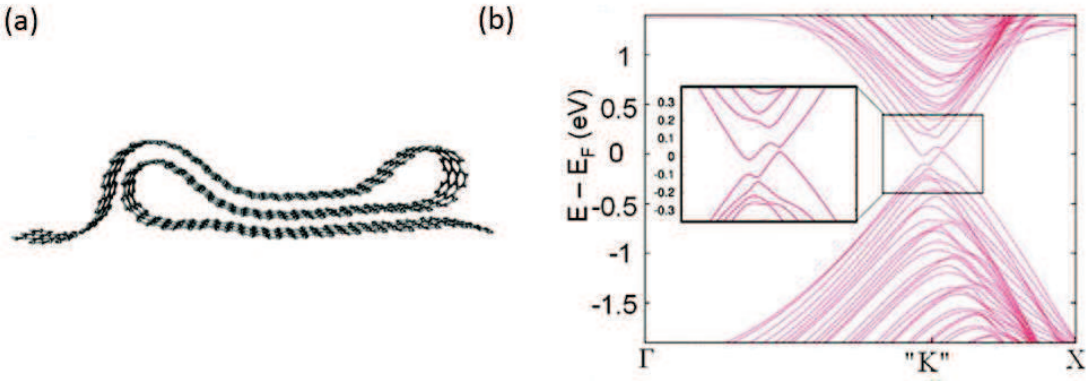

Figure 3.3 (a) Double folding structures in graphene sheets. (b) Electronic band structure of folded sheet along the direction of the fold. It shows a semimetallic system with a slight indirect overlap between the occupied and unoccupied states. Taken from Ref.[14].

3.1.1.2 Other properties

Besides the fascinating electronic band structure of graphene described above, this material features remarkable optical properties. Despite being one atomic layer thick, it absorbs a significant fraction of the incident light.[15] Furthermore, it is impermeable to standard gases[16] and it has excellent mechanical properties with a Young's modulus of 1 TPa and intrinsic strength of 130 GPa[17] making it an ideal reinforcement for material composites. Moreover,

graphene has a very high thermal conductivity > 3000 m^{-1} K^{-1}[18] which is higher than copper. More details about these properties can be found in Ref.[19].

3.1.2 Fabrication methods

There are lots of methods used and developed for the preparation of graphene with various sizes and quality; however the challenge is to achieve high yield of production. These preparation techniques can be classified in two different approaches: the bottom-up and the top-down approaches. Only scalable methods of each approach will be discussed. The bottom-up approach consists of synthesizing graphene from carbon sources using two methods: *i)* the Chemical Vapor Deposition (CVD) and *ii)* the synthesis using Silicon Carbide (SiC). CVD is a chemical process at high temperatures. It consists of the decomposition of hydrocarbon gases (such as H_2 or CH_4) subjected to a catalytic metal surface such as Copper and Nickel. The technique allows the growth of large size graphene monolayer[20] that can be transferred to any desired substrate. Alternatively, SiC is coated on a Silicon wafer and heated in an inert atmosphere at temperatures in excess of 1000 K in order to separate C and Si atoms. The latters then evaporate and only carbon atoms remain, resulting in the growth of graphene on the surface.[21] On the other hand, conversely to the bottom up-approach, the top-down approach (used in this thesis) is more advantageous in terms of high yield, solution processability and ease application. It consists of dispersing graphite in organic solvents (also aqueous solvents with surfactants can be used) and separating the sheets with the aid of sonication. This results in a suspension of pieces of different number of layers which can be separated by centrifugation.[22]**Figure 3.3** shows a comparison between all these techniques and the non-scalable ones (such as the mechanical exfoliation for separating graphene from graphite using an adhesive tape or the molecular assembly).

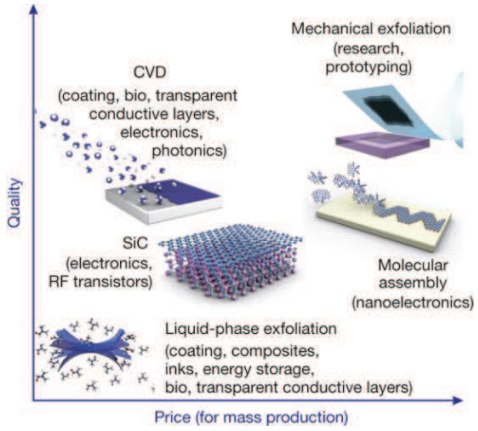

Figure 3.4 Comparison between quality and cost of production of graphene using several methods. Taken from Ref. [23].

It is important to highlight that the properties of graphene strongly depend on the production method.[23]

3.1.3 Field-effect transistors based on graphene.

The observation of an electric field-effect in graphene was first reported in 2004[10] where the transistor featured a bottom-contact configuration (with graphene as channel material). For a gapless graphene, the transfer characteristics displayed in **Figure 3.5** show an ambipolar behavior where both electrons and holes act as transport carriers. That is because when a positive gate bias is applied, the Fermi level of graphene is shifted to the conduction band favoring the transport of electrons and resulting in a pronounced *n*-type conduction in the channel of the transistor. At the Dirac point (where the conduction and the valence bands meet), the drain current is minimal due to a decrease in the carrier density. At this point, the type of conduction in the channel changes from *n*-to *p*-type and at negative gate bias the Fermi level shifts below the Dirac point downwards to the valence band enhancing the charge transport of holes. The position of the Dirac point is affected by the doping of graphene, or by other factors of which the density and the type of the charges at the interfaces at the top and the bottom of the channel.[24] While for a multilayer graphene based FET, a gate independence is observed.[10]

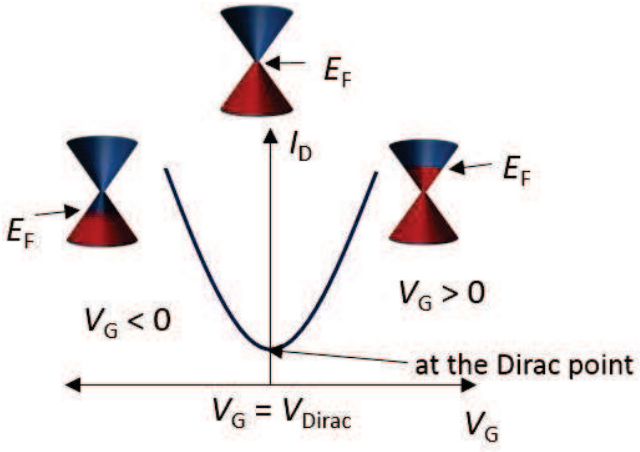

Figure 3.5 Transfer characteristics of a gapless graphene based field-effect transistor showing the ambipolar behavior and highlighting the variation of the position of the Fermi level with the applied gate bias**.**

The most stated advantage of graphene is its high carrier mobility ranging from 15 000 $cm^2 \cdot V^{-1} \cdot s^{-1}$ at room temperature for gapless graphene on SiO_2 substrate at room temperature[10] up to more than 100 000 $cm^2 \cdot V^{-1} \cdot s^{-1}$ for suspended graphene on SiO_2 measured at ~5K.[25] On the other hand, graphene FETs show I_{on}/I_{off} ratios of 2 to 10 which means that the device is always in the "on" state and cannot be switched off. This is not a problem for Radio Frequency RF FETs where a switching "off" is not required; whereas for complex logic circuits this switching ratio should be high and an "off" state is required. One possible way to overcome this problem is to open a band gap in graphene. This is possible either for a bilayer graphene[26] or by confining the width of the graphene sheet and thus forming the so called "graphene nanoribbons" which will be discussed in the following paragraph.

3.2 Graphene nanoribbons

3.2.1 Fundamental properties

3.2.1.1 Structure

Reducing the width of a graphene sheet forms a graphene nanoribbon GNR (i.e. elongated strips of graphene with a finite width) and results into different types of edges which strongly

influence the properties of the GNR. There are two types of edges: armchair and zigzag. Their atomic structure is displayed in **Figure 3.6a** and **b** respectively.

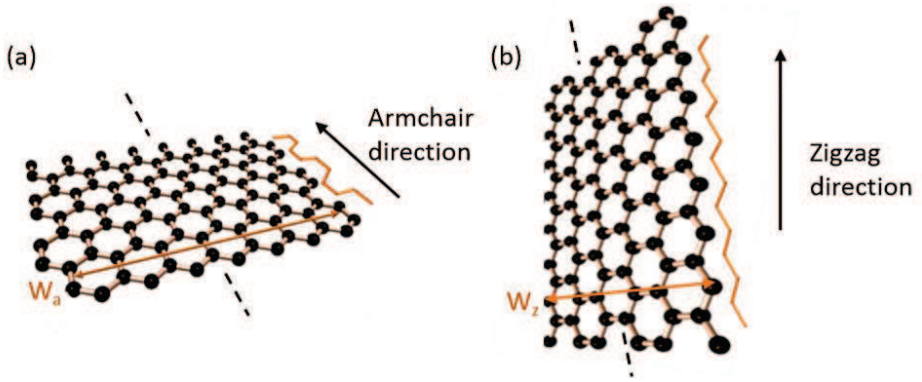

Figure 3.6 Edge structure of (a) an armchair and (b) a zigzag graphene nanoribbon with a corresponding finite width denoted as W_a and W_z. Dashed lines indicate an infinite length of the GNRs.

The atoms located at the edges are highlighted in orange and their width is denoted by *W*. Armchair graphene nanoribbon a-GNRs, are classified by the number of dimer chains N_a (zigzag lines) across the ribbon width W_a which is given by[27]: $W_a = (N_a - 1)\, a/2$. For a z-GNR, its width W_z is denoted by the number of zigzag chains N_z and defined as[27]: $W_z = (N_z - 1)\, \sqrt{3}a/2$.

3.2.1.2 Electronic properties

The edge effect on the band structure of a confined graphene was first studied in 1996 and calculated using the tight-binding approximation.[28] By assuming that the dangling bonds on the edge sites do not contribute to the electronic state near the Fermi level and by assuming that all the edge sites are terminated by hydrogen atoms, it was found that z-GNR are always metallic. This is because around the Fermi level the edge states are present as flat bands which become flatter with increasing N_z. Whereas a-GNR could be either semiconductive or metallic depending on the width. The band gap of the semiconducting nanoribbon can be tuned by the ribbon width; more precisely it is inversely proportional to the width and tends to zero for a very large N_a. Later on, theoretical calculations showed that a-GNR are always semiconductor with a band gap that scales ~$1/W_a$[29] arising from the quantum confinement and suggesting that the variation of the energy of the gap with the width of the ribbon can be grouped in three

different families: N_a=3p, 3p+1 or 3p+2 where p is an integer. In this case the 3p+2 family is semiconducting[29] (Figure 3.7a), whereas it was found metallic as per the tight binding approximation[28] (Figure 3.7b). Experimental results agreed well with the prediction for the band gap variation with the ribbon width.[30] Recently it has been demonstrated that a band gap as high as 1.88 eV can be obtained for GNR with a lateral width of ~1 nm[31] which makes it appealing for technological applications.

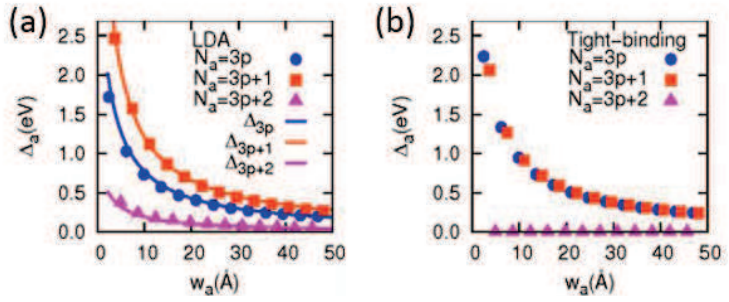

Figure 3.7 Variation of the band gap (here noted Δ_a) of a-GNR with the width W_a. Energy values obtained using (a) the first principles and (b) tight binding approximation methods. Image taken from Ref. [29].

It is important to note that the band gap of a ribbon doesn't depend only on the width of the ribbon[30] and its edge structure [32] but also on the number of layers.[33] For example in a-GNR the band gap decreases by 0.5 eV going from a monolayer to a bilayer and for multi layered a-GNR a nearly graphitic band gap is obtained.

3.2.2 Preparation methods

Similarly to the synthesis of graphene, GNRs can be obtained using the bottom-up and top-down approaches. The most widely used technique is the top down approach which consists of either: *i)* etching or cutting graphene sheets into narrow strips, or *ii)* unzipping carbon nanotubes.

i) **Etching or cutting graphene**

One of the fabrication techniques consists of patterning mechanically exfoliated or CVD grown graphene by e-beam lithography, followed by an oxygen plasma etching using masks (with variable width) in order to fabricate GNRs with variable width.[34-35] This approach was further

optimized and nanoribbons as narrow as 6 nm were obtained.[36] Recently, Helium ion beam lithography was used to pattern CVD grown graphene into narrow GNRs with tunable widths (< 10 nm).[37] This technique resulted in highly aligned, densely packed and high aspect ratio GNR arrays. Alternatively, GNRs can be prepared from bulk graphite using the solution approach resulting in sub-10 nm GNRs.[30] Briefly, expanded graphite was exfoliated then sonicated (in order to break down graphene sheets) in the presence of a polymer in an organic solvent and GNRs are obtained from the supernatant after centrifugation.

ii) **Unzipping carbon nanotubes**

In this technique the starting material is carbon nanotubes CNTs, unlike the above mentioned technique which uses graphite or CVD grown graphene as precursors. Using a chemical process, the shell of the carbon nanotube is oxidized which causes its opening along the longitudinal direction thus forming a nanoribbon.[38] On the other hand, another approach for making GNRs, consists of unzipping the CNTs which are partly embedded in a polymer matrix by plasma etching.[39] This results in GNRs with controlled width and edge structures which are the main challenges in the fabrication of graphene or GNRs allowing their application as alternative technology.

To this end, there are several problems accompanying the fabrication of GNRs by top-down approach such as the edge roughness, high aspects ratios and large scale production which is not yet achieved.

On the contrary, the bottom-up approach (used in this thesis) provides a full control of not only the edge structure of the GNRs but also their width which can be below 5 nm. More details can be found in Ref. [40]. Efforts have been devoted to make the synthesized GNRs solution processable;[31] even though, there are several drawbacks particularly for the application in devices which will be discussed in this thesis throughout chapter 6.

3.2.3 Field-effect transistors based on GNRs

The highest mobility around 2000 $cm^2 \cdot V^{-1} \cdot cm^{-1}$ at room temperature was obtained for FET based on GNR with ~20 nm width featuring a band gap around 100 meV.[41] Whereas, devices based on sub-10 nm GNRs showed field-effect mobility of ~200 $cm^2 \cdot V^{-1} \cdot cm^{-1}$ but with higher

I_{on}/I_{off} of ~10^5 which was attributed to the large band-gap.[42] In this work, devices based on GNRs with a width below 10 nm showed a semiconducting behavior with a gate dependence in contrast to wide GNRs which exhibited metallic like behavior with no gate dependence because of vanishingly small band gaps. For instance even in the sub-10 nm GNR-FETs which showed a dominant *p*-type behavior, the Dirac point was not observed at V_g=0 V due to doping. Unlike another study, where 16 nm wide GNR FET, the Dirac point was close to 0 V and the device exhibited ambipolar behavior with symmetric hole and electron transports similar to graphene.[39]This is to emphasize that the electronic properties of FETs based on GNRs strongly depend on the width of the nanoribbon and its edges which are influenced by the fabrication techniques and are uncontrolled in most of the cases. As above mentioned, the bottom-up approach enables the synthesis of well-defined carbon nanomaterials with a full control on their edges. There is only one example in literature investigating the electronic properties of solution processed GNRs (chemically synthesized) in FETs. In these devices, the hole transport was dominant and the field-effect mobility ~10^{-2} $cm^2 \cdot V^{-1} \cdot cm^{-1}$.[43] Nevertheless, for industrial applications requiring large I_{on}/I_{off} and mobilities comparable to Si, GNRs with a width narrower than 5 nm are the most anticipated candidates as they fulfill these requirements as depicted in **Figure 3.8**. In this figure, a comparison between the variations of the two figures of merit of a transistor (i.e. the I_{on}/I_{off} and the mobility) with the width of the nanoribbon is displayed. Basically, the trend with decreasing the width of the GNR is an increase in the band gap and in the I_{on}/I_{off} ratio while the mobility decreases.[44] However, the fabrication of devices with such narrow GNRs remains a challenge.

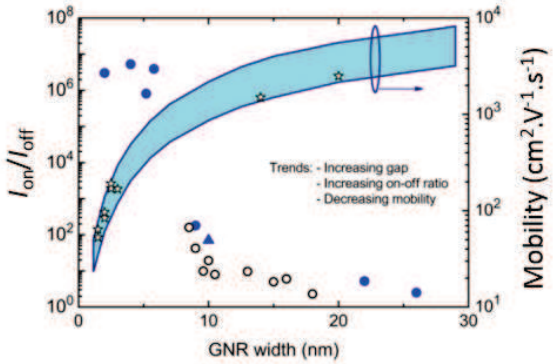

Figure 3.8 Variation of the I_{on}/I_{off} and mobility with the width of GNR. Data taken from: [45] for triangle, [30, 42] full circles and [36] open circles respectively and correspond to the I_{on}/I_{off} ratio. Stars taken from: [41-42, 46] and simulated data [47] (shaded area) and correspond to the mobility. Image taken from Ref. [44].

3.3 Graphene and GNRs

3.3.1 Defects

This following paragraph describes briefly the types of defects that influence particularly the electronic properties of graphene and GNRs.

Besides their edge defects, both graphene and GNRs can accommodate different kind of defects that influence their properties. Some of these defects which affect in particular the electronic properties can be: *i)* structural defects caused by the presence of non-hexagonal rings (i.e. octagons, heptagons) around the hexagonal ones,[13] *ii)* point defects such as Stone-Wales defects which are created by rotating a C-C bond by 90˚ within the four neighboring hexagons that are subsequently transformed into two heptagons and two pentagons as demonstrated in **Figure 3.9a**.[48] This kind of defect in a nanoribbon can create new states in the gap as predicted theoretically.[49] Point defects also include vacancies such as single vacancy (see Figure 3.9b) (i.e. a missing carbon atom in the lattice leading to a dangling bond that is a non sp^2 carbon and the formation of a five-membered and a nine-membered ring) or adatoms which can be additional non carbon atoms embedded in the hexagonal carbon lattice. This type of defect can change the type of conductivity and can shift the Dirac voltage in FETs.[10] Most of the above mentioned defects lead to scattering of the electrons and change their directions[50] thus influencing their conductivity.[51]

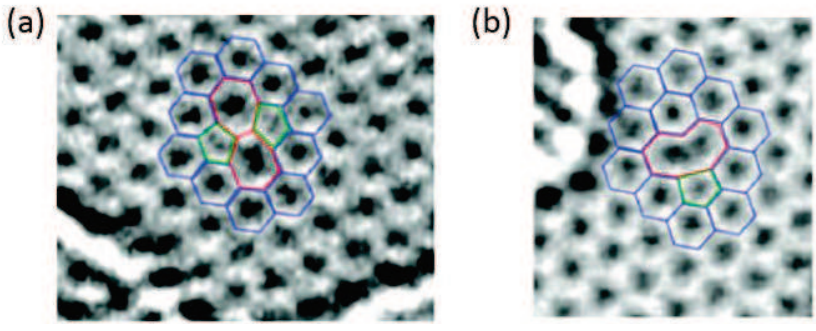

Figure 3.9 Experimental transmission electron microscope image of a lattice of graphene with: (a) stone-Wales defects and (b) single vacancy defect. Image taken from Ref. [48].

3.3.2 Characterization methods

Dealing with graphene and graphene nanoribbons requires an identification of their structure and the type of edges no matter of the technique used to prepare them because these parameters strongly influence their properties as above mentioned. The number of layers and their thicknesses can be determined by transmission electron microscopy (TEM) which is a powerful tool allowing as well the examination of the lattice structure at the atomic scale and the detection of defects as shown in **Figure 3.9**. Topographic contrast can be obtained by atomic force microscopy (AFM) which also allows thickness measurements and the determination of the width of the GNRs.[30] Raman spectroscopy is another convenient tool for characterizing graphene and GNRs.[52] It enables the determination the number of layers, the defects or the chemical modifications introduced during the preparation procedure. Other techniques can be found in Ref. [53].

3.4 Conclusion

In this chapter, a brief overview about some fundamental properties of graphene and GRNs was given; highlighting the approaches used for their fabrication and the factors influencing their electronic properties. Moreover, FETs based on these materials were discussed. The nature of defects present in the lattice graphene and GNR in addition to the techniques offered for the characterization and identification of their structure were briefly emphasized.

3.5 References

[1] A. K. Geim, K. S. Novoselov, *Nat. Mater.* **2007**, *6*, 183.
[2] A. H. Castro Neto, F. Guinea, N. M. R. Peres, K. S. Novoselov, A. K. Geim, *Rev. Mod. Phys.* **2009**, *81*, 109.
[3] H. Petroski, *The Pencil: A History of Design and Circumstance.*, Knopf, New York, **1989**.
[4] H. Raza, *Graphene Nanoelecronics*, Springer, **2012**.
[5] N. D. Mermin, *Phys. Rev.* **1968**, *176*, 250.
[6] P. R. Wallace, *Phys. Rev.* **1947**, *71*, 622.
[7] J. W. May, *Surf. Sci.* **1969**, *17*, 267.
[8] A. J. Van Bommel, J. E. Crombeen, A. Van Tooren, *Surf. Sci.* **1975**, *48*, 463.
[9] H.-P. Boehm, R. Setton, E. Stumpp, *Pure Appl. Chem.* **1994**, *66*, 1893.
[10] K. S. Novoselov, A. K. Geim, S. V. Morozov, D. Jiang, Y. Zhang, S. V. Dubonos, I. V. Grigorieva, A. A. Firsov, *Science* **2004**, *306*, 666.
[11] S. M. M. Dubois, Z. Zanolli, X. Declerck, J. C. Charlier, *Eur. Phys. J. B* **2009**, *72*, 1.
[12] Y. Wu, D. B. Farmer, F. Xia, P. Avouris, *IEEE Proc.* **2013**, *101*, 1620.
[13] M. Terrones, A. R. Botello-Méndez, J. Campos-Delgado, F. López-Urías, Y. I. Vega-Cantú, F. J. Rodríguez-Macías, A. L. Elías, E. Muñoz-Sandoval, A. G. Cano-Márquez, J.-C. Charlier, H. Terrones, *Nano Today* **2010**, *5*, 351.
[14] K. Kim, Z. Lee, B. D. Malone, K. T. Chan, B. Alemán, W. Regan, W. Gannett, M. F. Crommie, M. L. Cohen, A. Zettl, *Phys. Rev. B - Condensed Matter and Materials Physics* **2011**, *83*.
[15] R. R. Nair, P. Blake, A. N. Grigorenko, K. S. Novoselov, T. J. Booth, T. Stauber, N. M. R. Peres, A. K. Geim, *Science* **2008**, *320*, 1308.
[16] J. S. Bunch, S. S. Verbridge, J. S. Alden, A. M. van der Zande, J. M. Parpia, H. G. Craighead, P. L. McEuen, *Nano Lett.* **2008**, *8*, 2458.
[17] C. Lee, X. Wei, J. W. Kysar, J. Hone, *Science* **2008**, *321*, 385.
[18] A. A. Balandin, *Nat. Mater.* **2011**, *10*, 569.
[19] X. Huang, X. Qi, F. Boey, H. Zhang, *Chem. Soc. Rev.* **2012**, *41*, 666.
[20] S. Bae, H. Kim, Y. Lee, X. Xu, J.-S. Park, Y. Zheng, J. Balakrishnan, T. Lei, H. Ri Kim, Y. I. Song, Y.-J. Kim, K. S. Kim, B. Ozyilmaz, J.-H. Ahn, B. H. Hong, S. Iijima, *Nat Nano* **2010**, *5*, 574.
[21] K. V. Emtsev, A. Bostwick, K. Horn, J. Jobst, G. L. Kellogg, L. Ley, J. L. McChesney, T. Ohta, S. A. Reshanov, J. Rohrl, E. Rotenberg, A. K. Schmid, D. Waldmann, H. B. Weber, T. Seyller, *Nat. Mater.* **2009**, *8*, 203.
[22] A. Ciesielski, P. Samori, *Chem. Soc. Rev.* **2014**, *43*, 381.
[23] K. S. Novoselov, V. I. Falko, L. Colombo, P. R. Gellert, M. G. Schwab, K. Kim, *Nature* **2012**, *490*, 192.
[24] F. Schwierz, *Nat Nano* **2010**, *5*, 487.
[25] K. I. Bolotin, K. J. Sikes, Z. Jiang, M. Klima, G. Fudenberg, J. Hone, P. Kim, H. L. Stormer, *Solid State Commun.* **2008**, *146*, 351.
[26] Y. Zhang, T.-T. Tang, C. Girit, Z. Hao, M. C. Martin, A. Zettl, M. F. Crommie, Y. R. Shen, F. Wang, *Nature* **2009**, *459*, 820.

[27] C. G. Rocha, M. H. Rümmeli, I. Ibrahim, H. Sevincli, F. Börrnert, J. Kunstmann, A. Bachmatiuk, M. Pötschke, W. Li, S. A. M. Makharza, S. Roche, B. Büchner, G. Cuniberti, in *Graphene Synthesis and Applications*, (Eds: W. Choi, J.-W. Lee), CRC Press, **2011**, 1.
[28] K. Nakada, M. Fujita, G. Dresselhaus, M. S. Dresselhaus, *Phys. Rev. B* **1996**, *54*, 17954.
[29] Y. W. Son, M. L. Cohen, S. G. Louie, *Phys. Rev. Lett.* **2006**, *97*.
[30] X. Li, X. Wang, L. Zhang, S. Lee, H. Dai, *Science* **2008**, *319*, 1229.
[31] A. Narita, X. Feng, Y. Hernandez, S. A. Jensen, M. Bonn, H. Yang, I. A. Verzhbitskiy, C. Casiraghi, M. R. Hansen, A. H. R. Koch, G. Fytas, O. Ivasenko, B. Li, K. S. Mali, T. Balandina, S. Mahesh, S. De Feyter, K. Müllen, *Nat Chem* **2014**, *6*, 126.
[32] K. A. Ritter, J. W. Lyding, *Nat. Mater.* **2009**, *8*, 235.
[33] D. Finkenstadt, G. Pennington, M. J. Mehl, *Phys. Rev. B* **2007**, *76*, 121405.
[34] Z. Chen, Y.-M. Lin, M. J. Rooks, P. Avouris, *Physica E* **2007**, *40*, 228.
[35] M. Y. Han, B. Özyilmaz, Y. Zhang, P. Kim, *Phys. Rev. Lett.* **2007**, *98*, 206805
[36] J. Bai, X. Duan, Y. Huang, *Nano Lett.* **2009**, *9*, 2083.
[37] A. N. Abbas, G. Liu, B. Liu, L. Zhang, H. Liu, D. Ohlberg, W. Wu, C. Zhou, *ACS Nano* **2014**, *8*, 1538.
[38] D. V. Kosynkin, A. L. Higginbotham, A. Sinitskii, J. R. Lomeda, A. Dimiev, B. K. Price, J. M. Tour, *Nature* **2009**, *458*, 872.
[39] L. Jiao, L. Zhang, X. Wang, G. Diankov, H. Dai, *Nature* **2009**, *458*, 877.
[40] L. Chen, Y. Hernandez, X. Feng, K. Müllen, *Angew. Chem., Int. Ed.* **2012**, *51*, 7640.
[41] M. W. Lin, C. Ling, L. A. Agapito, N. Kioussis, Y. Zhang, M. M. C. Cheng, W. L. Wang, E. Kaxiras, Z. Zhou, *Phys. Rev. B* **2011**, *84*.
[42] X. Wang, Y. Ouyang, X. Li, H. Wang, J. Guo, H. Dai, *Phys. Rev. Lett.* **2008**, *100*.
[43] K. T. Kim, J. W. Jung, W. H. Jo, *Carbon* **2013**, *63*, 202.
[44] F. Schwierz, *IEEE Proc.* **2013**, *101*, 1567.
[45] L. Liao, J. Bai, R. Cheng, Y. C. Lin, S. Jiang, Y. Huang, X. Duan, *Nano Lett.* **2010**, *10*, 1917.
[46] L. Jiao, X. Wang, G. Diankov, H. Wang, H. Dai, *Nat. Nanotechnol.* **2010**, *5*, 321.
[47] M. Bresciani, A. Paussa, P. Palestri, D. Esseni, L. Selmi, *Tech. Dig. Int. Electron Devices Meeting* **2010**, 724.
[48] F. Banhart, J. Kotakoski, A. V. Krasheninnikov, *ACS Nano* **2010**, *5*, 26.
[49] D. W. Boukhvalov, M. I. Katsnelson, *Nano Lett.* **2008**, *8*, 4374.
[50] G. M. Rutter, J. N. Crain, N. P. Guisinger, T. Li, P. N. First, J. A. Stroscio, *Science* **2007**, *317*, 219.
[51] T. O. Wehling, S. Yuan, A. I. Lichtenstein, A. K. Geim, M. I. Katsnelson, *Phys. Rev. Lett.* **2010**, *105*.
[52] A. C. Ferrari, D. M. Basko, *Nat Nano* **2013**, *8*, 235.
[53] N. O. Weiss, H. Zhou, L. Liao, Y. Liu, S. Jiang, Y. Huang, X. Duan, *Adv. Mater.* **2012**, *24*, 5782.

Chapter 4 Experimental Techniques

4.1 Device fabrication

4.1.1 Substrate preparation

All the substrates used for the fabrication of bottom-gate transistors were purchased from Fraunhofer Institute. They are composed of 230 nm thin oxide serving as dielectric (capacitance 1.5×10^{-8} F·cm^{-2}) which is thermally grown on n++-doped silicon serving as gate. For bottom-contact geometry, these substrates exposed pre-patterned interdigitated Au electrodes (see Figure 4.1 left side) consisting of 30 nm Au on a top of a 10 nm thick adhesion layer of indium tin oxide (ITO). These electrodes have the same channel width (W=10 mm) and four different channel lengths (L=2.5, 5, 10 and 20 μm). The scanning electron microscopy image of a device with L=20 μm is displayed in **Figure 4.1** (left side) where each of the contact pads can be either the source or the drain electrode depending on how they are connected to the testing instrument. A zoom in of this image (Figure 4.1 right side) shows the channel width and the electrodes. On each testing chip, there are four devices of each channel length.

For the top-contact geometry the substrate has the same specifications as for the bottom-contact one mentioned above, except that it is bare and does not have the interdigitated electrodes. Nevertheless, both types of substrates (i.e. with or without the electrodes) are covered with a photoresist protective layer that is removed by ultrasonication in acetone (for 20 min) and isopropanol (for 20 min) then dried under a gentle flow of nitrogen before the preparation of the device.

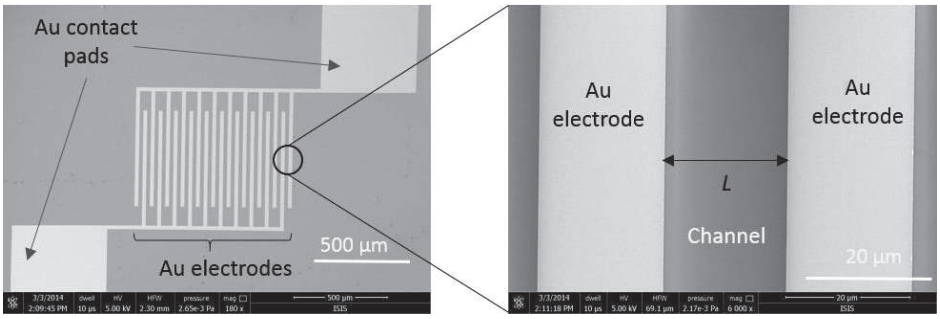

Figure 4.1 Scanning electron microscopy image showing the transistor's configuration (left side). A zoom in of this image (on the right side) shows a channel length L=20 µm between two electrodes.

4.1.1.1 Surface treatment

4.1.1.1.1 Surface cleaning

In some cases, after the cleaning procedure, the surface of the substrate is irradiated with intense short ultraviolet UV wavelengths (λ=185 and 254 nm emitted by a mercury vapor lamp) in the presence of oxygen in order to remove organic contaminants. Each cleaning cycle consists of 5 min irradiation with UV lights and 25 min of incubation. The mechanism is the following:[1] First, the oxygen is pumped into the chamber where the substrate is placed and is dissociated at λ=185 nm to form ozone and atomic oxygen. Then at λ=254 nm, the contaminants (i.e. organic molecules) on the surface of the substrate are excited and/or dissociated by the absorption of the UV light thus forming free radicals. The latters and the excited contaminant molecules react with atomic oxygen and are eliminated from the surface by forming volatile molecules such as CO_2 and H_2O vapor.

4.1.1.1.2 Dielectric passivation

In chapter 2, the importance of the passivation of the silanol groups present on the SiO_2 surface were highlighted. This treatment of the dielectric interface is crucial especially for *n*-channel devices because it prevents trapping the electrons[2] which are the majority of the carriers in the channel. One kind of SAMs used in this thesis is the Hexamethyldisilazane (HMDS) which can be easily formed on the surface by spin-coating (this technique will be descried later in this chapter) followed by a thermal annealing at 120°C.

4.1.1.2 Work function modification

SAMs of alkanethiol are used to modify the work function of Au by lowering the injection barrier formed at the electrode/semiconductor interface thus improving the charge injection into the channel of the device. After the ozone cleaning step, the substrates are transferred inside the glove box (N_2) atmosphere and dipped in a solution of alkanethiol (1 mM in ethanol) for around 12 hours (step 1 in Figure 4.2). Here we note that all the glassware used for the preparation of the alkanethiol were cleaned with a Piranha solution (formed by a mixture of 3:1 concentrated sulfuric acid to 30% hydrogen peroxide) to ensure the removal of any organic containments which can affect the formation of the SAMs. The dipping step for 12 h allows the chemisorption of the alkanethiol molecules on the metal's surface by forming a strong metal-sulfur bond (as explained in chapter 2 section 2.2.5.1). Then after, the substrates are removed and rinsed thoroughly with ethanol to remove the non-chemisorbed alkanethiol molecules from the surface (step 2 in Figure 4.2). This is followed by a gentle annealing in order to heal the defects.[3] This step is limited to an annealing temperature of 80˚C for 1 h (step 3 in Figure 4.2) as at temperature higher than 100 ˚C, molecular desorption starts to take place.[3]

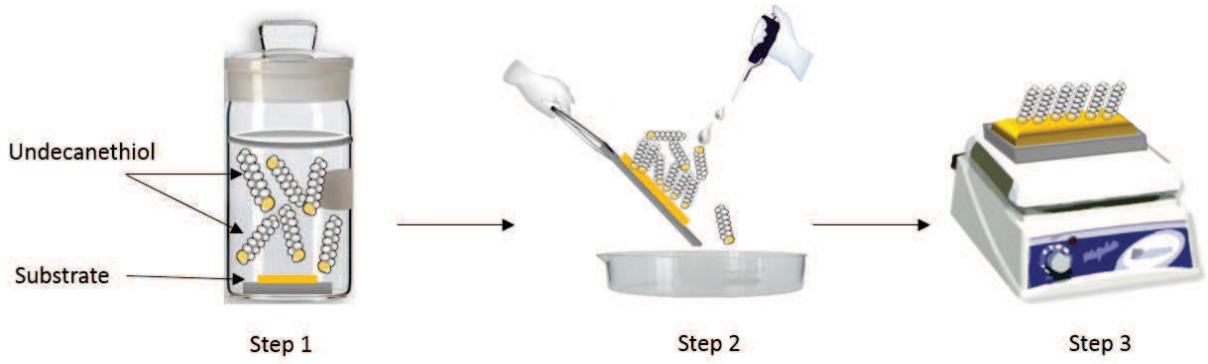

Figure 4.2 Schematic illustration of the procedure for the formation of the SAM on Au electrodes (dark yellow) deposited on a substrate. Undecanethiol was considered as an example here. Step 1 consists of dipping the substrate for overnight. Then in step 2, the substrate is removed from solution and rinsed. Finally in step 3, it is annealed.

4.1.2 Active channel material

4.1.2.1 Preparation

All the semiconductor materials were solution processed (i.e. dissolved in organic solvents) and used as received without any further purification. Some of the molecules are commercially available and some others are designed, synthesized and provided by the collaborators. This will be specified in the experimental part of each chapter. Concerning the blends, two different molecules were always dissolved in the same solvent then mixed at different ratios prior to their deposition on the substrate. As for graphene, it was prepared as per the standard top-down procedure:[4] First, commercially available graphite powder was dispersed in organic solvent, then placed in an ultrasonic bath (step 1 in Figure 4.3). The generated ultrasonic waves increase the distance between the solvent molecules. When this distance exceeds the molecular distance that holds the liquid intact, bubbles are formed due to the negative pressure generated when the acoustic energy is produced in the media.[5] This phenomenon is called "cavitation". Consequently, the bubbles grow and collapse, thus creating locally an intense shockwave with an extreme pressure that forms targeted shearing forces.[5] As a result, the graphite chunks break up as well as the van der Waals forces between the graphene sheets, hence forming isolated graphene layers (step 2 in Figure 4.3). A critical parameter in the exfoliation procedure is the surface tension γ of the solvent (i.e. the tendency of the surface of a liquid to resist to external forces). This parameter either favors the dispersion of the exfoliated sheets in the solvent or causes their poor dispersibility and therefore their aggregation (i.e. the graphene sheets adhere to each other) if the inter-sheet attractive forces are higher than the solvent graphene interaction. Ideal solvents able to disperse graphene by minimizing the interfacial tension between the solvent and graphene sheets, are those with γ around 40-50 $mJ \cdot m^{-2}$ [4] such as orthodichlorobenzene (*o*-DCB) or *N*-Methyl-2-pyrrolidone (NMP). After 6 hours of exfoliation, the obtained dispersion is left for 10 min to settle. Since it contains a mixture of flakes of different sizes and different number of layers, a centrifugation step (step 3 in Figure 4.3) is necessary in order to separate them and to obtain few-layer graphene sheets for the device fabrication.

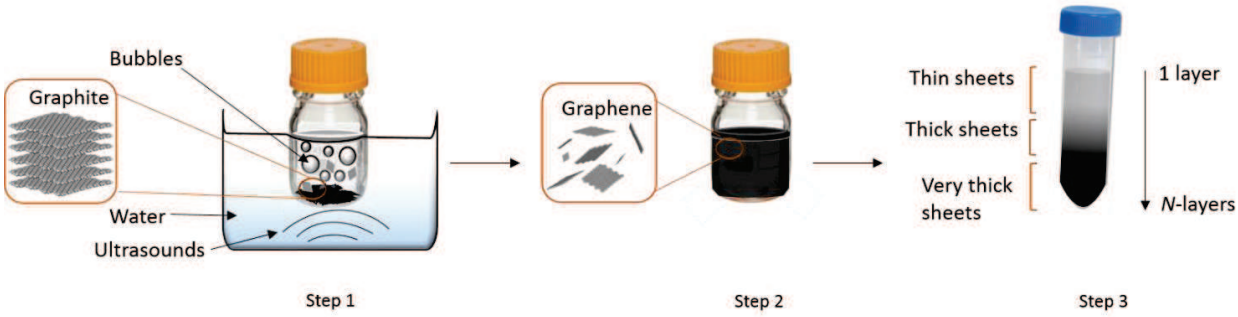

Figure 4.3 Schematic illustration of the procedure for the preparation of graphene. The first step consists of the dispersion of graphite flakes in organic solvent and the use of ultrasounds for the exfoliation of graphite. In step 2, graphene is obtained due to the sheering forces caused by the bubbles formed from the ultra-sonication. In step 3, graphene sheets are separated based on their number of layers by centrifugation and the supernatant is collected.

Consequently, the graphene dispersion is centrifuged at a certain speed for a certain time which allows the separation of the sheets based on their sedimentation rate in response to the centrifugal force acting on them. In our case, the centrifuge used (Eppendorf 5804) has a rotor with a fixed angle (rotor F-34-6-38). In this kind of centrifugation (at a fixed angle), the centrifugal force act on the suspended particles (i.e. graphene sheets) pushing them to the wall of the centrifuge tube and causing them to slide down to the tube thus forming a sediment at the bottom. The higher the rotation speed, the quicker the separation. It is important to note that the centrifugation time required for obtaining the desired separation depends on the rotor used. For example at the same centrifugation speed, if 10 min are required to separate the graphene sheets in one rotor with a certain angle, it will take different time to attain the same separation performance for the same sample using another rotor with different angle which affects the distance between the rotor axis and the tube.[6] After the centrifugation, only the supernatant is taken (because it contains graphene sheets composed of few number of layers) and then characterized in order to determine the exfoliation yield and the quality of the exfoliated graphene sheets (i.e. the number of layers forming the sheets).

4.1.2.2 Deposition

The semiconductor materials were deposited using two simple methods: *i)* spin-coating and *ii*) drop-casting. The former technique (i.e. spin-coating) is the most popular for the preparation of organic thin films processed from solution. The process is as follows:[7] first, a quantity of the solution containing the organic semiconducting material is dropped onto the substrate that is

held by vacuum on a rotating disk with a chuck (Figure 4.4a). Then, the substrate is rotated at a speed of several thousands of revolutions per minute (rpm) resulting in a radial flow of the solution outwards and a sweep off of most of the liquid from the surface. Therefore, the thickness of the liquid deposited on the substrate is reduced, the solvent evaporates and a uniform thin film is formed. The concentration of the solution used and the spin-coating speed are two important parameters that affect the film thickness. The latter is related to the spinning speed by an inverse power-law relationship:[8]

$$d = \left(\frac{\eta}{4\pi\rho\omega^2}\right)^{1/2} t^{-1/2} \tag{4.1}$$

where d is the thickness of the film; η and ρ are the viscosity coefficient and the density of the solution respectively; ω is the angular velocity of the spinning and t is the spinning time.

Some disadvantages of this technique are the waste of the swept off material from the substrate and the limitation to small area coverage.

On the other hand, drop casting technique consists of dropping the solution on the substrate and the evaporation of the solvent either spontaneously or by thermal annealing of the substrate (Figure 4.4b). In this technique there is no waste of material, however the main disadvantage is the minimal control over the thickness of the resulting organic thin film which will have a poor uniformity on the tens of micrometers scale. As the drop dries, a flow carries the molecules of the semiconductor towards the edges thus forming thick films around the edges of the original drop and thinner ones in the direction towards the center as depicted in **Figure 4.4c**.

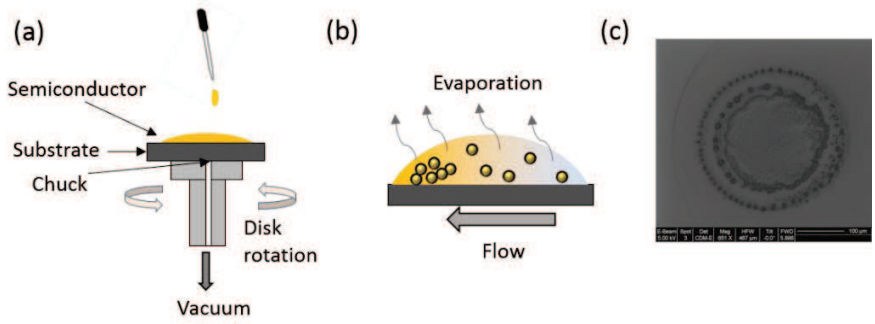

Figure 4.4 Schematic diagram of two deposition techniques: (a) spin-coating and (b) drop-casting. In (b) the evaporation causes flow from the bulk towards the edges forming concentrated areas (molecules represented in spheres). (c) Scanning electron microscopy image of a film formed by drop-casting.

4.1.3 Electrode deposition

For FETs with top-contact geometry, after the deposition of the semiconductor thin film on either treated or untreated substrates, the last step in the device preparation is the deposition of the metal electrodes by physical vapor deposition in vacuum using a shadow mask. First, the metal is placed in a crucible and heated to sufficient high temperatures for its evaporation. Then, the condensation of the vapor on the substrate forms a film which is patterned by the mask. Low pressure and vacuum environment are used for this process to avoid the contamination of the source material (such as oxidation) and the scattering of the vapor atoms when colliding with other gas atoms. The low pressure ($<10^{-4}$ mbar) allows a straight line path between the evaporated metal and the substrate.

Here we note that the preparation of the devices is performed in a nitrogen atmosphere (to avoid any doping or degradation of the organic semiconductor) except the step of cleaning the substrates that is performed in ambient atmosphere.

4.2 Characterization techniques

4.2.1 Electrical characterization

The electrical characterization of the devices was performed using a Keithley 2636A dual-channel sourcemeter as semiconductor parameter analyser controlled by associated software. The devices to be characterized were placed on a Cascade Microtech M150 probe station. Since all the FETs studied in this thesis featured bottom-gate geometry, thus the plate of the probe station on which the devices were placed, was used for contacting the gate electrode. As for the source and drain (S-D) electrodes, they were contacted using Süss probes under the microscope (used for magnifying the image of the device pads in order to be contacted with the probes). The setup is illustrated in **Figure 4.5** and the zoom in shows an optical micrograph image of the device contacted with the probes for the characterisation. All the measurement were done in a glove box (Jacomex) (filled with N_2 with O_2 levels lower than 15 ppm).

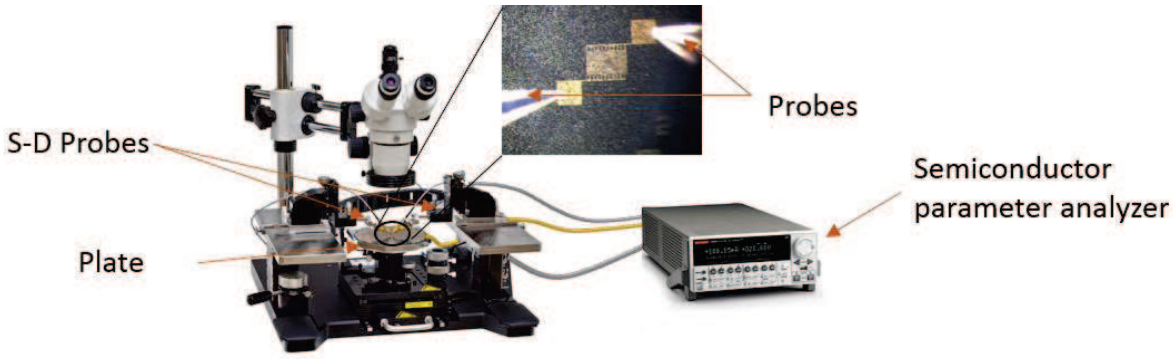

Figure 4.5 Schematic illustration of the electrical characterization setup. S-D stands for the source and drain electrodes. The zoom in shows a micrograph image of the device with the pads of the S-D electrodes contacted by the probes.

For the irradiation of the devices, it was performed from the top using a Polychrome V (Till Photonics) tunable light source providing a monochromatic beam with different wavelengths and irradiance levels.

4.2.2 Atomic Force Microscopy

Atomic Force Microscopy (AFM) images were recorded in ambient atmosphere using Nanoscope (Veeco Multimode V) in the tapping mode only (TM-AFM).

AFM is a scanning probe technique used to obtain images of the topography at the nm scale. In TM-AFM, the cantilever is driven by a piezo actuator and oscillates periodically at a frequency near its resonant frequency. The tip touches the surface of the sample intermittently (i.e. tapping occurs on the sample). During the scan, the oscillation amplitude of the cantilever varies with the interacting force between the tip and the sample. The cantilever's deflection is detected by a position photosensitive diode that receives a laser beam focused on and reflected of the backside of the cantilever as illustrated in **Figure 4.6a**. While scanning, the oscillation amplitude of the cantilever is altered by the surface topography and is maintained constant by a feedback loop that adjusts the cantilever's position either farther from or closer to the sample surface. Therefore, a topography image (Figure 4.6b) is obtained from variation of the vertical z-axis position plotted as a function of the xy position of the tip.

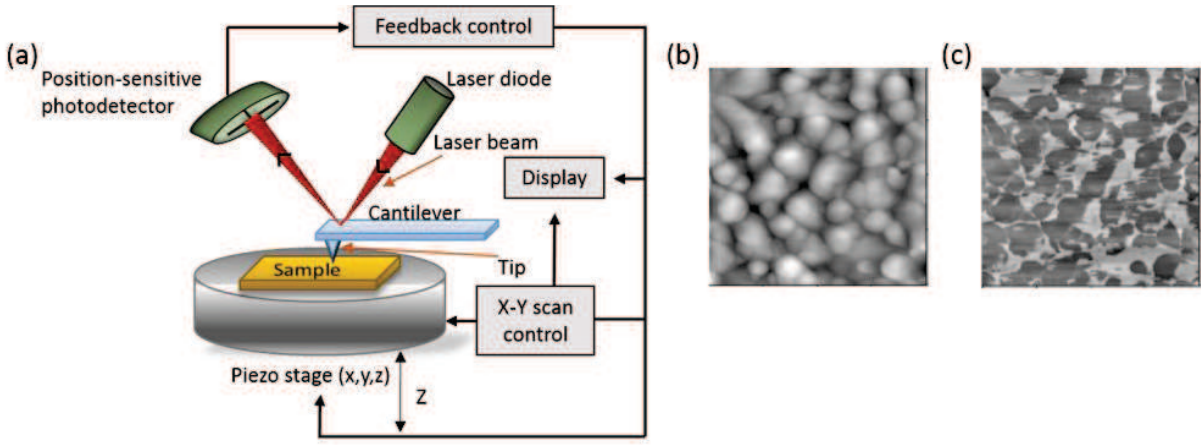

Figure 4.6 (a) Schematic of an AFM operation. (b) Topography and (c) phase-contrast images of a bicomponent thin film. (b) and (c) are taken from ref. [9].

Tapping mode can also generate phase-contrast image which is produced by monitoring the phase difference between the cantilever's oscillation and the standard signal that drives the piezoelectric while tapping. The phase contrast arises from the variations in the composition of the surface as well as from the variations of the topography caused by the changes in adhesion between the tip and the surface of the specimen[10] as shown in **Figure 4.6c** for a bicomponent film. In our case, for the semiconducting films composed of blends, phase contrast images were used in order to gain a better understanding about the phase separation of the blended material and the composition of the surface.

4.2.3 Scanning Electron Microscopy

Scanning Electron Microscope SEM was used to characterize graphene, in particular to determine the width of the exfoliated sheets. It was also used to acquire images of the morphology of the nanographene and graphene nanoribbon films.

In a scanning electron microscope (Figure 4.7), an electron beam of high energy electrons is generated by the filament of the electron gun (Tungsten in our case) which thermionically emits electrons (i.e. when sufficient heat is applied to the filament so that electrons can escape from it). This e-beam is then focused and reaches the anode which accelerates the free electrons down

the column. The condenser lens are used to reduce the diameter of the electron beam and to focus it. The e-beam is then focused on the surface by the objective lens. The scan coils in the final lens deflect the e-beam in the x and y axis so that it scans in a raster manner over a rectangular area of the surface of the sample. At the impact point of the primary e-beam (composed of accelerated electrons with significant amount of kinetic energy) with the sample surface, the energy of the incident electrons is decelerated. Therefore, the dissipation of this energy (arising from the electron-sample interaction) generates a variety of signals of which: secondary electrons (SE), back scattered electrons (BE) and X-rays. The SE are produced by the interactions between the energetic electrons and the weekly bonded valence electrons of the sample. They (i.e. the SE) emerge from the top-most nanometers of the sample, they have very low energy (< 50 eV) and they are collected by a SE detector. As for the BE (collected by the BE detector), they have high energies and they correspond to the primary electrons leaving the specimen after scattering (either elastically or inelastically) when they entered in collision with the electrons of the sample atoms. Finally, for the X-rays, they are collected by the X-ray detector also called EDX (energy dispersive X-ray) detector.

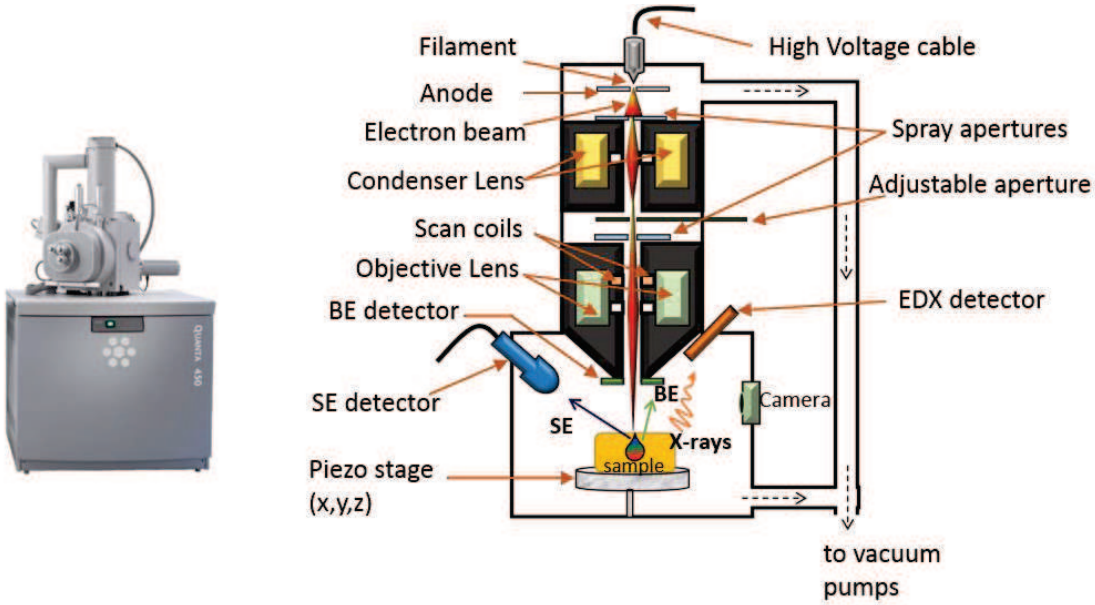

Figure 4.7 Scanning electron microscope (left side) and a schematic illustration of its operation.

It is worth mentioning that the SEM chamber is under vacuum to avoid the scattering of the electrons by air molecules.

All SEM images in this thesis were acquired with Quanta FEG 450 (FEI®) using the SE detector with 5 kV acceleration voltage and a spot size of 3.5.

4.2.4 Ambient photoelectron spectroscopy

The ionization energies IE (i.e. the minimum energy required to remove an electron from an atom or a molecule) of the studied molecules were determined on either films or powders using RIKEN AC-2 which is a new generation of ultra-violet photoelectron spectroscopy that operates under ambient conditions. The operating principle is illustrated in **Figure 4.8**. First, a D_2 lamp emits a UV light (with a wavelength of 200 to 300 nm) that enters a spectrometer. The latter selects the desired wavelength and the resulting UV beam irradiates the surface of the sample and results in an emission of electrons. Thereafter, the emitted electrons move towards the detector and by attaching to an oxygen molecule, they drift towards the open counter. The photoelectron yield ratio is then plotted versus the UV energy applied. The slope of the linear fit of the resulting plot corresponds to the value of the IE.

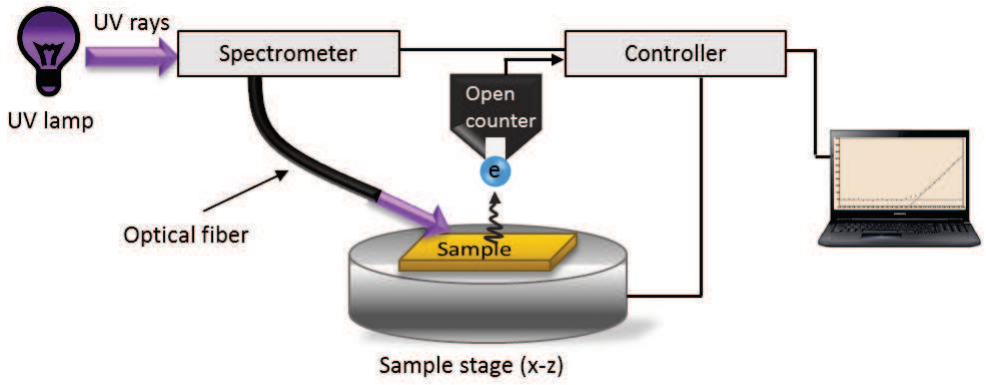

Figure 4.8 Schematic illustration of the operation of the ambient photoelectron spectrometer.

4.2.5 Ultraviolet-visible absorption spectroscopy

Ultraviolet-visible absorption spectra of thin films (prepared by drop-casting or spin-coating) and solutions were recorded on JASCO V-670 and Shimadzu UV-3101PC spectrophotometers. Quartz slides were used for the films, while 1cm quartz cuvettes were used for the solutions.

Mainly, the acquired spectra were used in order to select the convenient wavelength for the irradiation of the devices.

4.3 References

[1] J. Vig, in *Handbook Of Silicon Wafer Cleaning Technology*, (Ed: W. Kern), **1993**, 233.
[2] L.-L. Chua, J. Zaumseil, J.-F. Chang, E. C. W. Ou, P. K. H. Ho, H. Sirringhaus, R. H. Friend, *Nature* **2005**, *434*, 194.
[3] E. Delamarche, B. Michel, H. Kang, C. Gerber, *Langmuir* **1994**, *10*, 4103.
[4] Y. Hernandez, V. Nicolosi, M. Lotya, F. M. Blighe, Z. Sun, S. De, I. T. McGovern, B. Holland, M. Byrne, Y. K. Gun'Ko, J. J. Boland, P. Niraj, G. Duesberg, S. Krishnamurthy, R. Goodhue, J. Hutchison, V. Scardaci, A. C. Ferrari, J. N. Coleman, *Nat Nano* **2008**, *3*, 563.
[5] D. G. Shchukin, E. Skorb, V. Belova, H. Möhwald, *Adv. Mater.* **2011**, *23*, 1922.
[6] Eppendrof®, in *http://www.eppendorf.es/int/index.php?mode=print&sitemap=4.1&action=support&contentid=20&nodeid=52925*.
[7] T. Ohara, Y. Matsumoto, H. Ohashi, *Phys. Fluids A* **1989**, *1*, 1949.
[8] M. C. Petty, in *Molecular electronics from principle to practice*, **2007**, 242.
[9] Y. Qiu, Y. Hu, G. Dong, L. Wang, J. Xie, Y. Ma, *Appl. Phys. Lett.* **2003**, *83*, 1644.
[10] G. K. H. Pang, K. Z. Baba-Kishi, A. Patel, *Ultramicroscopy* **2000**, *81*, 35.

Chapter 5 Organic semiconductor blend with graphene

5.1 Introduction

Emerging technological demands require more and more the development of semiconducting materials[1-2] suitable for ambipolar field-effect transistors (FETs) as potential active components for organic complementary metal-oxide semiconductor (CMOS) to ultimately enable the development of robust, low-noise, low-power organic electronics.[3]

For a simple device fabrication process, single metal source and drain electrodes are preferred. Thus efficient ambipolar FETs can be ideally achieved by using symmetric electrodes and sophisticated single component semiconducting molecules with narrow band gaps, i.e. lower than 2 eV,[4-8] designed in such a way to be capable of transporting both electrons and holes under suitable biasing conditions and device configuration. Conversely, asymmetric electrodes having different work function (WF) can be employed to inject different charges in the active layer of the device,[9] although the fabrication procedure is more cumbersome since it requires multiple steps. An alternative approach relies on the use of bilayers of semiconductors[10-13] with high and low electron affinity (so called *n*-type and *p*-type) by choosing the materials carefully according to the relative position of their highest occupied molecular orbital (HOMO) and lowest unoccupied molecular orbitals (LUMO) levels. The combination of semiconductors in a bilayer provides a great opportunity to overcome the high injection barrier for one type of charge carrier when a single electrode material is employed, and renders the synthesis of the building block less challenging. However, the main disadvantage remains the need of controlled deposition of two layers on the top of each other. Alternatively, ambipolar transport was

achieved by blending unipolar *n*- and *p*-type materials either by co-evaporation[14-15] or co-deposition[16-19] from solutions resulting in an interpenetrating network of both materials.

The concept of blending materials was not only used for obtaining ambipolar devices but also for improving the device performance benefiting from the properties brought by each component,[20] as well as to incorporate more functions in a single device.[21-22]

Graphene is one among the most interesting candidates that can be embedded in polymer matrices [23-27] to improve the polymer performances. Graphene is a well-defined functional, 2-dimensional ambipolar material with a mobility for charge carriers exceeding 15,000 $cm^2 \cdot V^{-1} \cdot s^{-1}$ even under ambient conditions,[28] thus outperforming any organic semiconductor or even silicon. Despite its exceptional optical, mechanical and electronic properties,[29-30] the greatest challenge in graphene research remains the ability to process it in large quantities and high quality making use of up-scalable methods.

Among the various proposed methods, liquid-phase exfoliation is an extremely versatile and easily accessible procedure to produce graphene with a high yield starting from graphite powder.[30] Moreover, graphene is a zero band gap semiconductor: to impart to this 2D material a capacity to switch *on* and *off*, one can either confine it in space by generating graphene nanoribbons,[31-32] or having it interacting with molecular components that can act as dopant.[33-35] In this regard, graphene has been used for application in FETs by modulating its properties via blend with *p*-type semiconductors.[23-24, 26-27] Yet, until now, graphene was never exploited in *n*-type semiconductor matrices.

5.2 Scope

In this study, we show that the co-deposition of a solution containing both liquid-phase exfoliated graphene and an *n*-type polymer results in the leveraging of the ambipolar character, especially by enhancing the *p*-type conductivity. As a partner for graphene we selected *n*-type dominant poly [N, N 9-bis(2-octyldodecyl)-naphthalene-1,4,5,8-bis(dicarboximide)-2,6-diyl]-alt-5,59-(2,29-bithiophene)], P(NDI2OD-T2), Polyera ActivInk N2200) (Figure 5.1). This polymer has been widely investigated [18, 36-46] due to its high electron mobilities in field-effect devices (> 0.1 $cm^2 \cdot V^{-1} \cdot s^{-1}$) even in air environment, despite the use of high work function gold

electrodes.[37] Moreover, it can exhibit weak ambipolar characteristics which were demonstrated to be enhanced either through the use of a proper type of gate dielectric[45] or by blending with *p*-type polymer such as regioregular poly(3-hexylthiophene) (rr-P3HT).[18] Our approach exploits the exceptional electrical properties of graphene to enhance not only the charge transport but also the injection of both types of charge carriers into the transistor's active layer.

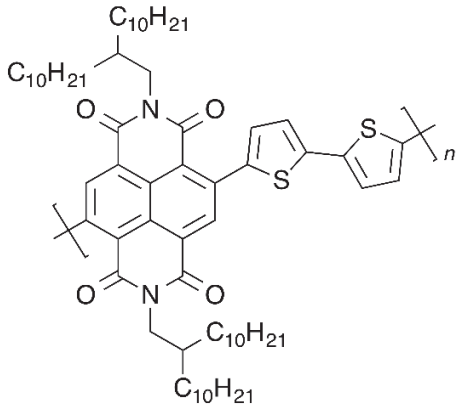

Figure 5.1 Chemical structure of P(NDI2OD-T2).

5.3 Experimental

5.3.1 Active materials

5.3.1.1 Organic semiconductor

P(NDI2OD-T2) has been purchased from Polyera® and used as provided. This polymer has a Mn=28.6 KDa and polydispersity of 2.5 determined using high temperature GPC (trichlorobenzene as mobile phase, temperature: 150 ˚C).

5.3.1.2 Graphene

Graphene dispersion was prepared by adding 98 mg of graphite powder (Aldrich product 332461, batch number 08722AH) in 7.7 mL of 1,2-dichlorobenzene (*o*-DCB) (spectrophotometric grade, 99.0%) (1 wt %) followed by bath ultrasonication (6h). Sonication of graphite powder led to grey liquid consisting of a homogeneous phase and large numbers of macroscopic aggregates. As previously reported,[47] these aggregates can be removed by

centrifugation (Eppendorf 5804, rotor F-34-6-38, 30 min at 5000 rpm followed by 15 min at 8000 rpm), yielding a homogeneous dark dispersion. Here we note that we did not perform the exfoliation in the presence of the polymer semiconductor because the control over the stoichiometry cannot be obtained when having the polymer present during the graphene exfoliation. This is in particular due to the fact that in the centrifugation based purification of graphene, the majority of the polymer is removed. Therefore, we preferred first to exfoliate graphene and then mix it at different amounts with the polymer semiconductor for the fabrication of devices.

To quantify the concentration after centrifugation, a mixture of graphene dispersion and $CHCl_3$ was passed through polytetrafluoroethylene (PTFE) membrane filters (pore size 100 nm). The remaining *o*-DCB solvent molecules were washed away with diethyl ether. Careful measurements of the filtered mass gave the concentration of ~100 $\mu g \cdot mL^{-1}$. The dispersion was characterized by UV–vis absorption spectroscopy. Additionally, the thickness of graphene flakes was analysed by high resolution Transmission Electron Microscopy (HR-TEM).

5.3.2 Device preparation

Bottom-gate bottom-contact transistors featuring 230 nm thermally grown oxide on n++-doped silicon (Fraunhofer Institute, capacitance 1.5×10^{-8} $F \cdot cm^{-2}$) and interdigitated Au source-drain electrodes (the channel width of 10 mm and channel length varying from 2.5 to 20 μm) were used. These substrates were exposed to ozone (5 min ozone generation and 25 min incubation), then transferred to the glove-box (N_2 atmosphere) and treated with Hexamethyldisilazane (HMDS) (spin coating at 1500 rpm 60 sec then annealing for 1 h at 120°C). The semiconducting layer was consisting either of pristine P(NDI2OD-T2) (5 $mg \cdot mL^{-1}$ in *o*-DCB prepared by heating at 60°C for 15 min and stirred overnight) or blends with graphene at different weight ratios (P(NDI2OD-T2) to graphene 3000:1, 750:1, 300:1, 150:1 and 100:1). It was deposited by spin-coating (1500 rpm for 60 sec) with subsequent thermal annealing at 70°C for 1h and left 2 days in a N_2 atmosphere before electrical characterization.

5.3.3 Instrumentation

Topographical AFM characterization has been performed in air using a Veeco Dimension 3100 operating on a Nanoscope IV control unit. Measurements of the thickness of the active layer were performed using Alpha step IQ profiler. High resolution Transmission Electron Microscopy (HR-TEM) images have been acquired using a JEOL 2100 F microscope. For the TEM analyses, a drop of solution containing graphene sheet fragments was deposited on a TEM grid covered by a lacey carbon membrane. The experimental data were recorded at 200 kV, equipped with a Cs probe corrector and a GATAN Tridiem imaging filter. To increase the graphene stability at high magnification, between each recorded image the electron beam was electronically moved from the sample surface allowing thus the electron discharge. In this way up to 5 images can be acquired before damaging the sample.

Scanning electron microscopy images were registered using FEI Quanta 250 FEG. Two dimensional Grazing Incidence X-Ray Diffraction (2D-GIXRD) measurements were performed to investigate the crystallinity of the semiconductor films. The 2D-GIXRD images were recorded at the ELETTRA-XRD1 beamline at Trieste's synchrotron facility (Italy) using a monochromatic beam with a wavelength (λ) of 1 Å. The incident angle of the X-ray beam, α_i, was chosen slightly larger than the critical angle for total reflection of the organic film (~0.12°), in order to penetrate through the full film depth.

Electrical characterization of the devices was performed at room temperature in a N_2 atmosphere inside a glove-box, using a Cascade Microtech M150 probe station and a Keithley 2636A source meter as semiconductor parameter analyser controlled by associated software.

Ambient photoelectron spectroscopy measurements were performed on drop casted films (annealed as indicated for the device preparation) and on powder using a new generation of photoelectron spectroscopies operating at atmospheric conditions produced by RIKEN AC-2. The same instrument was used for determining the work function of Au film evaporated prepared by vacuum evaporation onto mica substrates by keeping the substrate at 450ºC during the evaporation.

UV-vis measurements were acquired using Jasco V670 spectrophotometer. Dispersions were placed in 1 cm quartz cuvettes were used.

5.4 Results and discussion

5.4.1 Characterization of graphene

Graphene was prepared by liquid-phase exfoliation in 1,2-orthodichlorobenzene (*o*-DCB). The choice of *o*-DCB for the exfoliation is based on several criteria and the most important for our case study are: *i*) its surface tension of 36.6 mJ.m^{-2} [48] which makes it good candidate for the exfoliation,[47] and *ii*) its ability to solubilize also the selected polymer semiconductor which render it ideal for a single step process *via* co-deposition.

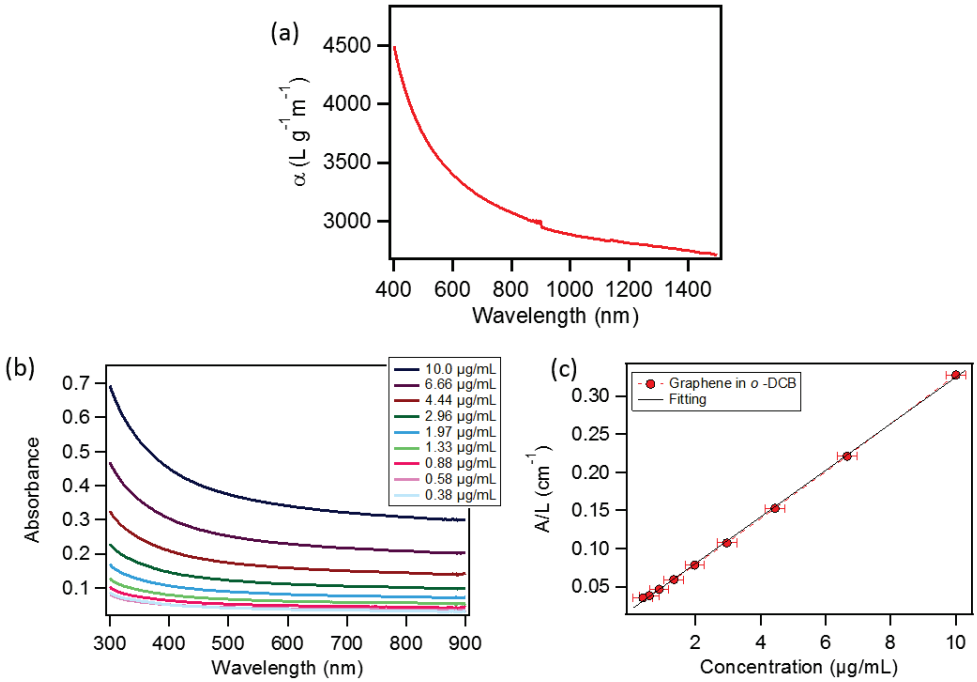

Figure 5.2 (a) Absorption spectrum of graphene in *o*-DCB at a concentration of 10 µg·mL^{-1}. (b) Absorption spectra of graphene in *o*-DCB at different concentrations, and (c) Optical absorbance (at λ=660 nm) divided by cell length (A/l) as a function of concentration for graphene in *o*-DCB, showing Lambert – Beer behavior. Red dashed line is a guide for the eye and the black full line is the fitting.

The exfoliated graphene was investigated using UV-vis absorption spectroscopy. The absorption coefficient has been plotted vs. wavelength (Figure 5.2a). The spectra is as expected being featureless in the visible – IR region.[47, 49] Graphene dispersion was diluted a number of times and the absorption spectra recorded (Figure 5.2b). The absorbance (at λ=660 nm) divided

by cell length is plotted versus concentration (Figure 5.2c). A Lambert – Beer behavior was observed with extracted values of the regression from the linear fitting amounting to 0.999.

The concentration was quantified by passing the graphene dispersion through a filter as detailed in the experimental part.

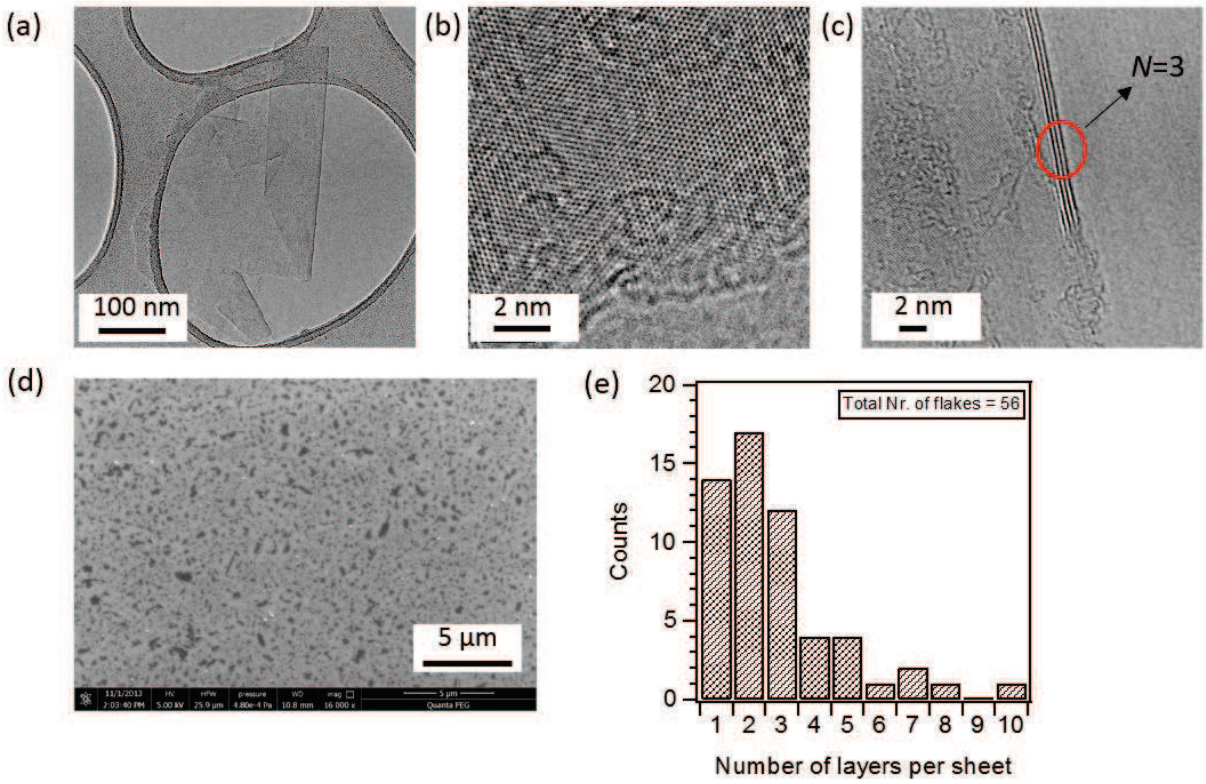

Figure 5.3 (a) Representative TEM image of graphene deposited from *o*-DCB dispersion showing folded graphene sheet; (c) HR-TEM image of selected edge region of (b). (c) HR-TEM image of a 3 layers thick graphene flake. (d) SEM image of graphene sheets prepared in *o*-DCB and deposited on SiOx substrate. (e) Histogram of the number of flakes observed as a function of number of layers per flake from o-DCB dispersion.

Graphene was also investigated using High Resolution-Transmission Electron Microscopy (HR-TEM) (Figures. 5.3a-c). In a number of cases we observed folded graphene sheet with a size below 1 µm as portrayed in **Figure 5.3a**. The lateral size of the sheets ranged between 100 nm and 650 nm as also obtained from the scanning electron microscope images as shown in **Figure 5.3d**. The number of layers per sheet was determined by analysing the flake edges using HR-TEM; **Figure 5.3b** shows a representative case consisting of a monolayer thick region; whereas **Figure 5.3c** shows a graphene flake consisting of three layers. The statistical analysis

of the flake thickness is displayed in the histogram in **Figure 5.3e**. It reveals that the majority of the flakes are 1-3 layer thick.

5.4.2 Electrical characterization of the devices

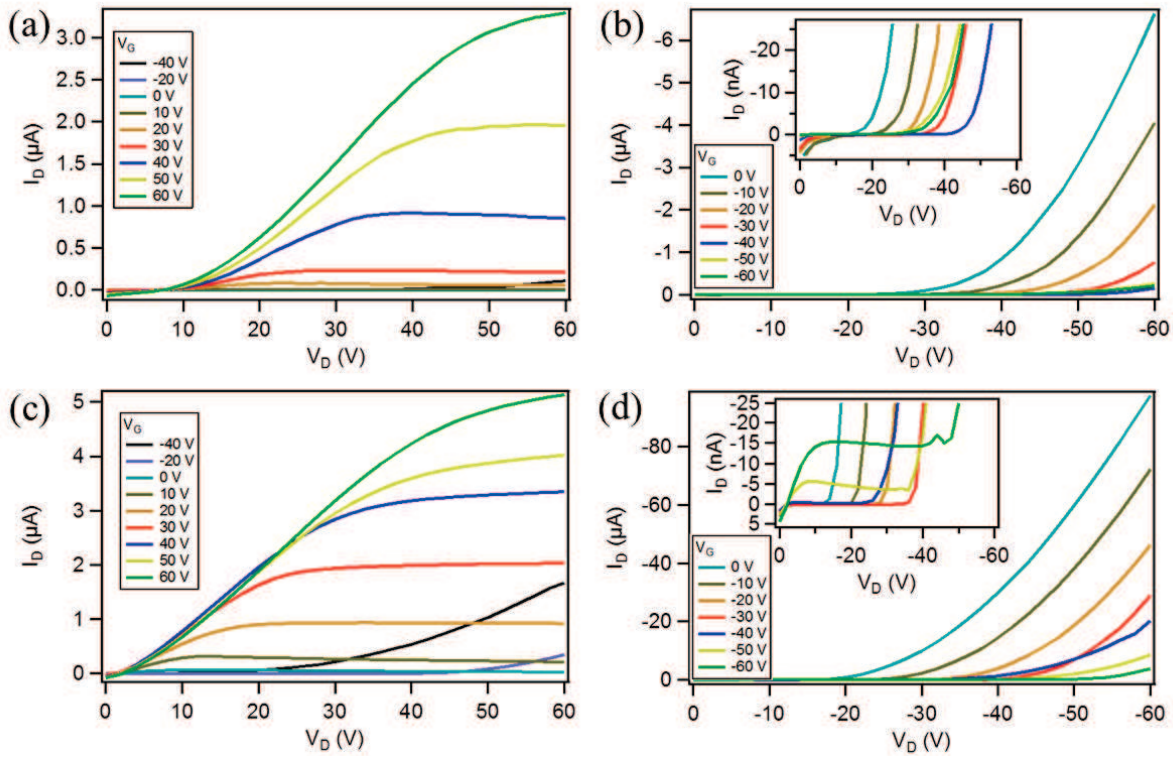

Figure 5.4 Output characteristics of 20 μm channel length devices based on pristine P(NDI2OD-T2) film (a) in the *n*-type mode and (b) in the *p*-type mode. (c) and (d) are the output characteristics of a device based on the blend with graphene at 750:1 weight ratio (P(NDI2OD-T2) to graphene in the *n*-type and *p*-type modes, respectively.

Graphene flakes were incorporated into the semiconductor film of P(NDI2OD-T2) at different loads for the fabrication of FETs with different channel lengths ranging from L=2.5 to 20 μm, by keeping constant the channel width being W=10 mm. **Figure 5.4** compares the output characteristics of two devices having the same channel length (L=20 μm) based on the pristine P(NDI2OD-T2) film (Figure 5.4a-b) and the blend at 750:1 weigh ratio (Figure 5.4c-d). In both cases when positive gate (V_G) and drain biases (V_D) are applied, a typical *n*-type transistor characteristic is observed (Figure 5.4a and 5.4c). However, for the reference device, i.e. based on mono-component P(NDI2OD-T2), at negative V_G and V_D, the drain current (I_D) increases

superlinearly with increasing V_D but it decreases with increasing V_G (Figure 5.4b), indicating a better injection of electrons as compared to holes, in line with previous reports.[18, 45] The current limitation for holes results from the injection barrier between gold electrodes (E_F (Fermi Energy)=4.78 eV) and the HOMO (5.77 eV) which is higher than that between gold and the LUMO (3.96 eV)[36] of P(NDI2OD-T2). Nevertheless, it still represents a high injection barrier for electrons as well, which is evidenced in the output characteristics at low V_D (**Figure 5.4a**) showing clearly the contact resistance for electrons. Upon addition of graphene, this contact resistance is reduced (as evidenced in **Figure 5.4c**) from ~10 to 2 MΩ cm for V_G =60 V. Although the interfacial resistance is still higher than what can be achieved in optimized devices,[38] this is a significant reduction in resistance obtained by adding just 0.13% of graphene. Furthermore, graphene also enhances charge transport for holes as shown in the inset of **Figure 5.4d,** differently from the pristine based FET (inset of Figure 5.4b). The same behaviour was observed at higher loads of graphene. **Figure 5.5** displays the transfer characteristics of both devices (output shown in Figure 5.4) for positive (blue plots) and negative V_D (red plots). It is evidenced that without graphene (full lines), electron transport is dominant over hole transport. However, after addition of graphene (dashed lines), the current is improved and especially there is a significant increase by at least one order of magnitude of the hole current.

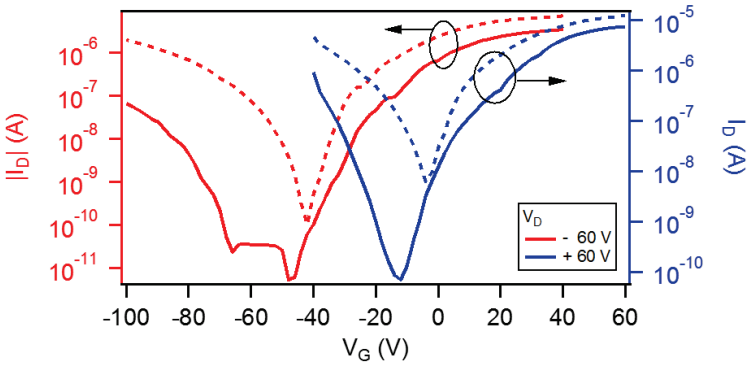

Figure 5.5 Transfer characteristics under positive (red plots) and negative gate biases (blue plots) for 20 µm channel length devices based on pristine P(NDI2OD-T2) (full lines) and blend with graphene at 750:1 weight ratio (P(NDI2OD-T2) to graphene) (dashed lines). Both left and right axis are in the logarithmic scale.

The threshold voltage for *n*-channel operation was shifted from 11 V to –3 V upon addition of graphene (ratio 750:1). For the reference device, the field-effect mobility (extracted from the

saturation regime at V_D=60 V) for electrons (μ_e) amounted to 1.30 x 10^{-3} $cm^2 \cdot V^{-1} \cdot s^{-1}$ (being in the range of mobilities reported for the same polymer processed from *o*-DCB in BG-BC devices[18]). As for holes, the field-effect mobility (μ_h) amounted to 2.78 x 10^{-5} $cm^2 \cdot V^{-1} \cdot s^{-1}$. While in the presence of graphene at this ratio, μ_e and μ_h amounted to 1.21 x 10^{-3} and 2.31 x 10^{-4} $cm^2 \cdot V^{-1} \cdot s^{-1}$, respectively. The increase of μ_h by approximately one order of magnitude can be attributed to *i*) the ionization potential of graphene (4.94 eV) which is close the work function of Au electrodes thus reducing the injection barrier and facilitating the injection of holes, and/or *ii*) the ease transport of charges by graphene which plays an additional role of connecting the domains of the polymer as demonstrated in similar studies.[23, 27] This enhanced performance is accompanied by a trade off with the drain current in the "off state" which tends to increase by more than one order of magnitude at high concentrations of graphene thus lowering the I_{on}/I_{off} ratio as shown in **Figure 5.6a**. By comparing the electrical performance of the devices at various graphene concentrations, we found that the threshold voltage (V_{Th}) for *n*-type operation is proportional to the mixing ratio and it shifts closer to zero value (Figure 5.6b). Similarly, a significant V_{Th} shift was also observed for the *p*-type operation (Figure 5.6c).

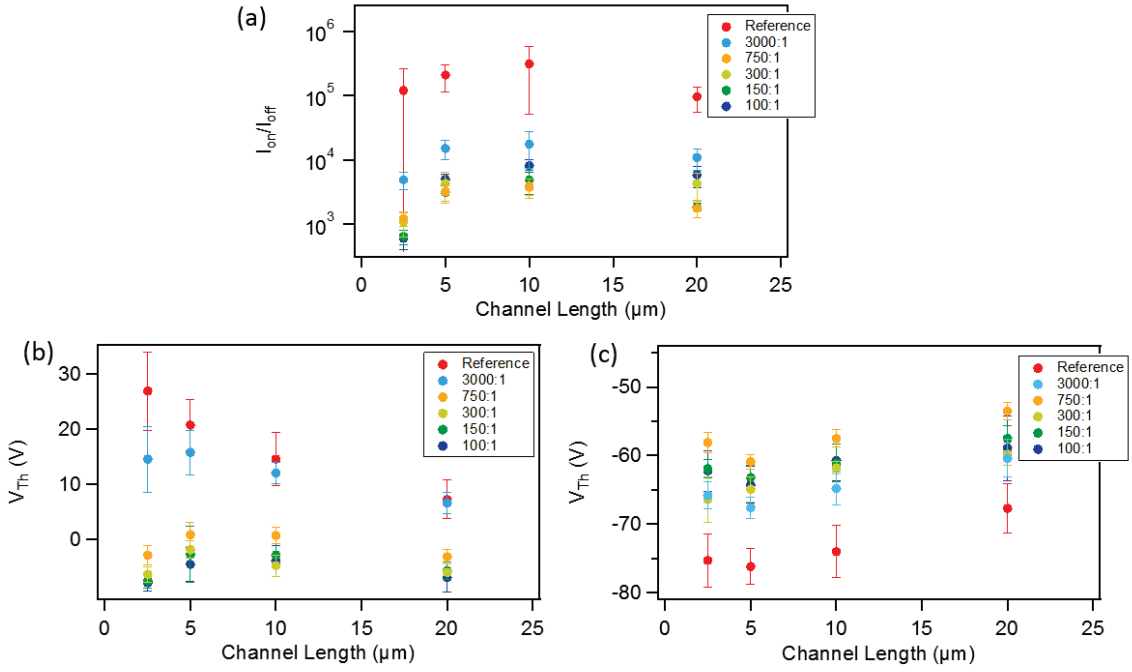

Figure 5.6 (a) Variation of the I_{on}/I_{off} ratio with the channel lengths at different weight ratios of P(NDI2OD-T2) to graphene. (b) and (c) correspond to the variation of the average threshold voltage with the channel lengths at different weight ratios of P(NDI2OD-T2) to graphene when the devices operate in the *n*-type (b) and *p*-type (c) regimes.

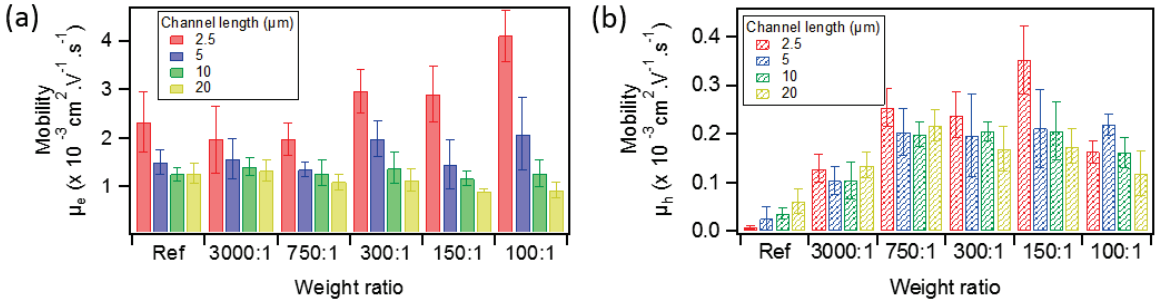

Figure 5.7 Variation of the field-effect mobility of (a) electrons, and (b) holes (extracted from the saturation regime) with the channel length at different weight ratio of P(NDI2OD-T2) to graphene for devices with different channel length and constant channel width (10 mm). Ref stands for the reference samples based on pristine P(NDI2OD-T2).

Figure 5.7 shows the variation of the field-effect mobility with the amount of graphene added for different channel lengths devices. On one hand, μ_e (see Figure 5.7a) (from the saturation regime at V_D=60 V), was almost unaffected by the blend for devices with L=10 and 20 µm, unlike short channel lengths devices L=2.5 and 5 µm where it increased slightly by a factor of 1.4 and 1.8 at a blend ratio of 100:1 as compared to reference devices. On the other hand, μ_h increased proportionally to the amount of graphene up to a blend ratio of 150:1, then it decreases regardless of the channel length (see Figure 5.7b). The increasing factor was ~45, 8.4 and 5.7 folds for L=2.5, 5 and 10 µm, respectively (as compared to reference devices).

The substantial improvement of the hole transport and particularly for the 2.5 µm channel length in addition to the above mentioned reasons can be a consequence of the size of the graphene sheets (i.e. lower than 1 µm) which shortens the effective channel length of the transistor. Therefore the distance for the charge to travel through the semiconducting film is reduced, leading to higher mobilities.[50] For L=2.5 µm, the connection between the sheets can be beneficial for bridging the electrodes resulting in a much better charge transport as compared to other channel lengths. For a channel length larger than 2.5 µm, considering the size of graphene sheets, the probability of bridging the electrodes decreases. The major increase of the hole current (which is not substantial for the electron current) can be attributed to the *p*-type properties of the exfoliated graphene, in which due to doping the hole conduction is often dominant over the electron one.[51-52]

5.4.3 Structural and morphological characterization

To gain further insight about the decrease of the mobility at high amounts of graphene which might be due to the altered crystalline structure of the polymer film, we performed two dimensional grazing incidence X-ray diffraction (2D-GIXD) measurements on our devices. It revealed that the crystallinity of the semiconducting P(NDI2OD-T2) film is unaffected by the presence of graphene at different loads

Figure 5.8 reports the typical 2D area detector images collected for the P(NDI2OD-T2) film (Figure 5.8a) and P(NDI2OD-T2) blends with graphene in different concentrations (Figure 5.8b-f). After the background subtraction, which allows the scattering signal coming from the film to stand out, all images were converted in the reciprocal space and reported in **Figure 5.9**. They show several weak rod-shape Bragg spots along the in-plane direction ($q_z \sim 0$), indicating an in-plane order of the polymeric films, regardless the graphene concentration. The positions of Bragg spots confirm the semicrystalline structure already reported in literature and the coexistence of two polymorphs.[39]

For the majority crystallites the lamellar stacking adopts the face-on orientation, as highlighted in **Figure 5.10**, where the scattering intensities along the in-plane and out-of-plane direction are reported. Indeed, lamellar peak (100) is narrower and higher along the in-plane direction. Moreover, the π-stacking peak (010) is observed only in the out-of-plane direction. The crystallite lateral size and thickness are estimated from the (100) and (010) width peak[53] to be 26 nm and ~3nm, respectively, regardless the graphene concentration.

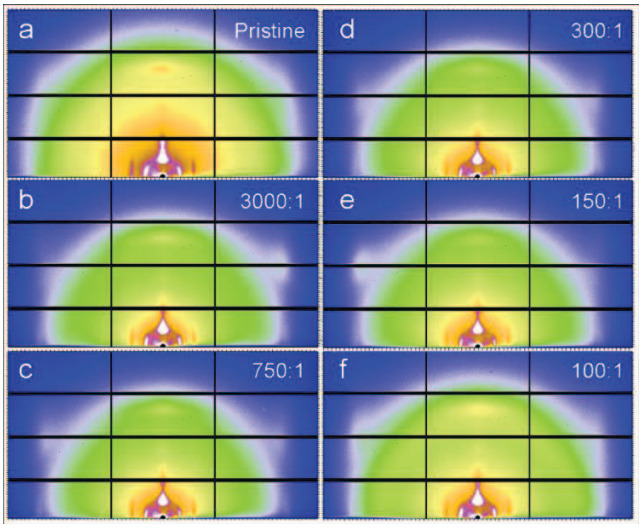

Figure 5.8 2D Pilatus area detector images showing GIXRD signal coming from layers of pristine P(NDI2OD-T2) film (a) and of P(NDI2OD-T2) blend with graphene in different concentrations (b-f). All images are reported with the same intensity range scale.

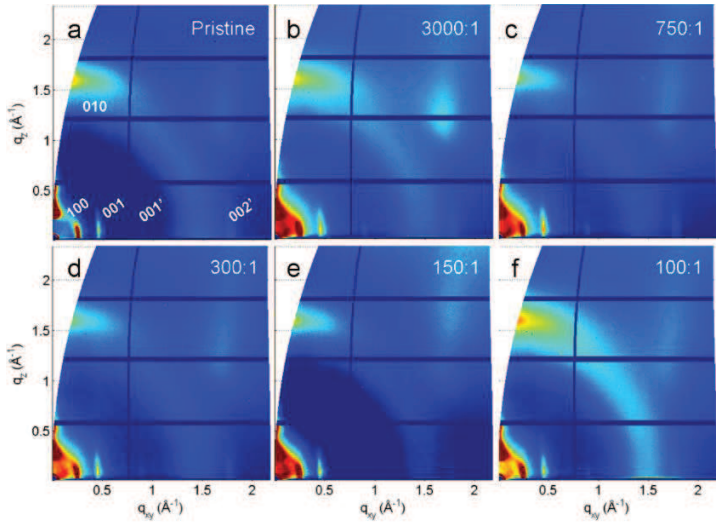

Figure 5.9 2D-GIXRD images of pristine P(NDI2OD-T2) film (a) and of P(NDI2OD-T2) blend with graphene in different concentrations (b-f).

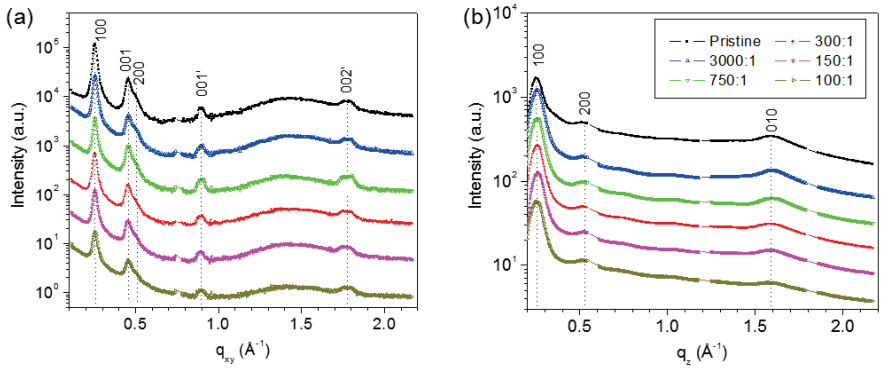

Figure 5.10 Scattering intensity integrated along the Yoneda (a) and the specular direction ($q_{xy} \sim 0$). Curves are shifted for clarity.

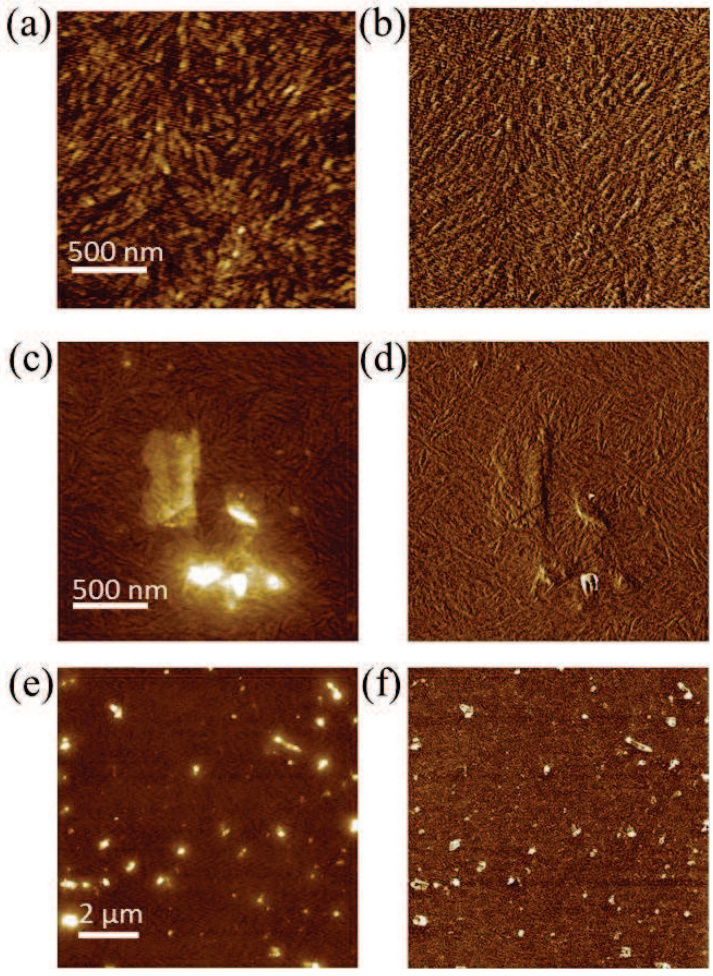

Figure 5.11 AFM (a) topography and (b) phase image of pristine P(NDI2OD-T2) film. (c, e) topography and (d, f) phase image of P(NDI2OD-T2) blend with graphene. Z-scales: (a) = 5 nm, (c, e) 28 nm. All these images were obtained for films prepared at a spin-coating speed of 1500 rpm.

In terms of energy levels, the polymer/graphene film is a disordered system due to the intrinsic defects in graphene sheets arranged randomly within the polymer matrix. Therefore at high concentrations, graphene seems to form aggregates which in turn might act as scattering centres therefore decreasing the mobility.

Additional detailed information on the morphology was obtained by tapping mode atomic force microscopy (AFM). The reference material, both in the topography (Figure 5.11a) and phase images (Figure 5.11b) showed a typical nematic-like texture in line with previous works.[42] AFM topography of the blend (Figure 5.11c) displays graphene sheets somehow folded and dispersed in the semiconductor polymer matrix. The phase image (Figure 5.11d**)** suggests that graphene sheets are effectively coated with the polymer. However, it is hard to quantify the number of graphene layers composing the sheets, since the overall thickness results from the sum of the polymer layer and the graphene aggregate(s). An AFM scan on a larger area, **Figure 5.11e**, shows a random distribution of graphene sheets in the polymer matrix. Their aggregation is also noticeable in some areas. The corresponding phase image (Figure 5.11f) shows a network of materials with two different phases suggesting a phase segregation, which was further investigated by analysing topography and phase images of the films keeping the same blend ratio and varying the film thickness from ~ 30 to 70 nm (by changing the spin-coating speed). All images as depicted in **Figure 5.12**, irrespective of the thickness were similar to **Figures 5.11e** and **f** (i.e. similar phase segregation, random distribution of size and thickness of sheets).

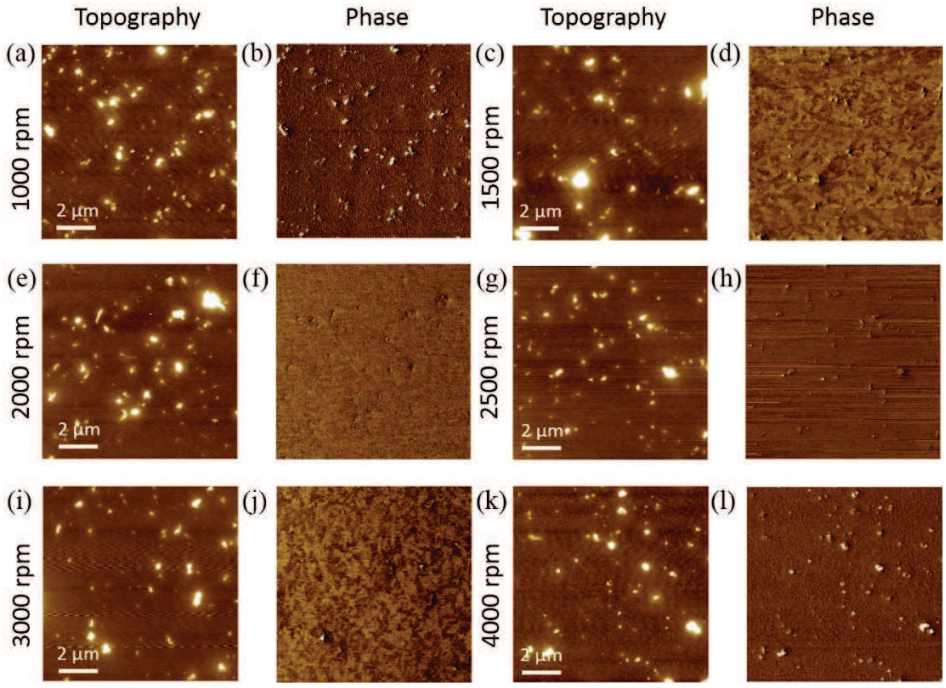

Figure 5.12 AFM topography and phase images of film of P(NDI2OD-T2) blend with graphene at the same ratio (100:1) prepared at different spin-coating speeds. (a, c, e, g, i and k) topography (Z scale=28 nm); (b, d, f, h, j and l) corresponding phase images.

From the electrical properties point of view, the results discussed above demonstrate without any doubt that graphene is present in the conducting channel. By combining this with the AFM images, one can conclude that graphene sheets are very well dispersed in the semiconductor film and are present everywhere in the device. Nevertheless, the presence of mono-, bi- and multi-layered sheets in the channel in addition to their aspect ratio and their random distribution play a crucial role in affecting the electronic properties[54-57] of the device. More influencing factors can be mentioned such as the presence of folds[58] and ripples[59] in the sheets, and the inter-sheet junction where, in the case of overlapping sheets, scattering can occur thus limiting the electron mean free path.[60] Consequently the effect of graphene size on the device performance would be interesting to study in addition to exploiting this interesting material in other *n*-type systems.

5.5 Conclusion

In summary, we have demonstrated that graphene prepared by liquid-phase exfoliation in *o*-DCB can be used in thin-film devices prepared by co-deposition with a polymeric semiconductor in order to boost the ambipolar character of the latter. In particular, we have shown that the field-effect mobility of holes can be enhanced by 45 folds for 2.5 μm channel length devices at the blend ratio 150:1 in weight of (P(NDI2OD-T2) to graphene, suggesting a favourable pathway for the charge transport. The improved performance of this particular channel length can be correlated to the size of the sheets, which were very well dispersed within the polymeric matrix. Our strategy combining the high performance of a 2D material and the ideal film forming ability of a polymer, provides a prospective pathway for the application of graphene in electronics requiring ambipolar devices for complimentary logic circuits.

5.6 References

[1] C. Wang, H. Dong, W. Hu, Y. Liu, D. Zhu, *Chem. Rev.* **2011**, *112*, 2208.
[2] Y. Zhao, Y. Guo, Y. Liu, *Adv. Mater.* **2013**, *25*, 5372.
[3] K.-J. Baeg, M. Caironi, Y.-Y. Noh, *Adv. Mater.* **2013**, *25*, 4210.
[4] E. J. Meijer, D. M. de Leeuw, S. Setayesh, E. van Veenendaal, B. H. Huisman, P. W. M. Blom, J. C. Hummelen, U. Scherf, T. M. Klapwijk, *Nat. Mater.* **2003**, *2*, 678.
[5] R. Blanco, R. Gómez, C. Seoane, J. L. Segura, E. Mena-Osteritz, P. Bäuerle, *Org. Lett.* **2007**, *9*, 2171.
[6] J. C. Bijleveld, A. P. Zoombelt, S. G. J. Mathijssen, M. M. Wienk, M. Turbiez, D. M. de Leeuw, R. A. J. Janssen, *J. Am. Chem. Soc.* **2009**, *131*, 16616.
[7] T. T. Steckler, X. Zhang, J. Hwang, R. Honeyager, S. Ohira, X.-H. Zhang, A. Grant, S. Ellinger, S. A. Odom, D. Sweat, D. B. Tanner, A. G. Rinzler, S. Barlow, J.-L. Brédas, B. Kippelen, S. R. Marder, J. R. Reynolds, *J. Am. Chem. Soc.* **2009**, *131*, 2824.
[8] P. Sonar, S. P. Singh, Y. Li, M. S. Soh, A. Dodabalapur, *Adv. Mater.* **2010**, *22*, 5409.
[9] A. Liscio, E. Orgiu, J. M. Mativetsky, V. Palermo, P. Samorì, *Adv. Mater.* **2010**, *22*, 5018.
[10] C. Rost, D. J. Gundlach, S. Karg, W. Rieß, *J. Appl. Phys.* **2004**, *95*, 5782.
[11] J. Wang, H. Wang, X. Yan, H. Huang, D. Yan, *Appl. Phys. Lett.* **2005**, *87*.
[12] F. Dinelli, R. Capelli, M. A. Loi, M. Murgia, M. Muccini, A. Facchetti, T. J. Marks, *Adv. Mater.* **2006**, *18*, 1416.
[13] S. D. Wang, K. Kanai, Y. Ouchi, K. Seki, *Org. Electron.* **2006**, *7*, 457.
[14] C. Rost, S. Karg, W. Riess, M. A. Loi, M. Murgia, M. Muccini, *Appl. Phys. Lett.* **2004**, *85*, 1613.
[15] K. N. N. Unni, A. K. Pandey, S. Alem, J.-M. Nunzi, *Chem. Phys. Lett.* **2006**, *421*, 554.

[16] M. Shkunov, R. Simms, M. Heeney, S. Tierney, I. McCulloch, *Adv. Mater.* **2005**, *17*, 2608.
[17] S. Cho, J. Yuen, J. Y. Kim, K. Lee, A. J. Heeger, *Appl. Phys. Lett.* **2006**, *89*.
[18] K. Szendrei, D. Jarzab, Z. Chen, A. Facchetti, M. A. Loi, *J. Mater. Chem.* **2010**, *20*, 1317.
[19] M. Treier, J.-B. Arlin, C. Ruzie, Y. H. Geerts, V. Lemaur, J. Cornil, P. Samorì, *J. Mater. Chem.* **2012**, *22*, 9509.
[20] J. Smith, R. Hamilton, I. McCulloch, N. Stingelin-Stutzmann, M. Heeney, D. D. C. Bradley, T. D. Anthopoulos, *J. Mater. Chem.* **2010**, *20*, 2562.
[21] C. Raimondo, N. Crivillers, F. Reinders, F. Sander, M. Mayor, P. Samorì, *Proc Nat Acad Sci USA* **2012**, *109*, 12375.
[22] E. Orgiu, N. Crivillers, M. Herder, L. Grubert, M. Pätzel, J. Frisch, E. Pavlica, D. T. Duong, G. Bratina, A. Salleo, N. Koch, S. Hecht, P. Samorì, *Nat Chem* **2012**, *4*, 675.
[23] J. Huang, D. R. Hines, B. J. Jung, M. S. Bronsgeest, A. Tunnell, V. Ballarotto, H. E. Katz, M. S. Fuhrer, E. D. Williams, J. Cumings, *Org. Electron.* **2011**, *12*, 1471.
[24] A. Liscio, G. P. Veronese, E. Treossi, F. Suriano, F. Rossella, V. Bellani, R. Rizzoli, P. Samorì, V. Palermo, *J. Mater. Chem.* **2011**, *21*, 2924.
[25] Z. Liu, Q. Liu, Y. Huang, Y. Ma, S. Yin, X. Zhang, W. Sun, Y. Chen, *Adv. Mater.* **2008**, *20*, 3924.
[26] F. Torrisi, T. Hasan, W. Wu, Z. Sun, A. Lombardo, T. S. Kulmala, G.-W. Hsieh, S. Jung, F. Bonaccorso, P. J. Paul, D. Chu, A. C. Ferrari, *ACS Nano* **2012**, *6*, 2992.
[27] P. Yadav, C. Chanmal, A. Basu, L. Mandal, J. Jog, S. Ogale, *RSC Advances* **2013**, *3*, 18049.
[28] K. S. Novoselov, A. K. Geim, S. V. Morozov, D. Jiang, Y. Zhang, S. V. Dubonos, I. V. Grigorieva, A. A. Firsov, *Science* **2004**, *306*, 666.
[29] A. K. Geim, K. S. Novoselov, *Nat. Mater.* **2007**, *6*, 183.
[30] A. Ciesielski, P. Samorì, *Chem. Soc. Rev.* **2014**, *43*, 381.
[31] C.-A. Palma, P. Samorì, *Nat Chem* **2011**, *3*, 431.
[32] J. Cai, P. Ruffieux, R. Jaafar, M. Bieri, T. Braun, S. Blankenburg, M. Muoth, A. P. Seitsonen, M. Saleh, X. Feng, K. Müllen, R. Fasel, *Nature* **2010**, *466*, 470.
[33] Y. H. Zhang, K. G. Zhou, K. F. Xie, J. Zeng, H. L. Zhang, Y. Peng, *Nanotechnology* **2010**, *21*.
[34] X. Dong, D. Fu, W. Fang, Y. Shi, P. Chen, L. J. Li, *Small* **2009**, *5*, 1422.
[35] D. Choudhury, B. Das, D. D. Sarma, C. N. R. Rao, *Chem. Phys. Lett.* **2010**, *497*, 66.
[36] Z. Chen, Y. Zheng, H. Yan, A. Facchetti, *J. Am. Chem. Soc.* **2008**, *131*, 8.
[37] H. Yan, Z. Chen, Y. Zheng, C. Newman, J. R. Quinn, F. Dotz, M. Kastler, A. Facchetti, *Nature* **2009**, *457*, 679.
[38] M. Caironi, C. Newman, J. R. Moore, D. Natali, H. Yan, A. Facchetti, H. Sirringhaus, *Appl. Phys. Lett.* **2010**, *96*, 183303.
[39] J. Rivnay, M. F. Toney, Y. Zheng, I. V. Kauvar, Z. Chen, V. Wagner, A. Facchetti, A. Salleo, *Adv. Mater.* **2010**, *22*, 4359.
[40] M. Caironi, M. Bird, D. Fazzi, Z. Chen, R. Di Pietro, C. Newman, A. Facchetti, H. Sirringhaus, *Adv. Funct. Mater.* **2011**, *21*, 3371.
[41] D. Fazzi, M. Caironi, C. Castiglioni, *J. Am. Chem. Soc.* **2011**, *133*, 19056.
[42] J. Rivnay, R. Steyrleuthner, L. H. Jimison, A. Casadei, Z. Chen, M. F. Toney, A. Facchetti, D. Neher, A. Salleo, *Macromolecules* **2011**, *44*, 5246.

[43] T. Schuettfort, S. Huettner, S. Lilliu, J. E. Macdonald, L. Thomsen, C. R. McNeill, *Macromolecules* **2011**, *44*, 1530.
[44] C. Sciascia, N. Martino, T. Schuettfort, B. Watts, G. Grancini, M. R. Antognazza, M. Zavelani-Rossi, C. R. McNeill, M. Caironi, *Adv. Mater.* **2011**, *23*, 5086.
[45] K.-J. Baeg, D. Khim, S.-W. Jung, M. Kang, I.-K. You, D.-Y. Kim, A. Facchetti, Y.-Y. Noh, *Adv. Mater.* **2012**, *24*, 5433.
[46] J. Li, J. Du, J. Xu, H. L. W. Chan, F. Yan, *Appl. Phys. Lett.* **2012**, *100*, 033301.
[47] Y. Hernandez, V. Nicolosi, M. Lotya, F. M. Blighe, Z. Sun, S. De, I. T. McGovern, B. Holland, M. Byrne, Y. K. Gun'ko, J. J. Boland, P. Niraj, G. Duesberg, S. Krishnamurthy, R. Goodhue, J. Hutchison, V. Scardaci, A. C. Ferrari, J. N. Coleman, *Nat. Nanotech.* **2008**, *3*, 563.
[48] *U.S. National Toxicology Program Database, http://ntp.niehs.nih.gov*.
[49] D. S. L. Abergel, V. I. Fal'ko, *Physical Review B* **2007**, *75*, 155430.
[50] H. Yanagi, Y. Kawai, *Jpn. J. Appl. Phys., Part 2* **2004**, *43*, L1575.
[51] *Previous paper on solution processed graphene showing a dominant p-type transport:* H. Kim, C. Mattevi, H. J. Kim, A. Mittal, K. A. Mkhoyan, R. E. Riman, M. Chhowalla, *Nanoscale* **2013**, *5*, 12365.
[52] D.-W. Shin, H. M. Lee, S. M. Yu, K.-S. Lim, J. H. Jung, M.-K. Kim, S.-W. Kim, J.-H. Han, R. S. Ruoff, J.-B. Yoo, *ACS Nano* **2012**, *6*, 7781.
[53] D. M. Smilgies, *J. Appl. Crystallogr.* **2009**, *42*, 1030.
[54] J. Nilsson, A. H. C. Neto, F. Guinea, N. M. R. Peres, *Phys. Rev. Lett.* **2006**, *97*, 266801.
[55] A. H. Castro Neto, F. Guinea, N. M. R. Peres, K. S. Novoselov, A. K. Geim, *Rev. Mod. Phys.* **2009**, *81*, 109.
[56] K. A. Ritter, J. W. Lyding, *Nat. Mater.* **2009**, *8*, 235.
[57] F. Schwierz, *Nat. Nanotech.* **2010**, *5*, 487.
[58] K. Kim, Z. Lee, B. D. Malone, K. T. Chan, B. Alemán, W. Regan, W. Gannett, M. F. Crommie, M. L. Cohen, A. Zettl, *Phys. Rev. B* **2011**, *83*, 245433.
[59] J. C. Meyer, A. K. Geim, M. I. Katsnelson, K. S. Novoselov, T. J. Booth, S. Roth, *Nature* **2007**, *446*, 60.
[60] G. Eda, M. Chhowalla, *Nano Lett.* **2009**, *9*, 814.

Chapter 6 Organic semiconductor blend with graphene nanoribbons

6.1 Introduction

Over the past few years, a great effort has been devoted to the development of new organic semiconducting materials, combining solution processability, stability under ambient conditions, and high charge carrier mobility[1-10] for applications in organic electronics and particularly in organic field-effect transistors (OFETs). OFETs can be fabricated by using either small molecules or polymeric semiconductors as electroactive layers. In the latter case, despite the fact that polydisperse molecules can form extended networks for efficient percolation of charges, due to their polycrystalline nature the obtained material is characterized by the presence of structural and morphological defects, grain boundaries and amorphous domains hampering efficient charge transport.[11] To circumvent this problem, polymeric semiconductors have been blended with either small molecules or other (semi)conducting systems.[11-19] By blending different components new functions can be conferred to the material and to the device,[20] benefiting the properties brought about by each component and exceeding its individual performance. Such an effect varies with the degree of phase segregation between the different components in the blend. Among polymeric semiconductors, regioregular poly(3-hexylthiophene) - P3HT is a prototypical system for solution processed OFETs. [21-25] Recently the performance of P3HT based OFETs has been improved by co-deposition with graphene, revealing an increase in charge carrier mobilities over 20 times when compared to the pure

P3HT.[26] This enhanced electrical characteristic can be ascribed to the beneficial role of graphene, which builds preferential paths for charge transport, therefore increasing the overall hole mobility,[27] similarly to previous findings in OFETs based on carbon nanotubes with P3HT;[28-29] however, this was accompanied by a decrease of the on-off current ratio (I_{on}/I_{off}) as discussed as well in chapter 5.

Due to the fact that graphene is a zero-gap semiconductor,[30] with high charge carrier mobilities[31], it cannot be used alone as electroactive component to be incorporated in the channel of a regular FET. A great deal of efforts have been dedicated to the opening of a band gap in graphene[32]. This was in one way achieved by geometrically confining the 2D graphene via designing graphene nanoribbons (GNRs).[33] Fabrication of GNRs has been predominantly carried out by top-down methods such as lithographic patterning of graphene sheets,[34-36] longitudinal unzipping of carbon nanotubes,[37-39] and chemical extraction from exfoliated graphite.[40] However, these methods lead to the production of GNRs exhibiting a broad (10-100 nm) width distribution[37-39] as well as defective edge structures, resulting in GNRs with non-uniform electronic properties, e.g. band gap and ionization potential. In addition, top-down methods for the production of GNRs typically suffer from very low yield, hindering practical applications of the GNRs.[37] In contrast, a bottom-up synthetic approach based on solution-mediated[41-44] and surface-assisted[45] cyclodehydrogenation[46-47] of tailor-made polyphenylene precursors has been developed, enabling the fabrication of a variety of uniform and structurally defined GNRs with lateral width of ca. 1–2 nm, which possess large and defined band gaps (1.1–1.7 eV).[42, 45] On the other hand, by solution-mediated method it is possible to render the GNRs dispersible in organic solvents by installing solubilizing groups at the peripheral positions.[41-42, 44] It has been theoretically revealed that the absolute value of the valence band, which is related to the ionization potential, decreases as the lateral extension of the GNRs.[48] Recently, laterally extended GNR with width of 1.54–1.98 nm have been reported, but the absolute value of the valence band of this GNR was estimated to be still higher than that of P3HT, hindering the use of this GNR for the blending with P3HT.[42, 48] Further, the edge of this GNR contains cove-type structure, and the fabrication of broad (~2 nm) and fully armchair edged GNRs has remained a challenge.

6.2 Scope

In this work, we present an unprecedented N = 18 armchair GNR **1** (Figure 6.1a), which possesses a lateral width of ~2.1 nm based on molecular modeling, surpassing all the GNRs hitherto fabricated by the bottom-up synthesis. Remarkably, GNR **1** features an ionization energy (IE) close to that of P3HT, making it the ideal candidate for the present study, in particular to avoid traps and energy barriers within the bi-component film. The edge decoration with long alkyl chains renders GNR dispersible in common organic solvents such as tetrahydrofuran (THF), chlorobenzene and *ortho*-dichlorobenzene (*o*-DCB), enabling its easy integration into organic electronic devices.

GNR has been blended with regioregular poly(3-hexylthiophene) - P3HT (Figure 6.1b). It is noteworthy that the alkyl chains exposed at the peripheral positions of GNR provide a good affinity for P3HT, as an attempt to minimize the occurrence of macroscopic phase segregation. This is particularly important because of the problems associated with the propensity of GNRs to form microscopic crystals that cannot be easily interfaced with metallic electrodes, therefore limiting charge injection at metal/(semi)conductor interface. Moreover, these microcrystals are alternated by domain boundaries hampering the charge transport within the film. The effect of the GNRs at different concentrations (in the blend) on the device performance in dark such as the field-effect mobility and the I_{on}/I_{off} has been investigated. The influence of illumination with monochromatic light on the electrical characteristics of the device has been studied aiming at exploring the potential use of this blend as active layer in hybrid organic phototransistors (OPTs).

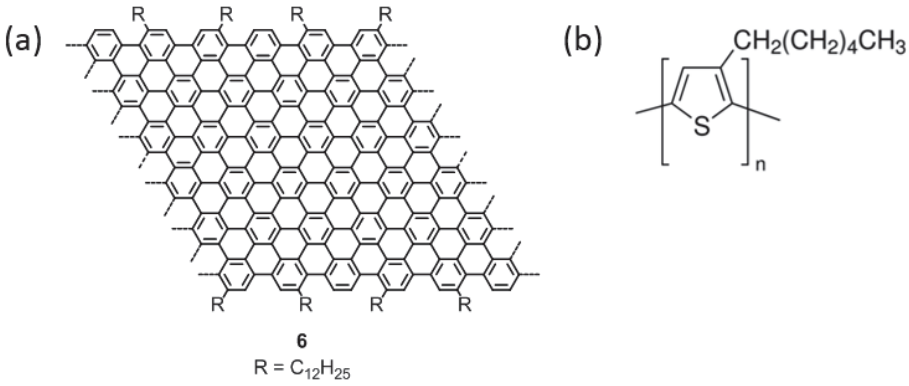

Figure 6.1 Chemical formulae of (a) GNR 1 and (b) poly(3-hexylthiophene) (P3HT).

6.3 Experimental

6.3.1 Materials

In this work, poly(3-hexylthiophene) (P3HT) (Figure 6.1b) (regioregularity >99%, Mw~50,000 g/mol, Sepiolid P-200 from BASF) was used as purchased. Other materials were purchased from Aldrich. As for the GNR **1** (Figure 6.1a), it was synthesized by the group of Prof. Müllen as per the reported procedure[49] and used as received.

6.3.2 Device fabrication

Bottom-gate bottom-contact transistors exposing 230 nm thermally grown oxide on n++-doped silicon (Fraunhofer Institute, capacitance 1.5×10^{-8} F·cm^{-2}) were used. Each substrate exposes prepatterned interdigitated Au source-drain electrodes with different channel length (L = 2.5, 5, 10, 20 μm) and constant channel width (W = 10 mm). These substrates were cleaned in an ultrasonic bath of acetone and isopropanol prior to device fabrication. For the devices with higher channel length (L = 60, 80, 100, 120 μm) and same width (W = 10 mm), interdigitated Au source-drain electrodes (40 nm) were evaporated (chamber pressure = 10^{-6} mbar, evaporation rate = 0.03 nm/s) on bare SiO_x substrates (having the same specifications as above mentioned) using a shadow mask. GNRs were dispersed in *o*-DCB and sonicated for at least 90 min then immediately transferred to the glove box (N_2 atmosphere) where they were mixed with a constant amount of P3HT (1.5 mg/mL in *o*-DCB) at different percentages (2, 5, 11 and 24 wt % with respect to P3HT). Thin films were prepared inside the glove box (N_2 atmosphere) by spin-coating the blend at 1200 rpm for 60 sec onto untreated substrates. This was followed by an annealing step at 200 °C for 15 min. For comparison, we prepared pristine P3HT devices that were processed in the same fashion as for the blended ones.

6.3.3 Electrical characterization of the devices

Electrical characterization of the devices was performed at room temperature in a N_2 atmosphere inside a glove box, using a Cascade Microtech M150 probe station and a Keithley 2636A sourcemeter as semiconductor parameter analyzer controlled by associated software.

To study the photoresponse, at least 6 devices for each channel length and each blend percentage were characterized under illumination from the top using a Polychrome V (Till Photonics) tunable light source providing a monochromatic beam with 605 nm and 560 nm wavelengths and irradiance levels of 8.17 and 9.44 $mW \cdot cm^{-2}$, respectively. The light intensity was measured using an analog optical power meter, PM100A (ThorLabs). These wavelengths were chosen in view of the absorbance spectra and correspond to two absorption peaks of the P3HT films as shown in **Figure 6.2**.

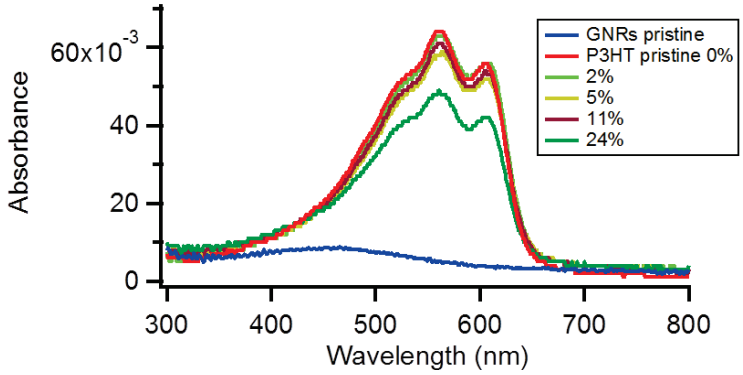

Figure 6.2 UV–vis absorbance spectra for films of pristine P3HT, GNRs and the blend of GNRs with P3HT at different percentages.

The measurement sequence used is as follows: two consecutive measurements for transfer and output characteristics in dark. The light is then switched on, and transfer and output characteristics under illumination are measured. For some devices only, this was followed by measurements in dark after 5 min of switching off the light to see if there is a photo-induced memory effect.

To study the relaxation of the photo-induced charges, 5 to 6 devices of L=20 µm for each blend percentage were characterized under illumination at λ=560 nm (9.44 $mW \cdot cm^{-2}$). Two

measurement sequences were used: in the first case, continuous gate bias V_G=0 V and drain bias V_D=-10 V were applied in dark for 30 sec then the light is switched on for 30 sec then switched off for 30 sec. whereas in the second case the same was followed except that the gate was floating (no gate bias applied).

6.3.4 Photocurrent mapping

Photocurrent mapping was done using a laser light (λ=633 nm, power density < 50 kW·cm^{-2}) generated from a He–Ne laser which was coupled to the sample by using a DM LM microscope (Leica) and a ×100 ultra-long working distance objective, resulting in a ~1 μm spot size. A Physik Instrument piezoelectric stage was used to translate the device with respect to the laser spot in the x/y directions with 500 nm steps, resulting in confocal, position-dependent recording of the generated photocurrent. Measurements were done at room temperature with a low pressure N_2 flow over the sample. Photocurrent signals were recorded by modulating the laser beam (1 kHz) using a mechanical chopper and the short circuit photocurrent was detected by lock-in amplifier. A 2400 Sourcemeter (Keithley) was employed to control the gate voltage. For this experiment, in order to overcome the air sensitivity issue of P3HT, an encapsulating film of poly(methyl methacrylate) (PMMA) (120k, Sigma Aldrich). First PMMA was dissolved in in Methyl Ethyl Ketone (70 mg/mL). The solution was heated for 60 min at 60°C and then filtered (Carl Roth PTFE 0.45 μm). Subsequently, it was taken inside the glove box and spin-coated (200 μL) at 1000 rpm for 30 sec on the top of the devices without post annealing.

6.3.5 Instrumentation

Atomic Force Microscopy (AFM) images were recorded using Nanoscope (Veeco Multimode V). Measurements of the thickness of the active layer were performed using Alpha step IQ profiler. Scanning electron microscopy (SEM) images for pure GNRs were taken using Strata 400 Dual Beam. Samples were prepared by drop casting (0.25 mg/mL in *o*-DCB) followed by annealing at 200°C for 15 min then sputtered with Au (30 sec, I=60 mA). Ambient photoelectron spectroscopy measurements were performed on drop casted films (annealed at 200 °C for 15 min inside the glove box) using a new generation of photoelectron spectroscopies

operating at atmospheric conditions (RIKEN AC-2). The same instrument was used for determining the work function of Au thin film prepared by vacuum evaporation (at $P=1.7x10^{-6}$ mbar) onto mica substrates (450ºC). UV-vis absorbance spectra were obtained using Shimadzu UV-3101PC spectrophotometer and were performed on films (of the pristine materials and the blends) prepared on quarts slides following the same procedure as for the device preparation. Moreover, for the UV–vis absorption spectroscopic analysis in dispersion, GNR in *o*-DCB with concentration of 0.25 mg/mL was sonicated for 1 h 30 min, then diluted with *o*-DCB by a factor of 5 and placed in 1 cm quartz cuvette. The film was prepared by drop casting GNR **1** dispersion on quartz substrate. The measurements were performed using Jasco V670 spectrophotometer.

X-ray diffraction (GIXD) measurements were performed using the grazing-incidence geometry. The experimental setup included a rotating copper anode X-ray source (Rigaku Micromax, operated at 42 kV and 20 mA), Osmic confocal MaxFlux optics and a three x/y-adjustable pin-hole collimation system (JJ X-ray). Samples deposited on top of silicone substrates were irradiated with a wavelength of λ=1.5418 Å at the incident angle (α_i) of 0.11°. The GIXD patterns were recorded for 5 hrs on a MAR345 image plate detector. Camera length (315 mm) and the range of detectable d-spacings (~35 Å $<d_{hkl}<$3 Å) were calibrated using silver behenate standard. The data was processed using Datasqueeze 2.2.9 program.

6.4 Results and discussion

6.4.1 Characterization of the GNR 1

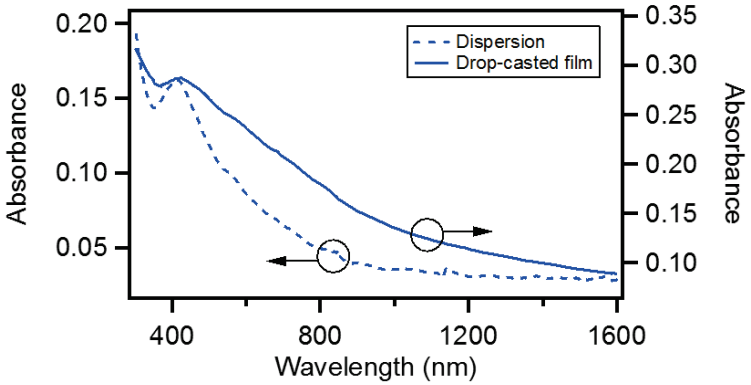

Figure 6.3 UV–vis absorption spectrum of a dispersion of GNR **1** in *o*-DCB (dashed line) and GNR film (full line).

The synthesized GNR **1** features an estimated longitudinal length up to ca. 10 nm[49] and a lateral width of ~2.1 nm based on molecular modeling.[49] The UV–vis absorption spectrum of a dispersion of GNR **1** in *o*-DCB showed an absorption maximum at 410 nm with the absorption edge at ~800 nm, corresponding to the optical bandgap of ~1.6 eV (Figure 6.3).

Ambient Photoelectron spectroscopy (PS) measurements of the pristine GNR **1** drop casted film provided a HOMO level of 5.010±0.063 eV being close to that of P3HT, i.e. 4.860±0.015 eV. Thereby, this result makes this GNR **1** an ideal candidate for our case study.

Subsequently, different volumes of such dispersion in *o*-DCB were mixed with solutions of P3HT for the fabrication of GNR-P3HT blend films with various GNRs loading ratio by co-deposition.

6.4.2 Electrical characteristics in dark

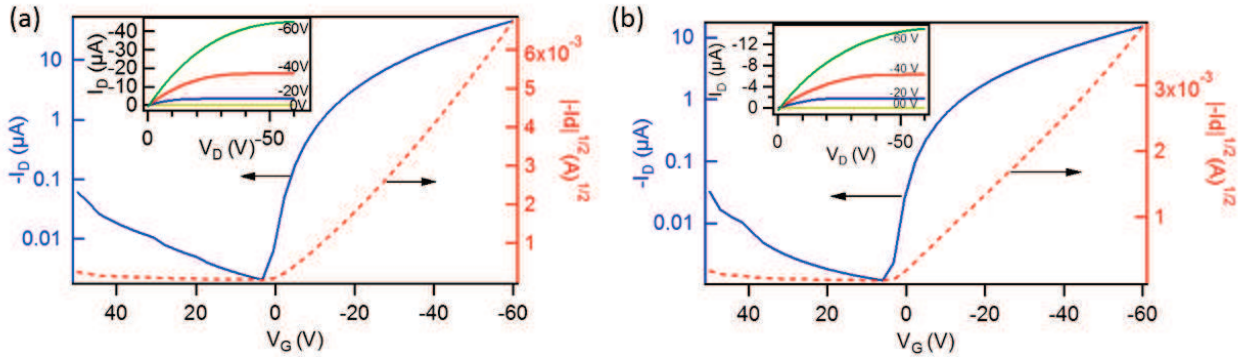

Figure 6.4 Transfer characteristics of bottom-gate bottom-contact device (L = 120 μm) based on (a) 24% blend of GNRs with P3HT and (b) pristine P3HT. Left axis in the log scale and the right axis is the square root of the absolute value of the drain current. The inset of both images shows the output characteristics of the corresponding devices.

We fabricated devices at various GNRs loading ratio (0, 2, 5, 11 and 24 wt % with respect to P3HT), having different channel length (L) ranging from 60 μm to 120 μm. **Figure 6.4** displays a comparison between the transfer characteristics of the same channel length devices (L=120 μm) based on 24% GNRs blend with P3HT (Figure 6.4a) and pristine P3HT (Figure 6.4b). Their corresponding output characteristics are shown as inset. In both cases, the devices exhibit a typical *p*-type behavior. The extracted hole mobility (from the saturation regime at V_D=–60 V), threshold voltage (V_{Th}) and I_{on}/I_{off} amounted to 2.8 × 10^{-2} $cm^2 \cdot V^{-1} \cdot s^{-1}$, –8.9 V and ~$10^3$ respectively for the device based on the blend (displayed in Figure 6.4a). By comparison with the pristine P3HT device, interestingly, the only parameter that exhibited a notable change is the field-effect mobility $\boldsymbol{\mu}$, which amounted to 7.3 × 10^{-3} $cm^2 \cdot V^{-1} \cdot s^{-1}$. This result shows that the performance of the device is enhanced in the presence of GNRs. Such an improvement can be ascribed to: *i)* the percolation pathway for the charges provided by the GNRs, or *ii)* the ionization energy of the 24% blend as determined by ambient PS which surprisingly amounts to 4.790±0.016 eV (i.e. it was lowered by 0.07 eV as compared to the pure P3HT 4.860±0.015 eV), thus it is better matching the workfunction of the Au electrodes (4.810±0.020 eV) enabling a better charge injection.

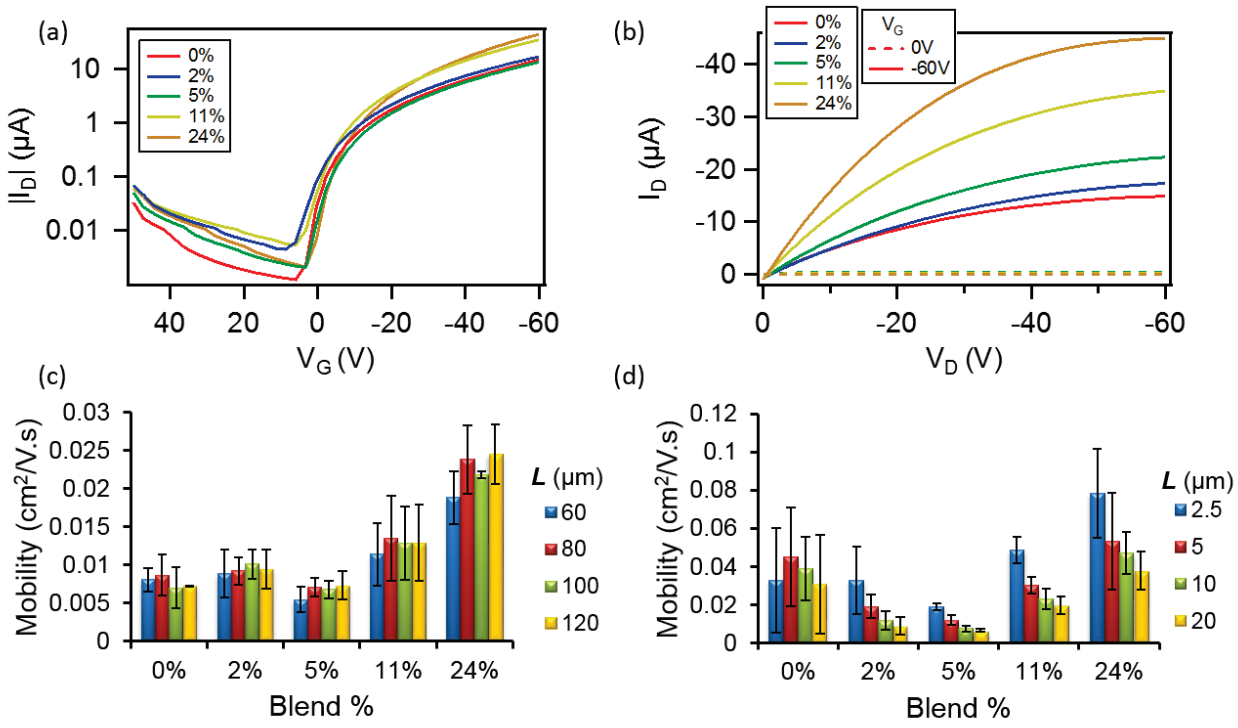

Figure 6.5 (a) Transfer characteristics of bottom-gate bottom-contact devices (L=120 μm) prepared by different blend percentages of GNRs with P3HT, and (b) their output characteristics (solid line at V_G=–60 V and dashed line at V_G=0 V; the rest of data at V_G =–20 V and –40V have been omitted for clarity). (c) and (d) represent the variation of the field-effect mobility with the concentration of the GNRs for the bottom gate bottom contact devices with: (c) long channel length (60, 80, 100 and 120 μm) and (d) short channel length (2.5, 5, 10 and 20 μm).

A comparison of the transfer characteristics (at V_D=–60 V) of the devices with the same L=120 μm at different concentrations of GNRs is shown in **Figure 6.5a**. It reveals an increase in the I_d with increasing the relative amount of GNRs up to a factor of 3 when comparing the 24% blend with the pristine devices (0% blend). Such a trend is also evident in **Figure 6.5b** which compares the output characteristics of the same blend device at V_G= 0 V (dashed line) and at V_G=–60 V (solid line). **Figure 6.5c** shows the variation of field-effect mobility of holes at different concentrations of GNRs and for devices with different L. In particular, at 2 and 5% loadings, the field-effect mobility is comparable to that of the devices with pristine P3HT. Interestingly, the mobility increased approximately by a factor of 1.7 when the content of GNRs augments to 11%, and by a factor of 3 at 24% with respect to P3HT. The enhanced performance can be attributed to the above mentioned reasons and mainly to the amount of GNRs that can facilitate the charge transport within the conduction channel as observed in similar studies on P3HT blend

with graphene[26] or with functionalized carbon nanotubes.[29] Enhanced performances were also observed for other *p*-type polymers printed on the top of a graphene layer inside the channel.[50] In fact, it has been demonstrated that when blending P3HT with another semiconductor, there is a critical concentration for the enhancement of the mobility.[17, 28] When comparing all the devices at different blend % and different *L* spanning from 60 µm to 120 µm, the average V_{Th} was found to range between 2 and –5 V, and to be slightly higher (up to –8 V) for those with 24% of GNR (see Figure 6.6a). Significantly, the average I_{on}/I_{off} ranged between 10^3 and 10^4, and appeared being uneffected by the presence of GNRs (see Figure 6.6b), unlike blends with graphene where the I_{on}/I_{off} markedly decreases at higher concentrations.[26] Electrical characterization was also performed on shorter channel lengths ranging from 2.5 µm to 20 µm. The field-effect mobility also increased by a factor of 3 when adding GNR **1** at 24% as compared to the reference devices (see Figure 6.5d). The variation of the threshold voltage and the I_{on}/I_{off} with the amount of GNR **1** and for different channel lengths was comparable to the devices with the long channel length as observed in Figures 6.6a and 6.6c.

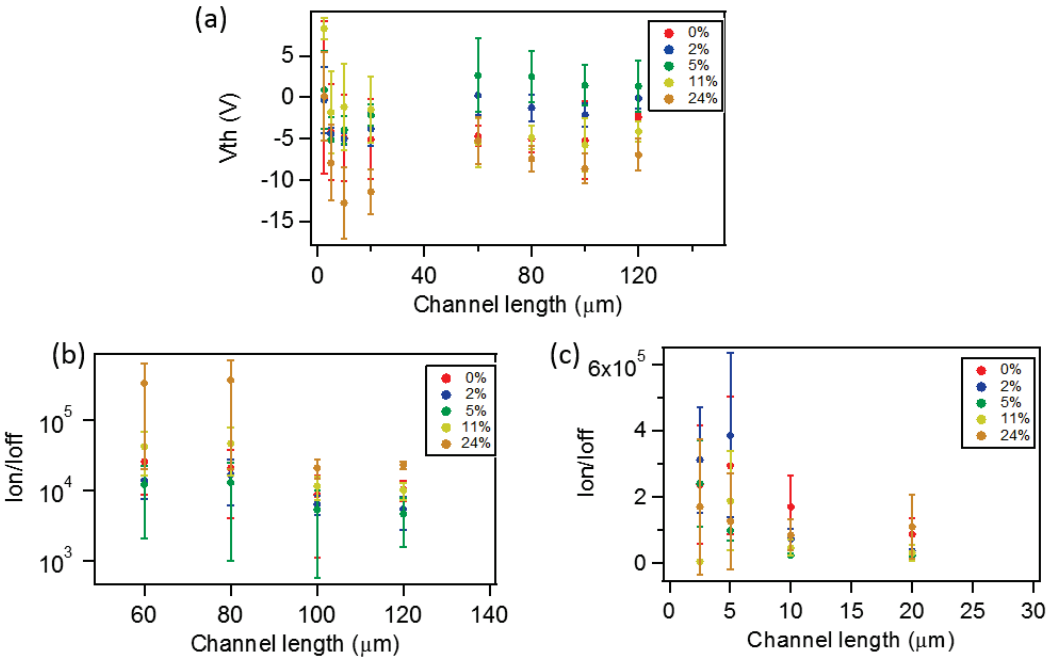

Figure 6.6 (a) Variation of the threshold voltage with the channel length at different blend percentages with respect to P3HT. (b) Variation of the I_{on}/I_{off} with the channel length *L=60*, 80, 100 and 120 µm at different blend percentages of GNRs with respect to P3HT. (c) Variation of the I_{on}/I_{off} with the channel length *L*=2.5, 5, 10 and 20 µm at different blend percentages of GNRs with respect to P3HT.

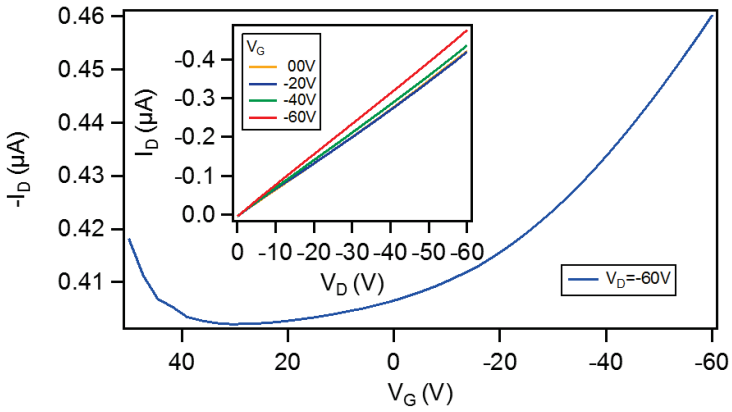

Figure 6.7 Transfer characteristics of bottom-gate bottom-contact device (*L*= 20 μm) based on pristine GNRs (prepared by drop-casting (0.25mg/mL in DCB) followed by annealing at 200°C for 15 min). The inset shows its output characteristics.

Here we note that we have also characterized FETs based on pure GNRs. They exhibited a metallic like behavior with a very small modulation of the drain current by the gate bias as observed in Figure 6.7 showing the transfer characteristics of a transistor with *L*=20 μm. The absence of a clear gate modulation is depicted in its output characteristics (inset of Figure 6.7). The maximum field-effect mobility amounted to 10^{-2} $cm^2 \cdot V^{-1} \cdot s^{-1}$. This value is underestimated since it is not corrected for the coverage. Yet, it is far below the predicted value (100 $cm^2 \cdot V^{-1} \cdot s^{-1}$) for such narrow armchair GNR[51] that is also expected to be semiconductor. However, in our case, the channel of the device is not formed by a single GNR, but by aggregates of nanoribbons as will be discussed later. Therefore, it is hard to compare the electrical characteristics of such devices with the ones for a single GNR.

6.4.3 Structural and morphological characterization

To gain further insight into the relationship between electrical properties and structure within the blend films, Grazing Incidence X-ray Diffraction (GIXD) measurements were carried out on the spin-coated films. This reveals that the addition of GNR **1** strongly influences the order within P3HT films. In the pattern recorded for the monocomponent P3HT film (Figure 6.8a) the *h*00 series, corresponding to the interchain distance measured in the plane of aromatic rings is discernible up to the third diffraction order. Another characteristic peak, originating from the π-π stacking of P3HT is visible on the equator, indicating that in the pure P3HT film the

macromolecules adopt an edge-on orientation in the crystalline domains. The chain-to-chain distance (16.4 Å), the π-stacking distance (3.6 Å) as well as the approximated coherence length of the π-π stacking derived from GIXD data (~70 Å; Figure 6.8a and c) are typical for P3HT films.[52-54] The addition of GNR to P3HT affects the arrangement of the crystalline structure of the polymer. The absence of characteristic equatorial reflections at $q_{x,y}\approx1.72$ Å^{-1} related to the π-stacking reflection in XRD patterns of all the blends (Figure 6.8b,d) indicates that even the presence of small amount of GNR such as 2 wt % hinders the formation of coherent π-stacks. Increasing amounts of the GNR cause also a gradual decrease in the integral intensity of the *100* reflection (at $q_z=0.377$ Å^{-1}), providing an evidence for a decrease in lamellar ordering of P3HT macromolecules and hence in the overall crystallinity of the polymer. Unfortunately, a strong diffuse scattering of X-rays on the GNR overlaps with P3HT peaks, which disables a quantitative analysis of the polymer crystallinity. On the other hand, such a strong scattering suggests the existence of a large interface area between the GNR and P3HT. Increasing the GNR content beyond 5 wt % causes almost complete disappearance of diffraction features from the crystalline fraction of P3HT, which indicates that at the higher content of GNR no significant polymer crystals are formed. By and large, it is suggested that the increase of the mobility in the blend can be attributed to the presence of GNRs and aggregates thereof, providing favorable pathways for the transport of charges counteracting the effect of the decrease crystallinity in the P3HT domains upon addition of GNR.

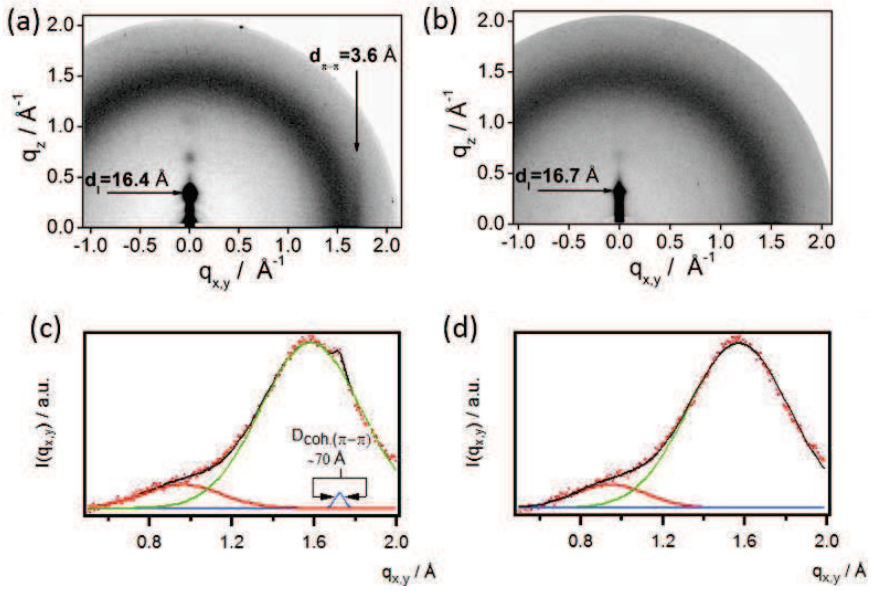

Figure 6.8 GIXD patterns of the P3HT film (a), P3HT+2 wt% GNR (b) and the corresponding horizontal integrations of P3HT (c) and the blend (d).

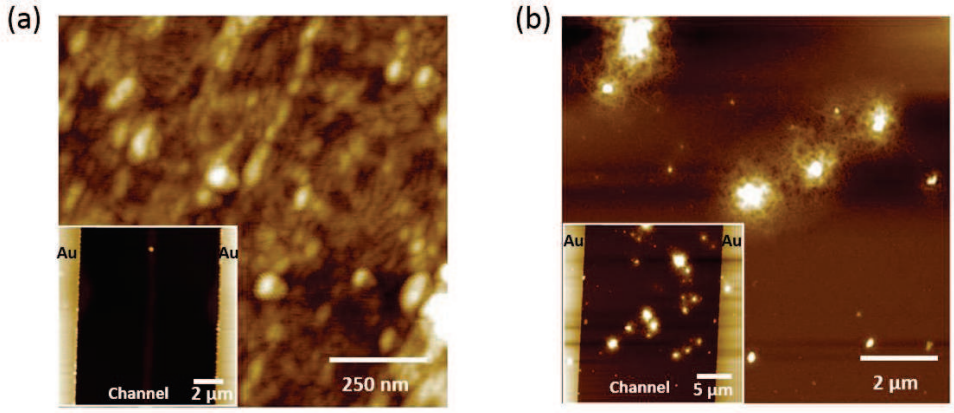

Figure 6.9 AFM images scanned inside the channel of films of: (a) pristine P3HT and (b) 24% GNR with P3HT. The insets show the scan at a larger scale. Z-scales: (a) 17 nm, (b) 75 nm, inset (a) 47 nm, inset (b) 92 nm.

As the q-range in the GIXD experiments allowed studying structures with length scales up to a very few nanometers, in order to analyze the occurrence of possible phase separation on a length scale ranging from a few nanometers up to a few tens of micrometers, we used atomic force microscopy in the tapping mode (TM-AFM). The pristine P3HT film from *o*-DCB solution is homogeneous featuring a fibrillar and grain-like structures on the tens of nanometers scale (Figure 6.9a). At 24%, the P3HT/GNRs films are inhomogeneous due to the aggregation of the

GNRs as shown in **Figure 6.9b**. These aggregates having a height ranging from 60 to 200 nm and a width spanning from 0.6 to 2 μm, were found to be randomly distributed within the polymer matrix. Their frequency of occurrence inside the channel, i.e. the number of aggregates located in the source-drain gap, was proportional to the concentration of GNRs; conversely, the aggregate size was found being independent on the concentration (see Figures 6.10a-c). This finding clarifies how the aggregates of GNRs, and not single GNRs, act as "electronic bridge" between P3HT domains. Because of the notably high propensity of our GNRs to undergo aggregation when deposited on a solid surface (as depicted in Figures 6.10 d-f), single component polycrystalline structures are obtained which are difficult to be characterized; this result is in line with observations on similar liquid phase-processable GNRs.[55] It is indeed surprising the mild increase in field-effect mobility we have measured upon blending P3HT with the GNRs, given that it is known that a 2 nm wide GNR can exhibit a mobility around 100 $cm^2 \cdot V^{-1} \cdot s^{-1}$.[51] Yet, a maximum field-effect mobility 3.25 x 10^{-2} $cm^2 \cdot V^{-1} \cdot s^{-1}$ was observed for a similar armchair GNR deposited from *o*-DCB.[56] Consequently, the reason for the limited increase in mobility is likely the simultaneous effect of decreased crystallinity with the P3HT film upon blending and the charge scattering when encountering GNR aggregates.

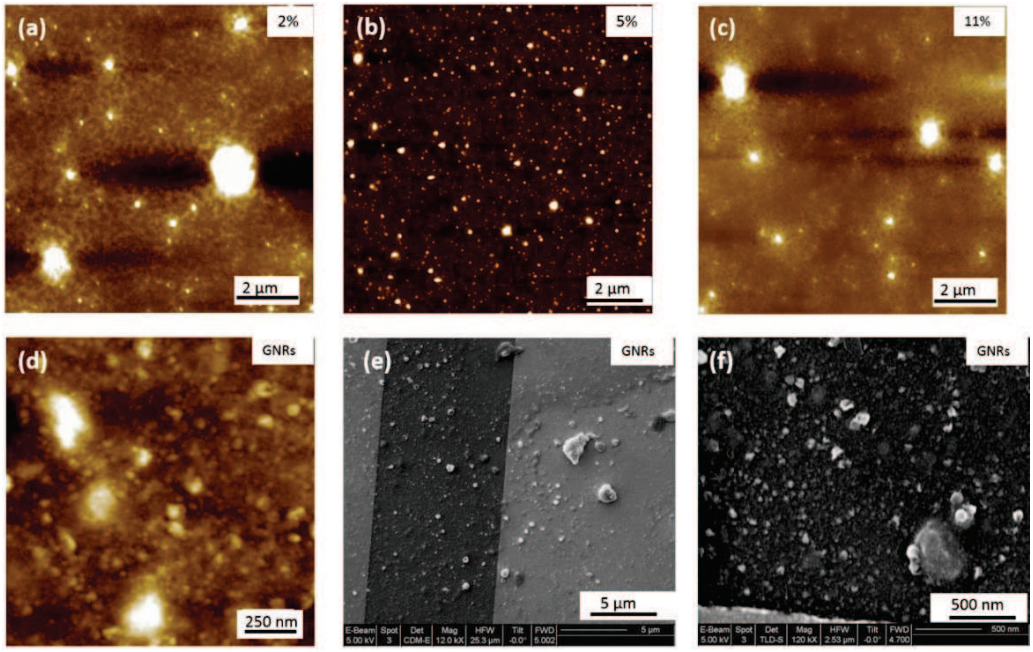

Figure 6.10 AFM images of films of GNRs with P3HT at (a) 2%, (b) 5% (c) 11%, and (d) 0%. (e) and (f) SEM images for device with pure GNRs (prepared by drop casting). Z scales: (a) 61.3 nm, (b) 47.8 nm, (c) 78.2 nm and (d) 40.8 nm

6.4.4 Electrical characteristics under illumination

Measurements of the photoresponse under illumination at 605 nm and 560 nm were carried out to investigate both the potential application of these OFETs in optoelectronics and the influence of the GNRs on the photo-generated carriers. The two wavelengths were chosen because they correspond to two absorption peaks of the films (Figure 6.2).

The difference in output (I_D-V_D) and transfer (I_D-V_G) characteristics of a 0% and 24% OFET (L=20 μm) in dark and under illumination with monochromatic light (8.17 mW·cm^{-2}) at λ=605 nm is illustrated in **Figure 6.11a-d**. The electrical characteristics of a pristine P3HT based device, i.e. with 0% GNR in the blend, is shown in **Figure 6.11a** and **b**. It displays an increase of the drain current in the I_D-V_D and I_D-V_G curves upon irradiation with monochromatic light as a result of the photogeneration of excitons that dissociate into free charge carriers which subsequently move towards the electrode under the influence of the electric field.[57] The same was observed for the 24% blend. The only difference is that at V_G=20 V (V_D=–60 V) the ratio of the photocurrent (I_{ph}) (calculated by subtracting the current in dark (I_{dark}) from the current under light (I_{light}, i.e. I_{ph}=I_{light}– I_{dark}) to the current in dark (I_{dark}) was 251.71 for the device with 0% GNR (see Figure 6.11b also Figure 6.11e red plot with solid line) whereas it was much lower (145.1) for the device with 24% blend (see Figure 6.11d also Figure 6.11e red plot with dashed line). This ratio, called photosensitivity P:

$$P = \frac{I_{Ph}}{I_{dark}} = \frac{I_{light} - I_{dark}}{I_{dark}} \tag{6.1}$$

P is one of the key figures of merit of an organic phototransistor. Another important parameter is the responsivity R:

$$R = \frac{I_{Ph}}{P_{ill}} = \frac{I_{light} - I_{dark}}{E \times A} \tag{6.2}$$

where E is the irradiance of the incident light and A is the effective device area. In contrast to P, R value (18 A·W^{-1}) of the device with 24% blend (Figure 6.11e blue plot with dashed line) was more than twice higher than that of the 0% blend (7.2 A·W^{-1}) at V_G=–60 V (V_D=–60 V) (Figure 6.11e blue plot with solid line). Considering Eq. 6.2 and since E and A are equal for both devices, higher R in the case of 24% blend indicates that I_{ph} is higher than that of the 0%.

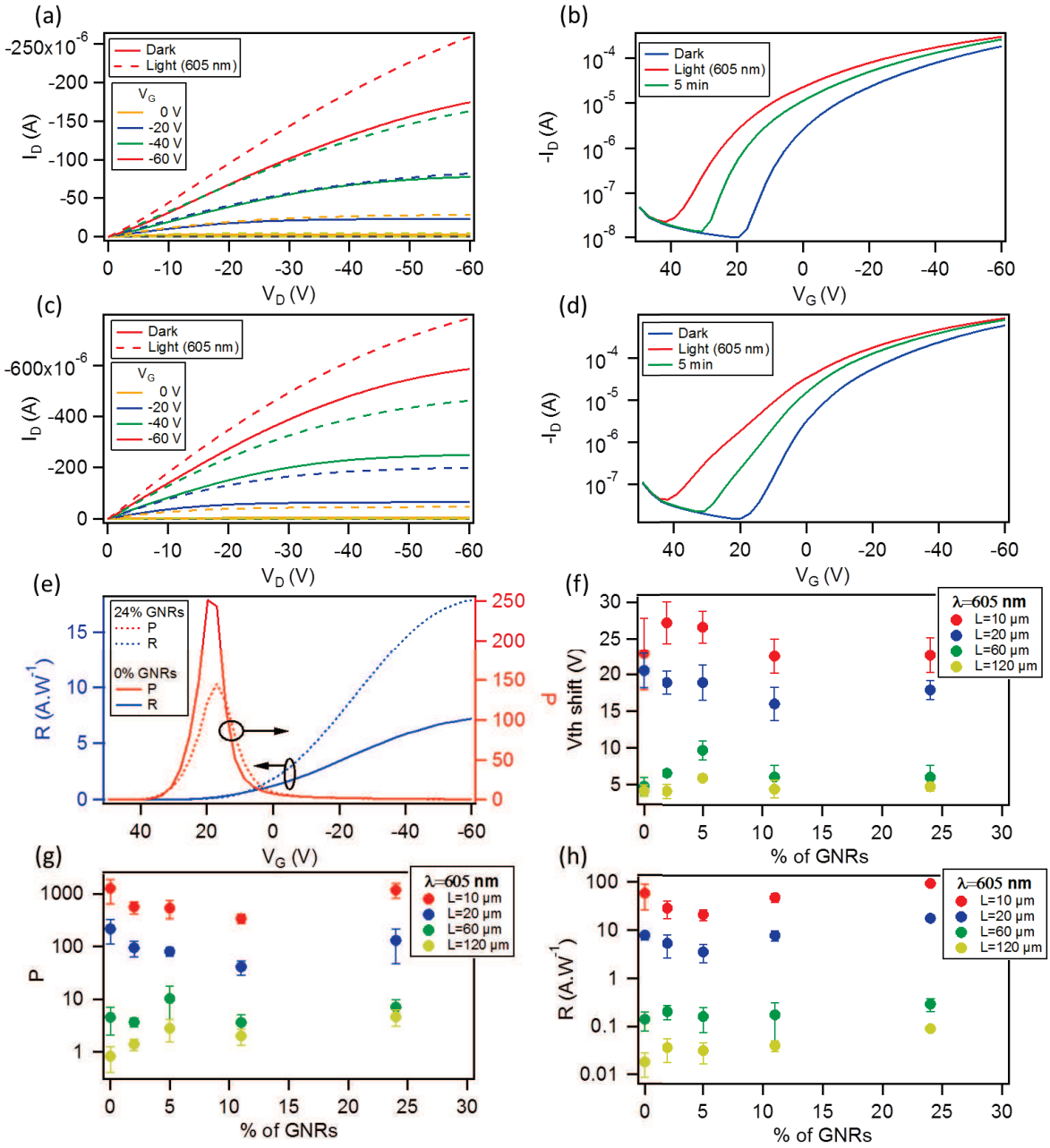

Figure 6.11 Comparison of (a) output and (b) transfer characteristics at V_D = –60 V of Pristine P3HT OFET; (c) output and (d) transfer characteristics at V_D = –60 V of a device with 24% GNR blend with P3HT with the same channel length *L*=20 µm measured in dark and under monochromatic light (λ=605 nm; 8.17 mW·cm^{-2}). (e) Variation of the responsivity *R* (blue curves) and photosensitivity *P* (red curves) with V_G at V_D = –60 V at λ=605 nm for OFETs (*L*= 20 µm) with 0% (solid lines) and 24 % blends of GNRs (dashed lines). (f) Threshold voltage shift under illumination with monochromatic light (λ=605 nm; 8.17 mW·cm^{-2}) for 4 channel lengths (*L*=10, 20, 60 and 120 µm) OFETs based on different blend percentages of GNRs with respect to P3HT. (g) Photosensivity (extracted at V_G=20 V), and (h) responsivity of these devices (extracted at V_G=-60 V) both at V_D = –60 V. Left axis is expressed in log-scale.

This might be due to: *i)* the presence of more carriers resulting from a better dissociation of excitons in the presence of GNRs, and/or *ii)* the GNRs at this concentration help in conducting more charges hence collecting more photogenerated ones at the electrodes. To assess the validity of these propositions, OFETs with different channel lengths (L=10, 20, 60 and 120 μm) and different loads of GNRs with respect to P3HT (0%, 2%, 5%, 11% and 24%) were studied under this wavelength. We observed the highest photoresponse, as quantified by a R= 94.46 $A \cdot W^{-1}$ and a P=1463.26 for the 24% device for the 10 μm channel length. Such a photoresponse decreases by several orders of magnitude with increasing the channel length (see Figure 6.11f, g and h). This is in line with the previous study done on perylenebis(dicarboximide)s (PDIs) based organic phototransistors.[58] When considering the devices with L=10 μm at different blend percentages, under illumination, the average threshold voltage shift was in the same range, ca. 23 V, for 0%, 11%, and 24% blends. However, it was slightly higher, ca. 27 V, for 2% and 5% blends. A similar trend was observed for all the channel lengths except for L=20 μm devices (see Figure 6.11f). In fact the origin of the threshold voltage shift has been attributed to: *i)* a reduction in energy level bending resulting from the Fermi level which moves close to the highest occupied molecular orbital under illumination,[59] and *ii)* the change in the trap states of the semiconductor[60-63]. Recently it was demonstrated that the apparent shift comes from the increase in the total current because of the photo-generated current[64]. In our case, under illumination, one cannot detect any trend in the V_{Th} shift with increasing the percentage of GNRs and with the channel length, probably due to the random distribution of the aggregates of GNRs inside the channel and the difference in their size as shown by AFM images. On the one hand, in OFETs with L=10 and 20 μm, the average photosensitivity P (Figure 6.11g) decreases with the increasing amount of GNRs and this is more significant at 2% and 5% (as compared to 0%) contrarily to the devices with L=60 and 120 μm. On the other hand, the responsivity R for L=10 and 20 μm (Figure 6.11h) decreases with increasing the % of GNR in the blend except for 24%, where it is higher than that of the 0% blend by a factor of two, approximately similarly to the devices with L=60 and 120 μm; however, in the latter case R increases with the blend percentage. This demonstrates that the ability of a device (with short L) to convert light into electric current is three times larger in the presence of GNRs at 24%.

The photoresponse was also conducted at λ=560 nm (9.44 $mW \cdot cm^{-2}$), corresponding to the maximum absorption of the P3HT films as shown in **Figure 6.2**. This is only seen for devices

with 10 and 20 µm channel lengths while a much lower photoresponse is seen for *L*=60 and 120 µm. By comparing the trend with the GNRs % for the responsivity and photosensivity to that at 605 nm, we find that *R* values are similar to those at 605 nm (Figure 6.12a), whereas *P* values were slightly higher (Figure 6.12b). Only a small increase in the photoresponse is observed by lowering the wavelength of the irradiation, which can only be explained by : *i*) the greater energy of photons of λ=560 nm when compared to λ=605 nm, and *ii*) the small difference in the absorbance peaks at λ=560 nm and 605 nm (Figure 6.2).

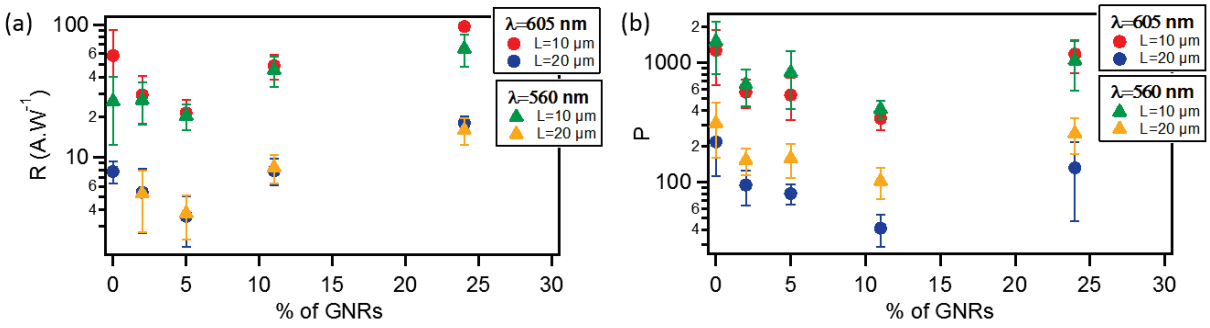

Figure 6.12 Comparison between: **(**a) Responsivity and (b) Photosensitivity for 2 channel lengths (*L* = 10, 20 µm) OFETs based on different blend percentages of GNRs with respect to P3HT; of these devices at V_D = –60 V under illumination with monochromatic light at two different wavelengths λ = 605 nm (8.17 mW·cm^{-2}) and λ = 560 nm (9.44 mW·cm^{-2}).

The field-effect mobility of the devices studied at both wavelengths remained relatively unaffected under illumination as compared to the one in dark (see Figure 6.13).

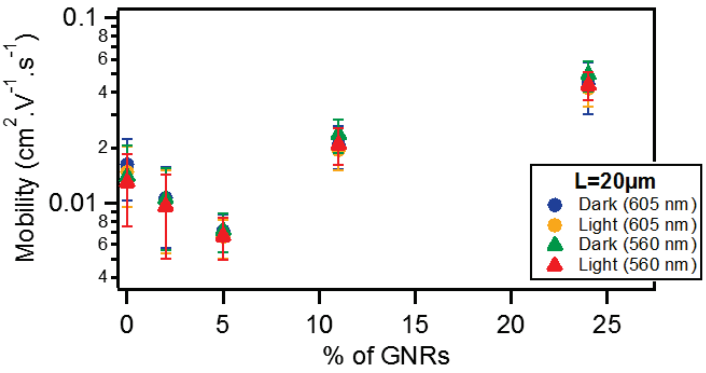

Figure 6.13 Comparison between the field effect mobility of *L* = 20 µm devices based on different blend percentages of GNRs with respect to P3HT measured in dark and under illumination with monochromatic light at two different wavelengths λ = 605 nm (8.17 mW·cm^{-2}) and λ = 560 nm (9.44 mW·cm^{-2}).

It is also important to note that for pristine P3HT devices, *R* and *P* values obtained in our case (prepared by spin-coating) with *L*=10 μm are close to the ones reported in literature.[57, 65] This suggests that the use of a monochromatic light source with a wavelength matching the peak of absorption of the semiconductor is expected to result in a higher photoresponse as compared to the use of a broad band illumination. To assess the validity of this hypothesis, two pristine P3HT devices of *L* = 20 μm were randomly selected and were investigated under monochromatic light at λ = 560 and 605 nm. The photoresponse under white light (5.06 mW·cm^{-2}) was measured following exactly the same procedure adopted for the measurements under monochromatic light. The results are shown in **Figure 6.14** and as expected under illumination with white light, the photoresponse is lower and consequently lower *P* (59) and *R* = 6.23 A·W^{-1} values were obtained as compared to the illumination under monochromatic light where *R* and *P* were 355 and 7.9 A·W^{-1} at λ = 605 nm and 387 and 7.19 A·W^{-1} at λ = 560 nm respectively.

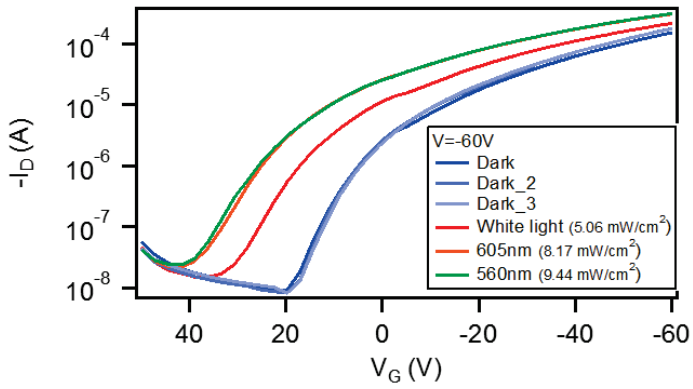

Figure 6.14 Transfer characteristics at V_D = –60 V of a pristine P3HT device (*L* = 20 μm) measured in dark, under monochromatic lights (λ = 605 nm; 8.17 mW·cm^{-2} and λ = 560 nm; 9.44 mW·cm^{-2}) and under white light (5.06 mW·cm^{-2}).

Furthermore, after 5 min of switching off the light, both devices at 0 and 24% did not regain their initial characteristics due to a photoinduced memory effect (Figure 6.11b and 6.11d green plots). In view of this finding, we extended our study to the examination of this slow relaxation at different blend percentages as a function of the gate voltage (with V_G=0 V and without V_G). Figures 6.15a and b depict the relaxation mechanism of the photoinduced charges after illumination for 30 sec for a 20 μm device with 0 and 24% blend respectively, measured at V_D=–10 V. In both cases, the photoinduced current decreases slowly once the light source is switched off at t=60 sec (see Figure 6.15a and b) and in the same manner regardless the application (blue

plots) or not (red plots) of a gate bias. The same result was observed for the other blend percentages. This decay has been reported for regioregular P3HT[66-67] and fitted to a stretched-exponential behavior (Kohlrausch's Law) (grey curves in Figure 6.15a and b) :

$$\sigma(t) = \sigma_0 \, exp\left[\left(\frac{-t}{\tau}\right)^{\beta}\right] \qquad 0 < \beta < 1 \tag{6.3}$$

where σ is the conductivity, τ is the relaxation lifetime and the exponent β that indicates the degree of the disorder of the material.

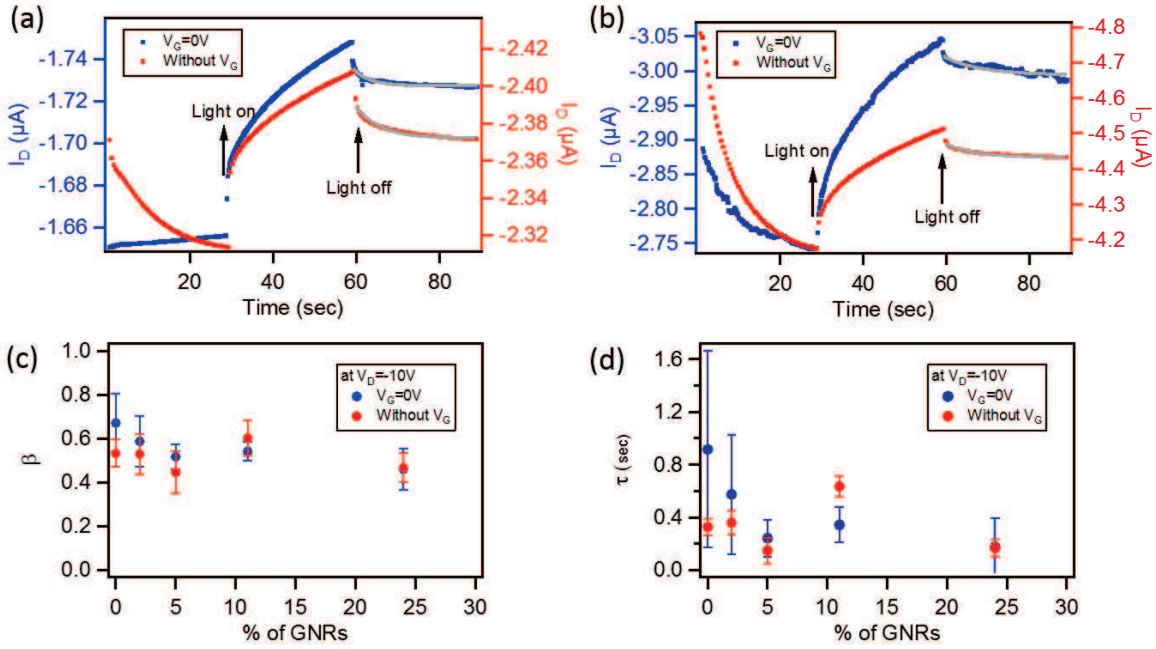

Figure 6.15 (a) Relaxation characteristics of the photoinduced current after irradiation with a monochromatic light (λ=560 nm, 9.44 mW·cm^{-2}) (light on at 30 sec, light off at 60 sec) for a 0% blend, and (b) 24% blend of Graphene nanoribbons with respect to P3HT). The gray line is the fitting by Kohlrausch's law. Average variation of: (c) the exponent β (indicating the degree of the disorder of the material), and (d) the relaxation lifetime τ at different blend percentages (done on 5 to 6 devices for each blend %).

Figure 6.15c portrays the average of the extracted values for β for different blend percentages. It reveals that β values are almost in the same range considering the error of the fitting and the error bars with or without V_G. As for the variation of the relaxation lifetime τ with the concentration of GNRs, the results are displayed in **Figure 6.15d**. The average τ values are found to depend on the fitting parameters, the blend % and the gate bias. If no gate bias is applied, τ does not following any trend with the blend %; whereas at V_G=0 V, when considering

the error bars, there is not a clear trend when increasing the blend %. This can be attributed to the random distribution of the GNRs within the P3HT domains inside the channel, which will result in the variation of the trap densities, thus affecting τ. In fact it was shown that the relaxation mechanism depends on the bulk trap densities, the insulator-semiconductor interface, the diffusion rate of the photoinduced charge carriers, the gate voltage[67] and mainly the presence of negatively charged electron accepting impurities[66] present in P3HT. This might explain the difference observed with τ and makes it difficult to understand if the aggregates of GNRs help in increasing the recombination rate of holes.

6.4.5 Photocurrent mapping

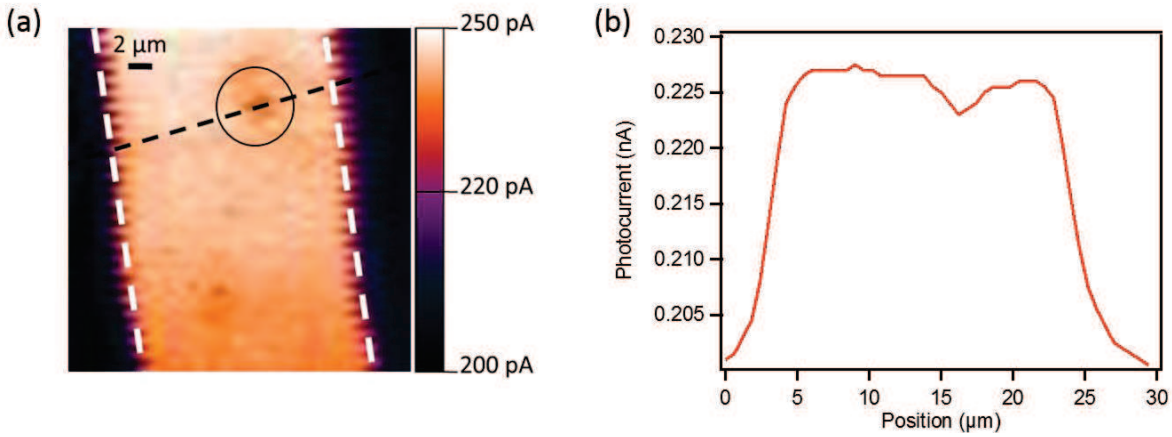

Figure 6.16 (a) Zero drain bias photocurrent response for OFET with 24% GNR/P3HT and L=20 µm in the off-state (V_G=+30 V). The dashed white lines indicate the edges of the source and drain electrical contacts; the black circle indicates the observed aggregate of GNRs. (b) Variation of the photocurrent as a function of the position of the black dashed line in (a).

To gain more information about the local origin of the generated photoresponse and the role of the GNRs under illumination, we studied these devices using scanning photocurrent microscopy. This technique has been employed widely for the local photocurrent study of devices based on carbon nanotubes and graphene[65, 68-71], and uses an optical microscope in combination with a multi-axis scanning stage for raster scanning the sample with respect to a laser beam focused on the device surface. We examined a device (L=20 µm) with 24% GNRs blended with P3HT at V_G=+30 V (in the off-state) and at zero source-drain bias under a ~1 µm spot size laser (λ=633 nm, power density < 50 kW cm^{-2}). The photocurrent image presented in

Figure 6.16 reveals uniform photocurrent response inside the channel indicating that the entire OFET channel is photoactive. However, a decrease in local photocurrent is observed in the areas where big aggregates of GNRs are present (see black circle in Figure 6.16a and photocurrent profile in Figure 6.16b). The difference could be explained by the fact that the photo-generated carriers in the aggregated region face higher impedance due to the potential barrier formed at the interface between the GNR aggregates (E_g GNR = ~1.6eV) and P3HT (E_g P3HT = 1.9 - 2.0 eV) due the difference in their band gap. Therefore, this barrier results in a lower photocurrent collected on local illumination in this region of the channel. However, this small difference does not strongly affect the overall performance of our phototransistors as demonstrated through measurements by illuminating the entire device area.

6.5 Conclusion

In summary, a new N = 18 armchair graphene nanoribbons (GNR) featuring a good dispersibility in organic solvents and an ionization energy matching that of P3HT, was blended with P3HT in a single step co-deposition process. While monocomponent GNR films suffer from the presence of macroscopic crystals alternated by domain boundaries, thereby lacks in terms of extended percolation pathways for charge transport, we have demonstrated that the addition of up to 24% of GNRs in a P3HT film enables improvement of percolation of charges in a P3HT transistor. In particular, it is possible to obtain a three-fold increase in the field-effect mobility in a P3HT device by adding 24% of GNRs to the thin film, without altering the other relevant electronic characteristics of the transistor such as the I_{on}/I_{off}. This behavior can be ascribed to the aggregates of GNRs acting as percolation patches for the charge carrier within the conduction channel by connecting the domains of the semiconductor film. The three-fold increase in μ is not outstanding because of the countereffects of the decrease in the crystalline nature in P3HT upon blending with GNR and the formation of hundreds of nm large aggregates of GNR as revealed by GIXD and AFM, respectively. Our P3HT – GNR blend approach, exhibiting an increased μ accompanied by an unaltered I_{on}/I_{off} ratio, represents a solution towards the enhancement of the performance of OFETs. The transistor's photoresponse in GNR – P3HT binary mixtures depends on the quantity of each component in the blend as well as on

the channel length. This finding represents a step forward toward the potential use of these devices in (opto)electronics, where light can function as an additional control parameter.

6.6 References

[1] H. Yan, Z. Chen, Y. Zheng, C. Newman, J. R. Quinn, F. Dotz, M. Kastler, A. Facchetti, *Nature* **2009**, *457*, 679.

[2] B. C. Schroeder, C. B. Nielsen, Y. J. Kim, J. Smith, Z. Huang, J. Durrant, S. E. Watkins, K. Song, T. D. Anthopoulos, I. McCulloch, *Chem. Mater.* **2011**, *23*, 4025.

[3] I. McCulloch, R. S. Ashraf, L. Biniek, H. Bronstein, C. Combe, J. E. Donaghey, D. I. James, C. B. Nielsen, B. C. Schroeder, W. Zhang, *Acc. Chem. Res.* **2012**, *45*, 714.

[4] J. E. Anthony, *Chem Rev* **2006**, *106*, 5028.

[5] J. E. Anthony, A. Facchetti, M. Heeney, S. R. Marder, X. W. Zhan, *Adv Mater* **2010**, *22*, 3876.

[6] A. C. Arias, J. D. MacKenzie, I. McCulloch, J. Rivnay, A. Salleo, *Chem Rev* **2010**, *110*, 3.

[7] A. Facchetti, *Mater Today* **2007**, *10*, 28.

[8] I. McCulloch, M. Heeney, C. Bailey, K. Genevicius, I. Macdonald, M. Shkunov, D. Sparrowe, S. Tierney, R. Wagner, W. M. Zhang, M. L. Chabinyc, R. J. Kline, M. D. Mcgehee, M. F. Toney, *Nat. Mater.* **2006**, *5*, 328.

[9] X. W. Zhan, A. Facchetti, S. Barlow, T. J. Marks, M. A. Ratner, M. R. Wasielewski, S. R. Marder, *Adv Mater* **2011**, *23*, 268.

[10] M. Zhang, H. N. Tsao, W. Pisula, C. D. Yang, A. K. Mishra, K. Müllen, *J. Am. Chem. Soc.* **2007**, *129*, 3472.

[11] J. Smith, R. Hamilton, Y. Qi, A. Kahn, D. D. C. Bradley, M. Heeney, I. McCulloch, T. D. Anthopoulos, *Adv. Funct. Mater.* **2010**, *20*, 2330.

[12] E. Orgiu, A. M. Masillamani, J.-O. Vogel, E. Treossi, A. Kiersnowski, M. Kastler, W. Pisula, F. Dotz, V. Palermo, P. Samorì, *Chem. Commun.* **2012**, *48*, 1562.

[13] R. Dabirian, V. Palermo, A. Liscio, E. Schwartz, M. B. J. Otten, C. E. Finlayson, E. Treossi, R. H. Friend, G. Calestani, K. Müllen, R. J. M. Nolte, A. E. Rowan, P. Samorì, *J. Am. Chem. Soc.* **2009**, *131*, 7055.

[14] J. Smith, W. Zhang, R. Sougrat, K. Zhao, R. Li, D. Cha, A. Amassian, M. Heeney, I. McCulloch, T. D. Anthopoulos, *Adv Mater* **2012**, *24*, 2441.

[15] R. Hamilton, J. Smith, S. Ogier, M. Heeney, J. E. Anthony, I. McCulloch, J. Veres, D. D. C. Bradley, T. D. Anthopoulos, *Adv Mater* **2009**, *21*, 1166.

[16] E. Lim, B. J. Jung, M. Chikamatsu, R. Azumi, K. Yase, L. M. Do, H. K. Shim, *Org Electron* **2008**, *9*, 952.

[17] D. M. Russell, C. J. Newsome, S. P. Li, T. Kugler, M. Ishida, T. Shimoda, *Appl. Phys. Lett.* **2005**, *87*, 222109.

[18] J. Smith, R. Hamilton, M. Heeney, D. M. de Leeuw, E. Cantatore, J. E. Anthony, I. McCulloch, D. D. C. Bradley, T. D. Anthopoulos, *Appl. Phys. Lett.* **2008**, *93*, 253301.

[19] J. Smith, R. Hamilton, Y. B. Qi, A. Kahn, D. D. C. Bradley, M. Heeney, I. McCulloch, T. D. Anthopoulos, *Adv. Funct. Mater.* **2010**, *20*, 2330.

[20] E. Orgiu, N. Crivillers, M. Herder, L. Grubert, M. Pätzel, J. Frisch, E. Pavlica, D. T. Duong, G. Bratina, A. Salleo, N. Koch, S. Hecht, P. Samorì, *Nat Chem* **2012**, *4*, 675.
[21] K.-J. Baeg, D. Khim, D.-Y. Kim, J. B. Koo, I.-K. You, W. S. Choi, Y.-Y. Noh, *Thin Solid Films* **2010**, *518*, 4024.
[22] Z. Bao, A. Dodabalapur, A. J. Lovinger, *Appl. Phys. Lett.* **1996**, *69*, 4108.
[23] Y. Fu, C. Lin, F.-Y. Tsai, *Org Electron* **2009**, *10*, 883.
[24] M. Surin, P. Leclere, R. Lazzaroni, J. D. Yuen, G. Wang, D. Moses, A. J. Heeger, S. Cho, K. Lee, *J. Appl. Phys.* **2006**, *100*, 033712.
[25] H. Sirringhaus, P. J. Brown, R. H. Friend, M. M. Nielsen, K. Bechgaard, B. M. W. Langeveld-Voss, A. J. H. Spiering, R. A. J. Janssen, E. W. Meijer, P. Herwig, D. M. de Leeuw, *Nature* **1999**, *401*, 685.
[26] J. Huang, D. R. Hines, B. J. Jung, M. S. Bronsgeest, A. Tunnell, V. Ballarotto, H. E. Katz, M. S. Fuhrer, E. D. Williams, J. Cumings, *Org Electron* **2011**, *12*, 1471.
[27] A. Liscio, G. P. Veronese, E. Treossi, F. Suriano, F. Rossella, V. Bellani, R. Rizzoli, P. Samorì, V. Palermo, *J. Mater. Chem.* **2011**, *21*, 2924.
[28] X. Z. Bo, C. Y. Lee, M. S. Strano, M. Goldfinger, C. Nuckolls, G. B. Blanchet, *Appl. Phys. Lett.* **2005**, *86*, 182102.
[29] Y. D. Park, J. A. Lim, Y. Jang, M. Hwang, H. S. Lee, D. H. Lee, H.-J. Lee, J.-B. Baek, K. Cho, *Org Electron* **2008**, *9*, 317.
[30] K. S. Novoselov, A. K. Geim, S. V. Morozov, D. Jiang, Y. Zhang, S. V. Dubonos, I. V. Grigorieva, A. A. Firsov, *Science* **2004**, *306*, 666.
[31] C. Mattevi, F. Colléaux, H. Kim, Y. H. Lin, K. T. Park, M. Chhowalla, T. D. Anthopoulos, *Nanotechnology* **2012**, *23*, 344017.
[32] C.-A. Palma, P. Samorì, *Nat Chem* **2011**, *3*, 431.
[33] L. Chen, Y. Hernandez, X. Feng, K. Müllen, *Angew. Chem. Int. Ed.* **2012**, *51*, 7640.
[34] M. Y. Han, B. Özyilmaz, Y. Zhang, P. Kim, *Phys. Rev. Lett.* **2007**, *98*, 206805.
[35] B. Ozyilmaz, P. Jarillo-Herrero, D. Efetov, P. Kim, *Appl. Phys. Lett.* **2007**, *91*, 192107.
[36] D. Yoon, H. Moon, H. Cheong, J. S. Choi, J. A. Choi, B. H. Park, *Journal of the Korean Physical Society* **2009**, *55*, 1299.
[37] L. Jiao, L. Zhang, X. Wang, G. Diankov, H. Dai, *Nature* **2009**, *458*, 877.
[38] D. V. Kosynkin, A. L. Higginbotham, A. Sinitskii, J. R. Lomeda, A. Dimiev, B. K. Price, J. M. Tour, *Nature* **2009**, *458*, 872.
[39] ShimizuT, HaruyamaJ, D. C. Marcano, D. V. Kosinkin, J. M. Tour, HiroseK, SuenagaK, *Nat. Nanotech.* **2011**, *6*, 45.
[40] X. Li, X. Wang, L. Zhang, S. Lee, H. Dai, *Science* **2008**, *319*, 1229.
[41] L. Dössel, L. Gherghel, X. Feng, K. Müllen, *Angew. Chem. Int. Ed.* **2011**, *50*, 2540.
[42] M. G. Schwab, A. Narita, Y. Hernandez, T. Balandina, K. S. Mali, S. De Feyter, X. Feng, K. Müllen, *J. Am. Chem. Soc.* **2012**, *134*, 18169.
[43] J. Wu, L. Gherghel, M. D. Watson, J. Li, Z. Wang, C. D. Simpson, U. Kolb, K. Müllen, *Macromolecules* **2003**, *36*, 7082.
[44] X. Yang, X. Dou, A. Rouhanipour, L. Zhi, H. J. Räder, K. Müllen, *J. Am. Chem. Soc.* **2008**, *130*, 4216.
[45] J. Cai, P. Ruffieux, R. Jaafar, M. Bieri, T. Braun, S. Blankenburg, M. Muoth, A. P. Seitsonen, M. Saleh, X. Feng, K. Müllen, R. Fasel, *Nature* **2010**, *466*, 470.
[46] P. Rempala, J. Kroulík, B. T. King, *J. Am. Chem. Soc.* **2004**, *126*, 15002.
[47] R. Scholl, C. Seer, *Justus Liebigs Annalen der Chemie* **1912**, *394*, 111.

[48] S. Osella, A. Narita, M. G. Schwab, Y. Hernandez, X. Feng, K. Müllen, D. Beljonne, *ACS Nano* **2012**, *6*, 5539.
[49] M. El Gemayel, A. Narita, L. Doessel, R. Shankar Sundaram, A. Kiersnowski, W. Pisula, M. R. Hansen, A. C. Ferrari, E. Orgiu, X. Feng, K. Muellen, P. Samori, *Nanoscale* **2014**, DOI: 10.1039/C4NR00256C.
[50] F. Torrisi, T. Hasan, W. Wu, Z. Sun, A. Lombardo, T. S. Kulmala, G.-W. Hsieh, S. Jung, F. Bonaccorso, P. J. Paul, D. Chu, A. C. Ferrari, *ACS Nano* **2012**, *6*, 2992.
[51] X. Wang, Y. Ouyang, X. Li, H. Wang, J. Guo, H. Dai, *Phys. Rev. Lett.* **2008**, *100*, 206803.
[52] D. Dudenko, A. Kiersnowski, J. Shu, W. Pisula, D. Sebastiani, H. W. Spiess, M. R. Hansen, *Angew. Chem. Int. Ed.* **2012**, *51*, 11068.
[53] N. Kayunkid, S. Uttiya, M. Brinkmann, *Macromolecules* **2010**, *43*, 4961.
[54] K. Rahimi, I. Botiz, N. Stingelin, N. Kayunkid, M. Sommer, F. P. V. Koch, H. Nguyen, O. Coulembier, P. Dubois, M. Brinkmann, G. Reiter, *Angew. Chem. Int. Ed.* **2012**, *51*, 11131.
[55] A. Narita, X. Feng, Y. Hernandez, S. A. Jensen, M. Bonn, H. Yang, I. A. Verzhbitskiy, C. Casiraghi, M. R. Hansen, A. H. R. Koch, G. Fytas, O. Ivasenko, B. Li, K. S. Mali, T. Balandina, S. Mahesh, S. De Feyter, K. Müllen, *Nat Chem* **2014**, *6*, 126.
[56] K. T. Kim, J. W. Jung, W. H. Jo, *Carbon* **2013**, *63*, 202.
[57] T. Pal, M. Arif, S. Khondaker, *Nanotechnology* **2010**, *21*, 325201.
[58] M. EL Gemayel, M. Treier, C. Musumeci, C. Li, K. Müllen, P. Samorì, *J. Am. Chem. Soc.* **2012**, *134*, 2429.
[59] M. J. Deen, M. H. Kazemeini, *Proceedings of the IEEE* **2005**, *93*, 1312.
[60] M. C. Hamilton, J. Kanicki, *IEEE J. Sel. Top. Quantum Electron.* **2004**, *10*, 840.
[61] M. C. Hamilton, S. Martin, J. Kanicki, *IEEE Trans. Electron Dev.* **2004**, *51*, 877.
[62] N. Marjanović, T. B. Singh, G. Dennler, S. Günes, H. Neugebauer, N. S. Sariciftci, R. Schwödiauer, S. Bauer, *Org Electron* **2006**, *7*, 188.
[63] T. P. I. Saragi, M. Fetten, J. Salbeck, *Appl. Phys. Lett.* **2007**, *90*, 253506.
[64] K. Wasapinyokul, W. I. Milne, D. P. Chu, *J. Appl. Phys.* **2011**, *109*, 084510.
[65] R. S. Sundaram, M. Steiner, H. Y. Chiu, M. Engel, A. A. Bol, R. Krupke, M. Burghard, K. Kern, P. Avouris, *Nano Lett.* **2011**, *11*, 3833.
[66] G. Dicker, M. P. de Haas, D. M. de Leeuw, L. D. A. Siebbeles, *Chem. Phys. Lett.* **2005**, *402*, 370.
[67] S. Dutta, K. S. Narayan, *Phys. Rev. B* **2003**, *68*, 125208.
[68] M. Burghard, A. Mews, *ACS Nano* **2012**, *6*, 5752.
[69] M. Engel, M. Steiner, R. S. Sundaram, R. Krupke, A. A. Green, M. C. Hersam, P. Avouris, *ACS Nano* **2012**, *6*, 7303.
[70] E. J. H. Lee, K. Balasubramanian, R. T. Weitz, M. Burghard, K. Kern, *Nat. Nanotech.* **2008**, *3*, 486.
[71] E. J. H. Lee, K. Balasubramanian, J. Dorfmuller, R. Vogelgesang, N. Fu, A. Mews, M. Burghard, K. Kern, *Small* **2007**, *3*, 2038.

Chapter 7 Polycyclic aromatic hydrocarbons and their application in FETs

7.1 Introduction

The fascinating properties of graphene (described in chapter 3) have raised enormous interest of the scientific community. More precisely, graphene field-effect transistors (FETs) have been intensively studied due to the interesting transport properties of this material, resulting in extremely high charge carrier mobilities[1-2] desirable in high-speed electronic applications.[3] However, the main drawbacks of graphene FETs are the low I_{on}/I_{off} (due to the zero band gap of graphene) which makes them unfavorable for logic circuits. Moreover, the various preparation techniques based on the top-down approach result in graphene sheets with disordered edges.

A viable method for overcoming these issues is the bottom-up approach.[4] Besides being an elegant way for tailoring and synthesizing graphene nanoribbons and nanographenes[5] (called also polycyclic aromatic hydrocarbons PAHs) with tunable band gaps, the bottom up-approach offers several advantages of which: *i)* it provides molecules featuring the same size and the same chemical structure, i.e. the same type of edges, unlike liquid phase exfoliated graphene; *ii)* the synthesized molecules are free of defects and can be chemically functionalized at the edges, thus allowing the manipulation of their chemical and physical properties;[6] and *iii)* tuning the electronic properties of the molecules (the GNR and PAH) through the variation of their size.[7]

PAHs are a type of compounds consisting of fused aromatic rings. In other words, in the absence of heteroatoms, they can be seen as 2D fragments of graphene[5], with a band gap different from zero. Despite being considered as pollutants,[8] PAHs are of a great interest for applications in organic electronics due to their unique electronic and optoelectronic properties. For instance, chemical functionalization of the edges with chlorine atoms enhances the solubility of the PAHs in common organic solvents and modifies their band gap which can be tuned as well by changing the number of carbon atoms in the core of the PAHs.[6]

Among PAHs derivatives, hexabenzocoronene (HBC)[9-11] and triangle-shaped PAHs[6, 9] have been studied as active material in the channel of FETs and proved their potential application in optoelectronics[11] or as sensors for detecting volatile organic compounds.[9] Nevertheless, solution processed devices still suffer from low field-effect mobility in the range of 10^{-7} $cm^2 \cdot V^{-1} \cdot s^{-1}$[9] and around 10^{-4} $cm^2 \cdot V^{-1} \cdot s^{-1}$ for the PAH derivative (with chlorinated edges) film deposited by vacuum evaporation.[6] However, it is worth mentioning a much higher mobility of 0.2 $cm^2 \cdot V^{-1} \cdot s^{-1}$ (as per time-resolved microwave-conductivity measurements) was obtained for the PAH molecules[12] when they are in the discotic phase (i.e. when the molecules self-organize into columnar structures and stack on the top of each other into columns).

7.2 Scope

In this work, we present a study on the effect of the edge functionalization on the electronic structure of a series of bottom-up synthesized PAHs with a number of carbon atoms in the main core ranging from 42 to 222 [$C_{42}R_{18}$ (**1**), $C_{48}R_{18}$ (**2**), $C_{60}R_{22}$ (**3**), $C_{60}R_{24}$ (**4**), $C_{96}R_{27}H_3$ (**5**), $C_{132}R_{32}H_2$ (**6**) and $C_{222}R_{42}$ (**7**)] (with R=Cl for the chlorinated series and R=H for the hydrogen terminated one). Their chemical structures are displayed in **Figure 7.1**.

More precisely, the variation of the ionization potential with the size of the chlorinated nanographenes was studied and compared to their hydrogen-terminated counterparts (whose chemical structures are also shown in Figure 7.1).

Benefiting of the advantages offered by the edge chlorination, one candidate of the edge chlorinated series was selected for investigating its electrical properties by fabrication of solution processed FETs. This selection was based on several criteria, mainly because it

combines a good solubility in common organic solvents (such as chloroform and *ortho*-dichlorobenzene (*o*-DCB) which are ideal for the fabrication of devices) and the energy of the lowest unoccupied molecular orbital (LUMO) level that is not so far from that of the metal electrodes such as Au or Al.

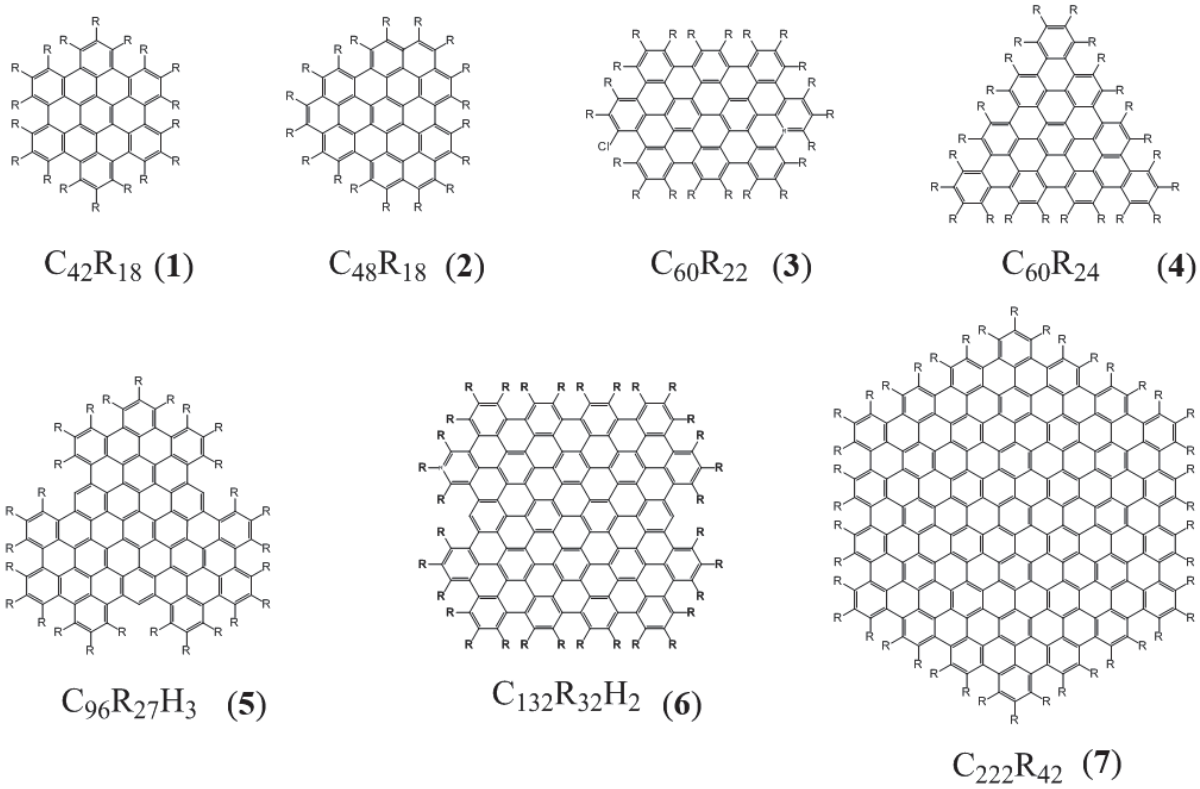

Figure 7.1 Structural formulae of the chlorinated and non-chlorinated nanographenes.

7.3 Experimental

7.3.1 Materials

All the investigated molecules were synthesized as per the reported procedure[6] and provided by the group of Prof. Müllen. As for chloroform and *o*-DCB, they were purchased from Sigma

Aldrich with the following specifications: anhydrous with a purity > 99%. Undecanethiol and hexadecanethiol were also purchased from Sigma Aldrich.

7.3.2 Device fabrication

Bottom-gate bottom-contact BG-BC transistors were fabricated on n++-doped silicon wafers serving as gate electrode with 230 nm thick thermally grown SiO_2 as the dielectric layer (1.5×10^{-8} F·cm^{-2}) and pre-patterned interdigitated Au source-drain electrodes with different channel length (L=2.5, 5, 10, 20 μm) and constant channel width (W=10mm). These substrates were ultrasonically cleaned with acetone and isopropanol prior to device fabrication. Subsequently, they were treated with ozone (1 cycle). In order to improve the charge injection by reducing the work function, Au electrodes were treated with self-assembled monolayers SAMs of undecanethiol (1 mM in ethanol) or hexadecanethiol (1 mM dissolved in ethanol and heated at 40°C then sonicated for half an hour to ensure the solubility of hexadecanethiol) by immersing the substrates for 12 hours. Then, they were thoroughly rinsed with ethanol, dried with Nitrogen and transferred to the glove box where the SiO_2 dielectric interface was treated with hexamethyldisilazane (HMDS) followed by thermal annealing at 80 °C for 1 h. Films were prepared by spin-coating 100 μL of $C_{60}Cl_{24}$ (i.e. nanographene **4** in Figure 7.1) (1 mg/mL in Chloroform) at 1500 rpm for 60 sec. In another set of devices, the substrates were not treated at all, neither the electrodes were functionalized. In some cases, films were prepared by spin-coating from 1 mg/mL in *o*-DCB. In other cases, we used bare substrates with the same specifications as above mentioned on which Aluminum source-drain electrodes (40 nm thick) were evaporated (chamber pressure = 10^{-7} mbar, evaporation rate = 0.03 nm·s^{-1}) using shadow mask with interdigitated electrodes pattern of L=60, 80, 100, 120 μm and constant W=10 mm.

7.3.3 Instrumentation

Electrical characterization of the devices was performed at room temperature in N_2 atmosphere inside a glove-box, using a Cascade Microtech M150 probe station and a Keithley 2636A sourcemeter as semiconductor parameter analyzer controlled by associated software.

The transfer characteristics were measured by sweeping the gate bias V_G from -60 to +80 V at drain biases V_D=80 and 10 V, while the output characteristics were acquired by sweeping the drain bias from 0 to 60 V at different V_G ranging from -40 to +80 V.

The ionization energy was determined by ambient photoelectron spectroscopy operating at atmospheric conditions produced by RIKEN AC-2. The measurements were performed on drop casted films (from chloroform) and on powder of a series of edge chlorinated and hydrogen terminated PAHs.

Topographical atomic force microscopy (AFM) characterization has been performed in ambient atmosphere using a Veeco Dimension 3100 operating on a Nanoscope IV control unit. Scanning electron microscopy (SEM) images were registered using FEI Quanta 250 FEG.

7.4 Results and discussion

7.4.1 Ionization energy

The energy of the highest occupied molecular orbital (HOMO) level (E_{HOMO}) was determined by ambient photoelectron spectroscopy. **Figure 7.2a** shows a comparison between the values obtained for the edge-chlorinated nanographenes **(1-7)** (full circles) (displayed in Figure 7.1) and their hydrogen-terminated counterparts (open circles). When comparing the same structure and for all the compounds, the addition of the Cl atoms at the edges increases the $E_{HOMO,}$ as expected by density functional theory (DFT) calculations that revealed also a decrease of the band-gap with increasing the size of the nanographenes.[6] The E_{HOMO} for the H-terminated PAHs (Figure 7.2b) was inversely proportional to the size of the nanographenes. This trend is in line with the theoretical values that were close to the ones obtained experimentally (for measurements on both films and powders) and varied by around 0.2 eV for all the compounds except for PAH **5** and PAH **7** where the difference was by 0.5 eV. Nevertheless, for PAHs with Cl substituents (Figure 7.2c), no clear trend was obtained mainly because of the difficulty for determining the E_{HOMO} which was close to the detection limit of our instrument. In most of the cases, a low signal was obtained even at high UV intensities (as high as 1200 nW) which resulted in uncertain values particularly for the small size PAHs (i.e. compounds **1** to **3**).

One of the advantages of the edge-chlorinated compounds is their solubility in chloroform and *o*-DCB, unlike the hydrogen-terminated nanographenes that were insoluble and could only be slightly dispersed in these solvents by means of sonication.

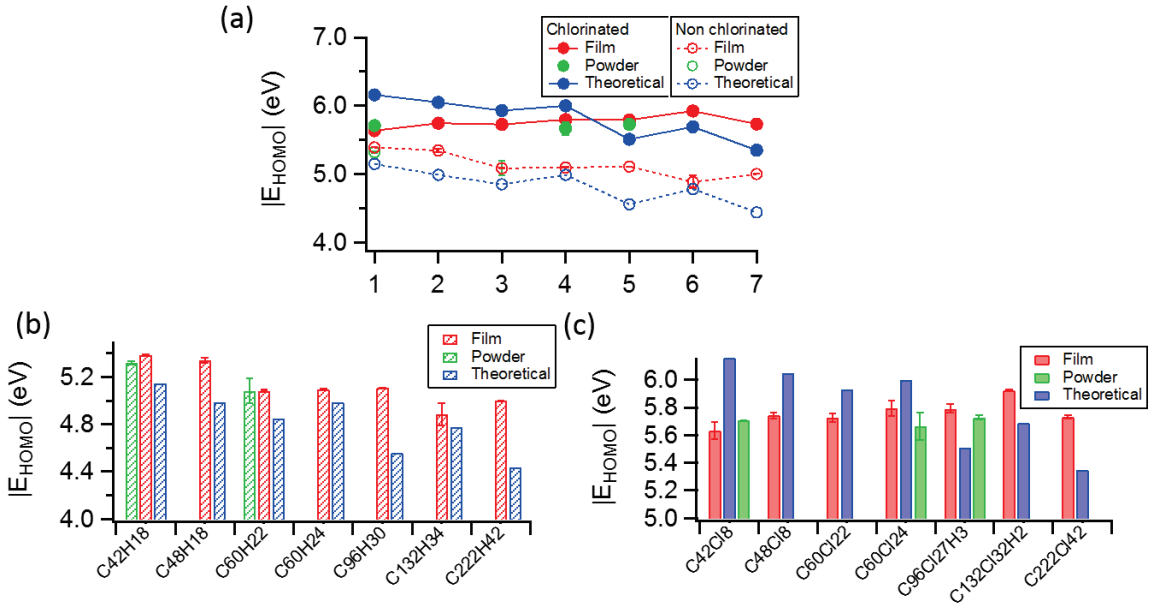

Figure 7.2 (a) Comparison between the energy of the HOMO levels of edge chlorinated nanographenes **(1-7)** (full circles) which chemical structure is displayed in Figure 7.1. It also compares the energy of the HOMO levels of their H-terminated counterparts (open circles). The experimental values (red and green circles) are compared to the theoretical ones (blue circles) obtained from Ref.[6]. Full and dashed lines are guides for the eyes. (b) and (c) are the same as (a) but plotted separately for each series to better visualize the variation of the HOMO energy level with increasing the size of the nanographene. The values for the H-terminated ones are shown in (b) while for the edge-chlorinated ones, their values are shown in (c). E_{HOMO} is represented in the absolute value.

7.4.2 Electrical characterisation

We fabricated BG-BC FETs based on $C_{60}Cl_{24}$ (herein noted as compound **4** or PAH **4)**. Au source-drain (S-D) electrodes were functionalized with SAMs of undecanethiol to reduce the injection barrier by ca. 0.4 eV between the injecting electrodes (with a work function of -4.78 eV) and the lowest unoccupied molecular orbital (LUMO) level (-3.71 eV[6]) of nanographene **4**. First, for the as-prepared device (with a channel length of 2.5 µm), the performance was very poor as depicted in **Figure 7.3a** that also indicates an *n*-type behaviour for this material. Surprisingly, by annealing the device at a temperature T=80°C[13] for almost one hour, the

performance of the FET was enhanced and improved even more with increasing the thermal annealing time as shown in **Figure 7.3b**. The output characteristics of the same device (after 13 h of annealing) (Figure 7.3c) demonstrate a nice linear behaviour of the drain current I_D at low drain biases (V_D) and a good I_D saturation at high V_D. As a result of this annealing procedure, the extracted field-effect mobility (from the saturation regime at V_D=80 V) increased by around 2 orders of magnitude as demonstrated in **Table 7.1** which shows the variation of μ with the annealing time. Additionally, I_{on}/I_{off} also improved by one order of magnitude with increasing the annealing time (Table 7.1) and V_{Th} slightly shifted to more positive values.

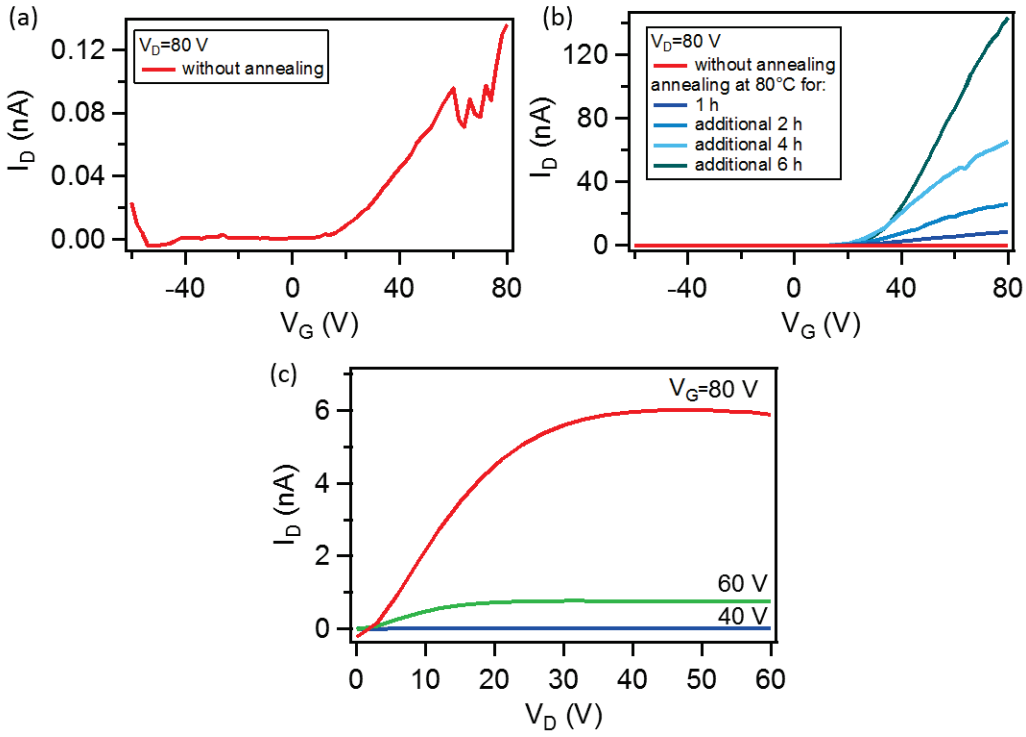

Figure 7.3 Transfer characteristics of nanographene **4** based FET (L=2.5µm) (a) as prepared and (b) after being annealed at 80°C for different time intervals. (c) Output characteristics of the same device measured after 13 hours of annealing at 80°C.

Table 7.1 Variation of the extracted field-effect mobility (μ), threshold voltage (V_{Th}) and I_{on}/I_{off} (from the saturation regime at V_D=80 V) with the annealing time for bottom-gate bottom-contact FET based

on compound **4** and which output and transfer characteristics are displayed in Figure 7.3. The values of the as-prepared devices couldn't be extracted due to the low performance.

Total number of hours (of annealing at 80˚C)	μ x 10^{-6} [$cm^2 \cdot V^{-1} \cdot s^{-1}$]	V_{Th} [V]	I_{on}/I_{off}
1	0.08	7.61	~1 x 10^3
3	0.27	9.90	~3 x 10^3
5	0.74	10.01	~7 x 10^3
13	1.41	14.53	~3 x 10^4

This enhanced performance upon annealing can be possibly due to: *i)* the improved contact between the semiconductor and the electrodes, *ii)* a better self-ordering of the molecules forming crystals that are more favourable for the charge transport, and/or *iii)* improving the size of the crystals, therefore the degree of crystallinity within the film. It is noteworthy that the packing of chlorinated nanographene **4** was found to be strongly influenced by the non-planarity of the molecules resulting from the severe steric hindrance caused by the Cl atoms;[6] therefore, the major intermolecular interactions within the crystals of **4** involve Cl-π and Cl-Cl short contacts without close π-π interactions.[6] This might explain why the μ is still low (as compared to other organic semiconductors) since it is influenced by the π-π interactions.[14]

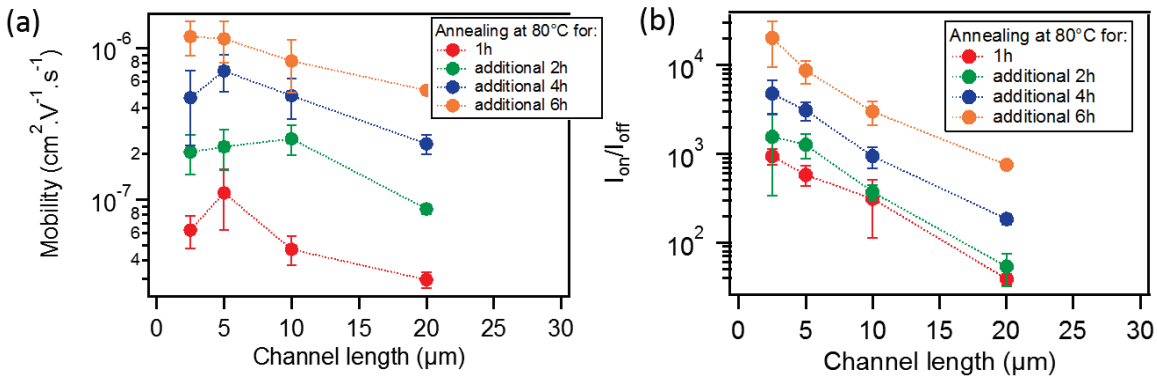

Figure 7.4 Variation of: (a) the field-effect mobility and (b) the I_{on}/I_{off} with the channel length of the FETs annealed for different time intervals at 80°C. Left axes of both (a) and (b) are in the logarithmic scale. S-D electrodes of these FETs are treated with SAMs of undecanethiol.

As for the other channel length devices, the same trend was observed (i.e. increase of μ by at least one order of magnitude) upon thermal annealing as depicted in **Figure 7.4a**. FETs with L=2.5 µm exhibited the highest field-effect mobility; probably because of the nanographenes' network that is well bridging the short electrodes (as will be discussed in the following paragraph concerning the investigation of the morphology). The highest μ value was 1.41×10^{-6} $cm^2 \cdot V^{-1} \cdot s^{-1}$ for L=2.5 µm device after 13 h of annealing. This value is much higher (by a factor of 11) than the one reported in literature for a hydrogen-terminated nanographene with the same core featuring alkyl terminations.[9]

On the other hand, I_{on}/I_{off} increased by at least one order of magnitude after 13 h of annealing as compared to the FETs treated only for 1h regardless of the channel length (see Figure 7.4b) and the highest values were for L=2.5 µm devices. The better performance of this particular channel length was also evident in the threshold voltage values which were lower than 10 V unlike high channel length FETs (see Figure 7.5). This is most likely due to the previously mentioned reason.

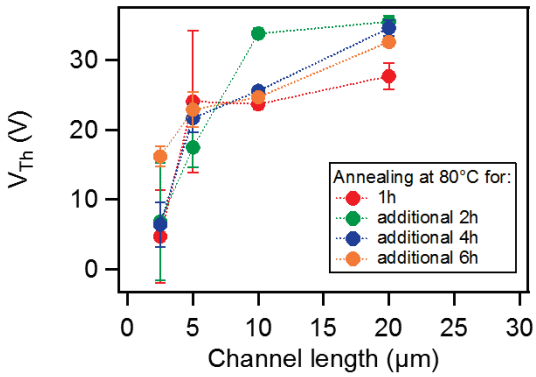

Figure 7.5 Variation of the threshold voltage with the channel length of the FETs annealed for different time intervals at 80°C.

In order to study the effect of the length of the alkyl chain (n) of the thiol based SAM, we have also fabricated devices with Au S-D electrodes functionalized with SAMs of hexadecanethiol (i.e. with n=16). Following the same annealing procedure at the same temperature, we have found that after being treated for 1 h, these devices exhibited slightly lower μ and I_{on}/I_{off} as compared to the FETs with SAMs of undecanethiol; however, a longer annealing time resulted in almost similar performances as depicted in **Figures 7.6a and b (**that compare the device performances after 1 h and 13 h of annealing at 80°C). The choice of an alkanethiol with a

longer alkyl chain was not ideal since by increasing the length of its alkyl chain, the tunnelling barrier increases.

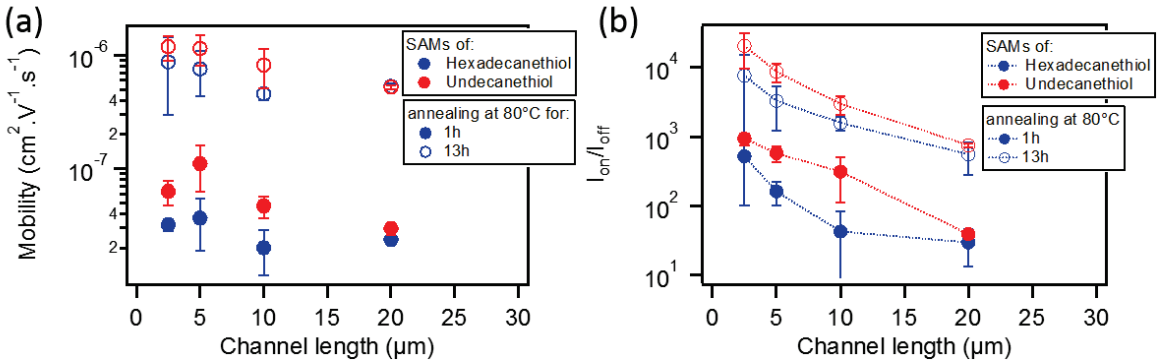

Figure 7.6 Variation of: (a) the field-effect mobility and (b) I_{on}/I_{off} with the channel length of the FETs treated with SAMs of undecanethiol (red) and hexadecanethiol (blue) annealed for 1h (full circles) and for 13h (open circles) at 80°C.

Moreover, for all the channel lengths FETs (with SAMs of hexadecanethiol), average μ, I_{on}/I_{off} and V_{Th} varied in the same fashion (see Figure 7.7) as the ones with SAMs of undecanethiol.

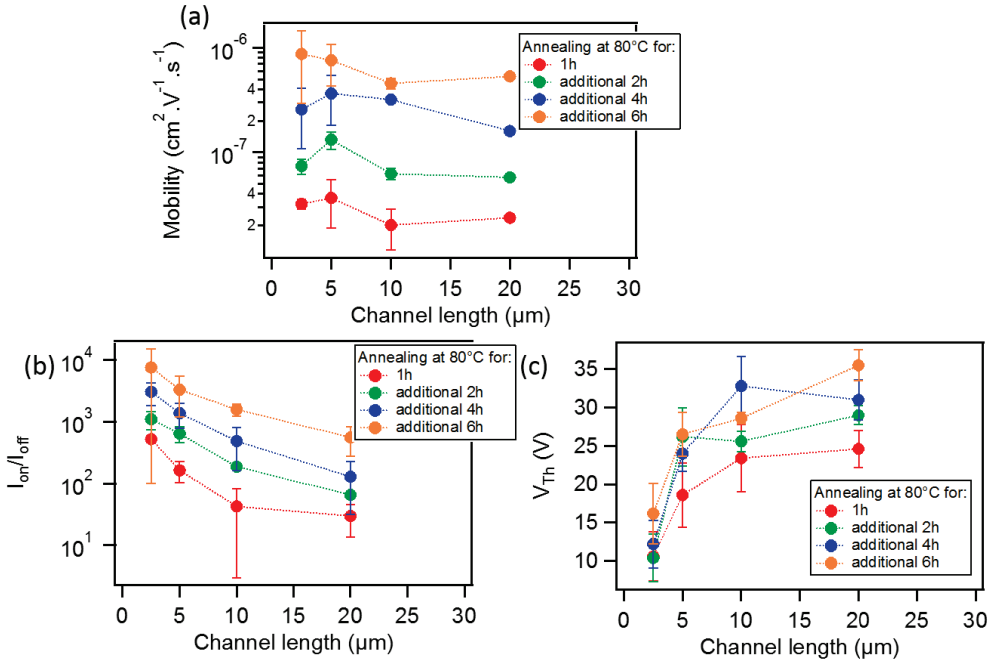

Figure 7.7 Variation of: (a) the field-effect mobility, (b) the I_{on}/I_{off} and (c) the threshold voltage with the channel length of the FETs annealed for different time intervals at 80°C. Left axes of both (a) and (b) are in the logarithmic scale. S-D electrodes of these FETs are treated with SAMs of hexadecanethiol.

We noticed that compound **4** has better solubility in *o*-DCB than in chloroform, therefore we thought that the device performance can be further enhanced by using high boiling point solvent[15] and by using Al electrodes (work function of ~4.28 eV[16]) to further reduce the charge injection barrier without the use of SAMs. The extracted μ, I_{on}/I_{off} and V_{Th} were 1.83×10^{-7} $cm^2 \cdot V^{-1} \cdot s^{-1}$, 27 and 10.38 respectively (the transfer characteristics of such device without any post-fabrication thermal annealing are shown in Figure 7.8a). For comparison, the same FET was produced (i.e. compound **4** deposited from *o*-DCB) but with untreated Au electrodes. The FET was performing only after being annealed and showed a maximum μ of 6.05×10^{-6} $cm^2 \cdot V^{-1} \cdot s^{-1}$ after annealing at T=200˚C (the transfer characteristics are displayed in Figure 7.8b). It is worth mentioning that the highest μ of FETs based on the same PAH derivative (i.e PAH **4**) deposited by vacuum evaporation was 1×10^{-4} $cm^2 \cdot V^{-1} \cdot s^{-1}$.[6]

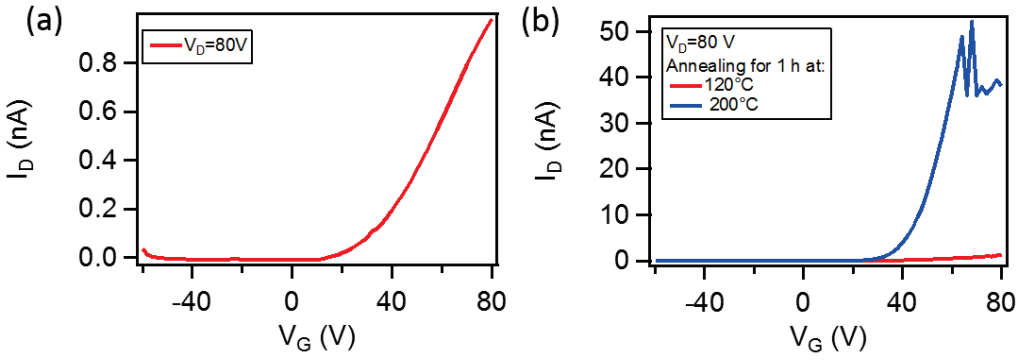

Figure 7.8 Transfer characteristics of OFET (prepared by spin-coating compound 4 from *o*-DCB) bearing un-functionalized (a) Al and (b) Au S-D electrodes. Channel length of (a) and (b) are 60 µm and 10 µm for (b).

7.4.3 Morphological characterisation

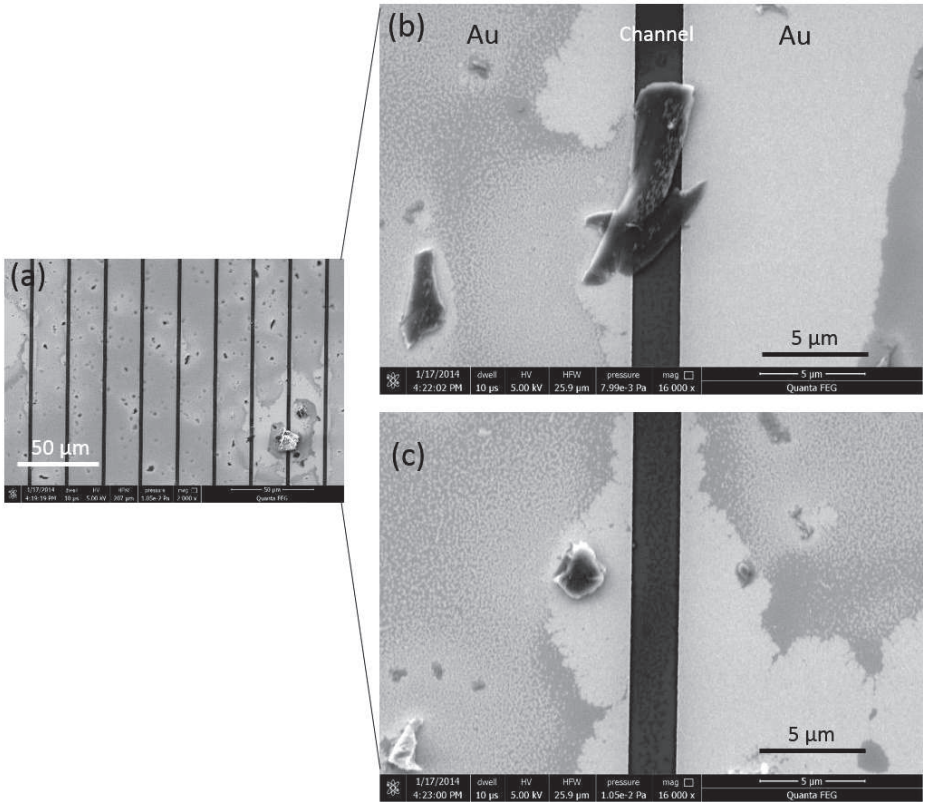

Figure 7.9 (a) Scanning electron microscopy (SEM) image of FET based on compound 4 (after 13h of annealing at 80˚C). (b) and (c) are SEM images of the same device in (a) acquired for different places of the channel at higher magnification.

Further investigation of the surface morphology of FETs (with Au electrodes treated with SAM of undecanethiol) based on compound **4** deposited from chloroform revealed µm sized aggregates as depicted in **Figure 7.9a**. Images at higher magnifications showed a discontinuous film (Figure 7.9b and c) particularly inside the channel and it seems that there is more material on the electrodes rather than inside the channel which clarifies why the field-effect mobility is low. In some cases, features similar to graphene sheets were observed as can be seen in **Figure 7.9b** and can be the non-dissolved molecules of PAH **4**. These features were very well bridging the electrodes (see Figure 7.9b) which can explain why FETs with L=2.5 µm exhibited a better performance as compared to higher channel length devices.

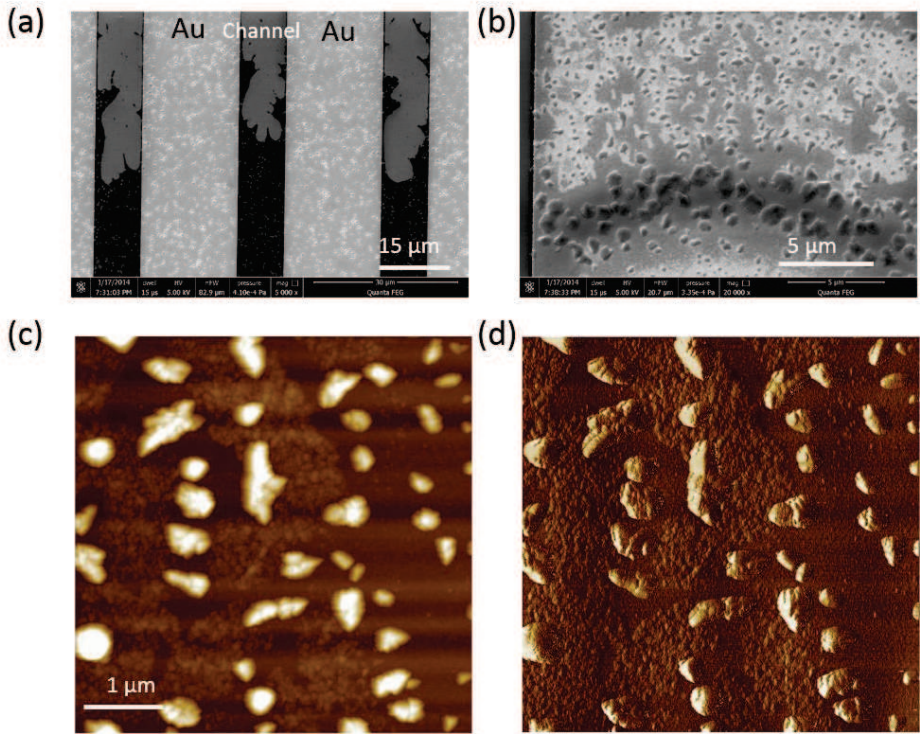

Figure 7.10 (a) SEM image of FET based on PAH 4 deposited from *o*-DCB annealed at 200˚C. (b) Zoom in of (a). AFM: (c) topography (Z scale=122 nm) and (d) phase images of the same device.

FETs prepared by depositing the semiconductor layer from *o*-DCB (and annealed at 200˚C) were also investigated by SEM that revealed a non-uniform and dewetted film (Figure 7.10a). At higher magnification, aggregates of several hundreds of nm to few µm width were observed (Figure 7.10b) and were further investigated by AFM. The topography image in **Figure 7.10c** shows that these nanographenes tend to organize themselves into structures with a non-well defined shape as some of them are spherical and some others are more rectangular like. Their height was found to range from 50 to 80 nm. It was also noticed a disconnected layer of ~20 nm height growing underneath these structures as depicted in the phase image (Figure 7.10d) as well as the topography image (Figure 7.10c).

7.5 Conclusion

In summary, we have demonstrated that the HOMO of bottom-up synthesized nanographenes can be tuned by either the size of the polyaromatic hydrocarbon molecule or by the chlorination of the edges. Moreover, the performance of field-effect transistors fabricated from PAH **4** could be simply enhanced by post fabrication thermal annealing process.

The tendency of these material to aggregate, which is as well a major problem of solution deposited graphene and graphene nanoribbons, in addition to the formation of a non-uniform discontinued film (as revealed when investigating the surface morphology), can explain the low performances of our devices. One would expect better electrical characteristics for such conjugated systems if a uniform semiconductor film covers the entire device area.

Nevertheless, these materials might not be appealing for technological applications where FETs with high μ are required but their niche applications can be in other area such as sensing.

7.6 References

[1] K. I. Bolotin, K. J. Sikes, Z. Jiang, M. Klima, G. Fudenberg, J. Hone, P. Kim, H. L. Stormer, *Solid State Commun.* **2008**, *146*, 351.

[2] K. S. Novoselov, A. K. Geim, S. V. Morozov, D. Jiang, Y. Zhang, S. V. Dubonos, I. V. Grigorieva, A. A. Firsov, *Science* **2004**, *306*, 666.

[3] Y.-M. Lin, C. Dimitrakopoulos, K. A. Jenkins, D. B. Farmer, H.-Y. Chiu, A. Grill, P. Avouris, *Science* **2010**, *327*, 662.

[4] L. Chen, Y. Hernandez, X. Feng, K. Müllen, *Angew. Chem., Int. Ed.* **2012**, *51*, 7640.

[5] X. Guo, M. Baumgarten, K. Müllen, *Prog. Polym. Sci.* **2013**, *38*, 1832.

[6] Y.-Z. Tan, B. Yang, K. Parvez, A. Narita, S. Osella, D. Beljonne, X. Feng, K. Müllen, *Nat Commun* **2013**, *4*, DOI:10.1038/ncomms3646.

[7] R. Rieger, K. Müllen, *J. Phys. Org. Chem.* **2010**, *23*, 315.

[8] A. Rubio-Clemente, R. A. Torres-Palma, G. A. Peñuela, *Sci. Total Environ.* **2014**, *478*, 201.

[9] A. Bayn, X. Feng, K. Müllen, H. Haick, *ACS Appl. Mater. Interfaces* **2013**, *5*, 3431.

[10] I. Diez-Perez, Z. Li, J. Hihath, J. Li, C. Zhang, X. Yang, L. Zang, Y. Dai, X. Feng, K. Muellen, N. Tao, *Nat Commun* **2010**, *1*, 31.

[11] X. Guo, S. Xiao, M. Myers, Q. Miao, M. L. Steigerwald, C. Nuckolls, *Proc. Natl. Acad. Sci. U.S.A.* **2009**, *106*, 691.

[12] X. Feng, V. Marcon, W. Pisula, M. R. Hansen, J. Kirkpatrick, F. Grozema, D. Andrienko, K. Kremer, K. Mullen, *Nat. Mater.* **2009**, *8*, 421.

[13] *The temperature was limited to 80˚C to avoid the molecular desorption of SAM as mentioned in chapter 4 of this theis*.
[14] S. Ando, R. Murakami, J.-i. Nishida, H. Tada, Y. Inoue, S. Tokito, Y. Yamashita, *J. Am. Chem. Soc.* **2005**, *127*, 14996.
[15] J.-F. Chang, B. Sun, D. W. Breiby, M. M. Nielsen, T. I. Sölling, M. Giles, I. McCulloch, H. Sirringhaus, *Chem. Mater.* **2004**, *16*, 4772.
[16] L. S. Hung, C. W. Tang, M. G. Mason, *Appl. Phys. Lett.* **1997**, *70*, 152.

Chapter 8 Photochromic molecules for multifunctional devices

8.1 Introduction

Organic optoelectronic materials[1] attracted particular attention for the development of low-cost multifunctional devices such as photosensors[2], organic photo-transistors[3-4] and optical memories.[5-6] In these devices, light is used as an additional remote control to modulate the electrical properties. In particular, the electrical conductivity can be tuned by tailoring materials incorporating photochromic molecules[7] which are molecular systems that are able to undergo isomerization between two or more states as a result of a light stimulus, resulting in isomers possessing markedly different physical and chemical properties[8] such as different ionization potentials. These different states should be thermally stable and the isomerization process should be fatigue resistant; all these criteria are met when using diarylethenes (DAE)[9-10] that are among the most interesting photochromic molecules to be embedded into thin-film transistors (TFTs) as a single semiconductor component.[11] However, this mono-component solution suffers from the modest charge transport properties possessed by DAE films. The latter problem can be solved by blending the DAE with organic semiconductors such as carbon nanotubes[12], pentacene[13] or poly(3-hexylthiophene) (P3HT)[14], in order to take advantage and combine the light responsive nature of the former component and the charge transport characteristics of the latter. Recently, it has been shown that by blending DAE and P3HT in solution processed bi-component films, the P3HT forms polycrystalline structures, and the DAE is to a great extent expelled out of the aggregated (crystalline) domains to be segregated in the liquid-like amorphous regions of the polymer.[14] The good current photo-response in the TFT

lacking any fatigue is determined by the capacity to introduce in the semiconducting film phototunable and bistable energy levels for the P3HT's hole transport, and thereby offering a remote control of the output drain current in an OTFT by light stimuli at defined wavelengths. The work on the blending of DAE with a polymer [14] raised the question whether such an approach is generally applicable to other organic semiconductors, in particular by substituting the polymer with a small molecule that is typically more performing, without suffering from the stronger aggregation tendency of small molecules and the absence of liquid-like amorphous domains that are typically found in polymeric polycrystalline films.

Moreover, most of FETs are based on metal source-drain (S-D) electrodes which generate a large contact resistance at the interface with the organic semiconductor, particularly for bottom-contact geometry (as discussed in Chapter 2). Therefore, the current challenge is to improve the device performance by decreasing its cost. This is possible by utilizing graphene as electrodes of an OTFT instead of being active material inside the channel, because of its high stability and high charge carrier injection efficiency which makes it a promising candidate for future electronic applications. However, the main challenge remains the fabrication of interdigitated S-D electrodes from liquid phase exfoliated graphene as such pattern was only successful by chemical vapor deposition[15] and can be done by e-beam lithography[16] which are expensive techniques as compared to the liquid phase exfoliation one. Consequently, we performed a preliminary study (presented in this chapter) on conventional metal S-D electrodes before extending it to the use of graphene, in order to investigate whether our approach of blending with photochromic molecules can be applicable for organic small molecules.

8.2 Scope

In this chapter, we present a comparative study exploring the effect of supramolecular organization mediated by the specific substitution pattern of the DAE (*tert*-butyl *vs*. methyl) on its photoswitching behavior when incorporated in both polymeric or small molecules matrices. For the sake of comparison with our previous study on DAE,[14] P3HT (chemical structure represented in Figure 8.1a) was chosen as a polymer semiconductor. On the other hand, as small semiconducting molecule, we selected 2,7-dialkyl-benzothieno[3,2-b]benzothiophene (BTBT) decorated with $C_{12}H_{25}$ alkyl chains (C_{12} BTBT) (Figure 8.1b). Alkylated BTBT derivatives are

particularly suitable as solution-processable air stable organic semiconductors since they possess an extended aromatic core and solubilizing long aliphatic chains rendering them soluble in common organic solvents. Their spin-coated films showed average mobility values as high as 0.1 $cm^2 \cdot V^{-1} \cdot s^{-1}$[17] by simple spin-coating, 0.9 $cm^2 \cdot V^{-1} \cdot s^{-1}$[18] using a method based on modified capillary force lithography (CFL) and 25 $cm^2 \cdot V^{-1} \cdot s^{-1}$[19] by using a novel off-center spin-coating-method; while by ink-jet printing, single crystals yielded thin-film transistors with average carrier mobilities as high as 16.4 $cm^2 \cdot V^{-1} \cdot s^{-1}$[20] and a maximum mobility of 5 $cm^2 \cdot V^{-1} \cdot s^{-1}$[21] by drop casting on inclined substrates. These values testify that BTBT is amongst the most performing *p*-type materials for TFTs thus competing with their amorphous silicon-based counterparts. As photochromic partner, we have selected two diarylethenes exposing different alkyl substituent DAE_1 (Figure 8.1c) and DAE_6 (Figure 8.1d), that should therefore exhibit different aggregation propensity due to a more (DAE_1) or less (DAE_6) pronounced aggregation capacity by virtue of their bulkiness.

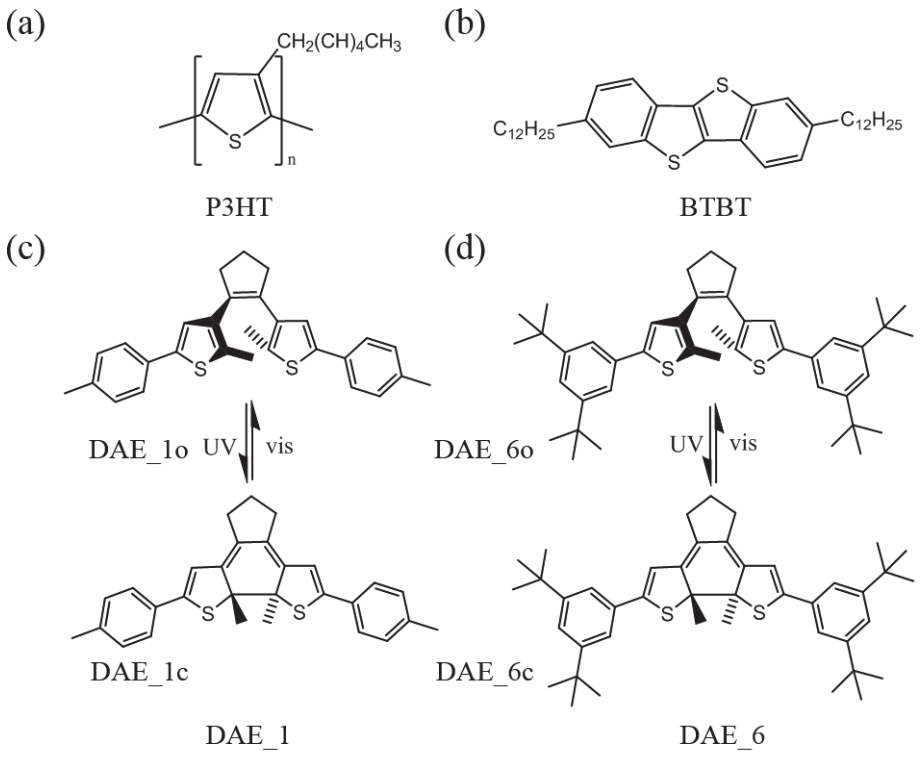

Figure 8.1 Chemical structure of: (a) P3HT, (b) BTBT, (c) DAE_1 and DAE_6 in their open and closed forms.

8.3 Experimental

8.3.1 Material

The synthesis of BTBT and DAE_1 was carried out according to published procedures.[14, 17, 22] For synthesis of *tert*-butyl-substituted DAE_6 see Appendix A. Poly(3-hexylthiophene) (P3HT) (regioregularity >99%, Mw~50,000 g/mol, Sepiolid P-200) was purchased from BASF and used as received.

8.3.2 Device fabrication

Bottom-gate top-contact (BG-TC) transistors were fabricated on heavily doped n-++ silicon wafers serving as gate electrode with 230 nm thick thermally grown SiO_2 as the dielectric layer (C_i=15 nF·cm^{-2}). These substrates were ultrasonically cleaned with acetone and isopropanol, then dried with nitrogen. This was followed by an ozone treatment (3 cycles consisting each of 5 min ozone generation followed by 25 min incubation). Then, they were transferred inside the glove box where the blends of DAE_1o or DAE_6o with BTBT or P3HT (at 20 wt % in chloroform which was chosen for comparison with our previous work[14]) were deposited by spin-coating at 3500 rpm for 30 sec followed by an annealing step at 80˚C for 30 min.[23] For comparison, reference devices based on pristine BTBT (4 mg/mL) and P3HT (1 mg/mL) were prepared. Right after, Au source and drain electrodes were evaporated using a shadow mask (thickness=35 nm, chamber pressure = 10^{-6} mbar, evaporation rate = 0.03 nm/s) with different channel length (L=60, 80, 100, 120 μm) and constant channel width (W=10 mm).

Also bottom-gate bottom-contact (BG-BC) devices based only on the blends with P3HT were fabricated for comparison with previous work on DAE_1.[14] Briefly, on substrates featuring prepatternend interdigitated electrodes (with L= 20 μm, and W= 10 mm) with the same specifications as above mentioned and without any ozone treatment of the surface, DAE blends with P3HT (20 wt % in chloroform) were spin-coated at 1500 rpm for 60 sec. The samples were left to dry overnight prior to the device characterization. For comparison, pristine P3HT devices were prepared using the same parameters and by spin-coating P3HT at 1 mg/mL in chloroform.

8.3.3 Electrical Characterization

Electrical characterization of the devices was performed at room temperature in a N_2 atmosphere inside a glovebox, using a Cascade Microtech M150 probe station and a Keithley 2636A controlled by Labtracer software. Field-effect mobility and threshold voltage were extracted from the saturation regime at V_D=-30 V (for BTBT) and at V_D=-80 V (for P3HT).

8.3.4 Irradiation procedure for the static switching

For the irradiation procedure, three cycles were performed consisting each of: *Step 0* in the dark. *Steps 1, 2 and 3*: irradiation with λ= 365 nm for 90 sec, additional 120 sec, and additional 600 sec, respectively. This is followed by 300 sec of relaxation under dark. *Steps 4 and 5*: irradiation with λ= 546 nm for 120 sec, and additional 600 sec, respectively. For all the steps after irradiation, the light was switched off and the value of the drain current at V_D=-10 V and V_G=-80 V is taken from the full I_D-V_G curve. We also performed another procedure by limiting the irradiation in the UV to 10 sec for each step and keeping the same irradiation time at λ= 546 nm. The wavelengths were chosen in view of the absorbance spectra P3HT films and in order to compare the results with previously published ones[14].

8.3.5 Cyclic voltammetry

For DAE_1 and DAE_6, cyclic voltammetry (CV) was performed (in collaboration with the group of Prof. S. Hecht) using a PG310 USB (HEKA Elektronik) potentiostat interfaced to a PC with PotMaster v2x43 (HEKA Elektronik) software for data evaluation. A three-electrode configuration contained in a non-divided cell consisting of a platinum disc (d = 1 mm) as working electrode, a platinum plate as counter-electrode, and a saturated calomel electrode (SCE) with an agar-agar-plug in a Luggin capillary with a diaphragm as reference electrode was used. Measurements were carried out in acetonitrile or methylene chloride (HPLC-grade, dried over calcium hydride and distilled) containing 0.1 M Bu4NPF6. The data is given in reference to the ferrocene redox couple (Fc/Fc+), which was used as external standard. Cyclic voltammograms of ring-closed isomers of diarylethenes were obtained by irradiation of the

electrochemical cell using a standard laboratory UV-lamp equipped with a 313 nm UV-tube. Also the highest occupied molecular orbital (HOMO) level of BTBT was determined by this technique.

8.3.6 Spectroscopy study

8.3.6.1 Spectroscopy study in solution

UV-vis spectroscopy was performed on a Cary 50 spectrophotometer equipped with a Peltier thermostated cell holder at 25 ± 0.05 °C using spectrophotometric grade solvents. Irradiation experiments were carried out in CH_3CN in a quartz cuvette using an Oriel 68810 500 W mercury-lamp in combination with an Oriel 77200 monochromator. Quantum yields were determined by comparing the initial reaction yields for the cyclization and the cycloreversion of the diarylethenes against the isomerization of azobenzene in methanol[24] and the commercial furyl fulgide Aberchrome 670 in toluene,[25] respectively.

8.3.6.2 Isomerization quantum yield in thin films of the closed to open transition

Isomerization quantum yields for the closed to open transition in thin films of DAE blends were determined by examining the absorbance change with respect to irradiation time. As a light source a Spex Fluorolog spectrofluorimeter (JY Horiba) with excitation monochromator set to 535 nm was used and the absorption at 535 nm was determined using a V630 spectrophotometer (JASCO). A handheld UV lamp was used to transform the open form to the closed form prior to experiment start. The photonflux at 535 nm was determined by chemical actinometry using Aberchrome 670 dissolved in toluene as a chemical standard[25] following exactly the same geometry (including a mask with known area) as used when measuring on the thin films. The photonflux was determined by fitting the acquired data to eq. 8.1 using an in-house made MATLAB program.

$$\frac{d[Photoisomer]}{dt} = -\frac{\varphi \cdot \omega \cdot \left(1-10^{-Abs}\right)}{N_A \cdot V} \qquad (8.1)$$

In eq. 8.1, the change in concentration with respect to irradiation time is a function of the photonflux (ω), quantum yield (ϕ), number of absorbed photons ($1\text{-}10^{-Abs}$), and the volume (V) of the sample. Thin films of DAE blends were made on glass chips using exactly the same

processing conditions as when making transistors. To analyze the quantum yield, eq. 8.1 was modified to be applicable on thin films by introducing the molar absorptivity (ε; solution value, see Table 8.2) and with the unit of the photonflux modified from E/s to E/(s*area).

$$\frac{dAbsorbance}{dt} = -\frac{\varphi \cdot \omega \cdot \epsilon \cdot \left(1-10^{-Abs}\right)}{N_A \cdot area} \tag{8.2}$$

The isomerisation quantum yields was determined in duplicates by fitting the acquired data to eq. 8.2 using an in-house made MATLAB program.

8.3.6.3 Isomerization of the open to closed transition in BTBT blends

The low absorptivities of the films prevented quantitative measurements of the open to closed transition, but qualitative measurements of the open to closed transition in the BTBT blends were performed. In these measurements the absorption (at 545 nm) of the product (the closed form) was determined as a function of irradiation time (at 365 nm, irradiation source was a M365F1 LED from Thorlabs), and a simplified version of eq. 8.2 was used to analyze the data using an in-house made MATLAB program.

$$\frac{dAbsorbance}{dt} = -k \cdot \left(1 - 10^{-\left(Abs_{final}-Abs\right)}\right) \tag{8.3}$$

In eq. 8.3, k is a rate constant and Abs_{final} is the absorbance value at infinite irradiation times (fitted). Samples were measured in triplicates.

8.3.7 Instrumentation

Devices were irradiated from the top using a Polychrome V (Till Photonics) tunable light source providing a monochromatic beam with λ=365 nm and λ=546 nm with irradiance levels of 0.6 and 13.94 $mW \cdot cm^{-2}$, respectively. The light intensity was measured using an analog optical power meter, PM100A (ThorLabs).

Ultraviolet-visible absorbance spectra were recorded on JASCO V-670 and V-630 UV-Vis spectrophotometers. Thin films of pure BTBT and the blend with DAE_1 or DAE_6 were deposited on quartz substrates following the same procedure adopted for the fabrication of

devices (i.e. ozone treatment of the surface, same spin-coating speed and post-fabrication annealing step).

On one hand, ambient photoelectron spectroscopy measurements were performed on drop casted films using a new generation of photoelectron spectroscopies operating at atmospheric conditions (RIKEN AC-2) in order to determine the HOMO levels of BTBT and P3HT. On the other hand, cyclic voltammetry was used as well to determine the HOMO levels of DAE molecules because of their in-situ photoisomerisation from the open to the closed form triggered by the UV light of our instrument. For comparison also HOMO levels of BTBT and P3HT were determined by CV as detailed in the previous paragraph.

2D grazing incidence x-ray diffraction (GIXD) with a MAR345 image plate was performed on beam line 11-3 at the Stanford Synchrotron Radiation Light source with an incident energy of 12.7 keV. The measurements were collected at a grazing angle of 0.1° and expressed as a function of the scattering vector $q = 4\pi\sin(\theta)/\lambda$. Here θ represents half of the scattering angle, λ is the wavelength of the incident beam, q_{xy} is the component of the scattering vector parallel to the substrate plane and q_z is the component perpendicular to the substrate plane.

Atomic Force Microscopy (AFM) images were recorded in tapping mode using a Nanoscope (Veeco Multimode V) on the same devices characterized and were also performed on pure DAE derivatives drop-casted on SiO_x substrates.

8.4 Results and Discussion

8.4.1 Determination of the energy levels

HOMO levels were determined for all studied molecules in order to investigate whether the addition of DAEs into BTBT or P3HT might result in charge trapping in case of energy level mismatches. Consequently, CV measurements were performed for DAE_1, DAE_6 (for open and closed isomers) and for BTBT as shown in **Figure 8.2a, b** and **c**, respectively. The one for P3HT is reported in ref. [14]. The obtained values of the HOMO levels are summarized in **Table 8.1**. For clarity, these values were plotted on the same graph and displayed in Figure 8.3. It is noticed that the HOMO level of BTBT is matching the HOMO levels of both DAEs in their

open form. On the contrary, the HOMO level of P3HT is matching the one of DAEs in their closed form.

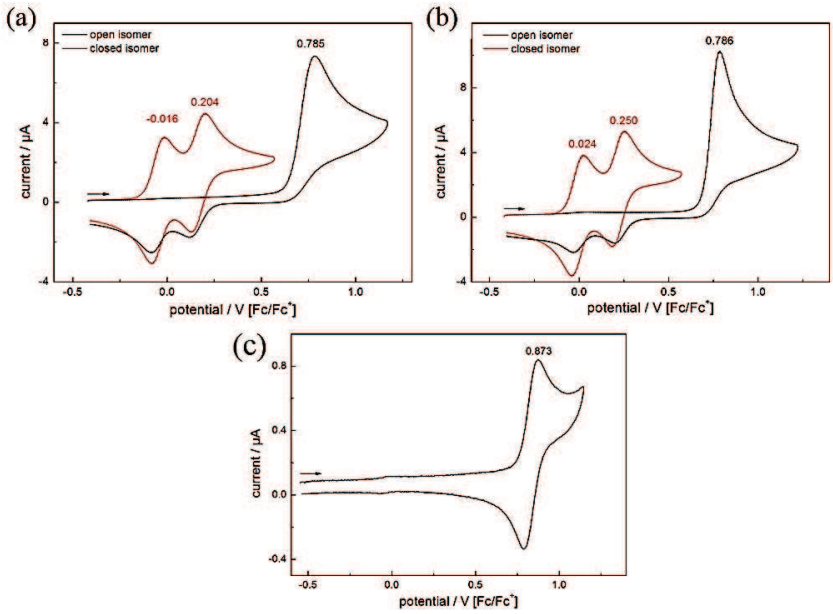

Figure 8.2 Cyclic voltammetry of: (a) DAE_1 and (b) DAE_6 in acetonitrile ($1 \cdot 10^{-3}$ M, dE/dt = 1 V s^{-1}). Whereas (c) is the one of a saturated solution of BTBT in methylene chloride (dE/dt = 0.1 V s^{-1}).

Table 8.1 Oxidation potentials and derived HOMO levels**.**

	E_p^{a1} [V] vs. Fc/Fc^+	E_p^{a2} [V] vs. Fc/Fc^+	HOMO [eV][a]
DAE_1o[b]	0.785	-	-5.6
DAE_1c[b]	-0.016	0.204	-4.8
DAE_6o[b]	0.786	-	-5.6
DAE_6c[b]	0.024	0.250	-4.8
BTBT[c]	0.873	-	-5.7
P3HT[d]	0.014	-	-4.8

[a] $E^{HOMO} = -e\ E_p^{a1}(Fc/Fc^+) - 4.8$ eV[26]
[b] in acetonitrile
[c] in methylene chloride
[d] onset potential of a film on the electrode in acetonitrile[14]

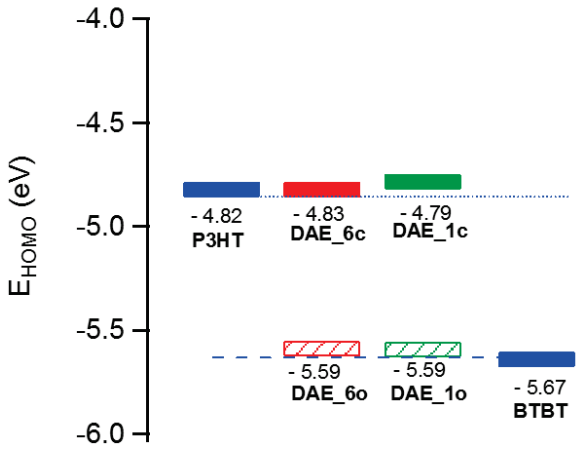

Figure 8.3 Schematic energy level diagram showing the HOMO level of the organic semiconductors used. These values are obtained from cyclic voltammetry. Dotted and dashed lines are guides for the eyes for comparing the HOMO level of P3HT with DAEs in their closed form, and BTBT with DAEs in their open form.

In the following section, spectroscopy study on DAEs in solution and in film was performed in order to gain insight into the optical and physical properties of the photochromic molecules in different environments (i.e. when added to small molecule or polymer semiconductor)

8.4.2 Spectroscopy study in solution

We determined the isomerization quantum yield (i.e. the number of isomerization events occurring divided by the number of absorbed photons) for both DAE derivatives in order to examine the effect of the alkyl substituent on their photoswitching. Thus, the absorbance spectra of pure DAE_1 and DAE_6 (for the open form isomers) were acquired in solution that was irradiated with UV until reaching the photostationary state as displayed in **Figure 8.4a** and **b**, respectively. The low energy band of the open form for both DAEs is located in the visible region which enables selective excitation of the closed form. The results are summarized in **Table 8.2**. Both molecules have similar photostationary state and quantum yield for the isomerization of the closed to open form; however, it slightly differs for the isomerization of the open to the closed form where DAE_1 showed higher conversion isomerization efficiency. This difference does not impose any hindrance for switching DAEs when incorporated into devices.

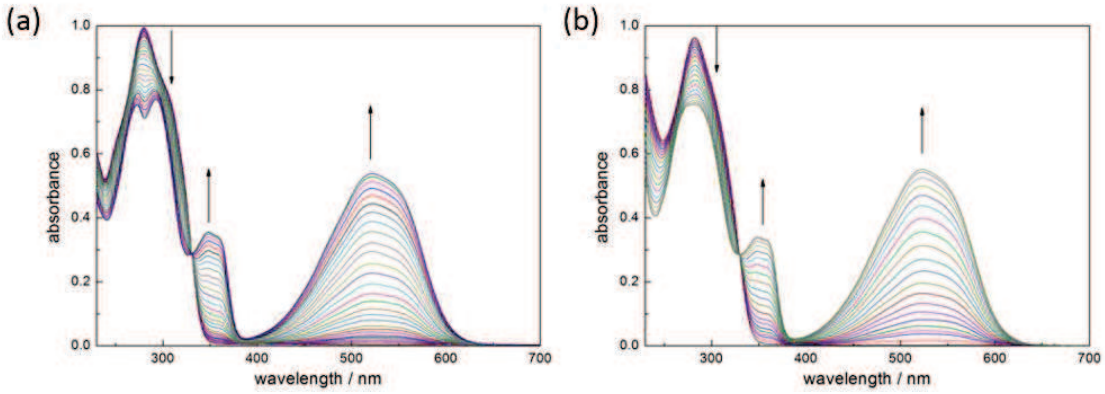

Figure 8.4 UV-vis absorption spectra of (a) DAE_1 ($2.8 \cdot 10^{-5}$ M) and (b) DAE_6 ($3.0 \cdot 10^{-5}$ M) in acetonitrile during the course of irradiation (λ_{irr} = 313 nm) until reaching the photostationary state.

Table 8.2 Photochromic properties of DAE_1 and DAE_6 in acetonitrile.

	λ_{max} / nm (ε / 10^4 L mol^{-1} cm^{-1})	$\Phi_{o\rightarrow c}$ (313 nm)	$\Phi_{c\rightarrow o}$ (546 nm)	PSS[a]
DAE_1o	279 (3.45)	0.50	0.008	92 %
DAE_1c	293 (2.67), 348 (1.31), 520 (1.98)			
DAE_6o	282 (3.21)	0.31	0.009	90 %
DAE_6c	279 (2.42), 348 (1.24), 523 (2.04)			

[a] Conversion to the closed isomer upon UV irradiation in the photostationary state.

8.4.2.1 Isomerization quantum yield in thin films of the closed to open transition

The isomerization quantum yield was also determined for DAEs in films of P3HT and BTBT in order to gain more information about the influence of the environment on the photoswitching behavior of the photochromic molecules.

An example of raw data of the absorption of films of BTBT+DAE_6 at different irradiation time is displayed in **Figure 8.5a**. The absorption of Aberchrome 670 (the chemical actinometer used) as a function of irradiation time is shown in **Figure 8.5b**. For all the films of blends of either DAE_1 or DAE_6 with BTBT or P3HT, the absorption spectra at different irradiation time were acquired. In order to determine the isomerization quantum yield of the photochromic molecules in a matrix of P3HT or BTBT, the value of the absorption at 535 nm was plotted in

function of time and fitted as detailed in the experimental part (see Figure 8.6). The results, summarized in **Table 8.3**, show lower isomerization quantum yields for films of DAE blends with P3HT or BTBT by approximately a factor 2 or 4, respectively as compared to solution. This proves that the DAEs indeed are able to photoswitch in the same environment as the ones used for devices.

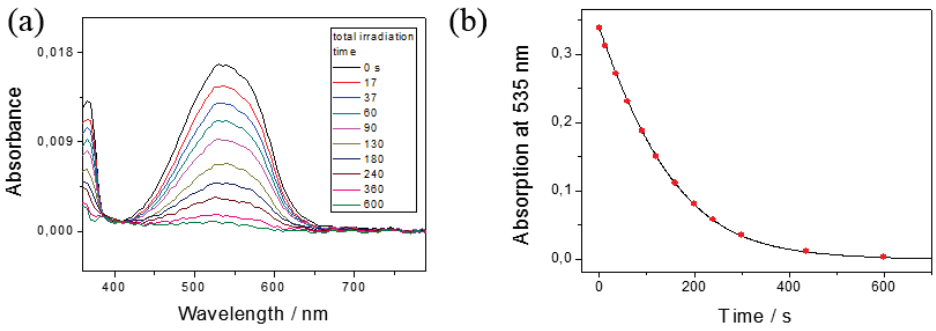

Figure 8.5 (a) Example of raw data, absorption of a BTBT/DAE_6 film at different amount of irradiation. (b) Absorption of Aberchrome 670 (the chemical actinometer used) as function of irradiation time (Red circles = measured data, black line = fit).

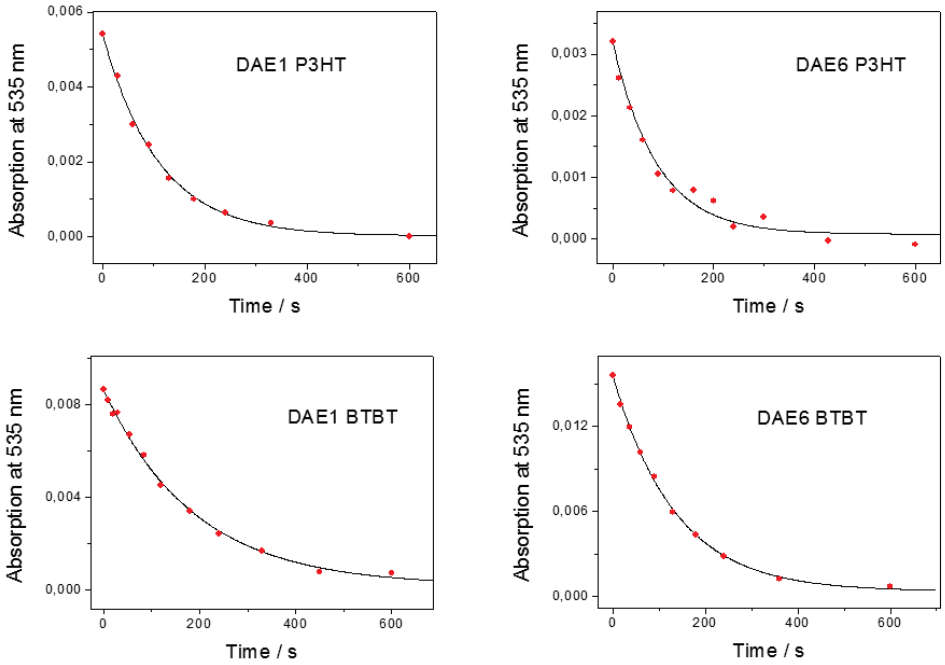

Figure 8.6 Absorption of DEA blends as function of irradiation time (Red circles = measured data, black line = fit).

Table 8.3 Photoisomerization quantum yields for the closed to open transition in thin films.

	DAE_1	**DAE_6**
P3HT	0.32 %	0.41 %
BTBT	0.17 %	0.27 %

8.4.2.2 Isomerization of the open to closed transition in BTBT blends

Devices based on DAE_1 blend with BTBT showed strange switching behavior under illumination (as will be detailed in the following paragraph). Therefore, qualitative measurements of the open to closed transition in the BTBT blends were performed. For the DAE_6 blend with BTBT, the data was well explained by theory (eq. 8.3) as depicted in **Figure 8.7** (bottom images). However, for DAE_1 incorporated in BTBT, systematic deviations could be seen in the residual (Figure 8.7 top images). Good fits could however be obtained by fitting the beginning and the end of the isomerization separately as shown **Figure 8.8** thus giving two rate constants. The values are summarized in **Table 8.4**. Of the two rate constants fitted to the DAE_1 isomerization, one was very similar to the DAE_6 one, and the other was considerably faster. This indicates that DAE_1 is present in two different environments inside the blend and that one of these environments is similar to that experienced by DAE_6.

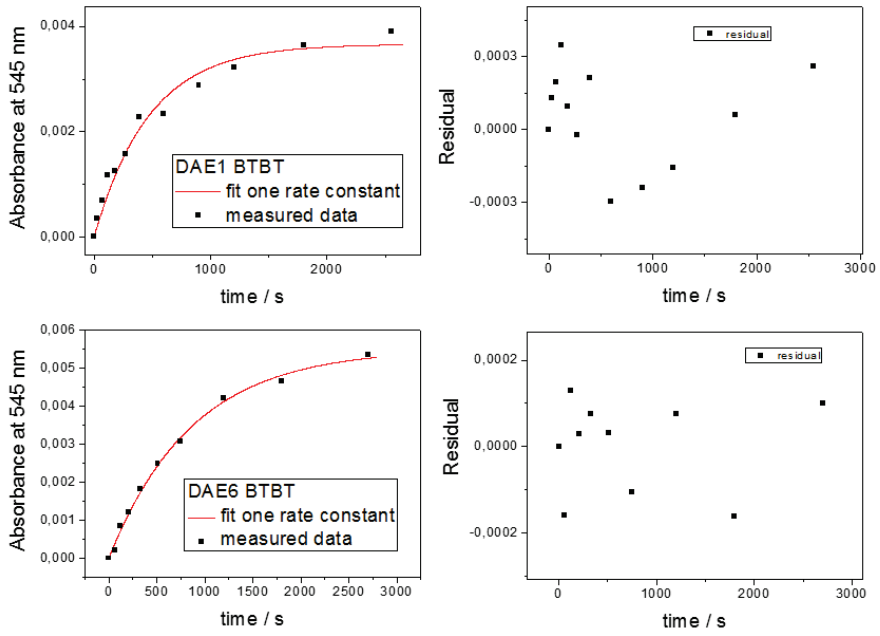

Figure 8.7 Absorption (left) and corresponding residuals (right) of BTBT blends as function of irradiation time (Red circles = measured data, black line = fit). Images on top correspond to DAE_1 blend with BTBT and the ones on the bottom correspond to DAE_6 blend with BTBT.

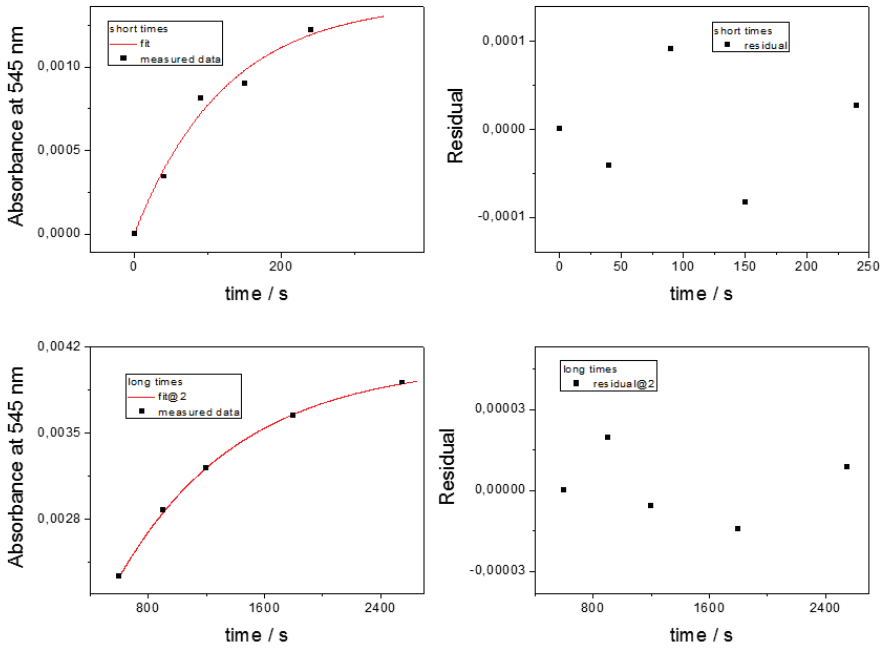

Figure 8.8 Absorption (left) and corresponding residuals (right) of DAE_1 blended in BTBT as function of irradiation time with the start (top) and end (bottom) of the trace in Figure 8.7 analyzed separately (Red circles = measured data, black line = fit).

Table 8.4 Rate constants for the open to closed isomerization in BTBT blends.

	-k1	-k2
DAE_6/BTBT	0.00050 Abs/s	-
DAE_1/BTBT	0.00051 Abs/s	0.0035 Abs/s

8.4.2.3 UV-vis absorption

To investigate if the incorporation of DAE into P3HT alters the molecular packing of P3HT molecules, we performed UV-vis absorbance spectra on films of pure P3HT and blends with DAE_6 (see Figure 8.9). It is evident from these spectra that the presence of DAE_6 does not affect the spectra envelope. Here we note that the absorbance spectrum of P3HT blend with DAE_1o was not performed since it is reported elsewhere[14] and it is similar to the one for the blend with DAE_6o (red plot).

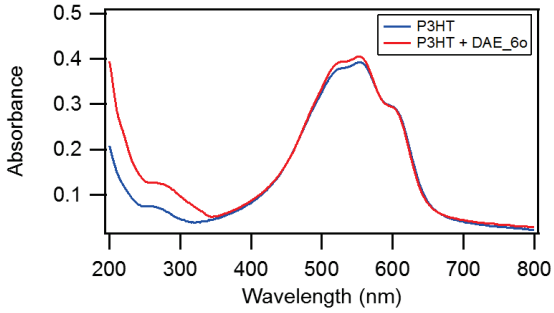

Figure 8.9 UV-vis absorbance spectra of P3HT and P3HT blend with DAE_6o films.

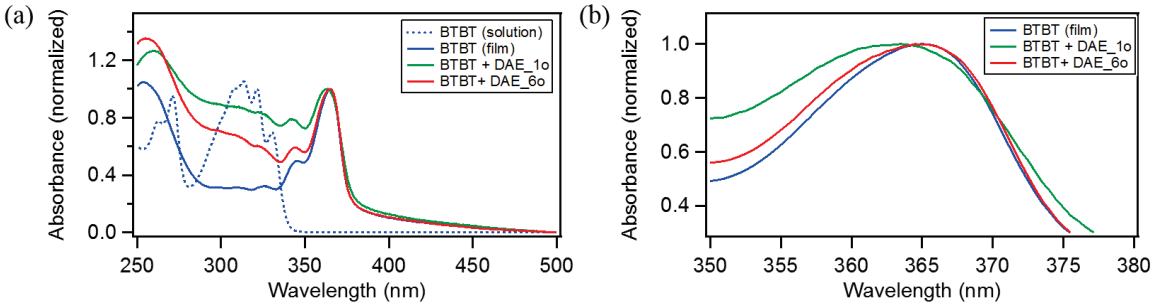

Figure 8.10 (a) UV-vis absorbance spectra of pure BTBT solution (dashed line) and film (solid line) and films of BTBT blend with DAE_1o and DAE_6o. (b) Zoom in of the absorbance peak at 365 nm.

Moreover, we investigated the influence of DAEs on BTBT. We performed absorption measurements on films that were prepared in the same manner as the devices. We found that DAE_6 only have a minor effect on the absorbance of BTBT as depicted in **Figure 8.10**. However, the absorption of BTBT broadens in the presence of DAE_1, indicating a possible change in packing of the molecules.

For reference, absorption spectra of films of pure DAE_1 and DAE_6 were acquired showing a maximum peak at around 546 nm (see Figure 8.11). This wavelength was selected for irradiating the devices in order to trigger the photoisomerisation from the closed to the open form.

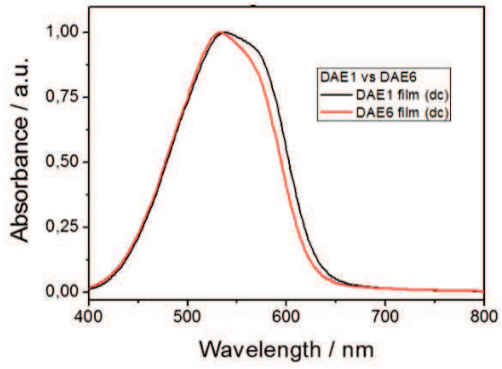

Figure 8.11 UV-vis absorbance spectra of DAE_1 (black) and DAE_6 (red) in their closed form as pristine films.

8.4.3 Electrical characterization in dark

(In the following, both DAE derivatives are in their open form and the devices did not undergo irradiation of any kind).

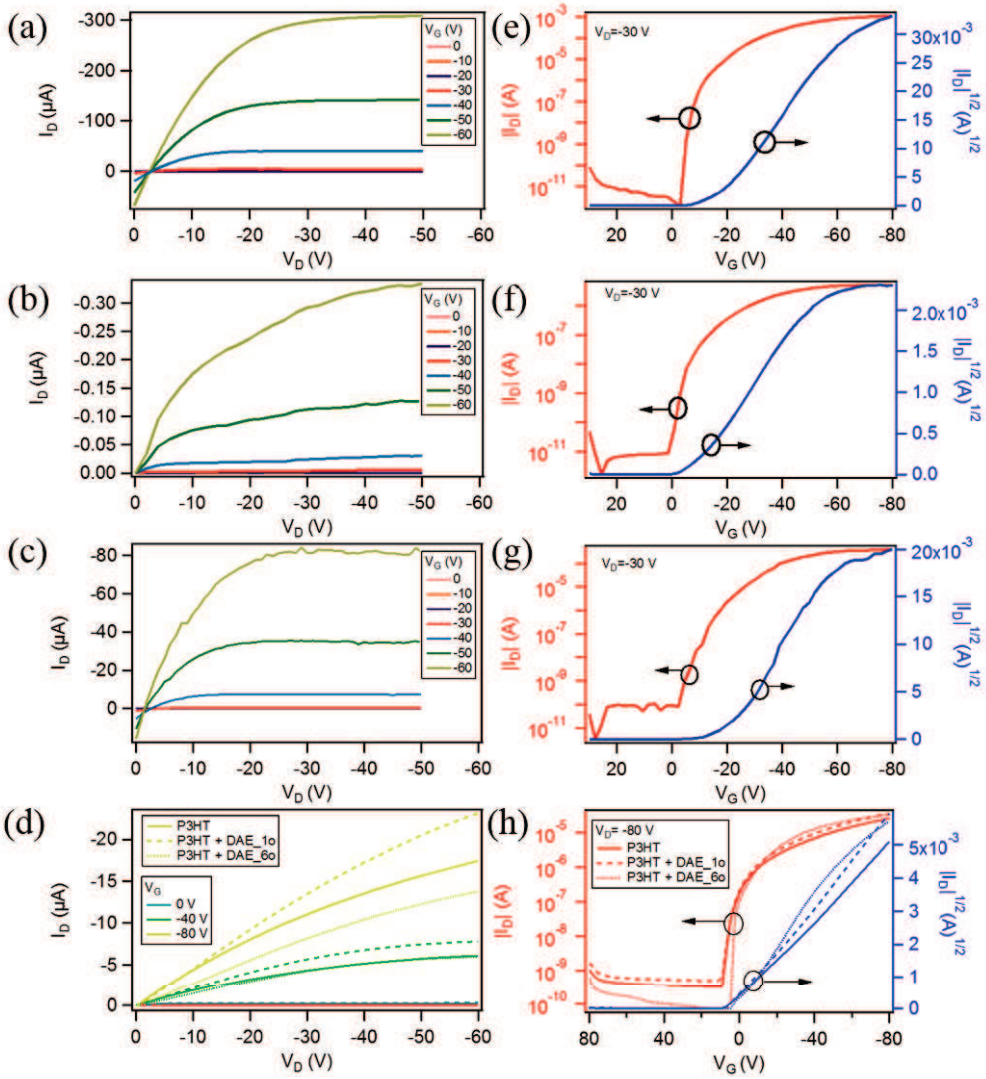

Figure 8.12 Output characteristics of devices based on: (a) pristine BTBT (L=100 μm), (b) BTBT blend with DAE_1o (L=120 μm), and (c) BTBT blend with DAE_6o (L=120 μm) along with their transfer characteristics (at V_D=-30 V) in (e), (f) and (g), respectively (Left axis in the logarithmic scale; right axis is the square root of the absolute value of the drain current. (d) Output and (h) transfer characteristics of P3HT devices (L=20 μm) blend with DAE_1o, DAE_6o and without the blend.

A comparison between the output characteristics (I_D-V_D) of bottom-gate top-contact devices based on pristine BTBT, BTBT blend with DAE_1o and DAE_6o is illustrated in **Figure 8.12a**,

b and **c**, respectively. They display typical *p*-type characteristics with good linear[27] and saturation behavior except for the blend with DAE_1o (Figure 8.12b), which shows drain currents that are not completely saturated at higher drain biases. Their corresponding transfer characteristics (I_D-V_G) are portrayed in **Figure 8.12e, f** and **g**. The relevant device performances in terms of field-effect mobility, threshold voltage and I_{on}/I_{off} are reported in **Table 8.5**. These extracted data reveal that the electronic properties of BTBT are mildly affected by the presence of DAE_6 in its open form unlike DAE_1o, which drastically decreases the field-effect mobility by two orders of magnitude as compared to the reference device (i.e. pristine BTBT). This observation is independent of the device channel length (*L)* as depicted in **Figure 8.13a** that clearly shows how μ, which almost does not vary with L, is significantly lowered by the presence of DAE_1. The latter lowers as well the I_{on}/I_{off} and affects the threshold voltage as observed in **Figure 8.13b** and **c** respectively. It is worth noting the poor reproducibility of the devices particularly the ones based on the blend with the DAE_1.

To further investigate whether this is due to the traps at the interface between the semiconductor and the dielectric upon addition of DAE_1 or DAE_6 to BTBT, we extracted the subthreshold swing *S* (in the transition region from the off to the on-state from the linear regime of the transfer characteristics) because it is directly proportional to the interface trap density as explained in Chapter 2. **Figure 8.13d** shows that *S* is independent (considering the error bars) of the channel length and of the presence of the photochromic molecules indicating that the addition of DAEs to BTBT do not induce additional traps at the dielectric/semiconductor interface.

Table 8.5 Extracted field-effect mobility (μ), threshold voltage (V_{Th}) and I_{on}/I_{off} for BTBT based devices (BG-TC with L=120 µm) (from the saturation regime at V_D=-30 V) and P3HT based devices (BG-BC with L=20 µm) (from the saturation regime at V_D=-80 V) which output and transfer characteristics are displayed in **Figure 8.12**.

	µ [$cm^2 \cdot V^{-1} \cdot s^{-1}$]	V_{Th} [V]	I_{on}/I_{off}
BTBT	0.64	-17.2	~10^6
BTBT + DAE_1o	4.32 x 10^{-3}	-8.5	~3 x 10^4
BTBT + DAE_6o	0.21	-21.24	~4 x 10^6
P3HT	1.02 x 10^{-3}	1.86	~3 x10^4
P3HT + DAE_1o	1.44 x 10^{-3}	1.50	~2 x 10^4
P3HT + DAE_6o	1.86 x 10^{-3}	2.75	~5 x 10^4

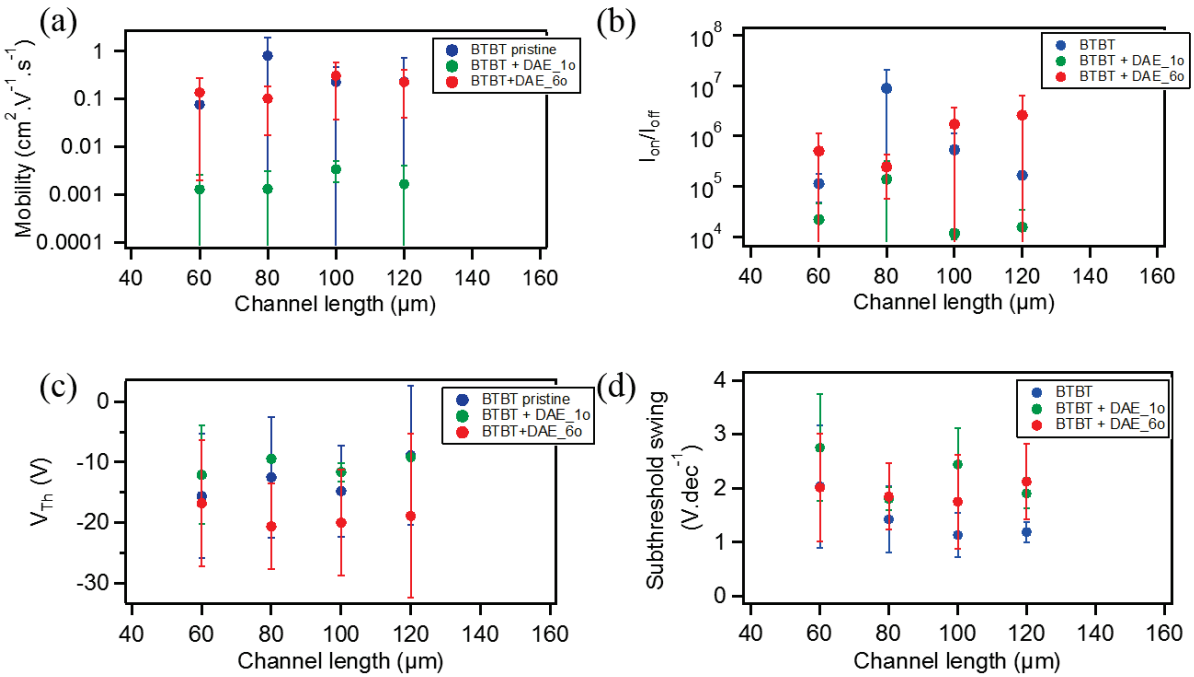

Figure 8.13 Variation of (a) the field-effect mobility (left axis in the logarithmic scale), (b) the threshold voltage (c) the I_{on}/I_{off} and (d) the subthreshold swing with the channel length of OFETs based on pristine BTBT, BTBT blend with DAE_1o and DAE_6o. Statistics done on at least 6 devices of each channel length.

Upon blending of both DAEs (in their open form) with P3HT, similar device characteristics as in the reference pristine P3HT were measured as reveled in the output (Figure 8.12d) and transfer characteristics (Figure 8.12h) as well as in **Table 8.5** for an OTFT with L=20 µm featuring BG-BC geometry. The average extracted parameters are reported in **Table 8.6** showing the same observation (i.e. similar device characteristics) which is in strike contrast with the results obtained with BTBT.

Table 8.6 Average values of field-effect mobility (μ), threshold voltage (V_{Th}) and I_{on}/I_{off} (from the saturation regime V_D=-80V) for bottom-gate bottom-contact un-annealed devices (L=20µm) based on pristine P3HT, P3HT blend with DAE_1o and DAE_6o. Statistics done on at least 6 devices of each channel length from different substrates.

	μ x 10^{-3} [$cm^2 \cdot V^{-1} \cdot s^{-1}$]	V_{Th} [V]	I_{on}/I_{off}
P3HT	1.05 ± 0.06	1.52 ± 1.12	~3.10^4
P3HT + DAE_1o	0.95 ± 0.22	5.05 ± 4.63	~6 x 10^4
P3HT + DAE_6o	1.33 ± 0.38	4.8 ± 4.4	~2 x 10^5

Since the fabrication of these P3HT based devices (with BG-BC geometry) did not involve any ozone treatment of the surface and any post-fabrication annealing step, we fabricated another set of TFTs with the same procedure and the same geometry (i.e. BG-TC) as the one used for the preparation of BTBT ones. Their field-effect mobility was as well almost unaffected by the presence of DAEs as depicted in **Figure 8.14**.

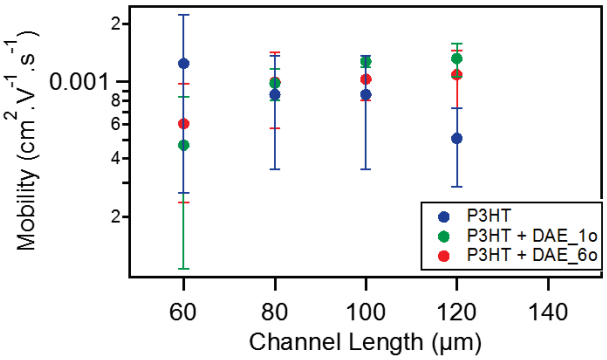

Figure 8.14 Variation of the field-effect mobility of the bottom-gate top-contact devices based on P3HT with and without the blend with DAE prepared using the same conditions as BTBT. Statistics done on at least 3 devices of each channel length from different substrates.

Such results are in line with our previous report on blends of DAE_1o with P3HT and are explained by the fact that the HOMO position of the open form is not accessible for holes and thus do not affect the charge transport.[14] This is also the case for DAE_6o bearing similar HOMO energy level as DAE_1o (see Figure 8.3). Similarly to DAE_1o, it is possible that DAE_6o is ejected from the polycrystalline domains into the amorphous regions of P3HT. Moreover, previous reports on blends of diarylethene with a small molecule such as pentacene, showed that the HOMO level of the open ring isomer of another DAE derivative did not act as a trap level[13] which is in agreement with our results for P3HT with DAEs. However, for BTBT, the scenario is different since its HOMO level is lying close to the HOMO levels[28] of both DAEs in their open form which renders them accessible for holes (see Figure 8.3). The HOMO levels of the investigated molecules were determined by cyclic voltammetry (as detailed in the previous paragraph) instead of ultraviolet photoelectron spectroscopy because the use of the latter method was found being invasive since the photons incident on the DAE do trigger their isomerization to the closed form. Since in their open form, the π-conjugation is partially lost, one would expect a decrease of the device performance.[11, 29] This might explain the lowering

in the electrical characteristics in BTBT devices upon addition of the DAE molecules in their open form; yet this does not clarify the large difference observed between the results obtained for the blends with DAE_1o and DAE_6o considering that they have similar HOMO energy levels. It may be a different phase segregation in blends of DAE_1o with BTBT affecting the crystallinity of the latter component thereby lowering the device performance.

8.4.4 Structural and Morphological characteristics

To further cast light onto the above mentioned issue, we performed 2D grazing incidence x-ray diffraction (GIXD) measurements.

A typical diffraction pattern for spin cast BTBT is shown in **Figure 8.15**. The indexed set of peaks agrees nicely with crystal structure data previously published by H. Ebata et al[17] and the observation of high order (n>10) diffraction peaks confirms the high degree of crystallinity in fabricated thin films.

Concerning the blends, the results surprisingly revealed unaffected crystalline structures of BTBT (Figure 8.16a-c) or P3HT upon addition of the photochromic molecules (see Figure 8.16e). This is apparent by the largely unchanged peak positions (as compared to the diffraction pattern of pristine P3HT film reported in reference[14] and the amorphous nature of DAE molecules (Figure 8.16d).

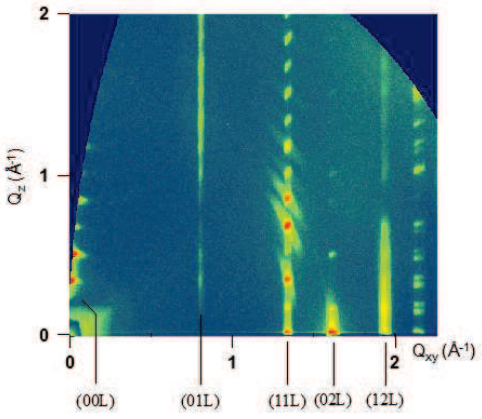

Figure 8.15 Indexed 2D GIXD pattern of a BTBT film.

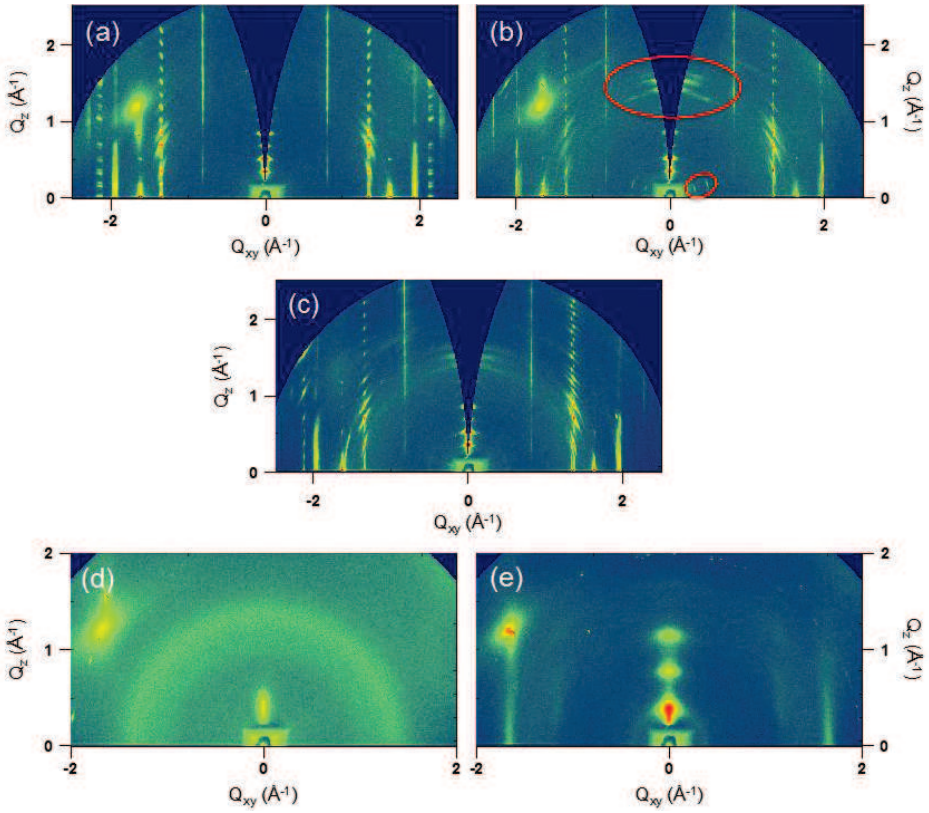

Figure 8.16 2D diffraction pattern for films of: (a) pure BTBT, (b) BTBT + DAE_1o, (c) BTBT + DAE_6o, (d) pure DAE_6o and (e) P3HT + DAE_6o.

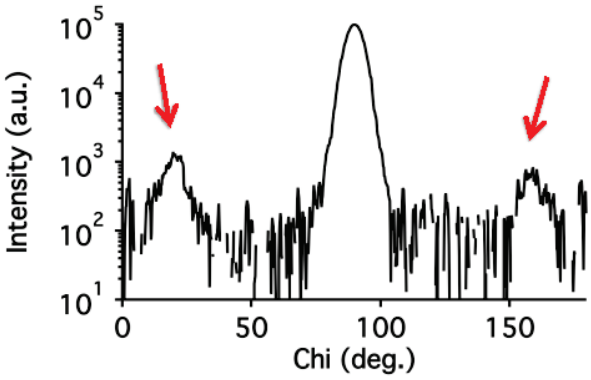

Figure 8.17 Constructed pole figure of the (003) peak intensity. Diffraction intensity from misoriented crystallites are pointed out by red arrows. Integrating the product of the intensity with the scaling factor Cos(Chi) as a function of Chi shows that 33% of BTBT crystallites are misoriented by ~70ºC.

Interestingly, only in the case of BTBT, unlike the blend with DAE_6o, the addition of DAE_1o molecules results in the appearance of two new diffraction peaks at low *q* values and three at

higher q_z, as highlighted in **Figure 8.16b**. Analysis shows that these peaks correspond to the (002) and (003) reflections (for low q) and (114), (115) and (116) of BTBT crystals that are oriented ~70^o from edge-on. From the constructed pole figures for the (003) peak (Figure 8.17), we found that ~33% of BTBT crystallites are oriented in this manner, which is a rather large fraction. Although, the exact locations of these misoriented crystallites couldn't be confirmed. If they resided at the substrate-film interface, they may act as insulating regions since the alkyl chains are now oriented close to parallel to the substrate. These misoriented crystals affect dramatically the charge carrier mobility thereby lowering the device performance and particularly the hole mobility of BTBT/DAE_1o blends compared to that of BTBT and BTBT/DAE_6o blends. In fact, this particular effect of DAE_1 on BTBT was also noticed in the absorbance spectra showing a slight blue shift about 4 nm of the BTBT peak (Figure 8.10b).

AFM investigation on the sub-micrometer scale (Figure 8.18) did not reveal a difference in the morphology in films of BTBT (Figure 8.16a) when blended with neither DAE_6o (Figure 8.18b) nor DAE_1o (Figure 8.18c). Topography image of BTBT (Figure 8.18a) shows that it crystallizes in two different manners. It forms a thin crystalline layer ranging from ~10 to 20 nm in height and thicker crystals of 100 up to 250 nm in height. In the presence of DAE_6o, larger BTBT crystals are obtained as depicted in **Figure 8.18b** that shows a thin layer (of 20 to 30 nm of height) beside the large crystals (with a height ranging from 50 to 70 nm) which are decorated with bumps of few hundreds of nm height. The same was observed for the blend with DAE_1o (Figure 8.18c). Nevertheless, we couldn't get any clear evidence of different phase segregation between the blends with DAE_1o and DAE_6o since they have similar phase images (Figure 8.18f and g).

As for P3HT with DAE_6 (Figure 8.18d and h), the topography image is similar to the one reported for the blend with DAE_1o and pure P3HT.[14]

For the films of pure DAE derivatives (which AFM images are reported in Figure 8.19a for DAE_1 and Figure 8.19b for DAE_6), a different wettability of the substrate was observed with a higher tendency of DAE_1 to self-aggregate as compared to DAE_6.

To this end, we can therefore conclude that the perturbation on the crystals or phase segregation is on a scale below 15 nm that is more easily accessible by GIXD than by AFM. This behavior was similarly detected for blends of P3HT with DAE_6o.

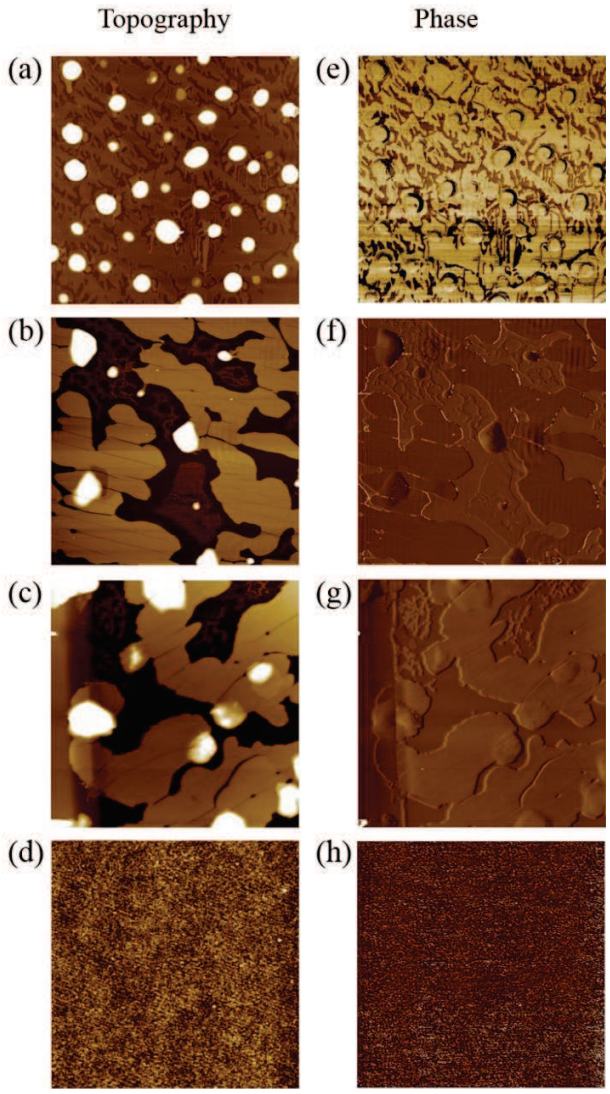

Figure 8.18 AFM topography images of films of (a) BTBT, (b) BTBT blend with DAE_6o, (c) BTBT blend with DAE_1o and P3HT blend with DAE_6o (for (a), (b) and (c) Z scale=150 nm and image size is 65 x 65 µm. For (d) Z scale=4 nm and image size is 5 x 5 µm). (e), (f) (g) and (h) are their corresponding phase images respectively.

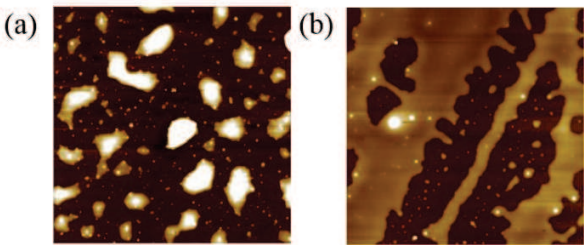

Figure 8.19 AFM topography images of pristine (a) DAE_1o and (b) DAE_6o prepared by drop-casting on ozone treated SiO_x substrates (Z scale=2 µm and image size is 65 x 65 µm) showing different surface wettability.

8.4.5 Photoswitching

We extended our study to the effect of the light irradiation at different wavelengths on the drain current. Concerning this part, only P3HT based devices with BG-TC geometry were considered for the comparison with BTBT based devices. That is because they feature the same geometry and the same preparation procedure (i.e. ozone treatment of the substrate and annealing after the deposition of the semiconductor).

Figure 8.20 shows the change in the drain current (normalized) at fixed gate (V_G=-80V) and drain biases (V_D=-10V) as a function of the irradiation sequence. Upon exposure to successive illumination of UV light (λ=365 nm) divided into 3 steps of 90 sec, 2 min and 10 min, the maximum drain current of the BG-TC P3HT based TFTs decreases consecutively at each step and reaches a maximum decrease of 68 % for the blend with DAE_1 and 22 % for DAE_6 as depicted in **Figure 8.20a**.

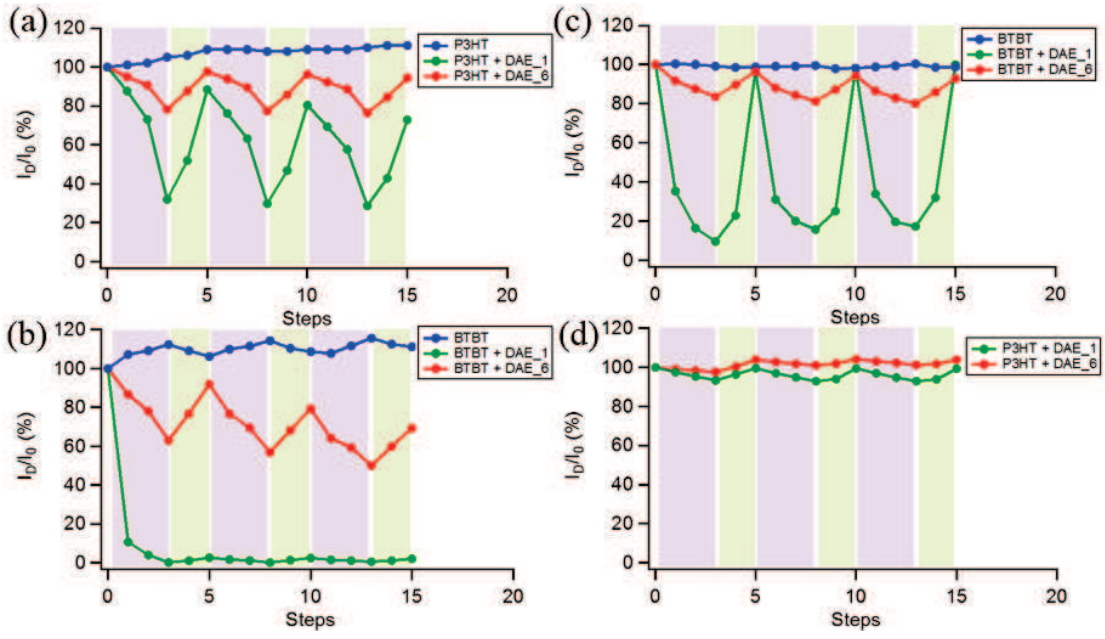

Figure 8.20 Repeated switching cycles. The normalized maximum drain current extracted from the transfer characteristics at fixed gate (V_G=-80 V) and drain biases (V_D=-10 V) is plotted in function of the irradiation sequence. Comparison between the photoswitching of: (a) P3HT based TFTs and (b) BTBT based devices for long UV irradiation time. (c) and (d) compare the photoswitching of BTBT and P3HT based TFTs respectively for a short UV irradiation time. In all the graphs, light violet and light green shaded areas correspond to the irradiation with light at wavelengths of 365 nm and 546 nm respectively. All the devices irradiated feature BG-TC geometry.

This is due to the fact that at this wavelength photoisomerisation from the open to the closed form occurs. As a consequence, the energy difference (ΔΦ) between the HOMO levels of the host and guest molecules is now an intragap level for the holes transported in the semiconductor layer (Figure 8.3); once there, the charges are trapped[13] in a shallower (for P3HT) or deeper (for BTBT) energy level. As for the large difference in the current modulation considering both DAE derivatives that have similar HOMO energy levels in the closed form, we attribute it to the difference in their interaction with P3HT and the possibility of different phase segregation. Moreover, we found that DAE_1 possesses a higher tendency to self-aggregate as compared to DAE_6 (Figure 8.19). Consequently, we think that when a charge carrier travels from P3HT to DAE_c, it got more trapped when encountering big DAE domains rather than small ones. Upon irradiation with visible light (λ=546 nm for 12 min in total), a reversible change in the drain current was obtained and the initial characteristics of the devices were regained progressively for both P3HT films with DAE_1 and DAE_6 due to the isomerization of DAE from the closed back to the open form. The photoswitching was reproducible for additional cycles alternating between UV and visible light irradiations.

For the sake of comparison with previously reported results,[14] we also tested P3HT based devices with BG-BC geometry (that were prepared without ozone treatment of the surface and without annealing). Upon exposure to successive illumination with UV light (λ=365 nm), a maximum decrease of the drain current by 60 % was obtained for the blend with DAE_1 and by 20 % for DAE_6 as depicted in **Figure 8.21**. These devices showed comparable trend obtained for the current modulation under illumination as the BG-TC ones (shown in Figure 8.20a) and similar to the ones reported for P3HT with DAE_1.[14]

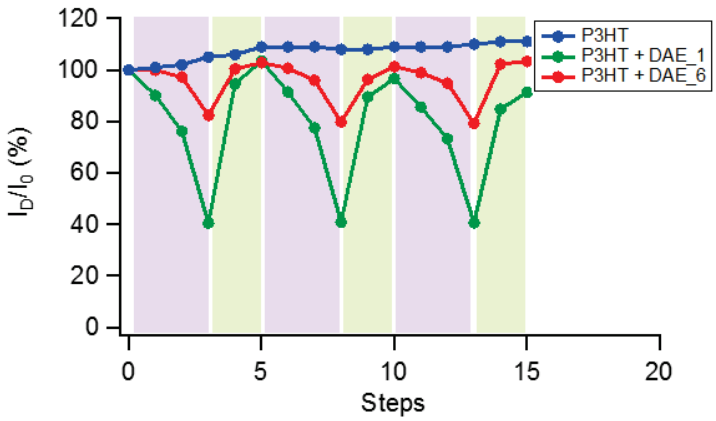

Figure 8.21 Repeated switching cycles under illumination with λ=365 nm (violet shades) and λ=546 nm (green shades). The normalized maximum drain current extracted from the transfer characteristics at fixed gate (V_G=-80 V) and drain biases (V_D=-10 V) is plotted in function of the irradiation sequence for P3HT based TFTs with L=20 µm.

As for BTBT blends with DAE_6 and DAE_1, the decrease of the current upon UV illumination (for 12 min in total) was by 40 % and almost 100 %, respectively (Figure 8.20b). This is indicative of deeper traps for holes due to higher ΔΦ with BTBT as compared to P3HT. Therefore, DAEs in their closed form act as shallow traps with P3HT and deep traps with BTBT in agreement to what was predicted for F8BT.[30] Comparing both DAEs, the trend in the current variation is similar to the one for the blends with P3HT but with higher modulation. Surprisingly, upon irradiation with visible light, the photo-switching was only reversible for BTBT+DAE_6 (with a gradual decrease of the drain current with repeated switching) (Figure 8.20b). A possible explanation for this could be that the molecules of DAE_1 within the network of BTBT are sterically hindered in their switching process, thus preventing a reversible process. In fact it was demonstrated by Irie's group that the photochromism of DAEs is environment dependent[31] as also shown by other studies.[32-33]

Here we note, that for the pristine P3HT and BTBT, a small increase of the drain current was observed during irradiation with either UV or visible light (Figure 8.20a and b blue plots) originating from the photo-generated carriers.

To gain further insight into the photo-switching of DAE and particularly on its irreversibility for DAE_1 blends with BTBT, we determined the isomerization quantum yield for the transition

from the closed to the open form in films of BTBT and P3HT (Table 8.3; the determination of the isomerization quantum yield is detailed in the experimental part).

We found that the isomerization quantum yield in the films is lower than in solution but still high enough for all blends to impose no practical problem of photoswitching in the TFT device. The quantum yield was higher in P3HT as compared to BTBT for both DAE derivatives and higher in the presence of the tert-butyl group in DAE_6 as compared to DAE_1 (see Table 8.3). Yet, due to the unexpected behavior of BTBT+DAE_1 and in order to regain the initial device characteristics upon irradiation with the visible light, we optimized the UV-irradiation time which was decreased by limiting it to a maximum of 30 sec (in 3 steps of 10 sec each). The same irradiation procedure was followed upon irradiation with visible light. Interestingly, BTBT+DAE_1 showed a reproducible and large (maximum variation up to 90 %) modulation of the drain current (Figure 8.20c) and only a small drain current modulation (by 20 %) for BTBT+DAE_6.

This large difference in the electronic properties cannot be explained purely by energetic, the rate constant for the open to closed isomerization in BTBT blends were examined. For DAE_1 two rate constants were needed to satisfactorily explain the isomerization, whereas only one was needed to explain the isomerization of DAE_6 blended with BTBT (Table 8.4). Of the two rate constants fitted to the DAE_1 isomerization, one was very similar to the DAE_6 one, and the other was considerably faster. This indicates that DAE_1 is present in two different environments inside the blend and that one of these environments is similar to that experienced by DAE_6. This explains the faster switching rate of BTBT+DAE_1 devices and also, if the second environment experienced by DAE_1 is more blended in the BTBT matrix, the higher modulation amplitude. This theory also supports the conclusions on different morphologies from the GIXD data.

In contrary to the BTBT blended devices, the current modulation for P3HT blends was very low (less than 10% for both DAE_1 and 3% for DAE_6 with P3HT, Figure 8.20d) at this short UV irradiation time. This proves that the investigated DAEs interact differently with the hosting matrix depending on the substituents and on their hosting environment. It should be noted the possibility of different dipole-dipole interaction between the host and the guest since the photoisomerisation induces a variation in the dipole moment (P) of DAE.[34] For DAE_1 the

dipole moment of the open form is 0.8 D and 2.1 D (determined experimentally)[30] while for the core without any substituents on the thiophene rings the values are 1.15 D and 2.89 D respectively.[34]

8.5 Conclusion

In summary, we extended our approach of blending photochromic molecules with a polymer to other organic semiconductors such as small molecules. In particular, by phototuning the energy-level in a bicomponent organic semiconductor, we have studied the effect of the photochromic molecules with different alkyl substituents on the electrical performance of TFTs based on P3HT and BTBT. It was found to be dramatically affected only when DAE_1o is added to BTBT. We have also demonstrated that the drain current modulation can be tuned differently depending on the energy levels of the hosting molecule whether it is a polymer or a small molecule. Additionally, the morphology of the blend can also be a factor. These findings are attractive for the development of optically controlled devices for potential applications in optoelectronics.

8.6 References

[1] H. Dong, H. Zhu, Q. Meng, X. Gong, W. Hu, *Chem. Soc. Rev.* **2012**, *41*, 1754.
[2] Q. Sun, G. Dong, L. Wang, Y. Qiu, *Sci. China Chem.* **2011**, *54*, 1017.
[3] B. Lucas, T. Trigaud, C. Videlot-Ackermann, *Polym. Int.* **2012**, *61*, 374.
[4] K.-J. Baeg, M. Binda, D. Natali, M. Caironi, Y.-Y. Noh, *Adv. Mater.* **2013**, *25*, 4267.
[5] S. Kawata, Y. Kawata, *Chem. Rev.* **2000**, *100*, 1777.
[6] R. C. Shallcross, P. Zacharias, A. Köhnen, P. O. Körner, E. Maibach, K. Meerholz, *Adv. Mater.* **2013**, *25*, 469.
[7] E. Orgiu, P. Samorì, *Adv. Mater.* **2014**, DOI: 10.1002/adma.201304695.
[8] T. Tsujioka, M. Irie, *Journal of Photochemistry and Photobiology C: Photochemistry Reviews* **2010**, *11*, 1.
[9] M. Irie, *Chem. Rev.* **2000**, *100*, 1685.
[10] K. Matsuda, M. Irie, *Journal of Photochemistry and Photobiology C: Photochemistry Reviews* **2004**, *5*, 169.
[11] R. Hayakawa, K. Higashiguchi, K. Matsuda, T. Chikyow, Y. Wakayama, *ACS Appl. Mater. & Interfaces* **2013**, *5*, 3625.

[12] C. Sciascia, R. Castagna, M. Dekermenjian, R. Martel, A. R. Srimath Kandada, F. Di Fonzo, A. Bianco, C. Bertarelli, M. Meneghetti, G. Lanzani, *J. Phys. Chem. C* **2012**, *116*, 19483.
[13] M. Yoshida, K. Suemori, S. Uemura, S. Hoshino, N. Takada, T. Kodzasa, T. Kamata, *Jpn. J. Appl. Phys.* **2010**, *49*, 04DK09.
[14] E. Orgiu, N. Crivillers, M. Herder, L. Grubert, M. Pätzel, J. Frisch, E. Pavlica, D. T. Duong, G. Bratina, A. Salleo, N. Koch, S. Hecht, P. Samorì, *Nat Chem* **2012**, *4*, 675.
[15] C. A. Di, D. Wei, G. Yu, Y. Liu, Y. Guo, D. Zhu, *Adv. Mater.* **2008**, *20*, 3289.
[16] H. H. Henrichsen, P. Bøggild, *Microelectron. Eng.* **2010**, *87*, 1120.
[17] H. Ebata, T. Izawa, E. Miyazaki, K. Takimiya, M. Ikeda, H. Kuwabara, T. Yui, *J. Am. Chem. Soc.* **2007**, *129*, 15732.
[18] P. S. Jo, A. Vailionis, Y. M. Park, A. Salleo, *Adv. Mater.* **2012**, *24*, 3269.
[19] Y. Yuan, G. Giri, A. L. Ayzner, A. P. Zoombelt, S. C. B. Mannsfeld, J. Chen, D. Nordlund, M. F. Toney, J. Huang, Z. Bao, *Nat Commun* **2014**, *5*, DOI:10.1038/ncomms4005.
[20] H. Minemawari, T. Yamada, H. Matsui, J. y. Tsutsumi, S. Haas, R. Chiba, R. Kumai, T. Hasegawa, *Nature* **2011**, *475*, 364.
[21] T. Uemura, Y. Hirose, M. Uno, K. Takimiya, J. Takeya, *Applied Physics Express* **2009**, *2*, 111501.
[22] K. Takimiya, H. Ebata, K. Sakamoto, T. Izawa, T. Otsubo, Y. Kunugi, *J. Am. Chem. Soc.* **2006**, *128*, 12604.
[23] S. Colella, C. Ruzié, G. Schweicher, J.-B. Arlin, J. Karpinska, Y. Geerts, P. Samorì, *ChemPlusChem* **2014**, DOI: 10.1002/cplu.201300414.
[24] G. Gauglitz, S. Hubig, *J. Photochem.* **1985**, *30*, 121.
[25] A. P. Glaze, H. G. Heller, J. Whittall, *J. Chem. Soc., Perkin Trans. 2: Physical Organic Chemistry* **1992**, 591.
[26] C. M. Cardona, W. Li, A. E. Kaifer, D. Stockdale, G. C. Bazan, *Adv. Mater.* **2011**, *23*, 2367.
[27] *Transfer characteristics show a good ohmic contact between the Au electrodes and BTBT (which features a HOMO of 5.3 eV as measured on films by ambient photoelectron spectroscopy) despite the small injection barrier.*
[28] *here we note that the absolute values of the HOMO levels of both DAEs can be higher by 0.1 eV than the values represented in Figure 3 if a different solvent is used. For instance, as per our cyclic voltammetry measurements in acetonitrile, DAE_1c has a HOMO energy of -4.784 eV whereas in dichloromethane, it was reported -4.676 eV in E. Orgiu, N. Crivillers, M. Herder, L. Grubert, M. Pätzel, J. Frisch, E. Pavlica, D. T. Duong, G. Bratina, A. Salleo, N. Koch, S. Hecht, P. Samorì, Nat Chem 2012, **4**, 675.*
[29] D. Dulić, S. J. Van Der Molen, T. Kudernac, H. T. Jonkman, J. J. D. De Jong, T. N. Bowden, J. Van Esch, B. L. Feringa, B. J. Van Wees, *Phys. Rev. Lett.* **2003**, *91*, 207402/1.
[30] J. Frisch, M. Herder, P. Herrmann, G. Heimel, S. Hecht, N. Koch, *Applied Physics A* **2013**, *113*, 1.
[31] T. Fukaminato, T. Umemoto, Y. Iwata, S. Yokojima, M. Yoneyama, S. Nakamura, M. Irie, *J. Am. Chem. Soc.* **2007**, *129*, 5932.
[32] D.-H. Kwon, H.-W. Shin, E. Kim, D. W. Boo, Y.-R. Kim, *Chem. Phys. Lett.* **2000**, *328*, 234.

[33] S. Nakamura, S. Yokojima, K. Uchida, T. Tsujioka, *Journal of Photochemistry and Photobiology C: Photochemistry Reviews* **2011**, *12*, 138.
[34] F. L. E. Jakobsson, P. Marsal, S. Braun, M. Fahlman, M. Berggren, J. r. m. Cornil, X. Crispin, *J. Phys. Chem. C* **2009**, *113*, 18396.

Chapter 9 Conclusion and Perspectives

9.1 Achievements

In summary this thesis was devoted to the study of the correlation between architecture vs. function in multicomponent materials for organic and graphene based electronics. In particular, we have explored the possibility of combining components via controlled blending in such a way that each component confers a given property to the material. The last two decades has witnessed extensive R&D endeavor on the use of organic and polymeric semiconductors as active layers for (opto)electronic applications such as light-emitting diodes, solar cells and field-effect transistors. While a continuous, yet slow, improve in the performance of these devices has been achieved, major breakthroughs appeared being a major challenge. In the last ten years 2D materials became very popular scaffolds because of their exceptional mechanical, optical and electrical properties that make them interesting for application in electronics. In this thesis we have combined the ease processability and property's chemical tunability of polymeric semiconductors with the outstanding electrical properties of graphene and related derivatives. In this framework, the following model systems have been explored when integrated in field-effect transistors (FETs): *i)* blends of graphene or graphene nanoribbons (GNRs) with polymeric organic semiconductors, *ii)* polycyclic aromatic hydrocarbons and *iii)* photochromic molecules blend with polymeric or small molecule organic semiconductor.

We have demonstrated the first *n*-type organic semiconductor blend with graphene (from liquid phase exfoliation) as a thin film for field-effect transistors. We have shown how an ambipolar behavior can be leveraged upon increasing the loads of graphene in the channel. Our approach

was not only beneficial for reducing the contact resistance but also for enhancing the device performance that was found to be correlated with the size of graphene sheets. In particular, the field-effect mobility of holes was enhanced by 45 folds for 2.5 μm channel length devices at the blend ratio 150:1 in weight of P(NDI2OD-T2) to graphene, suggesting a favourable pathway for the charge transport. The *n*-type semiconductor was also beneficial to disperse graphene within the polymer matrix. This proves that the combination of the ideal film forming ability of a polymer and the high performance of a 2D material produced by a very cheap and up-scalable technique, opens a potential application of graphene in ambipolar devices for complimentary logic circuits.

We have demonstrated the first blend of an unprecedented ultranarrow (with a width of ~ 2 nm) graphene nanoribbon (buttom-up synthesized) with a *p*-type polymeric semiconductor for thin-film transistors. We found that the addition of up to 24% of GNRs in a P3HT film enables improvement of percolation of charges in a P3HT transistor. In particular, it is possible to obtain a three-fold increase in the field-effect mobility (μ) in a P3HT device by adding 24% of GNRs to the thin film, without altering the other relevant electronic characteristics of the transistor such as the I_{on}/I_{off}, unlike graphene composites. However, this three-fold increase in μ is not outstanding because of the counter effects of the decrease in the crystalline nature in P3HT upon blending with GNRs and the formation of hundreds of nm large aggregates of GNRs. Similarly to the results obtained with graphene, we demonstrate that this carbon based materials represent a solution towards the enhancement of the performance of OFETs. Furthermore, we presented the first study under illumination of devices bearing such blend as active material. It revealed an enhanced photoresponse in the presence of GNR that was also found to be dependent on the channel length of the devices as well as on the amount of GNRs within the polymeric matrix.

We presented a study on the effect of the size and the edge functionalization of PAHs on the energy of the HOMO. We deeply investigated the electrical properties of $C_{60}Cl_{24}$ in FETs prepared by spin-coating from common organic solvents. The devices featured high I_{on}/I_{off}. Moreover, we suggested a simple method for improving the performance of the FETs.

In order to prove that an optical remote control can be added to organic field-effect transistors, we have fabricated the first high performing multifunctional FETs based on blends of photochromic molecules with small molecule organic semiconductor. The approach of blending

to introduce phototunable energy levels in the semiconducting film, was found to be applicable not only for polymeric semiconductors but also for small molecules. The electrical performance of FETs based on BTBT (small molecule) was influenced by the nature of the alkyl substituents of the DAE molecules. Additionally, we demonstrated that the drain current modulation can be tuned differently depending not only on the energy level of the hosting molecule (i.e. the polymer or the small molecule organic semiconductor), but also on the type of substituents on the photochromic molecules. Our findings present a cheap method for the development of optically controlled devices for applications in optoelectronics where graphene can serve as transparent electrodes.

9.2 Concerns and further developments

Despite all of the above mentioned advantages offered by the use of solution processed graphene, GNRs and PAHs, further research efforts in this field are required in order to gain a deep insight into the role of the size of graphene sheets, the type of edges and number of layers on the transistor's performance; particularly, their effect on the ambipolarity observed. It will be interesting to investigate whether the approach of blending graphene with an *n*-type polymeric semiconductor can be generally applicable for *n*-type small molecules. Furthermore, the addition of graphene into the organic semiconductor lowers the I_{on}/I_{off} of the device, therefore limiting its use: *i*) in applications requiring high I_{on}/I_{off}, and *ii*) as a material in the channel of a FET.

Moreover, despite its advantages for large-scale production, liquid phase exfoliation results in graphene sheets with uncontrolled sizes and thicknesses, thus affecting the reproducibility of the devices and their performances. Additionally, until now, none of the top-down approaches adopted for the production of graphene can result in sheets with controlled edges. There is a need of finding a low-cost method for solving these issues.

Once the ultimate control over the size, edges and thicknesses of graphene sheets can be obtained, it will be interesting to perform a systematic study on their influence on the electrical properties of the FETs when incorporated into the matrix of the polymer semiconductor.

Concerning the bottom-up approach, despite its advantages mainly the synthesis of GNR or PAH with controlled sizes and edges, there are still several problems that have to be solved. For example, when dispersed in organic solvents and deposited on SiO_x substrates, these carbon based materials tend to aggregate therefore forming a non-uniform film. Moreover, the use of high boiling point solvents such as *o*-DCB requires a further annealing step (to evaporate the solvent) that also leads to the aggregation of the deposited material, therefore forming scattering centers for the charge carriers thus resulting in lower performances as the ones expected or predicted theoretically. The current limit and the low μ are not because of the material properties but rather the experimental tools to deposit these carbon based structures and to fabricate the devices. It would be interesting to investigate the electrical properties of a single nanoribbon or nanographene bridging the electrodes. However, the fabrication of such devices remains a challenge.

Regarding the blends with graphene or GNR, their uncontrolled distribution within the semiconducting polymer matrix remains unsolved and it strongly influences the electrical properties as well as the reproducibility of the devices.

Finally, for the blends, a deeper investigation of the phase separation by other techniques than AFM is required. This is possible by scanning transmission X-ray spectro-microscopy that has been demonstrated to be a powerful tool for studying blends of organic components.[1]

9.3 Future of organic electronics and graphene materials

The key issue for graphene as a channel material is the zero band gap. Therefore, in the near future we do not expect to see FETs based on graphene active layers, in commercial high performance logic circuits. On the other hand, the research must be directed towards other routes exploiting the unique properties of this wonder 2D material.

For example, the electrical and optical requirements of transparent electrodes can be met in graphene paving the way for its application on flexible and fully transparent substrates that might revolutionize our future life.

Additionally, graphene can be a promising material for energy storage[2] and can be used in high-performance supercapacitors,[3] that can be scaled-up in the future for applications in electric vehicles. In the next few years, it is expected to implement graphene in touch screens or as passive component in integrated circuits.

The success obtained in isolating graphene layers and the intensive efforts devoted for studying this material have opened new horizons for extending these studies into other layered materials which blossomed in the last few years. For example, monolayers of boron nitride and molybdenum disulfide are among the future 2D materials beyond graphene as they are expected to be better than graphene for many applications and will be more likely present in the future technology.

To this end, as chemists continue to synthesize, tailor and improve organic and hybrid materials for use in electronic devices, and as long as physicists work on developing these devices, the field of organic electronics will likely expand in ways not even imaginable today. One can imagine electronic skin which mimics human skin with its tactility,[4] or windows with transparent solar panels[5] powering homes, office buildings or even airplanes; wearable electronics and some other applications that cannot be even foreseen.

9.4 References

[1] B. Watts, C. R. McNeill, J. Raabe, *Synth. Met.* **2012**, *161*, 2516.
[2] http://www.technologyreview.com/view/521651.
[3] X. Zhou, M. Wang, J. Lian, Y. Lian, *Sci. China Technol. Sci.* **2014**, *57*, 278.
[4] B. C. K. Tee, C. Wang, R. Allen, Z. Bao, *Nat Nano* **2012**, *7*, 825.
[5] R. Betancur, P. Romero-Gomez, A. Martinez-Otero, X. Elias, M. Maymo, J. Martorell, *Nat Photon* **2013**, *7*, 995.

Appendix A

A.1 Synthesis of DAE_6

General synthetic and analytical methods

Solvents and commercial starting materials were used as received. 1,2-Bis(5-chloro-2-methylthiophen-3-yl)cyclopent-1-ene was prepared as described in the literature.[1] THF was distilled under argon atmosphere over sodium prior to use. Column chromatography was carried out with silica gel (0.035–0.070 mm, 60 Å) using eluents as specified. All experiments involving light-sensitive compounds were carried out in the dark under red light. NMR spectra were recorded on a 500 MHz (125.8 MHz for ^{13}C) Bruker AV 500 or on a 300 MHz (75.6 MHz for ^{13}C) Bruker DPX 300 spectrometer at 25 °C using residual protonated solvent signals as internal standards (^{1}H: $\delta(CHCl_3)$ = 7.26 ppm and ^{13}C: $\delta(CHCl_3)$ = 77.16 ppm). UPLC/MS was performed with a Waters UPLC Acquity equipped with a Waters LCT Premier XE Mass detector for UPLC-HR-MS, with Waters Alliance systems (consisting of a Waters Separations Module 2695, a Waters Diode Array detector 996 and a Waters Mass Detector ZQ 2000).

1-Bromo-3,5-di-tert-butylbenzene

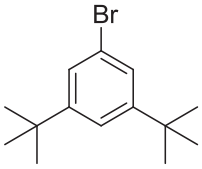

Following a literature procedure,[2] 1,3,5-tri-*tert*-butylbenzene (3.70 g, 15.0 mmol) was dissolved in 7.5 mL of CCl_4. To this solution iron powder (0.92 g, 16.5 mmol, 1.1 eq.) was added and the mixture was cooled to 0 °C. Bromine (1.62 mL, 31.5 mmol, 2.1 eq.) was added dropwise and the resulting mixture was stirred at room temperature for 18 h. Then the mixture was poured into 100 mL of water and extracted with 3x 25 mL of CH_2Cl_2. The combined organic phases were washed with sat. $Na_2S_2O_3$-solution, dried over $MgSO_4$, and evaporated. The residue was taken up in petrol ether, filtered through a pad of silica gel eluting with petrol ether and evaporated affording a colorless liquid. The crude product was distilled under reduced pressure (20 mbar) and fractions boiling at 140 – 150 °C were collected. The material was dissolved in a small amount of petrol ether and stored in a freezer overnight yielding 1-bromo-3,5-di-*tert*-butylbenzene (1.43 g, 5.3 mmol, 36 %) as colorless crystals.

^{1}H-NMR: ($CDCl_3$, 300 MHz): δ (ppm) = 7.34 (s, 3 H, CH_{ar}); 1.31 (s, 18 H, CH_3). **^{13}C-NMR:** ($CDCl_3$, 75.5 MHz): δ (ppm) = 153.1 (C_q); 125.9 (CH); 122.3 (C_q); 121.2 (CH); 35.1 (C_q); 31.4 (CH_3).

1,2-Bis(2-methyl-5-(pinacolatoboronyl)thiophen-3-yl)cyclopent-1-ene

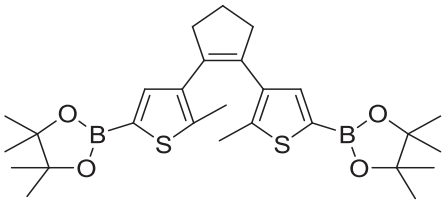

1,2-Bis(5-chloro-2-methylthiophen-3-yl)cyclopent-1-ene (0.336 g, 1.03 mmol) was dissolved in 10 mL of dry THF and cooled to 0 °C. *n*-BuLi (2.2 M in cyclohexane, 1.17 mL, 2.58 mmol, 2.5 eq.) was added dropwise and the resulting mixture was stirred at 0 °C for 30 min. 2-Isopropoxy-4,4,5,5-tetramethyl-1,3,2-dioxaborolane (0.63 mL, 3.09 mmol, 3.0 eq.) was added and the mixture was stirred further 30 min at 0 °C. Then the mixture was poured into 100 mL of sat. NH_4Cl solution and extracted 3x with 20 mL of diethylether. The combined organic phases were washed with brine, dried over $MgSO_4$, and evaporated affording the title compound (0.532 g, 1.0 mmol, quant.) as a yellow solid that was used without further purification.

^{1}H-NMR: ($CDCl_3$, 500 MHz): δ (ppm) = 7.38 (s, 2 H, CH_{ar}); 2.78 (t, $^{3}J(H,H)$ = 7.5 Hz, 4 H, CH_2); 2.02 (tt, $^{3}J(H,H)$ = 7.5 Hz, 2 H, CH_2); 1.81 (s, 6 H, CH_3); 1.32 (s, 24 H, CH_3). **^{13}C-NMR:** ($CDCl_3$, 125.8 MHz): δ (ppm) = 142.6 (C_q); 138.5 (CH); 137.7 (C_q); 134.4 (C_q); 84.0 (C_q); 39.1 (CH_2); 24.9 (CH_3); 23.1 (CH_2); 14.7 (CH_3); one C_q is not detected due to C-B coupling.

1,2-Bis(5-(3,5-di-tert-butylphenyl)-2-methylthiophen-3-yl)cyclopent-1-ene ***DAE_6o***

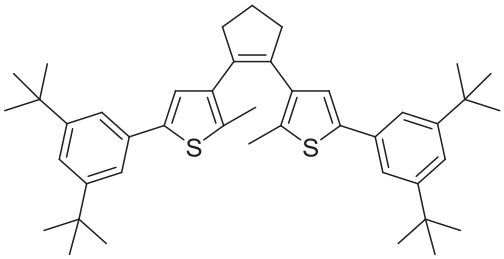

Into a Schlenk tube equipped with a teflon screw cap was put 1,2-bis(2-methyl-5-(pinacolatoboronyl)thiophen-3-yl)cyclopent-1-ene (425 mg, 0.83 mmol), 1-bromo-3,5-di-*tert*-butylbenzene (670 mg, 2.49 mmol, 3 eq.), $Pd(OAc)_2$ (9 mg, 0.04 mmol, 0.05 eq.), SPhos (34 mg, 0.08 mmol, 0.1 eq.), and K_3PO_4 (705 mg, 3.32 mmol, 4 eq.). The tube was evacuated and refilled with argon twice. Then 3 mL of degassed toluene was added, the screw cap was closed, and the mixture was stirred at 100 °C for 6 h. After cooling to room temperature the mixture was diluted with ethyl acetate and filtered through a pad of Celite eluting with ethyl acetate. The filtrate was evaporated and purified by column chromatography (petrol ether) affording **DAE_6o** (148 mg, 0.23 mmol, 28 %) as a white solid.

^{1}H-NMR: ($CDCl_3$, 500 MHz): δ (ppm) = 7.33 – 7.31 (m, 6 H, CH_{ar}); 7.02 (s, 2 H, CH_{ar}); 2.89 (t, $^{3}J(H,H)$ = 7.5 Hz, 4 H, CH_2); 2.11 (tt, $^{3}J(H,H)$ = 7.5 Hz, 2 H, CH_2); 2.06 (s, 6 H, CH_3); 1.33 (s, 36 H, CH_3). **^{13}C-NMR:** ($CDCl_3$, 125.8 MHz): δ (ppm) = 151.3 (C_q); 140.9 (C_q); 136.7 (C_q); 134.9 (C_q); 134.1 (C_q); 133.9 (C_q); 124.0 (CH); 121.5 (CH); 120.1 (CH); 38.5 (CH_2); 35.0 (C_q); 31.6 (CH_3); 23.2 (CH_2); 14.6 (CH_3). **HRMS (ESI^+):** m/z = 636.378 (M^+, calcd. 636.382 for $C_{43}H_{56}S_2^+$).

A.2 Transfer characteristics after irradiation

A.2.1 Bottom-gate bottom-contact FETs

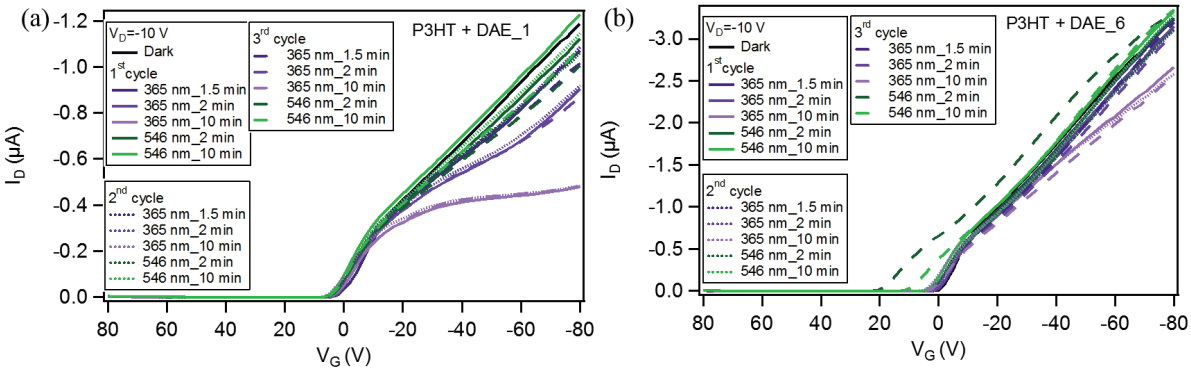

Figure A.1 Transfer characteristics (at V_D=-10 V) of BG-BC P3HT devices with L=20 µm based on the blend with (a) DAE_1 and (b) DAE_6 measured after irradiation with either UV or visible light for many cycles. Similar trend was obtained for BG-TC devices.

A.2.2 Bottom-gate top-contact FETs

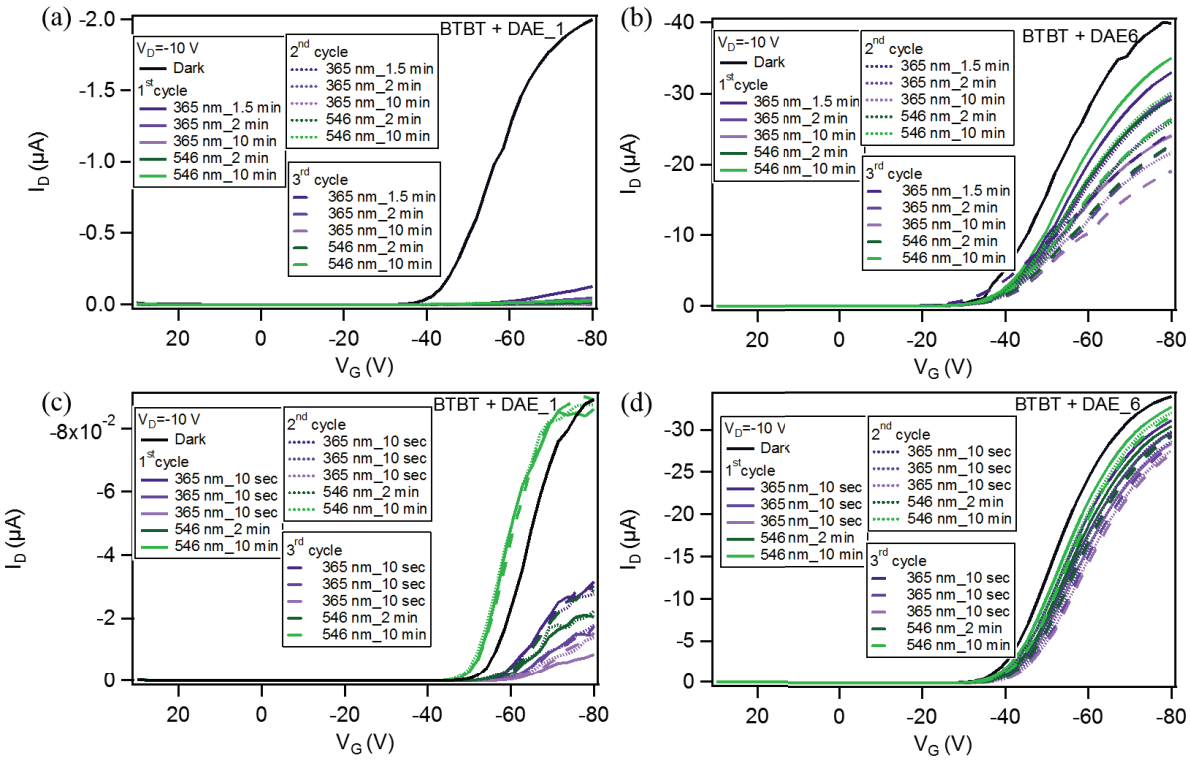

Figure A.2 Transfer characteristics (at V_D=-10 V) of BG-TC BTBT devices with L=80 μm based on the blend with (a) DAE_1 and (b) DAE_6 measured after irradiation with either UV or visible light for many cycles. (c) and (d) are the transfer characteristics of other BTBT based devices with DAE_1 and DAE_6 featuring the same channel length (L=80 μm) tested in the same manner except that the exposure time to UV irradiation was reduced to 30 sec in total for each cycle.

A.3 Variation of the extracted parameters after irradiation

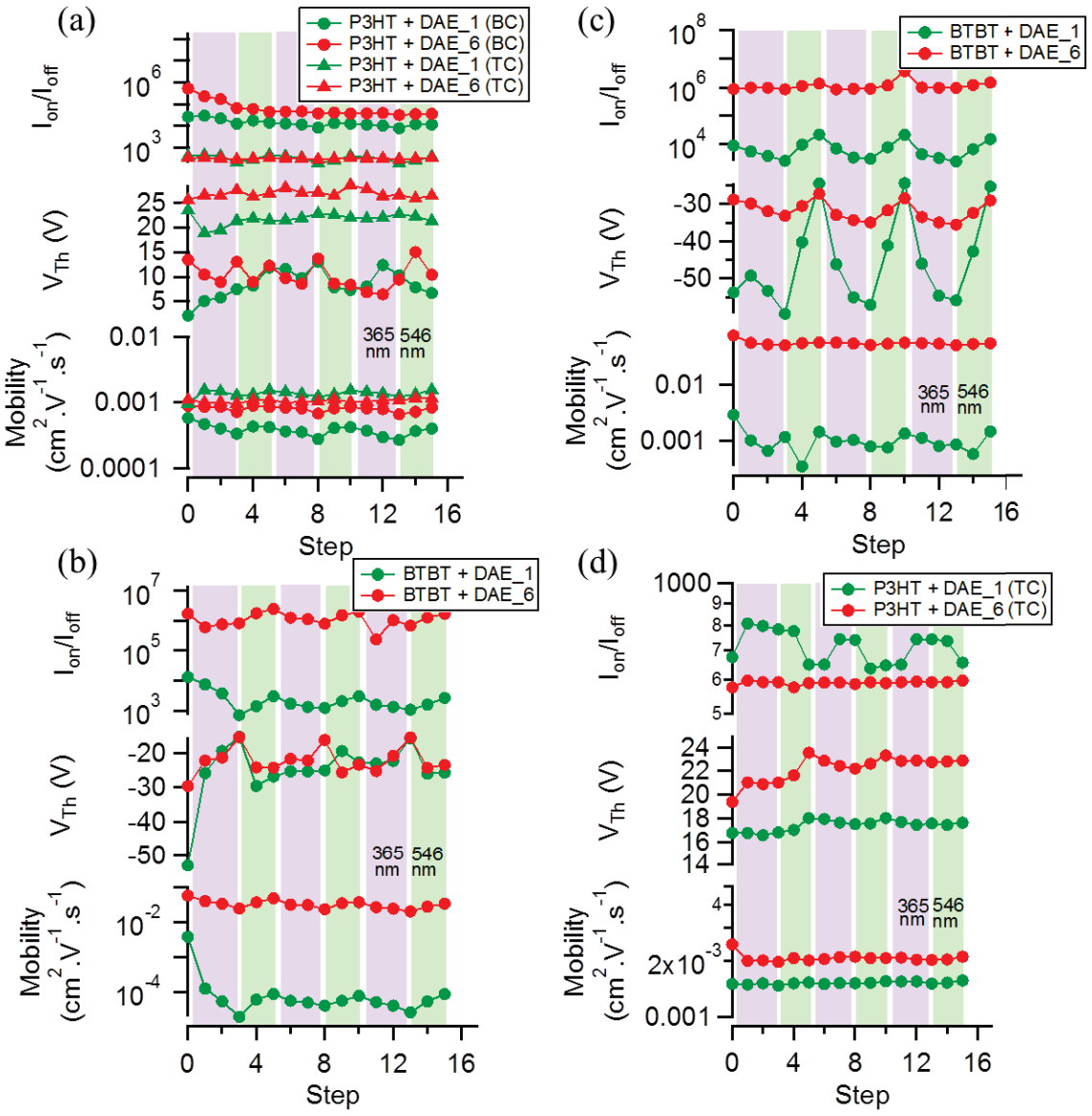

Figure A.3 Variation of the field-effect mobility, threshold voltage and I_{on}/I_{off} extracted (form the saturation regime at V_D=-30 V) at each illumination step for the devices discussed in the main text in Figure 8.10. (a) and (b) are for blends with P3HT (with two different geometries: BG-BC with L=20 µm and BG-TC with L=80 µm) and with BTBT (L=80 µm) for a long UV irradiation time. (c) and (d) are for devices (L=80 µm) based on blends with BTBT and P3HT (only TC) respectively for a short UV irradiation time.

A.4 References

[1] L. N. Lucas, J. J. D. De Jong, J. H. Van Esch, R. M. Kellogg, B. L. Feringa, *Eur. J. Org. Chem.* **2003**, *2003*, 155.
[2] P. D. Bartlett, M. Roha, R. M. Stiles, *J. Am. Chem. Soc.* **1954**, *76*, 2349.

Acknowledgements

The past few years at the Institute of Sciences and Supramolecular Engineering (ISIS) at the University of Strasbourg were very special to me. Not only because I was able to learn a lot, but also because I have fulfilled my desire and worked hard to achieve my goals. This was not possible without many people including my supervisor, the groups that I collaborated with, my colleagues, my friends and my family who directly or indirectly helped me and supported me with this thesis.

I am highly indebted to Prof. Paolo Samorì for giving me the opportunity to perform this PhD at the Nanochemistry laboratory within his group. I would also like to thank him for his patience, guidance, continuous support, supervision and for proofreading my thesis. I am deeply grateful to him for providing me the "Marie Curie" fellowship by the European commission (ITNs GENIUS (PITN-GA-2010-264694)) and for giving me the chance to perform a secondment at the University of Cambridge (in the United Kingdom), to attend several workshops and to participate in many conferences all over Europe.

I also appreciate Prof. Fabio Biscarini, Dr. Stéphane Campidelli and Dr. Stéphane Berciaud for taking their time to read my thesis and for being in my defense committee.

I would like to thank all my co-workers (members of the Nanochemistry laboratory) for making the past three years pleasant. Particularly, Dr. Emanuele Orgiu for the fruitful discussions and his suggestions. My deep gratefulness goes to Dr. Artur Ciesielski for the great friendship, his encouragements, interesting conversations, technical support, comments on my work, the theoretical calculations for the Polyaromatic Hydrocarbons and so many things that are impossible to list. Special thanks goes as well to Dr. Karl Börjesson for performing all the spectroscopy study for the blend with the photochromic molecules. It was a great pleasure

working with him. Many thanks to Dr. Oliver Fenwick for the discussions, for answering my questions and for explaining some concepts in physics. Dr. Marco Gobbi and Dr. Alexander Klekachev are also acknowledged for the valuable discussions. I also thank Dr. Mohamed El Garah for the nice time we spent in the lab. I would like to express my deep gratitude to Sébastien Haar, who performed the exfoliation and the UV-vis spectroscopic characterization of graphene. I also appreciate his friendship as he made my stay enjoyable and unforgettable. I would like to thank him for the great teamwork, for all the funny moments we shared, the delicious croissants in the mornings and for the walks. I also thank him for all his advices on a personal level and his help whenever I needed it.

I would like to express my deep gratefulness to the former members of the Nanochemistry laboratory from whom I learnt several techniques. I want to express my deep appreciativeness especially to Dr. Matthias Treier for guiding my first steps in the fabrication and characterization of devices as well as data analysis and interpretation. I would like to thank him also for passing his knowledge to me, particularly for teaching me how to use Igor Pro software for data analysis. From him, I learnt to work with high standards of accuracy and precision. He is also grateful for his valuable personal advices and private support especially when I went through difficult moments during my thesis.

My deep appreciations go to the former and present members of the Nanostructures laboratory, particularly to Prof. Thomas Ebbesen for his valuable advices for my job hunt. I always enjoyed our chats in the tram or during the social events. I would like to thank as well Dr. Eloïse Devaux for the training and Dr. Benedikt Stein for the support on the Scanning Electron Microscope.

I have been very privileged to collaborate with some of the leading researchers in the world. Many thanks to the group of Prof. Klaus Müllen (at Max-Planck Institute for Polymer Research, in Germany) and particularly to Dr. Xinliang Feng and Dr. Akimitsu Narita for designing, synthesizing and providing me with the graphene nanobribbons and polyaromatic hydrocarbons. I would like to thank Dr. Adam Kiersnowski and Wojciech Pisula who performed GIXD measurements on the films based on the blends with graphene nanoribbons. I am indebted to the following collaborators: Dr. Ravi S. Sundaram form the group of Prof. Andrea Ferrari (at Cambridge Graphene Center, Department of Engineering, UK) for performing photocurrent mapping measurements; Georgian Melinte from the group of Dr. Ovidiu Ersen (at IPCMS,

University of Strasbourg) for the TEM characterization of graphene; Dr. Fabiola Liscio from the group of Prof. Silvia Milita (CNR, Italy) for the GIXD measurements for the blends with graphene; Dr. Christian Ruzié from the group of Prof. Yves Geerts (at Université Libre de Bruxelles, Belgium) for providing BTBT molecules; Duc Trong Duong from the group of Prof. Alberto Salleo (at Stanford University, USA) for performing the GIXD measurements on the blends with photochromic molecules; and finally Dr. Martin Herder from the group of Prof. Stefan Hecht (at Humboldt-University of Berlin) for the synthesis of DAE molecules, for the spectroscopy study and for the CV measurements for the project of the blend with photochromic molecules.

I want to express my deep gratitude to the staff of ISIS particularly, Thierry, Philippe and Fabienne.

My friends have made my life in Strasbourg a precious memory. Particular thanks for Miled for his care, the wonderful time we spent together, for cheering me up, for encouraging me and for his continuous support with chocolate marzipan that made my days sweeter. I am indebted to the Ciesielski family (Artur, Anna, Dominik and Kornelia) for the unforgettable and beautiful memories and specially for making me feel a member of their family.

I want to express my deep gratitude to my teacher, the famous artist Mr. Kazem Rezvanian, who scaled my talent and improved my skills in oil painting. He helped me relieving the stress by taking me to another world each time I paint. I am privileged to be one of his students.

Last but not least, my family members, my parents and my brothers who gave me full support during my PhD. Quitting my career and going back to the university was one of the toughest decisions I took in my life; and without my family's continuous encouragements, I would not be strong enough to achieve what I achieved.

Finally, I dedicate all my work to my uncle and grandfather, who I never had the chance to say the last goodbye because I was dedicating all my time to my work. I hope you can forgive me.

Mirella El Gemayel

List of publications

M. EL Gemayel, M. Treier, C. Musumeci, C. Li, K. Müllen and P. Samorì. *Tuning the Photoresponse in Organic Field-Effect Transistors*. J. Am. Chem. Soc., Vol. 134, Pages 2429-2433, 2012

M. El Gemayel, A. Narita, L. F. Dössel, R. S. Sundaram, A. Kiersnowski, W. Pisula, A. C. Ferrari, E. Orgiu, X. Feng, K. Müllen and P. Samorì. *Graphene nanoribbons blends with P3HT for organic electronics*. Nanoscale, 2014, DOI: 10.1039/C4NR00256C

M. El Gemayel, S. Haar, A. Schlierf, M. Georgian, O. Ersen, A. Ciesielski, V. Palermo, P. Samorì. *Leveraging the ambipolar transport in polymeric field-effect transistors via blending with liquid-phase exfoliated graphene.* Manuscript in preparation

M. El Gemayel, K. Börjesson, M. Herder, A. Salleo, Y. Geerts, S. Hecht, E. Orgiu and P. Samorì. *Tunable optical switching influenced by guest-host relationship.* Manuscript in preparation

A. Ciesielski, S. Haar, **M. El Gemayel**, H. Yang, P. May, E. Orgiu, N. Koch, C. Casiraghi and P. Samorì. *Liquid-Phase Exfoliation of Graphene Using Aliphatic Intercalating Compounds: A Supramolecular Approach.* Manuscript in preparation

S. Rao Pathipati, E. Pavlica, A. Schlierf, **M. El Gemayel**, P. Samorì, V. Palermo, and G. Bratina. *Graphene-induced enhancement of n-type mobility in perylenediimide thin films*. Manuscript in preparation

Contributed talks

M. El Gemayel, A. Narita, L. F. Dössel, R. S. Sundaram, A. Kiersnowski, W. Pisula, A. C. Ferrari, E. Orgiu, X. Feng, K. Müllen and P. Samorì. *Synthetic Arm-Chair Graphene Nanoribbon-Based Electroactive Composites*. Presented at:

- Euromat, Sevilla, Spain, 2013
- E-MRS, Strasbourg, France, 2013

Posters

M. EL Gemayel, M. Treier, C. Musumeci, C.Li, K. Müllen and P. Samorì. *Tuning the Photoresponse in Organic Field-Effect Transistors*. Presented at:

- E-MRS, Strasbourg, France, 2012
- Elecmol, Grenoble, France, 2012
- Discussion Meeting "Challenges and Prospects of Polymer Chemistry", Schluchsee, Germany, 2012
- Colloque Matériaux et Nanostructures π-Conjugués (MNPC), Obernai, France, 2011

Mirella EL GEMAYEL

Dispositifs et architectures supramoléculaires électroactives à base de graphène

Résumé

Cette thèse démontre le potentiel d'utilisation du graphène pour la fabrication de transistors à effet de champ à couche minces. Celui-ci est préparé par exfoliation en phase liquide et co-déposé avec un polymère semi-conducteur. Cette stratégie montre qu'au sein d'une matrice polymérique du type n, le graphène joue un rôle important en améliorant non seulement les caractéristiques électroniques des dispositifs, mais aussi le comportement ambipolaire et plus particulièrement le transport des trous. La combinaison de la haute performance de ce matériel 2D avec la capacité du polymère à former un film, en plus de la simplicité du procédé de dépôt, renforce l'application des matériaux composites au graphène dans les circuits logiques.
Par la même approche de mélange, de nouveaux nanorubans de graphène dispersés en solution, ont été utilisés pour améliorer la performance des dispositifs basés sur un polymère amorphe de type p. Pareil au graphène, l'introduction de ces nanorubans forme une voie de percolation pour les charges améliorant ainsi la performance des dispositifs dans l'obscurité ainsi que sous illumination. Ce qui ouvre la possibilité à des applications dans dispositifs optoélectroniques.
En outre, on montre que le niveau d'énergie du HOMO d'une série d'hydrocarbures aromatiques polycycliques est modifié par la taille de ces nanaostructures ainsi que par les substituants sur les bords. Les dispositifs basés sur l'un des candidats de la série chlorée montrent un type n avec une basse mobilité qui augmente par traitement thermique. Finalement, les dispositifs photosensibles multifonctionnels ont été examinés par l'introduction de molécules photochromiques avec différents substituants au sein des films semi-conducteurs à base de polymère ou de molécules de petite taille qui ont été trouvés influer la photo-commutation.

Mots clés: Graphène, nanorubans de graphène, Transistor organique à effet de champ.

Résumé en anglais

This thesis demonstrates that graphene produced by liquid-phase exfoliation can be co-deposited with a polymeric semiconductor for the fabrication of thin film field-effect transistors. The introduction of graphene to the n-type polymeric matrix enhances not only the electrical characteristics of the devices, but also the ambipolar behavior and the hole transport in particular. Combining the high performance of a fascinating 2D material with the ideal film forming ability of the polymer in addition to the simple one-step deposition process, provides a prospective pathway for the application of graphene composites for logic circuits.
The same approach of blending was adopted to enhance the electrical characteristics of an amorphous p-type polymer semiconductor by addition of an unprecedented solution processable ultra-narrow graphene nanoribbon. Similarly to graphene, the introduction of GNRs forms percolation pathway for the charges resulting in enhanced device performance in dark as well as under illumination therefore paving the way for applications in (opto)electronics.
Moreover, the energy of the HOMO level of a series of polycyclic aromatic hydrocarbons was found to be tuned by their size as well as their edge decoration. Devices based on one of chlorinated candidates exhibited n-type behavior with a low mobility that was shown to be enhanced by thermal annealing.
Finally, multifunctional photoresponsive devices were examined by introducing photochromic molecules exposing different substituents into small molecule or polymeric semiconductor films that were found to affect the photoswitching behavior.

Keywords: Graphene, graphene nanoribbons, organic field-effect transistor.